IMPERIAL

Imperial College London

Department of Electrical and Electronic Engineering

Transient Stability Analysis of Power Systems Containing Grid-Following Inverters

Yifan Zhang

October, 2025

Submitted in part fulfillment of the requirements for the degree of Doctor of Philosophy in Electrical Engineering of Imperial College London and the Diploma of Imperial College London.

Declaration of Originality

I, Yifan Zhang, declare that the work in this thesis is my own. The work of others has been appropriately referenced. A full list of references is given in the bibliography.

Copyright

The copyright of this thesis rests with the author. Unless otherwise indicated, its contents are licensed under a Creative Commons Attribution-Non Commercial 4.0 International Licence (CC BY-NC).

Under this licence, you may copy and redistribute the material in any medium or format. You may also create and distribute modified versions of the work. This is on the condition that: you credit the author and do not use it, or any derivative works, for a commercial purpose.

When reusing or sharing this work, ensure you make the licence terms clear to others by naming the licence and linking to the licence text. Where a work has been adapted, you should indicate that the work has been changed and describe those changes.

Please seek permission from the copyright holder for uses of this work that are not included in this licence or permitted under UK Copyright Law.

Abstract

Electric power systems are undergoing a fundamental transition from synchronous generator (SG)-dominated systems to inverter-based resource (IBR)-dominated systems. Grid-following (GFL) inverters are widely deployed as interfaces for renewable generation. The large-signal stability properties of IBRs differ substantially from SGs. More importantly, the stability assessment tools that have served well in SG-dominated systems, such as the equal-area criterion and global energy functions, cannot be directly applied to IBR-dominated grids.

This thesis tackles three key stability questions: (i) how might energy function methods be adapted for use in IBR grids, (ii) how can large-signal stability of mixtures of GFL and GFM inverters be analyzed, and (iii) how can models of IBR with multiple nest control loops be simplified for analysis.

First, the large-signal stability of PLLs is investigated in depth using both manifold theory and energy functions. A new energy function tailored for proportional–integral controllers is proposed.

Second, this thesis elucidates the interaction mechanisms among heterogeneous inverters—including GFL, grid-forming (GFM), and grid-supporting (GSP) types. It is proven that no energy function exists for such systems. To overcome this barrier, a manifold theory is employed to accurately determine the region of attraction (ROA). To address the computational complexity, reduced-order models of the inverter are used. The metric - stability radius (SR) - is defined to evaluate the large-signal stability margin.

Third, to analyze the large-signal coupling between PLL and outer control loops such as DC-link voltage control (DVC) and terminal voltage control, an asymptotic analysis approach, termed the bandwidth separation method, is proposed. Through this method, it is revealed that there is a tradeoff between phase-angle stability and DC-link stability in PLL–DVC bandwidth configuration. Optimal bandwidth configurations are identified under various grid fault conditions.

Power hardware-in-the-loop and control hardware-in-the-loop experiment platforms are built and used to validate all theoretical analyses.

Acknowledgements

I would like to express my deepest gratitude to my PhD supervisor, Professor Timothy C. Green, for his exemplary guidance, constant encouragement, and unwavering support throughout my time at Imperial College London. His profound knowledge, rigorous standards, and passion for research will continue to shape both my career and my life.

I am also sincerely grateful to my co-supervisor, Dr. Yunjie Gu, for his constructive guidance on my research, his continuous academic support, and his long-standing care and encouragement throughout my doctoral studies. His insightful advice and thoughtful supervision have been invaluable to my academic development.

My visit to Cornell University was truly unforgettable. I am deeply grateful to Professor Hsiao-Dong Chiang for his selfless help and support with both my research and daily life during my time in the United States. He introduced me to the field of power system transient stability and nonlinear theory, and his mentorship has had a profound influence on my academic thinking. It is a great privilege and honor to have studied under his supervision.

I would also like to express my sincere appreciation to the examiners, Professor Balarko Chaudhuri and Dr. Michael Merlin, for their careful reading of this thesis and their insightful comments and suggestions, which have helped to improve the clarity, quality, and presentation of the final manuscript.

I would like to thank Dr. Yitong Li and Dr. Yue Zhu, for the many technical suggestions I received from them. They have been academic mentors and role models to me, and I am deeply grateful for their help throughout my four years in London.

Many thanks to my colleagues at Imperial College London for their help and friendship, including Dr. Philip Clemow, Dr. Adrià Junyent-Ferré, Mr. Guoqing Gao, Mr. Zitian Qiu, Mr. Yaoxin Wang, for his valuable assistance with the experimental work, and all my other colleagues. I am also grateful to my friends in the UK and in China for the wonderful times we have shared.

Last, and most importantly, I would like to thank my parents for their immense support and endless love.

List of Abbreviations

CCT Critical clearing time

CHIL Control hardware-in-the-loop

DAE Differential-algebraic equation

DOA Domain of attraction (same as ROA)

DVC DC-link voltage control

EMT Electromagnetic transient

EP Equilibrium point

GFL Grid-following

GFM Grid-forming

GSP Grid-supporting

HIL Hardware-in-the-loop

IBR Inverter-based resource

LPF Low-pass-filter

ODE Ordinary differential equation

PCC Point of common coupling

PHIL Power hardware-in-the-loop

PI Proportional–integral

PLL Phase-locked loop

PSC Power synchronization (p–ω droop) control

pu Per-unit

RES Renewable energy resources

ROA Region of attraction

SEP Stable equilibrium point

SG Synchronous generator

SPO Stable periodic orbit

SR Stability radius

TVC AC terminal voltage control

UEP Unstable equilibrium point

UPO Unstable periodic orbit

Contents

1 Introduction **12**

1.1 Background and Motivation . . . 12

1.1.1 Trend toward IBR-dominated power systems . . . 12

1.1.2 Need for New Transient Stability Analysis for Power Systems with GFL Inverters . . . 15

1.1.3 Challenges of Transient Stability Analysis for Power Systems with GFL Inverters . . . 18

1.2 Literature Review . . . 22

1.2.1 Large-signal stability of single GFL inverter system . . . 22

1.2.2 Large-signal stability of multiple inverter systems containing GFL inverters . . . 29

1.3 Research Gaps, Problem Statement, and Research Objectives . . . 30

1.4 Research Approaches, Original Contributions, and Thesis Structure . . . 33

1.4.1 Research Approaches . . . 33

1.4.2 Original Contributions . . . 34

2 Manifold Property and Revisiting of Energy-Function-based Method for GFL Inverter **36**

2.1 Modeling of PLL . . . 37

2.1.1 Manifold Theory and ROA . . . 39

2.1.2 Impact of Modeling Choices . . . 40

2.2 Manifold and Bifurcation Properties . . . 42

2.2.1 Inverter Mode . . . 42

2.2.2 Rectifier Mode . . . 43

2.3 Energy-Function-based Method for PLL . . . 46

2.3.1 Overview of the existing energy function for PLL . . . 46

2.3.2 PI-controller energy function . . . 49

2.3.3 More applications of the PI-controller energy function . . . 52

2.4 Results of HIL Experiment and EMT Simulation . . . 53

2.5 Summary . . . 60

3 Large-Signal Stability of Power Systems with Mixtures of GFL, GFM and GSP Inverters **61**

3.1 Modelling and Order-reduction of Two-Inverter Systems . . . 61
3.1.1 Large-signal modeling and order reduction of different inverter types 62
3.1.2 Complete two-inverter system . . . 63
3.2 Non-existence of Energy Function in the System Containing GFL inverters . 64
3.3 Stability Radius (SR) based on Manifold Theory . . . 66
3.4 Manifold Property and Bifurcation Phenomenon in Two-Inverter System . . 70
3.4.1 Bifurcation in two GFL inveter system [$D_1 \neq 0, D_2 \neq 0$ in (3.3)] . . . 70
3.4.2 Bifurcation in the GFL and GFM inverter system [$D_1 = 0, D_2 \neq 0$ in (3.3)] . . . 71
3.4.3 Existence of SPO . . . 71
3.5 PHIL Platform and EMT Simulation Setup . . . 72
3.6 GFL-GFL Interaction . . . 74
3.6.1 Large-Signal Instability Mode versus Grid Inductance . . . 75
3.6.2 Validation of the Order Reduction Approach . . . 79
3.7 GFL-GFM(GSP) Interaction . . . 80
3.7.1 Comparison of GFM and GSP inverters . . . 80
3.7.2 Impact of the location of GFM and GSP inverter on transient stability enhancement . . . 84
3.8 GFM-GSP Interaction . . . 86
3.9 Summary . . . 89

4 Consideration of Control-Loop Interaction in Transient Stability of Grid-Following Inverters using Bandwidth Separation Method 91
4.1 Proposed Bandwidth Separation Method . . . 91
4.1.1 Modelling of Multiple Control Loops in GFL Inverter . . . 91
4.1.2 Bandwidth Separation Method and Analysis Steps . . . 93
4.2 Control Loops Analysis based on Proposed Method . . . 95
4.2.1 Bandwidth sequence: ω_{pll} sufficiently larger than ω_{dvc} . . . 95
4.2.2 Bandwidth sequence: ω_{dvc} sufficiently larger than ω_{pll} . . . 98
4.2.3 Impact of TVC control loop . . . 101
4.2.4 Stability region (ROA) versus bandwidth configuration . . . 104
4.3 ROA Trends with Changes in Control-Loop Bandwidth . . . 104
4.4 Analysis under Various Faults and HIL Experiment Results . . . 106
4.4.1 Voltage sag fault . . . 107
4.4.2 Phase jump . . . 111
4.4.3 Input power variation . . . 113
4.5 Summary . . . 115

5 Conclusions and Future Work 117
5.1 Contributions and Conclusions . . . 117
5.2 Future Work . . . 118

Bibliography 120

A Appendix for Chapter 3 **131**
A.1 Derivation for Two-Inverter Systems . . . 131
A.1.1 Both IBRs are GFM inverters . . . 131
A.1.2 Both IBRs are GFL inverters . . . 131
A.1.3 Combination of a GFL and GFM inverter . . . 132
A.1.4 Combination of a GFL and GSP inverter . . . 132
A.1.5 Combination of GFM and GSP inverter . . . 133
A.2 Source Code and Simulations . . . 134

B Appendix for Chapter 4 **135**
B.1 Full-Order ODE Model of GFL Inverter . . . 135
B.2 Reduced-Order Model Derivation . . . 136
B.2.1 Bandwidth sequence: ω_{pll} larger than ω_{dvc} . . . 136
B.2.2 Bandwidth sequence: ω_{dvc} larger than ω_{pll} . . . 137
B.2.3 Stability analysis of TVC subsystem . . . 138
B.3 System Parameters . . . 139
B.4 Source Code and Simulations . . . 140

List of Figures

1.1 Renewable energy installed capacity trend (2015–2024) [2]. 13
1.2 Power systems with high penetration of IBRs. 13
1.3 Two fundamental types of IBRs and their variants. 15
1.4 Schematic phase-plane illustration of transient stability. The shaded gray region denotes ROA of the post-fault system; the black dashed curve represents the fault-on trajectory; fault clearing at state 1 leads to a stable post-fault trajectory (shown in blue), whereas fault clearing at state 2 results in a unstable post-fault trajectory. 16
1.5 Comparison of SG, GFM and GFL dynamics under large disturbance [8, 17, 20, 21]. 17
1.6 Multi-inverter system containing both GFM and GFL inverters shown as a generic single-line network diagram in part (a) and as a control block diagram in part (b). 20
1.7 Research scopes on a single GFL inverter system. (Blue blocks indicate topics that are explicitly studied in this thesis, while white blocks represent related areas reviewed for completeness.) 22
1.8 Research directions in transient stability of multi-inverter systems. (Blue blocks indicate topics that are explicitly studied in this thesis, while white blocks represent related areas reviewed for completeness.) 29
1.9 Conceptual diagram of thesis. 34

2.1 (a) Modeling of PLL in Grid-following converter. (b) Relationship of variables in different frames. 37
2.2 Stability region with respect to the line dynamics. ($k_{\mathrm{p,pll}} = 10 \cdot 2\pi$, $I_d = 1$, $I_q = 0$, $R_g = 0$, $U_g = 1$ pu) 41
2.3 Bifurcation of GFL inverter (parameters: $k_{\mathrm{p,pll}} = 10 \cdot 2\pi$, $I_d = 1$, $I_q = 0$, $R_g = 0$, $U_g = 1$ pu). 42
2.4 Bifurcation of GFL rectifier (parameters: $k_{\mathrm{p,pll}} = 10 \cdot 2\pi$, $I_d = -1$, $I_q = 0$, $R_g = 0$, $U_g = 1$ pu). 44
2.5 Limit cycle of the studied system. 46
2.6 ROA estimation by traditional energy / Lyapunov function[1]. 47
2.7 ROA estimation by Lyapunov function (2.18). 48
2.8 ROA estimation by Lyapunov function (2.20). 49

2.9 Control block diagram of the nonlinear system. 50
2.10 ROA of PLL estimated by proposed PI-controller Energy function. 52
2.11 control structure of VFM inverter (DC-voltage-controlled GFM). 52
2.12 ROA of VFM inverter (DC-voltage-controlled GFM). 53
2.13 HIL Experiment Setup. 54
2.14 Results of Inverter Mode under critical fault clearing time, and comparison of different models. 55
2.15 Results of rectifier Mode under critical fault clearing time, and comparison of different models (phase portrait). 56
2.16 Time-domain HIL results of rectifier Mode under critical fault clearing time, and comparison of different models. 57
2.17 EMT simulation results with FRT, compared with the corresponding non-FRT cases under identical system parameters and fault conditions. All cases are consistent with Figure 2.14 (b),(d), with the same fault-clearing time $t_{\text{fault}} = 0.062$ s. FRT strategy 1 maintains active power during the fault, whereas FRT strategy 2 enforces zero active power. 58

3.1 Large-signal modeling of different types of inverters. 62
3.2 Two-inverter system. 63
3.3 Comparison between SR and other large-signal stability assessment methods. On the phase-plane plot, the ROA is shown with a solid black line (manifold theory), gray rectangular shading (CCA method), and green line (local Lyapunov method). The SR is a red dashed line. The SEP is an open blue circle. 67
3.4 Relationships among proposed metrics. 67
3.5 Procedure for ROA and SR computation in multi-inverter systems. 68
3.6 Illustration of the SR concept for a three-dimensional system: (a) three-IBR infinite-bus network; (b) visualization of the ROA and SR, where the grey surfaces represent the real stability boundary (boundary of the ROA), and the red sphere denotes the SR centered at the SEP. 69
3.7 Bifurcation diagram for two GFL inverter systems. [$k_{\text{pll1}} = 2.5 \times 2\pi$, $k_{\text{pll2}} = 10 \times 2\pi$, that is, $k_{\text{pll1}}/k_{\text{pll2}} = 0.25$ in (b), (c), (d)] 70
3.8 Bifurcation diagram for paralleled GFM and GFL inverter systems. [$k_{\text{pll}} = 1.5 \times 2\pi$, $k_{\text{droop}} = 2.5 \times 2\pi$, that is,$k_{\text{pll}}/k_{\text{droop}} = 0.6 \times 2\pi$ in (b), (c), (d)] . . 72
3.9 PHIL experimental platform. 73
3.10 Phase portraits of two GFL inverters for four test conditions as assessed by the manifold theory. Pre-fault SEP is marked with a solid blue dot, the post-fault SEP with a hollow blue dot, and the fault clearing point with a yellow triangle. The dashed black line represents the analytical trajectories. Trajectories generated by EMT simulations are represented as red lines during the fault and blue lines post-fault. The green dashed line, where it exits, is a stable periodic orbit. This color convention is applied in subsequent similar figures. 76

3.11 PHIL experiment results of two paralleled GFL inverters under $X_g = 0.35$ pu. 77
3.12 PHIL experimental results of two paralleled GFL inverters under $X_g = 0.4$ pu, $t_{\text{fault}} = 0.212$ s. 78
3.13 Comparison of EMT simulation results with different $k_{\text{i,pll}}$ in PLL for different X_g and t_{fault}. 79
3.14 The phase portrait of the system before, during and after the fault for various t_{fault} as marked on the figures. Color scheme for lines and markers follows that of Figure 3.10. 82
3.15 PHIL experimental results for the case where IBR2 is realized by GFM inverter. 83
3.16 PHIL experimental results under $t_{\text{fault}} = 0.28$ s for the case where IBR2 is configured as a GSP with two different values of k_v. 84
3.16 PHIL experimental results under $t_{\text{fault}} = 0.28$ s for the case where IBR2 is configured as a GSP with two different values of k_v. (continued) 85
3.17 The change of ROA with respect to voltage control gain k_v and PLL bandwidth of GSP inverter. 86
3.18 The EMT simulation results, ROA and SR under various locations of IBR2 (t_{fault}=0.4 s, 1 s). Color scheme for lines and markers follows that of Figure 3.10. 87
3.19 The phase portraits of GFM inverter and GSP inverter with three choices of voltage control gains. Fault duration set to estimated critical clearing time for each case ($t_{\text{fault}} = 0.15$ s, 0.31 s, and 0.45 s respectively). Color scheme for lines and markers follows that of Figure 3.10. 89
3.20 The change of ROA and SR with respect to (a)(b) voltage control gain k_v, and (c)(d) location of GSP inverter in the transmission line (The total impedance of transmission line $X_g + X_1 = 1.1$ pu is kept constant). 90

4.1 System diagram of grid-following inverter. 92
4.2 Example curve of $p(i_d)$ (blue line on upper axes) and stability region (ROA) of DVC (lower axes) when $\omega_{\text{pll}} \gg \omega_{\text{dvc}}$. 96
4.3 Theoretical and simulation results under $\omega_{\text{pll}} = 15$ Hz$\times 2\pi$, $\omega_{\text{dvc}} = 2$ Hz$\times 2\pi$, with a 0.9 pu voltage sag fault. The corresponding CCT is approximately 0.16 s. 97
4.4 Example curve of $h(\delta)$ (blue line on upper axes) and stability region (ROA) of PLL (lower axes) when $\omega_{\text{dvc}} \gg \omega_{\text{pll}}$. 99
4.5 Theoretical and simulation results under $\omega_{\text{pll}} = 2$ Hz$\times 2\pi$, $\omega_{\text{dvc}} = 15$ Hz$\times 2\pi$, with a 0.9 pu voltage sag fault. The corresponding CCT is approximately 0.2 s. 100
4.6 Example curve of $p'(i_d)$ (upper axes) and stability region (ROA) of DVC (lower axes) when ω_{tvc} and $\omega_{\text{pll}} \gg \omega_{\text{dvc}}$. 101
4.7 Example curve of $h'(\delta)$ (upper axes) and stability region (ROA) of PLL (lower axes) when $\omega_{\text{tvc}} \gg \omega_{\text{dvc}} \gg \omega_{\text{pll}}$. 102

4.8 The phase portrait comparison between simulation and reduced-order model, with a 0.6 pu voltage sag fault, $\omega_{\text{tvc}} = 20$ Hz $\times 2\pi$, $k_v = 2$. 103
4.9 Examples of how the ROA varies with control parameters in the δ–i_d phase plane. 105
4.10 HIL experimental platform. 106
4.10 HIL experimental platform. (continued) 107
4.11 PLL standalone system under 0.6 pu voltage sag fault with $\omega_{\text{pll}} = 16$ Hz$\times 2\pi$, $i_d = i_{\text{d,sep}}$ to achieve $P_{\text{in}} = 1$ pu active power output. 108
4.12 GFL inverter under 0.9 pu voltage sag fault with slow TVC. $\omega_{\text{tvc}} = 0.3$ Hz $\times 2\pi$, $\omega_{\text{pll}} = 16$ Hz $\times 2\pi$, $\omega_{\text{dvc}} = 2$ Hz $\times 2\pi$, and fault clearing time t_{fault}=0.24 s. 109
4.13 Adverse interaction between PLL and DVC and the resulting voltage-collapse mechanism. 110
4.14 GFL inverter under 0.9 pu voltage sag fault without fault clearance, with fast TVC $\omega_{\text{tvc}} = 20$ Hz$\times 2\pi$,$\omega_{\text{pll}} = 16$ Hz$\times 2\pi$,$\omega_{\text{dvc}} = 2$ Hz$\times 2\pi$, and without fault clearance. 110
4.15 GFL inverter under 0.6 pu voltage sag fault with fast TVC. $\omega_{\text{tvc}} = 20$ Hz $\times 2\pi$, $\omega_{\text{pll}} = 2$ Hz $\times 2\pi$, $\omega_{\text{dvc}} = 15$ Hz $\times 2\pi$, and fault clearing time t_{fault}=0.1 s. 111
4.16 Phase portraits of phase jump fault under $_{\Delta}\varphi$ =15, 19, 21, 25, 48 degrees. Blue trajectories: $\omega_{\text{pll}} = 1$ Hz $\times 2\pi$, $\omega_{\text{dvc}} = 8$ Hz $\times 2\pi$, no TVC; green trajectories: ω_{pll} increased to 20 Hz $\times 2\pi$; orange trajectories: fast TVC is added with $\omega_{\text{tvc}} = 20$ Hz $\times 2\pi$, ω_{pll} remained at 1 Hz $\times 2\pi$. The red rectangles represent the fault-occurring point. 112
4.17 Time-domain results for GFL inverter under 25 degree phase jump fault with $\omega_{\text{dvc}} = 8 \times 2\pi$. 112
4.18 Phase portrait under input power step changes from 0, 0.2 pu, and 0.45 pu to 1 pu. Blue trajectories: $\omega_{\text{pll}} = 18$ Hz $\times 2\pi$, $\omega_{\text{dvc}} = 3$ Hz $\times 2\pi$, no TVC. Green trajectories: ω_{pll} decreased to 0.5 Hz $\times 2\pi$, ω_{dvc} unchanged, no TVC. Orange trajectories: ω_{pll} decreased to 0.5 Hz $\times 2\pi$, ω_{dvc} unchanged, with fast TVC added at $\omega_{\text{tvc}} = 20$ Hz $\times 2\pi$. The red rectangles represent the initial operating point. 114
4.19 Time-domain results of the GFL inverter under input power step changes. . 114
4.20 Time-domain response of the GFL inverter during restart. The output power steps from 0 to 1 pu. Control parameters: $\omega_{\text{pll}} = 0.5$ Hz $\times 2\pi$, ω_{dvc} unchanged, and fast TVC added with $\omega_{\text{tvc}} = 20$ Hz $\times 2\pi$. 115

B.1 Stability region of PLL subsystem under different i_d ($\omega_{\text{pll}} = 15$ Hz $\times 2\pi$). . . 136

List of Tables

1.1 Comparison of transient stability assessment methods 26

2.1 Simulation and HIL experiment parameters 54

3.1 Coefficients of the Expression of Two-Inverter System 64
3.2 System Parameters in PHIL Platform 74
3.3 Detailed System Parameters in GFL-GFL Inverters System 75
3.4 Comparison between SR-based CCT estimation and the theoretical CCT obtained from the real ROA 75
3.5 Detailed System Parameters in GFL - GFM(GSP) Inverters System 81
3.6 Comparison between SR-based CCT estimation and the theoretical CCT for different IBR2 configurations 81
3.7 Detailed System Parameters in GFM - GSP Inverters System 88
3.8 Comparison between SR-based CCT estimation and the theoretical CCT obtained from the real DOA under different GSP voltage gains 88

4.1 ROA Comparison and Parameters Feasible Region under Different Control Loop Configurations 104

B.1 Parameters in Simulation and HIL Experiment 139

Chapter 1

Introduction

This chapter introduces the motivation for and importance of studying the transient stability of inverter-based resources (IBRs). Particular emphasis will be placed on grid-following (GFL) inverters, how they are represented and methods for analyzing large-signal stability.

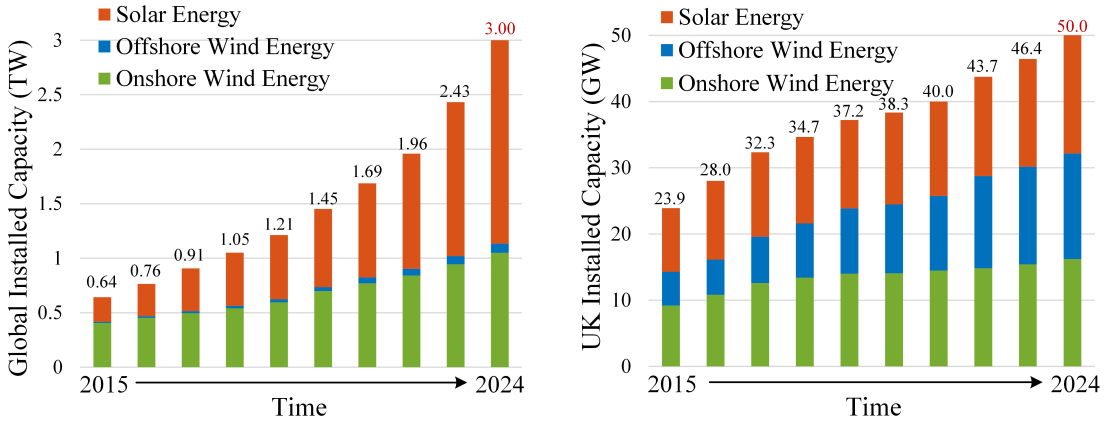
Against the backdrop of rapid renewable energy development and the increasing penetration of power-electronic inverters, GFL inverters are playing an increasingly important role as a key interface for renewable energy integration into modern power systems. The fundamental differences in synchronization mechanisms exist among GFL inverters, synchronous generators (SGs), and grid-forming (GFM) inverters, and those differences give rise to stability challenges for GFL inverters. In this chapter, current research progress on large-disturbance synchronization stability and transient analysis methods is reviewed, and the key challenges and research gaps for analyzing power systems with high penetration of GFL inverters are summarized. The main contributions of this thesis are outlined, followed by the organization of the subsequent chapters and a summary of related publications.

1.1 Background and Motivation

1.1.1 Trend toward IBR-dominated power systems

In response to the challenge of climate change, carbon emission reduction has become a consensus within the international community. Many countries are actively developing clean energy supply systems with renewable energy as the core [1], thereby facilitating the transition of human society from industrial civilization to ecological civilization. Against this backdrop of energy transition and environmental concerns, renewable energy resources (RES), particularly wind and photovoltaic energy, have experienced rapid development. The installed capacity of RES has grown significantly and it has become the primary means of global energy growth.

Global cumulative installed capacity of RES increased rapidly from 0.64 TW in 2015 to 3 TW in 2024, accounting for 46.2% of total electricity capacity, with an average annual growth rate of over 20%, as shown in Figure 1.1 [2]. In the UK, RES capacity has more



(a) Global renewable energy installed capacity.

(b) UK renewable energy installed capacity.

Figure 1.1: Renewable energy installed capacity trend (2015–2024) [2].

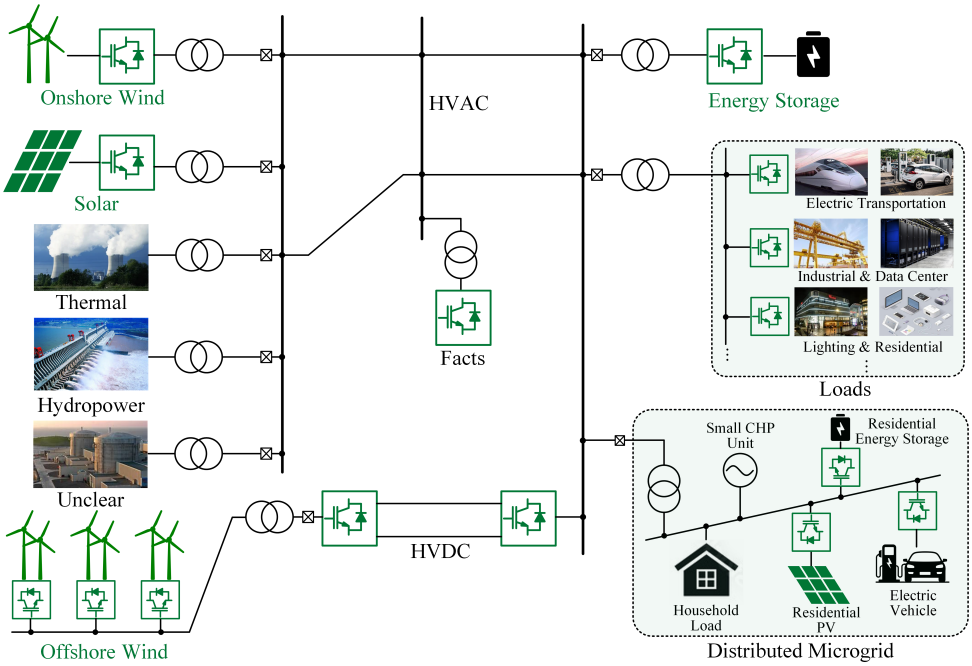


Figure 1.2: Power systems with high penetration of IBRs.

than doubled over the past decade. By 2024, the installed RES capacity reached 50 GW, including 32 GW of wind power, which represented the highest share in the national electricity mix to date at 35.8%.

This remarkable growth of RES has propelled IBRs to the forefront, such that they have become the dominant interface in modern power systems. IBRs can realize efficient grid connection of RES and are steadily replacing SGs on the generation side. Besides this change in generation, power electronic inverters are also rapidly expanding in transmission, distribution, and consumption, driving modern power systems toward inverter-rich architectures (an illustrative schematic diagram is shown in Figure 1.2). On the transmission side, advanced technologies such as HVDC and flexible AC transmission are increasingly

deployed for offshore wind integration, long-distance power delivery, and interconnection of grids (e.g., Germany's DolWin3 offshore project [3] and the UK–Belgium Nemo Link [4]). On the distribution side, microgrids leverage power electronic inverters to coordinate local sources, storage, and loads, while on the consumption side, electrified transportation, large data centers, and residential demand are also increasingly enabled by power electronic inverters. As a result, the system is evolving from the traditional SG-dominated paradigm toward an IBR-dominated system, exhibiting richer and more complex dynamics under disturbances, which poses significant challenges for dispatch, operation, and control [5].

IBRs are composed of semiconductor power devices, with a hardware architecture fundamentally different from that of synchronous machines. Unlike SG, whose port characteristics are determined by electromagnetic structures, the behavior of IBRs is dominated by diverse software-based control strategies [6]. Regarding small-signal stability, although these control strategies vary significantly, the approach of linearizing the relevant equations around an operating point remains applicable to inverter-dominated power systems. This methodology has been extensively studied and is now well established, yielding substantial results [7, 8]. In contrast, for the more complex issue of transient stability, the governing mechanisms differ: whereas the transient characteristics of synchronous machines are driven by rotor electromechanical dynamics, those of IBRs are primarily dictated by the transient response mechanisms of various synchronization control strategies.

Based on their synchronization principles, IBRs can be classified into GFL inverters and GFM inverters. A GFL inverter detects the phase of the voltage at the Point of Common Coupling (PCC) using a classical phase-locked loop (PLL) and this is how synchronization with the power grid is achieved. It typically does not regulate system frequency or voltage and is commonly modeled as a current source in parallel with a large impedance [9]. In contrast, a GFM inverter actively synthesizes a reference voltage with a phase and magnitude set according to the power synchronization control (PSC) loop, thereby participating in system frequency and voltage regulation. A GFM inverter is typically modeled as a voltage source in series with a small impedance.

The synchronous reference frame PLL (SRF-PLL) is the most widely adopted configuration in practical GFL inverters. To enhance robustness under asymmetrical or distorted grid conditions, various advanced PLL structures have also been proposed, including the decoupled double synchronous reference frame PLL (DDSRF-PLL) [10, 11] and the double second-order generalized integrator PLL (DSOGI-PLL) [12, 13]. However, their synchronization dynamics can be interpreted as a modified SRF-PLL with additional filtering dynamics, and under symmetrical faults or positive-sequence-dominated operating conditions, they are effectively equivalent to those of an SRF-PLL [14, 12]. Unless otherwise specified, this thesis select SRF-PLL as a representative and analytically tractable synchronization mechanism, owing to its simple structure, widespread adoption in large-signal and transient stability studies [6], and well-understood dynamic behavior. The large-signal analysis of SRF-PLL provides fundamental insights into PLL-induced instability mechanisms and offer a theoretical basis that can be extended to more advanced PLL variants.

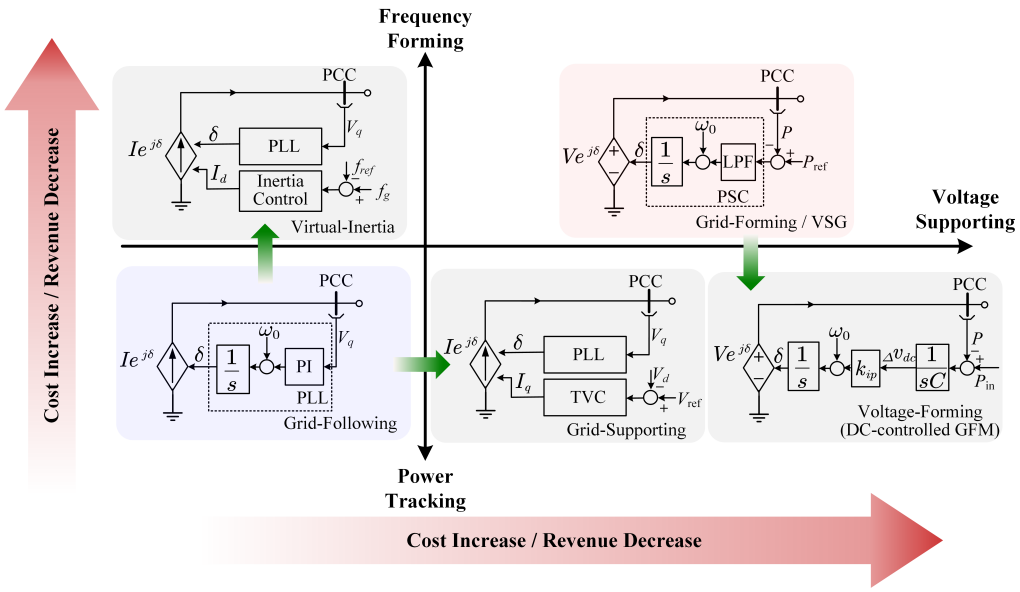


Figure 1.3: Two fundamental types of IBRs and their variants.

At present, most grid-connected equipment in power systems still adopts GFL control. It has been found that performance of PLL-synchonised GFL depends strongly on the grid strength [8]. In weak grids, the coupling between the PLL and grid impedance becomes pronounced, sharply increasing the risk of instability [8, 6, 15]. GFM inverters can address the synchronization-stability issues of GFL units under weak grids; by emulating the SG rotor dynamics / active-power–frequency droop, they can achieve synchronization behavior comparable to SGs, and even surpass them in some respects. Nevertheless, operating GFM inverters typically necessitates power headroom in order to provide grid support, leading to renewable curtailment and revenue reduction, or else requires installation of energy storage and additional costs, thus, GFM operation is not always economically reasonable [16, 17]. The literature [8] also indicates that the GFM and GFL inverters will coexist long-term in future power systems, and GFL remains indispensable.

Building on these two fundamental IBR categories, some additional variants have been developed in both academia and industry. Figure 1.3 presents a conceptual classification of IBRs into four families, according to their grid services provided and synchronization mechanisms. GFM inverters are capable of providing both frequency and voltage support, whereas typical GFL inverters primarily operate in a power-tracking mode and do not inherently provide both of such supports [9]. To enhance grid support while retaining the grid-following (GFL) synchronization structure, AC voltage regulation can be incorporated into GFL schemes; such inverters are referred to as grid-supporting (GSP) inverters [18, 19].

1.1.2 Need for New Transient Stability Analysis for Power Systems with GFL Inverters

Transient stability is defined as the ability of a power system to maintain synchronism following a large disturbance [20, 21]. Such disturbances, commonly referred to as contin-

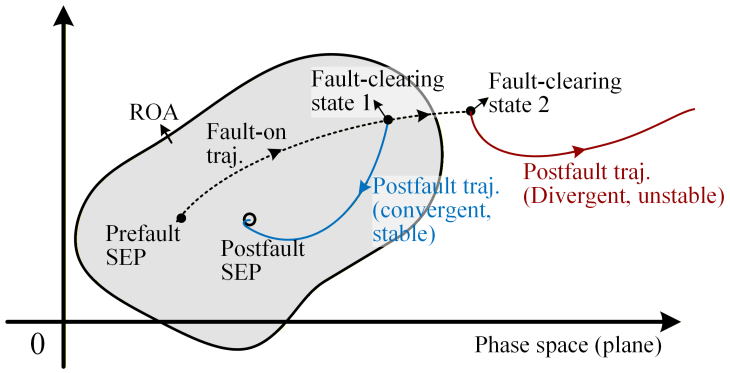


Figure 1.4: Schematic phase-plane illustration of transient stability. The shaded gray region denotes ROA of the post-fault system; the black dashed curve represents the fault-on trajectory; fault clearing at state 1 leads to a stable post-fault trajectory (shown in blue), whereas fault clearing at state 2 results in a unstable post-fault trajectory.

gencies, typically include short circuits, loss of generation units, loss of significant loads, line outages, or phase jumps caused by sudden power flow changes. Since the system exhibits non-linear behavior under such conditions, transient stability is also called large-signal stability, particularly in the context of IBRs [8], in contrast to small-signal stability analysis, which relies on linearization around an operating point.

Transient stability assessment in power systems is commonly carried out by estimating the stability region, which is also referred to as the region of attraction (ROA) or the domain of attraction (DOA). All of these terms describe the same concept in nonlinear control theory and the context of this thesis. When the system is subjected to a large disturbance, it evolves along the "fault-on trajectory" until the fault is cleared. If the "fault-clearing state" lies within the ROA of the corresponding post-fault stable equilibrium point (SEP), the system will converge back to that SEP, and the post-fault system is deemed to be transiently stable under the considered contingency. Otherwise, the post-fault system is deemed to be transiently unstable, which leads to severe consequences for the entire power system, including cascading outages [22] or even large-scale blackouts [23]. The above concepts of transient stability and stability region (i.e. ROA) are illustrated schematically in Figure 1.4. This geometric interpretation highlights that transient stability is jointly determined by the system state at fault clearing—which depends on the fault trajectory and its duration—and the size of the corresponding ROA. The ROA size will be quantified later in this thesis through the definition of the stability radius (SR).

In recent years, with increasing penetration of IBRs, especially GFL inverters, blackout incidents have become more frequent, causing substantial economic losses. On September 28, 2016, in South Australia, extreme weather triggered transmission faults, and many wind farms disconnected due to inappropriate inverter protection and control settings, leading to severe generation loss, interconnector tripping, and a state-wide blackout under low-inertia conditions [24]. On August 16, 2016, during the Blue Cut Fire in California, multiple transmission faults caused about 1,200 MW of solar PV to disconnect or enter momentary cessation due to poor PLL disturbance rejection and limited low-voltage ride-

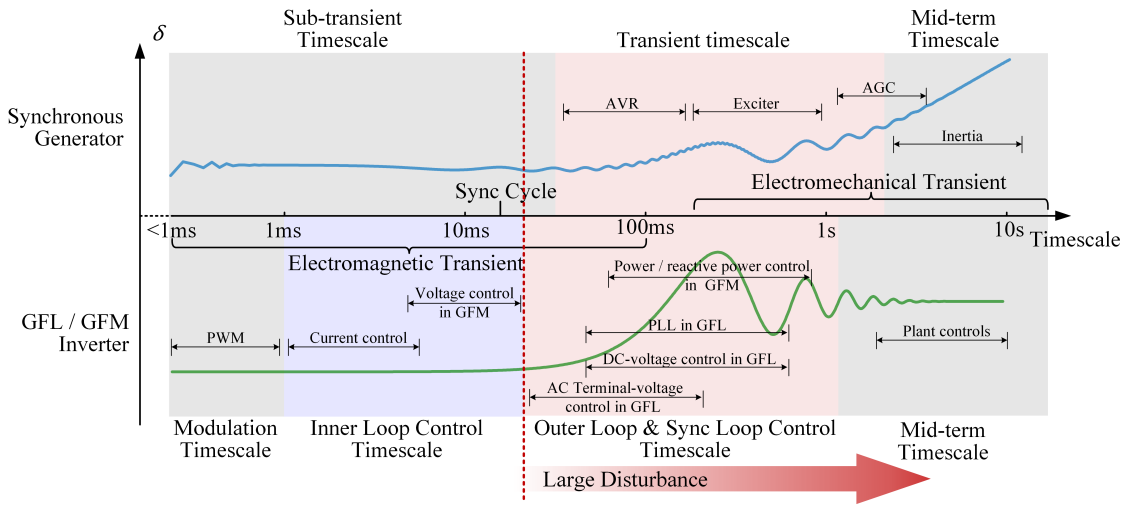


Figure 1.5: Comparison of SG, GFM and GFL dynamics under large disturbance [8, 17, 20, 21].

through capability, resulting in significant frequency fluctuations [25]. On April 28, 2025, the Iberian Peninsula suffered a massive blackout when a voltage surge and cascading trips caused the loss of over 15 GW of generation, with the system characterized by extensive reliance on GFL photovoltaic generation. Available evidence points to voltage regulation deficiencies, and adverse interactions between GFL inverters and the grid during large disturbances as key contributing factors to the cascading instability and eventual system collapse [26].

Motivated by the critical necessity of practical applications, the transient stability of IBRs has become a research hotspot in academia [6, 27, 28, 29]. The diversity of control algorithms and the fast response of controllers have significantly influenced the dynamic behavior of modern power systems and as a result, transient stability in today's power systems exhibits novel characteristics, making traditional modeling and analysis methods, developed based on conventional AC system properties, less suitable for emerging grids and their operational requirements. In particular, since the synchronization mechanism of GFL inverters (relying on PLLs) fundamentally differs from that of GFM inverters and SGs, transient stability assessment and stability region characterization for systems with GFL inverters require new approaches.

There are various control loops for an inverter and, to simplify design, they are designed to operate on distinct time scales defined by their bandwidth settings, as illustrated in Figure 1.5. The timescale of the inner control loop is typically within 10 ms, and under large disturbances, it usually converges rapidly owing to its high bandwidth, thereby exerting only a minor influence on the overall dynamics. Large-disturbance behavior is instead dominated by outer loops [6, 27] and for this reason, most studies of large-signal disturbance neglect inner-loop dynamics, modeling GFM inverters as controlled voltage sources and GFL inverters as controlled current sources. Since synchronization is the cornerstone of stable operation in three-phase AC systems, and the PLL is the core synchronization

mechanism of GFLs, the research community has concentrated on PLL dynamics as the basis for modeling GFLs, while neglecting inner-loop, DC-link voltage control (DVC), and AC terminal voltage control (TVC) dynamics. Moreover, under severe grid faults, GFL inverters usually operate in constant-current mode or with saturated current output. Consequently, academic studies have predominantly modeled GFLs by focusing on PLL dynamics, while neglecting the inner-loop current control. When the DVC is relatively slow, such simplifications appear reasonable, however, the bandwidth settings of outer control loops remain unsettled, and in fault scenarios, GFLs are not always able to detect grid faults or switch to fault-specific control modes, highlighting the necessity of multi-loop interaction analysis [30].

GFL, GFM, and GSP inverters often coexist within the same system and so PSC loops and PLL loops coexist, which complicates analysis. The incorporation of voltage control further complicates large-signal interactions. Traditional principles for analyzing large-signal interactions developed for SGs are no longer applicable [8]. It is therefore essential to investigate the large-signal interactions introduced by GFL inverters from a multi-inverter perspective, and to develop new methodologies for transient stability assessment of power systems with GFL inverters.

1.1.3 Challenges of Transient Stability Analysis for Power Systems with GFL Inverters

For traditional SG-dominated power systems, the direct method, which avoids the computationally expensive time-domain integration of the post-fault system dynamics, is well-established and has become one of the classic approaches for transient stability analysis [23]. The essence of the direct method is to estimate the stability region (ROA) through an energy function (or Lyapunov function). An energy function has been viewed as an extension of, or a special case of, the Lyapunov function, tailored for global system analysis. Unlike a Lyapunov function, which must be positive definite with a locally non-positive derivative, an energy function requires its derivative to be non-positive globally, while its value does not need to be strictly positive. The ROA can be estimated by using the level set

$$\Omega_c = \{\, x \mid W(x) \leqslant c \,\},$$

where $W(x)$ denotes a Lyapunov or energy function [31]. The set Ω_c contains the stable equilibrium point (SEP) of the system and satisfies $\Omega_c \subseteq D$, where

$$D = \{\, x \mid \dot{W}(x) \leqslant 0 \,\}$$

is the region in which the derivative of $W(x)$ is non-positive. For energy functions, the value at a relevant unstable equilibrium point (UEP) is chosen as the critical energy (since the energy function attains a minimum at UEP on the stability boundary). The ROA is then typically estimated by the level set, that is, all states whose energy is less than or equal to this critical energy. By contrast, Lyapunov functions are generally valid only locally,

and for ROA estimation it is necessary to ensure that $\dot{W}(x) \leqslant 0$ throughout the level set, i.e., $\Omega_c \subseteq D$. This requirement makes it analytically challenging to determine the critical energy (or level). It should also be emphasized that the existence of an energy function (with a globally non-positive derivative) does not imply global Lyapunov stability, since boundedness of the trajectories is not guaranteed. Instead, a level set definition can bound trajectories and ensure positive invariance. In classical SG-dominated systems, however, analytical energy functions can often be readily constructed.

To operationalize the direct method, several well-known techniques—such as the closest UEP, the controlling UEP (CUEP), and the boundary-of-stability-region–based CUEP (BCU) methods—have been developed to locate the critical energy more reliably, thereby improving the estimation of the ROA [32]. A key prerequisite for these methods is the availability of analytical energy functions for transient stability analysis. In lossy networks, however, the transfer conductance introduced by resistance makes constructing both energy functions and Lyapunov functions difficult [33, 34]. Moreover, it has been rigorously shown that energy functions do not exist in the presence of such transfer conductance [35, 23]. Given that the transfer conductance is typically small, even considering the losses, there are still various methods or remedies, such as numerical approximations [23], methods based on the extension of the invariant principle [36], and dissipative systems theory [37], which can mitigate this issue.

In IBR-dominated power systems, constructing an energy function is particularly challenging: GFL inverters operating as PLL-synchronized controlled-current sources introduce cosine terms in the network coupling that manifest as transfer-conductance effects [19].

As an illustration, consider a multi-inverter system comprising j GFL inverters and k GFM inverters, as shown in Figure 1.6.

The GFL inverters are modeled as controlled current sources synchronized by PLLs. For the i^{th} GFL inverter, the PLL dynamics (in a frame rotating at the nominal frequency) are approximated by a proportional law:

$$\dot{\delta}_{l,\mathrm{i}} = k_{\mathrm{pll,i}} U_{q,\mathrm{i}} \tag{1.1}$$

where $U_{q,i}$ is the q-axis PCC voltage input to the PLL of the i^{th} inverter, $\delta_{l,i}$ denotes the PLL angle deviation of the i^{th} GFL inverter, and $k_{\mathrm{pll},i}$ is the proportional gain. This expression follows from neglecting the integral branch of the standard proportional–integral (PI) regulator, i.e., the PLL is assumed to be dominated by its proportional term, for analytical simplicity.

The GFM inverters are modeled as controlled voltage sources synchronized by PSC. Under power-frequency droop, the i^{th} GFM satisfies:

$$\dot{\delta}_{m,\mathrm{i}} = k_{\mathrm{droop,i}} \left(P_{m,\mathrm{i}} - P_{e,\mathrm{i}} \right) \tag{1.2}$$

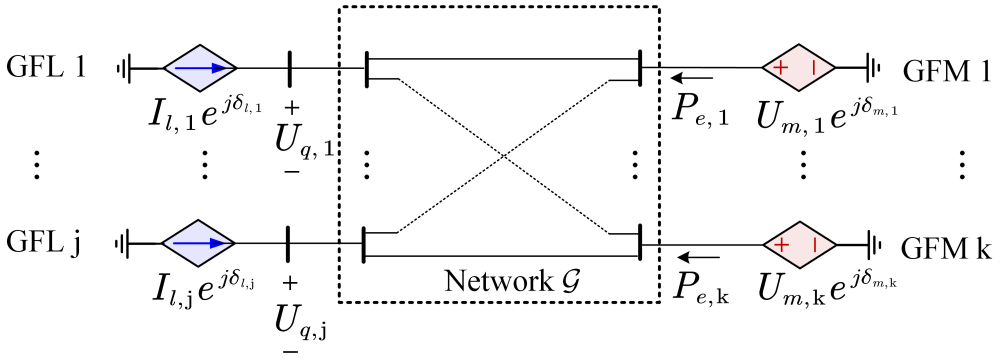
where $\delta_{m,i}$ is the GFM phase angle, $P_{m,\mathrm{i}}$ the active-power setpoint, $P_{e,\mathrm{i}}$ the measured/exported

active power, and $k_{\text{droop},i} > 0$ the droop gain.

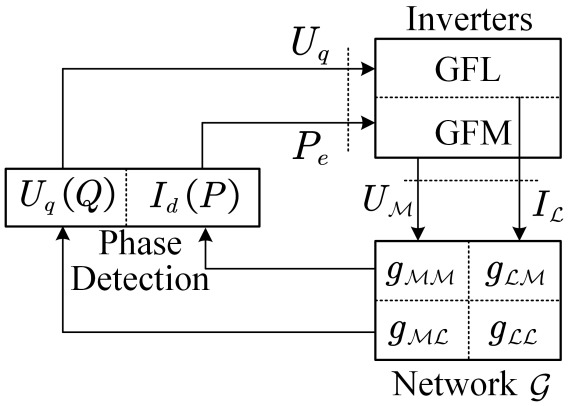
The synchronization mechanism is abstracted in Figure 1.6 (b). The current output of the GFLs is $I_{\mathcal{L}} = \begin{bmatrix} I_{l,1} & \cdots & I_{l,j} \end{bmatrix}^{\mathsf{T}}$, and the voltage output of GFM is $U_{\mathcal{M}} = \begin{bmatrix} U_{m,1} & \cdots & U_{m,k} \end{bmatrix}^{\mathsf{T}}$. After $I_{\mathcal{L}}$ and $U_{\mathcal{M}}$ are injected to the network $\mathcal{G}$, the GFMs measure the d-axis current (for power computation) and GFLs measure the q-axis voltage (as the PLL input) for their respective synchronization loops. The matrix $\mathcal{G}$ is derived from the nodal admittance matrix and satisfies

$$\begin{bmatrix} I_{\mathcal{M}} \\ I_{\mathcal{L}} \end{bmatrix} = \underbrace{\begin{bmatrix} y_{11} & y_{12} \\ y_{21} & y_{22} \end{bmatrix}}_{\text{nodal admittance matrix}} \begin{bmatrix} U_{\mathcal{M}} \\ U_{\mathcal{L}} \end{bmatrix} \tag{1.3a}$$

$$\begin{bmatrix} I_{\mathcal{M}} \\ U_{\mathcal{L}} \end{bmatrix} = \mathcal{G} \begin{bmatrix} U_{\mathcal{M}} \\ I_{\mathcal{L}} \end{bmatrix} \tag{1.3b}$$



(a) Power systems containing j GFL inverters shown as controlled-current sources on the left of the network g and k GFM inverters shown as controlled voltage-sources on the right.



(b) Abstracted block diagram of synchronization mechanism in which the GFL synchronize by detecting a voltage at the point of connection to network $\mathcal{G}$ and the GFM synchronize by detecting a current. The GFL and GFM then inject currents and voltages into the network.

Figure 1.6: Multi-inverter system containing both GFM and GFL inverters shown as a generic single-line network diagram in part (a) and as a control block diagram in part (b).

$$\mathcal{G} = \left[\begin{array}{c:c} g_{\mathcal{MM}} & g_{\mathcal{LM}} \\ \hdashline g_{\mathcal{ML}} & g_{\mathcal{LL}} \end{array}\right] = \left[\begin{array}{ccc:ccc} g^{11}_{\mathcal{MM}} & & & g^{11}_{\mathcal{LM}} & & \\ & \ddots & & & \ddots & \\ & & g^{kk}_{\mathcal{MM}} & & & g^{kj}_{\mathcal{LM}} \\ \hdashline g^{11}_{\mathcal{ML}} & & & g^{11}_{\mathcal{LL}} & & \\ & \ddots & & & \ddots & \\ & & g^{jk}_{\mathcal{ML}} & & & g^{jj}_{\mathcal{LL}} \end{array}\right] = \left[\begin{array}{c:c} y_{11} - y_{12}y_{22}^{-1}y_{21} & y_{12}y_{22}^{-1} \\ \hdashline -y_{22}^{-1}y_{21} & y_{22}^{-1} \end{array}\right] \tag{1.3c}$$

where $I_{\mathcal{M}}$ and $U_{\mathcal{L}}$ denote the GFM current and the GFL voltage, respectively. The inputs to (1.2) and (1.1)—the GFM active power and the GFL q-axis voltage—are given by

$$U_{q,\mathrm{i}} = \underbrace{\sum_{r=1}^{j} \left|g^{\mathrm{ri}}_{\mathcal{LL}}\right| I_{l,r} \cos\left(\delta_{l,\mathrm{i}} - \delta_{l,\mathrm{r}} - \phi^{\mathrm{ri}}_{\mathcal{LL}}\right)}_{\text{transfer conductance effect}} - \sum_{s=1}^{k} \left|g^{\mathrm{si}}_{\mathcal{ML}}\right| U_{m,\mathrm{s}} \sin\left(\delta_{l,\mathrm{i}} - \delta_{m,\mathrm{s}} - \phi^{\mathrm{si}}_{\mathcal{ML}}\right) \tag{1.4}$$

and

$$P_{ei} = \underbrace{-\sum_{r=1}^{j} \left|g^{\mathrm{ri}}_{\mathcal{LM}}\right| I_{l,r} \cos\left(\delta_{l,\mathrm{i}} - \delta_{l,\mathrm{r}} - \phi^{\mathrm{ri}}_{\mathcal{LM}}\right)}_{\text{transfer conductance effect}} + \sum_{s=1}^{k} \left|g^{\mathrm{si}}_{\mathcal{MM}}\right| U_{m,\mathrm{s}} \sin\left(\delta_{l,\mathrm{i}} - \delta_{m,\mathrm{s}} - \phi^{\mathrm{si}}_{\mathcal{MM}}\right) \tag{1.5}$$

When the network is lossless (conductance in transmission lines neglected), $\phi = 0$ in the above. It can be observed that the GFL inverter will introduce a cosine term of the angle difference in the differential equations, similar to the characteristics of transfer conductance. From a nonlinear systems viewpoint, these cosine terms break the symmetry/gradient structure required by classical energy-function constructions; indeed, it has been proved that no energy function exists for this nonlinear system [23, 35]. Moreover, the cosine interactions induced by GFL inverters are typically much larger than those caused by actual transfer conductance, further exacerbating the difficulty. As a consequence, an energy function does not exist for power systems containing GFL inverters, and—so far—there are no effective remedies, which leads to the breakdown of the traditional direct method in IBR-dominated systems. The detailed discussion of this issue is provided in Chapter 3, where a manifold-based geometric perspective is adopted and the stability radius (SR) is introduced for transient stability assessment without relying on an energy function.

One alternative to the energy function approach in multiple inverter systems is manifold theory [38], which uses the geometry of the manifold to determine or estimate the stability boundary of a power system. The manifold theory is less dependent on the structural form of the models and therefore offers broader applicability. However, for high-order systems, it still suffers from limited computational efficiency, making model reduction a necessary step for its practical application.

The difficulties encountered in analyzing multi-inverter setting has been discussed above but even a single GFL inverter presents challenges. The PLL-based synchronization mech-

anism itself has not been fully analyzed, and the characterization of its stability region and its nonlinear analysis remain at an exploratory stage. Although a GFL behaves as a PQ node at steady state, in practice, it contains multiple coupled outer control loops (not only the PLL but also DVC and TVC loops). These couplings raise the effective order and nonlinearity of the model; as a result, different bandwidth allocations, even under identical steady-state setpoints, can lead to markedly different transient responses and stability margins, which further complicates the use of traditional direct methods. Therefore, nonlinear model-reduction analysis is also particularly important in this scenario.

1.2 Literature Review

Recognizing the challenges discussed above, many researchers have investigated the transient stability of power systems with GFL inverters. We review the latest research attempts, directions, and methodologies, and these are organized into two parts: the first focuses on transient stability analysis of a single GFL inverter, and the second addresses transient stability of systems with multiple GFLs. Each part contains a discussion of both methodological approaches and research subjects.

1.2.1 Large-signal stability of single GFL inverter system

Research on a single GFL inverter can be broadly summarized in Figure 1.7. Items highlighted in blue mark the themes that will be developed in the subsequent chapters of this thesis. It is widely accepted that a GFL inverter can be modeled as a PLL-synchronised controlled current source [39, 27, 40, 6, 41].

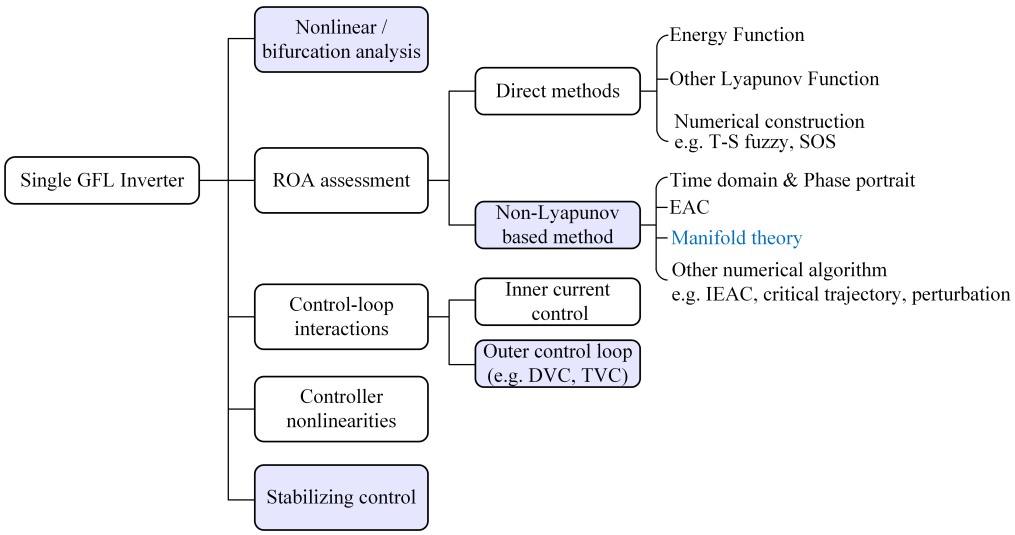


Figure 1.7: Research scopes on a single GFL inverter system. (Blue blocks indicate topics that are explicitly studied in this thesis, while white blocks represent related areas reviewed for completeness.)

Based on this model, one major scope of study isnonlinear analysis and the characterisation of such systems with manifold [42, 43, 44, 45, 46, 47, 48]. Specifically, [42] shows that the differential equations of a PI-controlled PLL can be written in the form of a swing equation,

whose dynamics share structural similarities with those of GFM inverters or SGs (see Fig. 5 in [42]). Building on this, [47] further analyzes the swing-equation representation of GFL inverters, deriving how different parameters affect their damping and inertia, and providing an initial discussion of the manifold properties. Meanwhile, [46] offers a more detailed study of the bifurcation behavior of the GFL inverter manifold. Negative damping and the emergence of unstable limit cycles in GFL inverters have been studied [44, 45], highlighting a significant contrast with SG and GFM inverters, which do not exhibit such limit cycles [49]. Additionally, the presence of negative damping in GFL inverters can undermine the accuracy of stability estimations using the Lyapunov function method, as discussed in [48]. However, existing research primarily focuses on GFL inverters, with limited exploration of GFL inverters operating as rectifiers.

Another important research aspect is the characterization and assessment of the stability region, namely the ROA. Although this can be evaluated through time-domain simulation this approach typically suffers from very high computational cost, making it difficult to calculate critical clearing times (CCT) and other indices in a reasonable period. Nevertheless, it has the advantage of widespread applicability. For example, [50, 51, 52] employ time-domain simulations to estimate the ROA of high-order GFL systems with multiple control loops, thereby avoiding the difficulty of constructing a Lyapunov function in the direct method. The phase portrait method, which is also based on time-domain simulation, has been widely adopted in the literature such as in assessing large-signal stability of PLL, [53], GFM inverter transients [54], DC-voltage-controlled GFM inverters [55], and GFL inverters with multi-loop coupling [56]. This approach can provide some qualitative insights into how transient stability changes with parameters, but again, this is computationally expensive.

In the single SG system, the swing-equation ROA can be approximated by the equal area criteria (EAC). Works such as [47, 27] extend EAC to PLL scenario. EAC can be viewed as a special case of using a Hamiltonian energy function for single-machine ROA estimation [57]. However, as [27] points out, the PLL structure can exhibit negative damping, so EAC cannot give a fully accurate estimation of ROA. Moreover, EAC is also not suitable for over-damped PI designs of the PLL. Therefore, in GFL large-signal studies, EAC is usually used for qualitative analysis only and in combination with a PLL angle–voltage curve.

As introduced above, the energy–function–based method is the classic approach to assess the transient stability of traditional power systems, but the construction of the energy function is model-dependent and relies on the system structure having certain properties. Several works have already applied energy functions to the nonlinear structure of PLLs [48, 58, 57, 41, 59, 60, 61]. In [58, 57, 60], the traditional Hamiltonian energy function was directly applied to PLL dynamics, and it was found that the damping is not always positive, which is a major difference compared with GFM inverters and SGs. [41] extended this structure of energy function to a two–GFL inverter system; however, as analyzed in Chapter 3 Section 3.3, this type of energy function degenerates to a local Lyapunov function due to the transfer conductance effect (which causes the the derivative of energy function

to be no longer non-positive), and thus its ROA estimation becomes overly conservative. To mitigate this drawback, [61] took up the idea of a generalized energy function [62] and applied it to a two-GFL inverter system. The positive-damping region is enlarged but still does not cover the entire phase plane; therefore, the critical energy and the level set of the energy function that crosses this value—used to estimate the ROA—must be determined explicitly, rather than by simply using the UEP as the critical energy. In the single-inverter case, [48] proposed a new Lyapunov function by taking the PLL angle and the integrator output of the PI controller as the state variables, rather than the PLL frequency. To facilitate the construction of energy functions, [63, 59] introduce an approach based on an equivalent-circuit to define the energy function, which makes the energy function easier to construct and provides clear physical meaning. However, in practice, most energy functions constructed through this method still contain path-dependent terms, and thus it cannot be guaranteed that their derivative is strictly non-positive.

In the direct method, another way to construct a Lyapunov function is through numerical approaches such as the Takagi–Sugeno (T-S) fuzzy method and sum-of-squares (SOS) programming. T-S fuzzy method decomposes a nonlinear system into multiple sub-models and casts them as local linear representations; a common quadratic Lyapunov function is then obtained via LMI-based convex optimization to estimate the ROA, thereby avoiding reliance on the nonlinear differential-equation structure for energy-function construction [64, 65, 66]. However, this method incurs a computational burden that grows rapidly with system dimension, and tends to be conservative due to the quadratic Lyapunov assumption. Similarly, SOS programming also avoids reliance on the nonlinear differential-equation structure by numerically constructing local polynomial Lyapunov functions and enlarging their invariant level sets to estimate the ROA. Specifically, the positivity and derivative conditions of the candidate polynomial Lyapunov function are enforced through SOS constraints, which admit equivalent semidefinite programming (SDP) formulations [67]. The ROA is then refined via an iterative procedure that alternates between feasibility SDPs and Lyapunov function reconstruction. With higher-order candidates it is often less conservative than T-S/LMI [68, 69, 70]. Before using SOS, the model need to be re-casted in polynomial form. Numerical Lypunov functions typically suffers from a heavy computation cost that grows fast with state dimension and polynomial degree, and the Lyapunov function coefficients come from numeric optimization, so it is hard to explain how changes in system parameters affect the ROA.

In addition to the direct method, numerical approaches exist that do not rely on constructing an energy function. References [63, 57] propose an iterative EAC algorithm, where the damping effect is equivalently superimposed onto the power/voltage–angle curve of the conventional EAC. Through iteration, the critical angular velocity at different angles can be obtained. In essence, this method still searches for the critical trajectory, which serves as the ROA. References [71, 72] develop critical trajectory approximation methods. Path-dependent terms that are not explicitly represented, or damping that is not captured in the original formulation, are estimated geometrically by evaluating the dissipated energy (or

the path-dependent contribution) along the trajectory from the ideal stability boundary to the UEP. This yields a less conservative ROA estimate. This method have been applied to both single-machine GFM and GFL systems, but they still require a candidate energy function as the baseline on which the path-dependent terms are estimated. In addition, some works adopt the perturbation method to derive analytical time-domain expressions of the post-fault angle dynamics for single-machine GFM [73] and GFL systems [74]. The resulting expressions are series expansions with respect to system parameters and do not require numerical integration. However, this method is valid only under transiently stable conditions; if the system becomes unstable, the analytical expressions are no longer applicable. Although [74] assesses stability by checking whether the post-fault analytical solution converges, this criterion is essentially equivalent to the existence of an SEP after the disturbance, and thus does not provide a stability boundary characterization.

Another important stream is manifold theory [38], originally proposed by Chiang et al. [23, 32], which indicates that the ROA of a wide class of nonlinear systems (including power systems) is the region encircled by the stable manifolds emitted from all UEPs of the system. This result is general and yields the true stability region, but it is computationally demanding: all UEPs must be located and reverse integration must be performed. Compared with brute-force time-domain simulation, however, the computational effort is still significantly lower.[43] applied this method in the single GFL inverter. Our previous work [19] applied this method to two-inverter systems in combination with model-order reduction, and proposed the stability radius as a transient-stability index. Similarly, in order to obtain more analytical ROA estimates, [75, 76] adopts the hyperplane approximation method. Since the stability boundary is formed by the stable manifolds of the UEPs, the local tangent hyperplane at the UEP can be used for estimation. This avoids reverse integration but still requires identifying UEPs and their stable eigenvectors. The resulting ROA estimates are, however, overestimates of the true stability region.

Before moving to other research scopes and multi-inverter cases in the next subsection, we summarize the large-signal stability assessment methods (including multi-machine scenarios) in Table 1.1, based on the above discussion. The phase-portrait approach provides only qualitative insight. In multi-machine systems, the EAC is extended to the Extended Equal-Area Criterion (EEAC) [77, 78]. The key idea of EEAC is to identify a critical cluster of machines (based on electrical distance, initial acceleration, or prior simulation experience) and to partition the original multi-machine system into two groups, which as a result, reduced to an equivalent critical two-machine system. The EAC is finally applied to this reduced two-machine system to evaluate transient stability. EEAC has been widely used for SG systems [79]. However, as noted earlier, in GFL systems, due to the presence of non-positive damping, EAC methods itself tend to overestimate ROA along certain state-space directions and therefore remain qualitative rather than quantitatively accurate (such overestimation can be observed and explaned in detail in Chapter 2, Section 2.3.1). More fundamentally, for multi-GFL inverter systems, the energy function generally does not exist. Since EAC is intrinsically based on the equivalence between kinetic energy and

Table 1.1: Comparison of transient stability assessment methods

Method	**Accuracy**	**Computational complexity [Runtimes[a,b]]**	**Extendability (multi-mach./loop)**	**Usable as metric?**
Time-domain (incl. phase portr.)	Fully accurate	Extremely high [39.64 s]	Yes	No (qualitative)
EAC	Often inaccurate[c] (over/under estimate)	Low [0.60 s]	Multi-mach.: EEAC Multi-loop: No	Yes
Analytical energy / Lyapunov fun.	Relatively accurate (conservative)	Moderate [0.61 s]	Hard to construct or may not exist	Yes
Numerical Lyapunov	Relatively accurate (conservative)	Relatively high [26.7 s]	Yes	No
Manifold theory	Fully accurate	Moderate → high (w/ system order) [1.73 s→4.79 s]	Yes	No
Other numerical algorithms	Relatively accurate	Relatively high	Not yet explored	No

[a] All runtimes are obtained on an Intel i7-1185 CPU using MATLAB 2022a.
[b] Unless otherwise stated, reported runtimes correspond to two-dimensional system examples.
[c] Misleading in GFL settings.

critical potential energy, directly applying energy-based EAC formulations leads to inaccurate ROA estimation in this context (which will be discussed in detail in Chapter 3, Section 3.3). Other numerical methods, while applicable, typically offer limited physical insight and estimation of ROA is under estimated. For systems of low order, manifold theory can compute the exact stability boundary with manageable effort, but it requires a metric to be established for multi-GFL systems.

Transient stability analysis of IBRs, particularly in multi-inverter settings, remains a frontier research topic and is not yet fully resolved. Nevertheless, this thesis makes an original attempt to implement and apply the assessment methods summarized in Table 1.1 to two- and three-dimensional examples[1], with representative computational runtimes to provide practical insight into the relative computational burden of different approaches. As for time-domain simulation, its computational cost is mainly determined by the resolution of the fault-clearing time and the length of post-fault integration. Although the fault-on trajectory is computed only once, each candidate clearing instant requires a sufficiently long post-fault simulation to assess stability, since stability of each candidate fault-clearing state cannot be determined a priori. In practice, a bracketing search is therefore used to reduce exhaustive enumeration. With a 1 ms clearing-time resolution, the runtime in our implementation is still as long as 39.64 s, which mainly comes from repeatedly integrating the post-fault dynamics. As for the manifold-theory-based approach, the computation follows Algorithm 2.1 introduced in Chapter 2. The computational cost mainly consists of two parts: locating UEPs by solving nonlinear algebraic equations, and constructing manifolds via numerical integration. Compared with time-domain simulation, the number of numeri-

[1]For the EAC and analytical energy-function methods, two-dimensional examples are chosen as two-GFM–infinite-bus system with parameters identical to those in Table 3.2 and Table 3.7 in Chapter 3. All remaining methods are evaluated using the same GFL–GFL test case in Chapter 3, with parameters identical to those in Table 3.2 and Table 3.3. In particular, for the manifold-theory-based method, a three-dimensional case is considered, corresponding to the case study presented in Figure 3.6 in Chapter 3.

cal integrations is greatly reduced, and real ROA can be obtained. For the two-dimensional case, the total runtime is 1.679 s, including 0.525 s for algebraic equation solving and 1.204 s for numerical integration. For the three-dimensional case, the runtime increases to 4.786 s (2.6697 s for algebraic equations and 2.1163 s for differential equations). As the system dimension increases, the computational burden grows accordingly, with the dominant cost arising from the UEP search. As for the EAC and analytical energy-function-based methods, the ROA is obtained in analytical form. Consequently, apart from locating the relevant UEPs, the computational cost is negligible, and the total runtime in our test cases is about 0.6 s. In traditional large-scale SG systems, the computational efficiency can be further improved. The BCU method [23] can be employed to accelerate UEP location in energy-function-based methods. Compared to energy-function-based methods, EEAC benefits from machine grouping and system reduction, leading to a significantly lower effective system order and computational burden. As for the numerical Lyapunov approach (take SOS programming as an example), the computation is dominated by solving a sequence of SDPs, as the algrithm introduced above. In our implementation, the algorithm converges after 12 iterations with a total runtime of 26.7 s. Although computationally intensive, it remains significantly faster than time-domain simulation, and the resulting ROA is an intrinsic property of the post-fault system, independent of the fault-on trajectory or fault type.

In practice, the PLL-controlled ideal current-source assumption does not hold exactly. Several studies include controller nonlinearities: a PLL frequency limiter can constrain frequency excursion during faults, therefore making the system more stable [80]. For the voltage limiting, [81] shows that with a circular limit, over-modulation does not degrade synchronizing stability, since the inverter behaves more like a voltage source. Moreover, [82] reports that during post-fault resynchronization, the terminal of GFL can experience over-voltage if the PLL angle undergoes a 2π rotation.

Beyond the PLL itself, many studies examine loop interactions in GFL inverters. As for large-signal stability considering the inner current loop (not only the PLL), [83, 66, 84, 85, 86] study this scope. [86] shows that in extreme cases—such as low current-loop bandwidth and small filter inductance—current-loop dynamics do affect the dynamic of large-signal disturbance; [87] also supports this result. [84] further gives a qualitative reason: when a deep voltage sag occurs, the sudden drop of grid voltage introduces a perturbation inside the current loop that causes a temporary increase of current, which in turn worsens transient (synchronizing) stability. Based on this, [83] uses an iterative EAC algorithm based on EAC and [66] uses the Takagi–Sugeno approach to estimate ROA with the current loop included. [85] shows that when the current loop has high bandwidth, it can be singularly perturbed and decoupled: if its small-signal dynamics are stable, it behaves like an algebraic current source in the large-signal study. In practice, the current loop bandwidth is usually much higher than the PLL bandwidth, and with the application of wide-bandgap devices in the future, the bandwidth keeps increasing with switching frequency [88]. Further, [83] points out that with proper feedforward and decoupling design, large grid disturbances

have little impact on the current loop. In small-signal analysis, a close bandwidth between the inner current loop and the PLL can also trigger instability[9]. Overall, the inner current loop does influence the ROA—especially under weak grids and during severe sags—but in typical designs with a fast, well-tuned loop it is not the main bottleneck for transient stability.

Another line of work on loop interactions focuses on the outer control loops of GFL inverters—PLL, DVC, and TVC. In the small-signal stability domain, these interactions are well studied: e.g., [89, 90, 91] analyze coupling among the outer loops and how their bandwidths shape stability margins. The selection of these bandwidths remains an open problem even in small-signal stability studies, with no consensus tuning rules. In practice, they are chosen conservatively (e.g., below ∼20 Hz) to avoid interaction with the current loop and validated through small-signal analysis. In contrast, large-signal analysis involving multiple control loops has only been covered in a few papers [51, 50, 56, 92, 93, 82, 94, 95, 59]. Reference [92, 93] modifies the differential equation of a PLL to incorporate the impact of the DVC loop on PLL, but the dynamics of the DVC loop itself are not considered. Although the instability caused by the variation of input power is discussed in [96], the influence of control parameters and the underlying instability mechanism are not analyzed. Reference [56] investigates the effect of DVC parameters using phase portraits from simulation studies, but focuses solely on relative stability without examining the impact on the stability region. In [82, 94], the instability of the DVC control loop is studied; however, the PLL dynamics and their interactions with the DVC loop are neglected. Nevertheless, these studies collectively indicate that transient instability cannot be solely attributed to the loss of synchronization of the PLL. In [50, 51], GFL inverters with all three outer control loops are modeled, leading to fifth-order nonlinear ordinary differential equations (ODEs) that describe the system dynamics. In [95], the PLL is regarded as the fastest control loop and its dynamics are ignored, which is similar to our previously proposed method [30]. However, the combination of bandwidths and their effect on large-signal stability are not discussed. Due to the difficulty of performing theoretical analysis on high-order nonlinear ODEs, all these works rely on numerical methods for stability analysis. An analytical simplification approach for high-order inverter models has yet to be established. To address this issue, a bandwidth separation method was first proposed for GFL inverters in our previous work [30] to reveal the instability mechanism of the GFL inverter considering multiple control loops.

Many studies propose stabilizing controls for GFL transient stability. For the PLL, reducing bandwidth and adopting an overdamped design ($k_{\mathrm{p,pll}} \gg k_{\mathrm{i,pll}}$) improve robustness [97, 42]. Active-current reduction has been suggested—either voltage-drop–based or PLL-frequency-error–based [98, 99, 100]—and PLL freezing during faults has also been explored [101, 102]. However, modifying active power can conflict with fault-ride-through requirements, and PLL freezing is unsuitable for phase or frequency jumps [103]. A broad body of work supports overdamped PLL design [104, 105, 106, 53, 107]; e.g., [106] adapts the integral gain using an estimated frequency change, and [53, 107, 108] recommend switch-

ing to proportional-only control (instead of PI) under large frequency deviations or during faults. Nevertheless, a mature stabilizing strategy that explicitly accounts for interactions among multiple outer loops is still lacking.

1.2.2 Large-signal stability of multiple inverter systems containing GFL inverters

The landscape of multi-inverter research can be organized into the branches illustrated in Figure 1.8. In this section, the representative papers within each branch are highlighted and distill the specific transient-stability assessment techniques they employ which correspond to Table 1.1 summarized earlier.

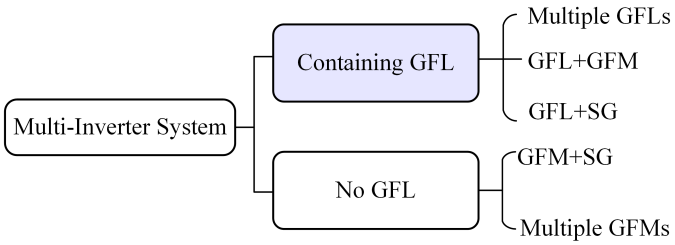


Figure 1.8: Research directions in transient stability of multi-inverter systems. (Blue blocks indicate topics that are explicitly studied in this thesis, while white blocks represent related areas reviewed for completeness.)

At present, the literature is still largely centered on two-inverter systems. The classic insight of [77] shows that multi-machine dynamics can often be reduced to the interaction between two coherent clusters. This motivates the focus on two-inverter configurations as a natural first step toward understanding general multi-inverter behavior. Building on this idea, [109, 110, 111] investigate aggregation in, respectively, multi-GFL systems and mixed GFM–GFL systems, where similar inverters are combined into an equivalent unit to reduce model order and facilitate transient-stability analysis.

The large-signal stability of two GFL inverters infinite-bus settings has been examined in [112, 113, 114, 41, 115, 116]. The cases where multiple GFL units tied to the grid are also analyzed in [28, 117]. Oscillation modes arising from parallel connection of large- and small-capacity inverters are characterized in [112], while current-injection strategies for the lower-capacity units are studied in [113, 114]. Among these, [117, 114, 28] adopt quasi-static analyses centered on the existence of a stable equilibrium point (SEP), without assessing the surrounding ROA. In [113, 112], the equal-area criterion (EAC) is used for qualitative assessment, treating the second inverter as a disturbance. [41] employed the traditional Hamiltonian energy function without carefully examining its applicability; as discussed in Chapter 3, Section 3.3, transfer-conductance effects reduce it to a local Lyapunov function, yielding an overly conservative ROA estimate. Building on generalized energy ideas [62], [61] extends the approach to two GFL inverters: the positive-damping region is expanded but still does not cover the entire phase plane, so the critical level cannot be set by the UEP and must be specified explicitly (see the earlier discussion). [115]

adopts a perturbation-based approach to derive the post-fault angle trajectory of the GFL inverter and examines how parameters affect its convergence; however, as noted earlier, this method cannot quantify the ROA. [116] employs an iterative EAC to obtain a conservative boundary estimate which is not the exact stability region, and cannot characterize instability modes.

Lierature [118, 29] examine systems where GFL inverters operate in parallel with an SG feeding the grid, neglecting the GFL dynamics under the assumption that the GFL is faster than the SG. In [119], the transient behavior of an induction motor in a microgrid is analyzed during faults; the GFL is presumed stable, and only the motor transients are studied. For islanded systems composed of a GFM and a GFL, [120] analyzes the swing-equation and the impact of parameter variations on overall stability, while [121, 122] apply the EAC to the swing equation—both being qualitative in nature.

In summary, when GFLs are present, effective methods for estimating the domain of attraction and characterizing instability modes are still lacking; most existing approaches are qualitative or rely on very strong assumptions—e.g., weak coupling between the two inverters or a second inverter that is negligible relative to the first.

In the absence of GFL inverters, energy-function–based methods remain applicable in multi-machine systems. Compared with SGs, GFM inverters are characterized by larger and tunable damping [71], which has motivated several extensions of classical energy-function approaches. For example, [123] directly applies an energy-function framework to a two-GFM system by incorporating a damping-related energy term originally proposed for SGs [124], leading to improved stability region estimation. In [125], the energy-function method is refined by estimating the damping energy of GFM inverters via critical-trajectory approximation, while [126] constructs an energy function that accounts for reactive power control loops and can be extended it to multi-machine GFM systems. From a mechanistic perspective, [127] shows that, in mixed systems, a first-order GFM inverter can provide effective damping energy to a second-order SG. However, as further discussed in [128], increased damping does not always enhance transient stability; in certain cases, higher damping in lagging units may cause fault-on trajectories to deviate further from the stable equilibrium, since the transient stability is determind by both ROA and fault-on trajectory. Compared with GFL-dominated systems, classical methods developed for SG systems, such as EEAC, can still be adapted to GFM-based systems, as demonstrated in [129]. Overall, while GFM inverters introduce additional modeling and analysis challenges in multi-machine settings, these challenges can be addressed within existing analytical frameworks.

1.3 Research Gaps, Problem Statement, and Research Objectives

From the foregoing literature review, GFL inverters—owing to their synchronization mechanism fundamentally different from GFM inverters and SGs—pose critical challenges to

transient stability analysis. Despite considerable progress, several gaps remain:

(1) Single-inverter, PLL-based nonlinear analysis. Despite extensive research, how PI parameters and operating mode affect the stability region, invariant manifolds, and bifurcations, and modeling choices influence ROA estimation has not yet been systematically summarized or synthesized. (a) Modeling: While model–detail requirements have been extensively articulated in traditional power-system studies [130], GFL modeling practice is less uniform: most works adopt a PLL-driven controlled-current-source and consider line dynamics; whereas studies adopt simplified phasor models without line dynamics [28, 120, 131]. This approach is common for GFMs [6] and SGs. How these alternative choices affect ROA estimation has yet to be systematically clarified. (b) Operating mode: GFL operation as a rectifier remains underexplored, and its consequences for the above manifold properties and ROA are not well characterized. (c) Controller parameters: How PI parameters in the PLL shape manifold, trigger bifurcations, and expand/contract the ROA remain to be summarized. (d) Energy functions: The energy function can still be applied to a single-inverter scenario. The construction of the classic energy functions are typically based on the second-order swing-equation, they naturally fit low-pass-filter (LPF)-type synchronizers but not PI-based PLLs. Recasting the PLL dynamics into swing form introduces negative damping, making the derivative of the energy function not non-positive and often unreliable for ROA estimation. To date, an energy-function formulation tailored to PI-based PLL dynamics has not been established.

(2) Multi-inverter systems with GFL inverters. This line of research remains at an early stage. Our prior work [19] shows that, in multi-machine settings, introducing GFL inverters leads to the nonexistence of an energy function, which breaks classical direct methods. Many studies have attempted, in a trial-and-error fashion, to construct energy functions but without success. Others reuse existing energy-function forms: either their conservatism cannot be guaranteed and ROA is overestimated, or they are overly conservative and fail to capture the ROA characteristic. Numerical ROA algorithms face similar limitations, as summarized in Table 1.1. Other studies transform two-inverter systems into single-inverter systems, by neglecting the dynamics of the second inverter, or treating the second inverter as disturbances. These methods are based on very strong assumptions, that is, the two inverters are not tightly coupled, or the second inverter is less significant than the first inverter. Among current ROA assessment tools, ROA computation based on the manifold theory is one of the promising approaches because it gives the exact stability boundary; however, it still (i) incurs a high computational burden and (ii) like other numerical approaches, calls for a suitable metric to assess large-signal stability.

(3) Multi-control-loop interactions. Despite extensive small-signal results, large-signal interactions remain preliminary. In terms of the large-signal stability mechanism, the literature shows that GFL transient instability cannot be attributed solely to PLL loss of synchronism. In steady state, GFL units act as P−V or P−Q nodes; under the same steady state, different bandwidth allocations across the control loops can materially

alter the stability region, yet the associated instability mechanisms have not been clarified. In terms of Methodology, most studies rely on qualitative or quasi-steady analyses, and available tools are limited for high-order nonlinear models with multiple coupled loops. An analytical simplification framework for large-signal stability of high-order inverter models has yet to be established.

Based on the above research gaps, this thesis addresses the following objectives:

Q1: PLL large-signal stability revisiting. Revisit the large-signal stability of PLLs and the origin of negative damping; then systematically assess how line dynamics impact the ROA estimation, and PI-controller gains, operating mode (rectifier vs. inverter) shape the stability region, manifolds, and bifurcations.

Q2: Energy function constructions for PI-based synchronization. Review existing energy/Lyapunov functions and investigate whether an energy-function formulation tailored to PI-controlled nonlinear systems can be established; apply such a construction to PI-based synchronization loops (e.g., PLL).

Q3: Existence of energy functions in multi-inverter systems with GFL. Determine the existence (or nonexistence) conditions of energy functions in multi-machine power systems containing GFL inverters.

Q4: If energy functions do not exist: ROA framework and evaluation metric. When the above existence fails, develop a framework for ROA estimation in multi-inverter systems and define a quantitative large-signal stability margin.

Q5: Instability modes and interactions (two-inverter case). Building on the ROA framework, analyze large-signal instability modes and interaction mechanisms in two-inverter systems.

Q6: Multi-loop GFL: model reduction and ROA analysis. Propose a model-reduction and large-signal ROA analysis framework for GFL inverters with multiple coupled loops (PLL, DVC, TVC).

Q7: Mechanisms and stabilization via bandwidth design. Using the above framework, reveal instability mechanisms in multi-loop GFL control and devise transient-stability enhancement measures based on bandwidth allocation/design.

Q8: Hardware validation. Ensure that all proposed models, methods, and findings are thoroughly validated through Electro-magnetic transient (EMT) simulations, and real-world hardware experiments [including control-hardware-in-the-loop (CHIL), and power-hardware-in-the-loop (PHIL)].

1.4 Research Approaches, Original Contributions, and Thesis Structure

1.4.1 Research Approaches

Based on the above research problems, this thesis adopts the following research approaches across different chapters.

One of the core methodologies is the manifold theory. The manifold theory is not dependent on a global energy function and therefore can be applied to IBR-dominant systems. Another nonlinear tool employed in this thesis is singular perturbation theory [132, 31, 133], which allows model order reduction in systems exhibiting multiple time scales, so that complex nonlinear dynamics can be approximated by their dominant dynamics.

In Chapter 2, manifold theory is applied to single-inverter systems to numerically compute the ROA and manifold features (such as the existence of limit cycles) under different modeling assumptions, PI controller parameters, and operating modes. In addition, a review of existing energy functions is provided, and a new formulation tailored to PI-based controllers is proposed, which ensures positive damping across the entire phase plane and thereby enables accurate and tractable stability-region estimation for PLLs. The results are validated via CHIL experiments, EMT simulations, and cross-comparisons among different modeling approaches.

In Chapter 3, manifold theory is further extended to two-inverter systems to analyze their transient stability. Compared with single-inverter cases, multi-inverter systems face significant challenges in computing and visualizing the stable manifolds due to their higher order. To address this, model order reduction is performed via multiscale analysis, enabling the application of manifold theory to two-inverter systems. This extension makes it possible to examine the large-signal interaction between heterogeneous inverters (GFL, GFM, and GSP). Furthermore, a stability metric, termed the stability radius (SR), is introduced to assess the large-signal stability margin. SR provides a conservative but generalizable stability index, independent of fault location and type. With SR, the contributions of different inverter types to system stability are quantified, and the instability modes under strong inverter interactions are systematically analyzed. Applied to two-inverter systems, the framework quantifies SR variations across GFL–GFL/GFL–GFM/GFL–GSP pairings, classifies the dominant large-signal instability modes, and summarizes the regimes of strong inter-inverter interaction.

In Chapter 4, we observe that the bandwidth design of multiple control loops naturally exhibits a singular-perturbation structure. Based on this, a bandwidth separation method was first proposed in our previous work [30] to explain instability mechanisms of GFL inverters under multiple coupled loops. In this thesis, the proposed bandwidth separation method is further extended to a more general range of parameter configurations, and a more detailed analysis is presented. Under various categories of bandwidth settings, the proposed method yields a reduced model that makes it easier to compute the ROA (also referred to

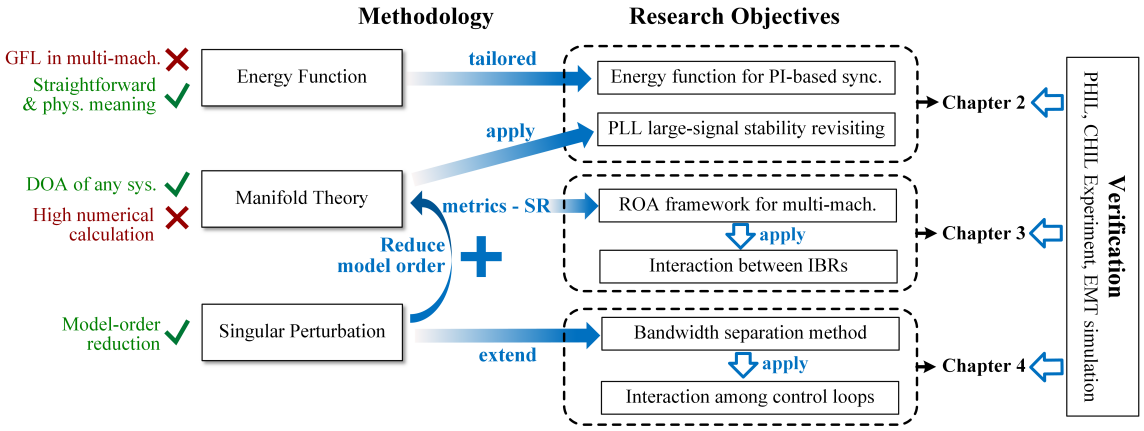


Figure 1.9: Conceptual diagram of thesis.

as ROA) and visualize it in the phase plane. A broader set of cases, including various large-signal disturbances, is considered. It should be noted that, unlike the conventional method directly focuses on the coupling effects of different control loops, the proposed method first intentionally separates the bandwidths of the outer control loops. This separation enables a clearer understanding of how bandwidth configurations influence transient stability and provides insight into the interaction mechanisms among the loops. Using this method, the stability region can be readily derived.

Finally, PHIL and CHIL experimental platforms are developed in the laboratory to support and validate the proposed models, analysis approaches, and findings throughout the thesis.

The conceptual diagram of this thesis is illustrated in

1.4.2 Original Contributions

In Chapter 2, our contributions are as follows.

- Derive the model for rectifier mode and find that the intrinsic positive damping introduced by line dynamics exist in the GFL rectifier, which is different from the inverter case. And the impact of line dynamics is discussed for rectifier mode and inverter mode.

- A detailed analysis of manifold characteristics and bifurcation behavior of GFL rectifiers under varying control parameters. Additionally, it is rigorously proven that no limit cycle exists under rectifier operation, in clear distinction to the inverter mode.

- Propose the new type of energy function tailored for the PI controller, which can be used to estimate the ROA of PLL, and it can also be applied to other types of inverters that utilize the PI controller to realize synchronization.

- Development of a hardware-in-the-loop (HIL) experimental setup, with comparative analyses conducted across theoretical, phasor, and EMT simulation models, verifying the theoretical findings.

Parts of this chapter have been accepted for publication in [134].

In Chapter 3, our contributions are as follows.

1) Derivation of the generalized large-signal expression for different kinds of inverters, and indication that there is no energy function for a system containing GFL Inverters;

2) Proposal of a combination approach with both manifold theory and model order reduction, and introduction of the metric stability radius (SR) to assess the transient stability.

3) Study of large-signal interactions in various two-inverter systems leading to identification of various new oscillation patterns;

4) Investigation of the similarities between GSP inverters and GFM inverters, revealing the role of voltage support in enhancing system dynamics.

Parts of this chapter have been submitted to *IEEE Transactions on Power Electronics* (under review). A preliminary version is available on arXiv [19].

In Chapter 4, our contributions are as follows.

1) Propose the bandwidth separation method that utilize the characteristic of control loop bandwidth to realize the model order reduction in a GFL inverter.

2) The adverse interaction between the DVC and PLL degrades overall stability; moreover, a trade-off exists between phase-angle stability and DC-link voltage stability, governed by the relative bandwidths of DVC and that of PLL.

3) A sufficiently high TVC bandwidth enhances transient stability: it enlarges the ROA of both angle and DC-link dynamics and attenuates the adverse interaction between the PLL and DVC.

Parts of this chapter have been published in [30]; an extended journal version has been submitted to *IEEE Transactions on Power Electronics* and is currently under review.

Finally, Chapter 5 concludes the key findings of this thesis and suggests directions for future work.

Chapter 2

Manifold Property and Revisiting of Energy-Function-based Method for GFL Inverter

The manifold theory is emerging as a prominent analytical tool for transient stability of GFL inverter. While most studies have focused on the inverter mode, the transient stability characteristics and bifurcation phenomena in rectifier mode remain relatively unexplored. This Chapter investigates and summarizes the manifold characteristics and bifurcation behaviors of GFL converters, highlighting key distinctions between inverter and rectifier modes. It demonstrates that commonly used phasor models neglecting inductive line dynamics lead to inaccuracies, specifically causing an overestimation of the ROA in inverter mode and an underestimation in rectifier mode. Furthermore, rigorous proof is provided that limit cycles cannot exist in GFL rectifier mode, which is different from the inverter mode scenario. This chapter compares various modeling approaches, including phasor models, EMT averaging models, and experimental validations. Additionally, hardware-in-the-loop (HIL) experiments are performed to confirm model validity.

This Chapter also revisits Lyapunov- / energy-function–based methods for GFL analysis. It is emphasized that the traditional energy function, although naturally compatible with LPF-type controllers, is not well-suited for PI-controlled systems due to the state-dependent nature of their equivalent damping. To resolve this issue, a *PI-controller energy function* is developed. This formulation explicitly incorporates the PI control structure, resulting in less conservative ROA estimates for single-GFL systems and allowing the UEP critical energy to serve as a valid level set. Furthermore, the PI-controller energy function is not limited to PLL-based GFL inverters but can be generalized to other nonlinear systems with PI control, which is demonstrated later through the example of a DC-voltage-controlled GFM inverter.

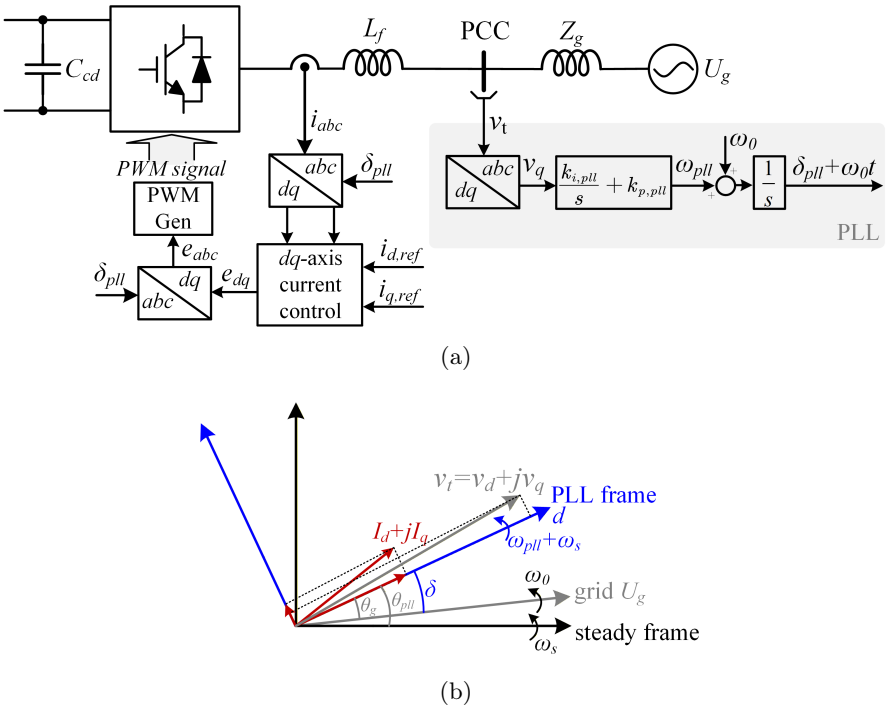


Figure 2.1: (a) Modeling of PLL in Grid-following converter. (b) Relationship of variables in different frames.

2.1 Modeling of PLL

Figure 2.1 (a) shows the diagram of a single-GFL-converter infinite-bus system and the structure of the PLL. The grid is represented by U_g with frequency ω_0. As analyzed in the Introduction, the inner current control loop is typically designed to operate at a bandwidth that is much higher than that of the PLL. This clear separation of time scales allows the overall system to be interpreted within a singular perturbation framework [85, 40], in which the current-loop dynamics evolve much faster than the PLL dynamics and therefore have a limited impact on the slow synchronization behavior. With appropriate feedforward decoupling, the interaction between the current loop and the PLL can be further reduced [83]. It is well accepted that, under these assumptions, a GFL converter can be modeled as an ideal controlled current source for large-signal transient stability analysis [6]. This thesis adopts the same modeling assumption.

In PLL, the dq transform is used as a phase detector, and a proportional-integral (PI) controller is used to drive the observed q-axis voltage v_q to zero. The nonlinear dynamics can be expressed as follows:

$$\begin{cases} \dot{x}_{\text{int,pll}} = k_{\text{i,pll}}\, v_q \\ \omega = x_{\text{int,pll}} + k_{\text{p,pll}}\, v_q \\ v_q = -U_g \sin\delta + I_d X_g + I_q R_g + I_d L_g \omega/\omega_s \\ \dot{\delta} = \omega + \omega_s - \omega_0 \end{cases} \tag{2.1}$$

In (2.1), v_q is defined as the voltage on the q-axis in PLL's reference frame. I_d and I_q are

the reference currents of the GFL converter in the PLL frame. I_d is positive in inverter mode and is negative in rectifier mode. The base frequency is denoted as ω_s. $x_{\text{int,pll}}$ is the integral term in the PI controller. The PLL phase-angle deviation δ is defined as the difference between the PLL-estimated phase angle and the actual grid voltage phase angle, i.e., $\delta = \theta_{\text{pll}} - \theta_{\text{g}}$, as illustrated in Figure 2.1(b). With this definition, a positive δ indicates that the PLL reference frame leads the grid voltage vector, whereas a negative δ indicates a lagging PLL frame. At steady state, the PLL achieves zero steady-state phase error with respect to the terminal voltage v_t, resulting in $v_q = 0$.

The sign conventions for the dq-axis currents follow the generator convention throughout this thesis. Specifically, a positive d-axis current $I_d > 0$ corresponds to active power injection from the inverter into the grid (inverter mode), whereas $I_d < 0$ represents active power absorption from the grid (rectifier mode). The q-axis current I_q is defined as positive when reactive power is injected into the grid and negative when reactive power is absorbed.

Normally, the grid frequency equals to base frequency, which is $\omega_0 - \omega_s = 0$. (2.1) can be further rearranged to (2.2), which has a similar form to the swing equation of a typical synchronous machine.

$$\begin{aligned} \dot{\delta} &= \omega \\ M_{eq}\dot{\omega} &= X_g I_d + R_g I_q - U_g \sin\delta - D_{eq}\omega \end{aligned} \tag{2.2}$$

Where,

$$M_{eq} = \frac{1 - k_{\text{p,pll}} L_g I_d/\omega_s}{k_{\text{i,pll}}},\ D_{eq} = \frac{k_{\text{p,pll}}}{k_{\text{i,pll}}} U_g \cos\delta - I_d L_g/\omega_s \tag{2.3}$$

In this second-order swing equation form, M_{eq} (with the unit of s^2) denotes the equivalent inertia and D_{eq} (with the unit of s) denotes the equivalent damping. However, compared with the second-order swing equation of SG or GFM inverter, the equivalent damping term D_{eq} for PLL is not constantly positive, which will cause the existence of the limit cycle [44, 46]. More precisely, the sign of D_{eq} depends on the value of δ, the operating condition, and the control parameters of the PLL. D_{eq} is non-negative when

$$\delta \in \left[-\arccos\left(\frac{I_d L_g/\omega_s}{U_g} \cdot \frac{k_{\text{i,pll}}}{k_{\text{p,pll}}} \right),\ \arccos\left(\frac{I_d L_g/\omega_s}{U_g} \cdot \frac{k_{\text{i,pll}}}{k_{\text{p,pll}}} \right) \right].$$

When δ lies outside this interval, D_{eq} becomes negative. It should be noted that δ is a periodic variable with a period of 2π, and the above condition applies modulo 2π.

In the phasor model, the inductive line dynamics are ignored to simplify the modeling, as it is considered much faster than PLL [120, 28, 131]. Under this circumstance, the term $I_d L_g \omega/\omega_s$ in (2.1) is omitted, and M_{eq}, D_{eq} in (2.2) can be represented by

$$M_{eq} = \frac{1}{k_{\text{i,pll}}},\ D_{eq} = \frac{k_{\text{p,pll}}}{k_{\text{i,pll}}} U_g \cos\delta \tag{2.4}$$

2.1.1 Manifold Theory and ROA

The stability region (ROA) is calculated by manifold theory herein. The manifold theory regarding the ROA, as proposed by Chiang [23, 32], is articulated as follows. Consider any nonlinear autonomous dynamical system described by:

$$\frac{d\boldsymbol{x}}{dt} = f(\boldsymbol{x}),\ \boldsymbol{x} \in R^n \tag{2.5}$$

If (2.5) meets the following criteria: 1) All the equilibrium points (EPs) on the stability boundary are hyperbolic; 2) The stable and unstable manifolds of EP on the stability boundary satisfy the transversality condition; 3) Every trajectory on the stability boundary approaches one of the critical elements as $t \to \infty$, and these assumptions are commonly satisfied in power systems with IBRs. Then the stability boundary of a SEP, denoted $\partial A(x_{\text{sep}})$, is the union of the stable manifolds of UEPs, $\mathcal{W}^s(x_{\text{uep}})$, and the stable manifolds of closed orbits (γ), $\mathcal{W}^s(\gamma)$:

$$\partial A(x_{\text{sep}}) = \bigcup_i \mathcal{W}^s(x_{\text{uep,i}}) \bigcup_j \mathcal{W}^s(\gamma_j) \tag{2.6}$$

Moreover, the stable manifolds of the UEPs are tangent, at the UEPs, to the eigenvectors corresponding to the stable eigenvalues. In practice, one can compute branches of $\mathcal{W}^s(x_{\text{uep}})$ by integrating the system backward in time from initial conditions perturbed along the corresponding stable eigenvectors in phase space.

For completeness and clarity, the practical implementation procedure for computing the ROA based on manifold theory is summarized in detail in Algorithm 2.1.

Algorithm 2.1 Manifold-based real ROA computation

Input: Nonlinear system $\dot{x} = f(x)$
Output: Stability boundary $\partial A(x_{\text{sep}})$
Solve $f(x) = 0$ from multiple initial guesses (e.g., grid-based sampling) to obtain distinct EPs; classify them via the Jacobian eigenvalues.
for each boundary-relevant UEP $x_{\text{uep},i}$ **do**
    Compute Jacobian $J = \frac{\partial f}{\partial x}\Big|_{x_{\text{uep},i}}$ and the stable eigenspace $\mathcal{E}^s(x_{\text{uep},i})$.
    Select unit perturbation directions d within $\mathcal{E}^s(x_{\text{uep},i})$ and generate nearby initial conditions $x_0 = x_{\text{uep},i} + \varepsilon d$.
    for each selected initial condition x_0 **do**
        Integrate $\dot{x} = -f(x)$ by ODE solver.
        Terminate if the trajectory enters a prescribed EP neighborhood; otherwise stop when integration horizon is reached.
        Record and update the minimum distance from the trajectory to x_{sep} (used later as SR in Chapter 3).
        Store the resulting trajectory as a branch of $\mathcal{W}^s(x_{\text{uep},i})$.
    end for
end for
Aggregate the stored branches to construct $\partial A(x_{\text{sep}})$.

Inparticular, for two-dimensional systems, the UEPs located on the stability boundary are

either type-I or type-II [1], and the boundary is formed by the stable manifolds of type-I UEPs. Accordingly, the real ROA is obtained via backward-time integration along the stable eigenvector(s) of each type-I UEP in the phase plane.

2.1.2 Impact of Modeling Choices

Herein, two modeling choices that affect the stability region (ROA) and the associated invariant manifolds are compared. Figure 2.2 illustrates a comparison of stability boundaries when the line dynamics are considered (black curves) versus when they are ignored (blue curves). The grey-shaded area surrounded by black curves represents the actual stability region.

To quantitatively compare between the ROA area obtained by considering and ignoring line dynamics, a quantitative error based on the ROA width along the δ axis has been introduced

$$\Delta\mathrm{ROA}_{\delta} = \frac{\Delta\delta_{\mathrm{no-line}}}{\Delta\delta_{\mathrm{with-line}}} - 1,$$

specifically, $\Delta\delta$ denotes the width of the ROA projection onto the δ axis at $\omega = 0$. These quantitative deviations for each operating condition are also annotated in Figure 2.2.

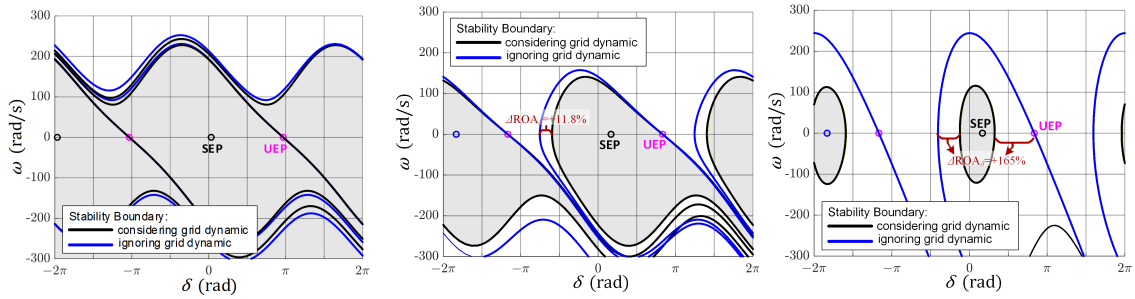
For inverter mode, since the equivalent damping D_{eq} when ignoring line dynamics is larger than the actual value, the stability region without line dynamics appears larger than the actual stability region. As shown in Figure 2.2 (a)(b)(c), the blue curves extend outside the grey-shaded area, and the ROA error $\Delta\mathrm{ROA}_{\delta}$ increases from 0% to 11.8% and further to 165%, respectively. However, in rectifier mode, since the D_{eq} when ignoring line dynamics is smaller than the actual value, the stability region without line dynamics is smaller than the actual stability region. Figure 2.2 (d)(e)(f) show the blue curves inside the grey-shaded area, with the ROA error $\Delta\mathrm{ROA}_{\delta}$ decreasing from 0% to −11.1% and −29%, respectively. When $k_{\mathrm{p,pll}}$ and grid impedance X_g are small, the error caused by ignoring line dynamics is relatively minor, as seen in Figure 2.2 (a)(d). However, as $k_{\mathrm{i,pll}}$ increases or X_g rises, the difference between the two cases becomes significant. This is especially noticeable in Figure 2.2 (f), where the real stability region is constituted by a limit cycle but is defined by the stable manifold of the UEP when ignoring line dynamics, resulting in a substantial stability domain error. Moreover, it can be proven that there is no limit cycle when ignoring line dynamics.

Proposition 2.1. *(nonexistence of limit cycle when ignoring the grid dynamic) When the grid dynamic is ignored, the limit cycle cannot appear.*

Proof. Define an energy function $W(\delta, \omega)$,

$$\begin{aligned} W(\delta,\omega) =& \frac{1}{2k_{\mathrm{i,pll}}}\left(\omega + k_{\mathrm{p,pll}}U_g\sin\delta - k_{\mathrm{p,pll}}I_dX_g - k_{\mathrm{p,pll}}I_qR_g\right)^2 \\ & - U_g\cos\delta - X_gI_d\delta - R_gI_q\delta \end{aligned} \tag{2.7}$$

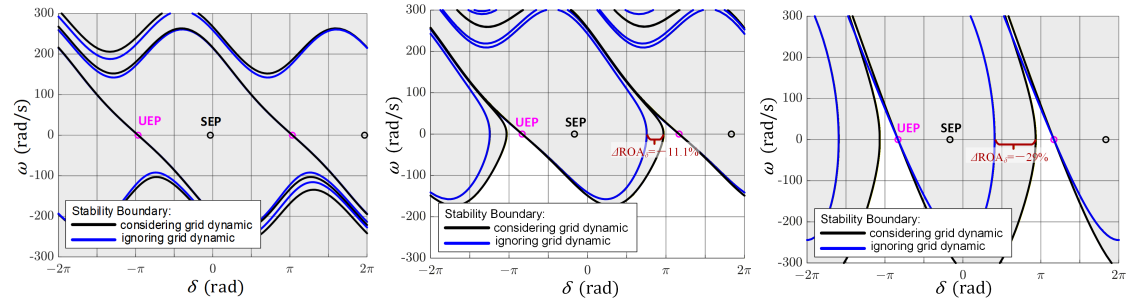
[1]The type of a UEP is defined by the number of its unstable eigenvalues. In particular, a type-I UEP has exactly one unstable eigenvalue, whereas a type-II UEP has two unstable eigenvalues.



(a) Inverter mode (X_g=0.1 pu, $k_{\mathrm{i,pll}} = 100 \cdot k_{\mathrm{p,pll}}$).

(b) Inverter mode (X_g=0.5 pu, $k_{\mathrm{i,pll}} = 100 \cdot k_{\mathrm{p,pll}}$).

(c) Inverter mode (X_g=0.5 pu, $k_{\mathrm{i,pll}} = 500 \cdot k_{\mathrm{p,pll}}$).



(d) Rectifier mode (X_g=0.1 pu, $k_{\mathrm{i,pll}} = 100 \cdot k_{\mathrm{p,pll}}$).

(e) Rectifier mode (X_g=0.5 pu, $k_{\mathrm{i,pll}} = 100 \cdot k_{\mathrm{p,pll}}$).

(f) Rectifier mode (X_g=0.5 pu, $k_{\mathrm{i,pll}} = 500 \cdot k_{\mathrm{p,pll}}$).

Figure 2.2: Stability region with respect to the line dynamics. ($k_{\mathrm{p,pll}} = 10 \cdot 2\pi$, $I_d = 1$, $I_q = 0$, $R_g = 0$, $U_g = 1$ pu)

The derivative of this energy function with respect to time, under the dynamic system represented by (2.2) and (2.4), can be expressed as follows:

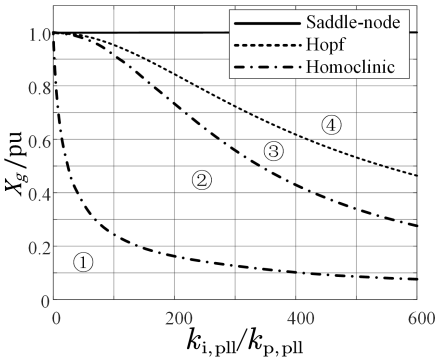
$$\frac{dW}{dt} = -k_{\mathrm{p,pll}} \left(X_g I_d + R_g I_q - U_g \sin\delta\right)^2 \leqslant 0 \tag{2.8}$$

It can be seen that dW/dt is non-positive. Moreover, $\dot{W}(t) = 0$ if and only if the trajectory is confined to the EP, i.e., $(\delta(t), \omega(t)) \equiv (\delta_{\mathrm{uep}}, 0)$ or $(\delta_{\mathrm{sep}}, 0)$. Nontrivial trajectories, including periodic orbits, necessarily satisfy $\dot{W}(t) < 0$ over a finite time interval. That is, $dW/dt = 0$ does not contain the whole trajectories of the system represented by (2.2) and (2.4). Assuming the existence of a closed orbit Γ, the following line integral is taken along a trajectory:

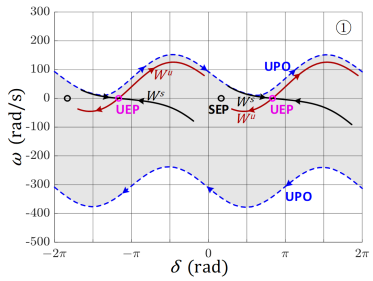
$$\oint_{\Gamma} \frac{\partial W}{\partial \delta_1} d\delta_1 + \frac{\partial W}{\partial \delta_2} d\delta_2 = W\left(\delta_1, \delta_2\right) - W\left(\delta_1, \delta_2\right) = 0 \tag{2.9}$$

This implies $W(\delta_1, \delta_2) \equiv 0$ along this limit cycle. However, this contradicts the fact that W is equal to 0 only at EP. Thus, the proposition is proved. □

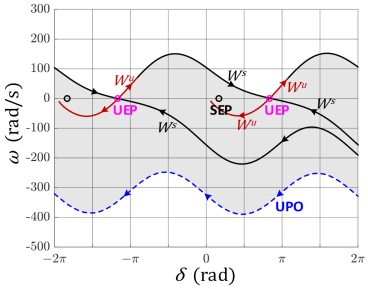
Consequently, when the grid impedance or integral gain $k_{\mathrm{i,pll}}$ in PI controller is large, the phasor model can introduce relatively significant errors in the modeling process. While, under an overdamped PLL or a relatively strong grid, the phasor model provides a good approximation.



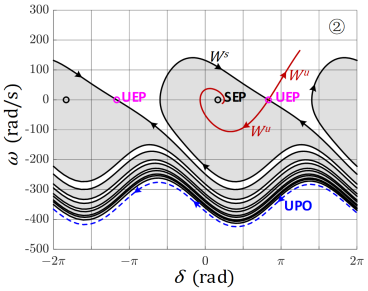
(a) Parametric portrait.



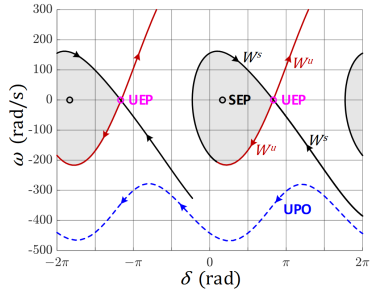
(b) $X_g = 0.5$ pu, $k_{\mathrm{i,pll}} = 10\,k_{\mathrm{p,pll}}$, within region ①.



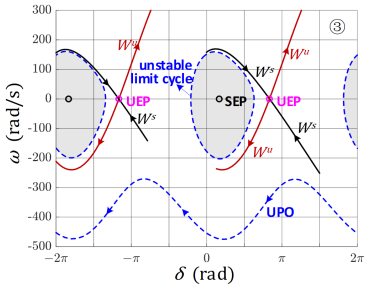
(c) $X_g = 0.5$ pu, $k_{\mathrm{i,pll}} = 25\,k_{\mathrm{p,pll}}$, critical case.



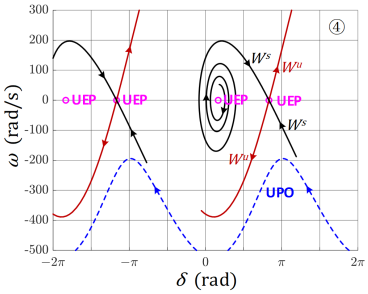
(d) $X_g = 0.5$ pu, $k_{\mathrm{i,pll}} = 100\,k_{\mathrm{p,pll}}$, within region ②.



(e) $X_g = 0.5$ pu, $k_{\mathrm{i,pll}} = 340\,k_{\mathrm{p,pll}}$, critical case.



(f) $X_g = 0.5$ pu, $k_{\mathrm{i,pll}} = 400\,k_{\mathrm{p,pll}}$, within region ③.



(g) $X_g = 0.5$ pu, $k_{\mathrm{i,pll}} = 500\,k_{\mathrm{p,pll}}$, within region ④.

Figure 2.3: Bifurcation of GFL inverter (parameters: $k_{\mathrm{p,pll}} = 10 \cdot 2\pi$, $I_d = 1$, $I_q = 0$, $R_g = 0$, $U_g = 1$ pu).

2.2 Manifold and Bifurcation Properties

2.2.1 Inverter Mode

The manifold and bifurcation of the GFL converter have been covered in [44, 46, 47], and they indicate that with increasing grid impedance X_g and integral gain in PI controller $k_{\mathrm{i,pll}}$, the stability region of the system decreases, and finally, the limit cycle will appear. This Chapter reviews the bifurcation and manifold of the GFL inverter, which are summarized in Figure 2.3. In each case of Figure 2.3, the SEP and UEP are plotted as black and magenta hole dots. The black and red lines represents the stable manifold $\mathcal{W}^s$ and unstable manifold $\mathcal{W}^u$ of UEP. The unstable periodical orbit (UPO) is drawn in a blue dotted line, and the grey-shaded area represents the stability region.

It can be observed from Figure 2.3 (a), bifurcation regions are jointly determined by the ratio $k_{\mathrm{i,pll}}/k_{\mathrm{p,pll}}$ and the grid strength, and this ratio plays a key role in shaping the large-

signal stability properties. With the increase of X_g and $k_{\mathrm{i,pll}}$, the manifold property changes from region to region.

In the region ①, the stability region is enclosed by two UPOs, as shown in Figure 2.3 (b). This region exhibits the largest stability domain, with the ROA extending over $\delta \in [-\pi, \pi]$. For example, when $X_g = 0.5$ pu, maintaining $k_{\mathrm{i,pll}}/k_{\mathrm{p,pll}} < 25$ ensures that the system remains in this favorable region.

As $k_{\mathrm{i,pll}}$ increases, the upper UPO get close to UEP and its stable manifold, and finally, the UPO is annihilated and the stable manifold $\mathcal{W}^s$ and unstable manifold $\mathcal{W}^u$ overlap with each other to form a homoclinic orbit, as shown in Figure 2.3 (c). In this case, a homoclinic bifurcation occurs. Then, with further increase of $k_{\mathrm{i,pll}}$, $\mathcal{W}^s$ and $\mathcal{W}^u$ will separate, as shown in Figure 2.3 (d). When the state is outside the stability region but above the UPO in Figure 2.3 (d), δ and ω will diverge to $+\infty$, and when the state is below the UPO, δ and ω will diverge to $-\infty$.

In Figure 2.3 (e), when $k_{\mathrm{i,pll}}$ is large enough, stable manifolds $\mathcal{W}^s$ and unstable manifolds $\mathcal{W}^u$ will overlap with each other again and constitute a homoclinic orbit. If $k_{\mathrm{i,pll}}$ increase further , the limit cycle will emerge, as shown in the blue dotted line in Figure 2.3(f). When D_{eq} at SEP is not positive, there is no SEP as shown in Figure 2.3 (g).

From these results, it can be concluded that an overdamped PLL design (i.e., $k_{\mathrm{i,pll}} \ll k_{\mathrm{p,pll}}$) is beneficial to transient stability, since it provides the largest ROA. In this case, the stability region of δ can span from the left UEP to the right of the SEP. Moreover, the integral gain in the PI controller primarily serves to gradually eliminate the steady-state error in grid frequency deviation, and therefore a small $k_{\mathrm{i,pll}}$ is sufficient. In practice, overdamped PLL designs are common in engineering applications. Under such an overdamped condition, the influence of line dynamics on the overall stability margin is also very small (as shown in Figure 2.2). As a result, in the following chapters, the PLL is designed to be overdamped. In contrast, the present chapter considers cases where $k_{\mathrm{i,pll}}$ is not necessarily small, in order to facilitate academic rather than practical discussion.

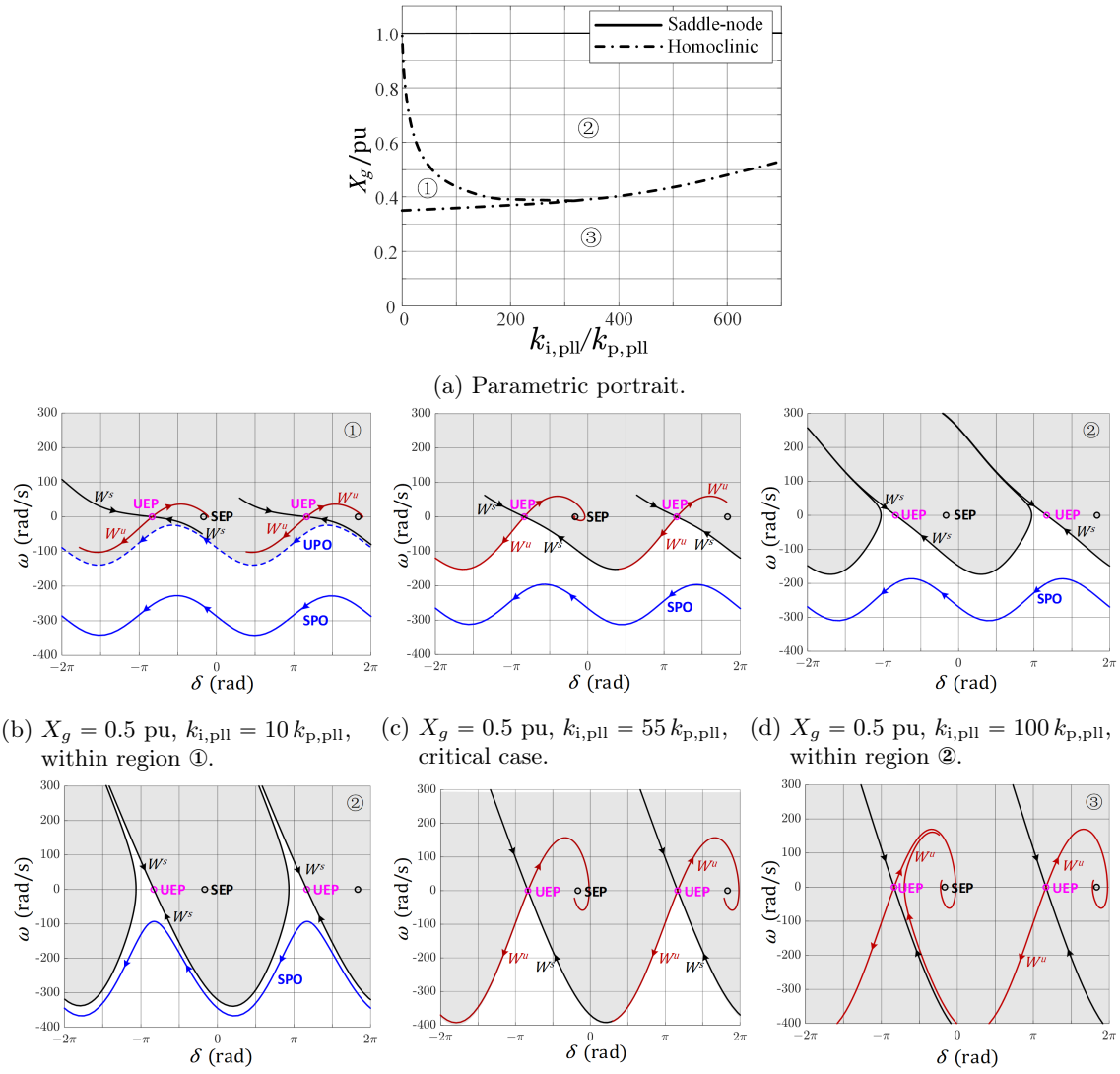
2.2.2 Rectifier Mode

Following the generator convention adopted in this thesis, rectifier operation corresponds to $I_d < 0$. In the equivalent damping term, $-I_d L_g/\omega_s$, however, contributes a positive component. The manifold property of the GFL rectifier is summarized in Figure 2.4. According to Figure 2.4 (a), the manifold property changes from region to region under different X_g and $k_{\mathrm{i,pll}}$. When $k_{\mathrm{i,pll}}$ is small and X_g is not too small, the stability region is enclosed by UPO as shown in Figure 2.4 (b). If the state is outside the stability region (grey-shaded area), δ and ω will converge to a stable periodical orbit (SPO), leading to instability. With the increase of $k_{\mathrm{i,pll}}$, the homoclinic bifurcation occurs, as shown in Figure 2.4 (c). And then, the stability region is constituted by a stable manifold of UEPs, as shown in Figure 2.4 (d)(e). If $k_{\mathrm{i,pll}}$ increases further, the SPO will get close to the stability region, and finally, the SPO will annihilate as illustrated in Figure 2.4 (f). In Figure 2.4 (g), the

stability region is the whole phase plane; this is because M_{eq} becomes small and D_{eq} is dominated by $-I_d L_g/\omega_s$, and the system can be considered as an overdamped system.

It can be observed that, unlike in inverter mode, the parameter $k_{\mathrm{i,pll}}$ does not exert a significant negative impact on the stability region in rectifier mode, and no limit cycle arises in this case. The limit cycle has been recognized as an important dynamic characteristic of PLLs, and its existence has been rigorously proven in [135]. Proposition 2.1 further indicates that the emergence of the limit cycle originates from the negative damping induced by line dynamics. Nevertheless, the subsequent proposition demonstrates that such a limit cycle does not exist in rectifier mode, which distinguishes it from the inverter-mode behavior.

Proposition 2.2. *(nonexistence of limit cycle in rectifier mode) If the GFL converter works as a rectifier (that is, $I_d < 0$), no limit cycle exists for any parameter configuration.*



(a) Parametric portrait.

(b) $X_g = 0.5$ pu, $k_{\mathrm{i,pll}} = 10\,k_{\mathrm{p,pll}}$, within region ①.

(c) $X_g = 0.5$ pu, $k_{\mathrm{i,pll}} = 55\,k_{\mathrm{p,pll}}$, critical case.

(d) $X_g = 0.5$ pu, $k_{\mathrm{i,pll}} = 100\,k_{\mathrm{p,pll}}$, within region ②.

(e) $X_g = 0.5$ pu, $k_{\mathrm{i,pll}} = 500\,k_{\mathrm{p,pll}}$, within region ③.

(f) $X_g = 0.5$ pu, $k_{\mathrm{i,pll}} = 640\,k_{\mathrm{p,pll}}$, critical case.

(g) $X_g = 0.5$ pu, $k_{\mathrm{i,pll}} = 800\,k_{\mathrm{p,pll}}$, within region ④.

Figure 2.4: Bifurcation of GFL rectifier (parameters: $k_{\mathrm{p,pll}} = 10 \cdot 2\pi$, $I_d = -1$, $I_q = 0$, $R_g = 0$, $U_g = 1$ pu).

Proof. Assume there exists a limit cycle Γ in the system, as shown in Figure 2.5. On any trajectory of (2.2) and (2.3), we have $d\delta/dt = f_\delta$ and $d\omega/dt = f_\omega$. Therefore, along the limit cycle Γ, we have

$$\oint_{\Gamma} f_\omega(\delta,\omega)\,d\delta - f_\delta(\delta,\omega)\,d\omega = 0 \tag{2.10}$$

Since the vector field is continuously differentiable in the considered region, and the closed curve under consideration is piecewise smooth; therefore, Green's theorem is applicable. This implies, by Green's theorem, that

$$\begin{aligned}\iint_S \left(\frac{\partial f_\delta}{\partial \delta} + \frac{\partial f_\omega}{\partial \omega}\right) d\delta d\omega =& \frac{1}{M_{eq}} \iint_S D_{eq} d\delta d\omega \\ =& \frac{1}{M_{eq}} \left(\int_{\overset{\frown}{ABCD}} D_{eq}\omega d\delta + \int_{\overset{\frown}{AHGD}} -D_{eq}\omega d\delta\right) = 0\end{aligned} \tag{2.11}$$

Here S is the region enclosed by the limit cycle Γ. S can be divided into the region enclosed by the arc $\overset{\frown}{ABCD}$ where ω is greater than 0, and the region enclosed by the arc $\overset{\frown}{AHGD}$ where ω is less than 0. Now, consider the terms on the right side of the above equation. Applying the mean value theorem for definite integrals, we obtain:

$$\begin{aligned}\int_{\overset{\frown}{ABCD}} D_{eq}\omega d\delta =& \int_{\overset{\frown}{AB}} D_{eq}\omega d\delta + \int_{\overset{\frown}{BC}} D_{eq}\omega d\delta + \int_{\overset{\frown}{CD}} D_{eq}\omega d\delta \\ =& \omega_1 \int_{\delta_A}^{\delta_B} D_{eq} d\delta + \omega_2 \int_{\delta_B}^{\delta_C} D_{eq} d\delta + \omega_3 \int_{\delta_C}^{\delta_D} D_{eq} d\delta\end{aligned} \tag{2.12}$$

Where ω_1, ω_2, and ω_3 are values between points A and B, B and C, C and D, respectively. Since the arc $\overset{\frown}{ABCD}$ is convex, D_{eq} is positive between B and C, but negative between A and B, C and D. Define $\omega_{\min} = \min\{\omega_1, \omega_2, \omega_3\}$. Thus

$$\begin{aligned}\int_{\overset{\frown}{ABCD}} D_{eq}\omega d\delta >& \omega_{\min} \left(\int_{\delta_A}^{\delta_B} D_{eq} d\delta + \int_{\delta_B}^{\delta_C} D_{eq} d\delta + \int_{\delta_C}^{\delta_D} D_{eq} d\delta\right) \\ =& \omega_{\min} \int_{\delta_A}^{\delta_D} D_{eq} d\delta\end{aligned} \tag{2.13}$$

According to the expression of D_{eq} in (2.3), since $I_d < 0$ in rectifier mode, it is easy to derive that $\delta_A < \delta_B < -\pi/2$ and $\delta_D > \delta_C > \pi/2$.

Due to the system having a period of 2π in δ, $\delta_D - \delta_A < 2\pi$ and thus $\sin\delta_D - \sin\delta_A > 0$ (Equality cannot occur unless $\delta_D = \delta_A + 2\pi$, in which case the two trajectories would be tangent to each other, contradicting the uniqueness of trajectories in an autonomous system). Therefore, we can derive

$$\begin{aligned}\int_{\delta_A}^{\delta_D} D_{eq} d\delta =& \int_{\delta_A}^{\delta_D} \left(\frac{k_{\mathrm{p,pll}}}{k_{\mathrm{i,pll}}} U_g \cos\delta - I_d L_g/\omega_s\right) d\delta \\ =& \frac{k_{\mathrm{p,pll}}}{k_{\mathrm{i,pll}}} U_g (\sin\delta_D - \sin\delta_A) - I_d L_g/\omega_s (\delta_D - \delta_A) > 0\end{aligned} \tag{2.14}$$

Similarly, we have

$$\int_{\overline{AHGD}} -D_{eq}\omega d\delta > 0 \tag{2.15}$$

Consequently, these results contradict the assumption that the expression equals zero. The proposition is therefore proved. □

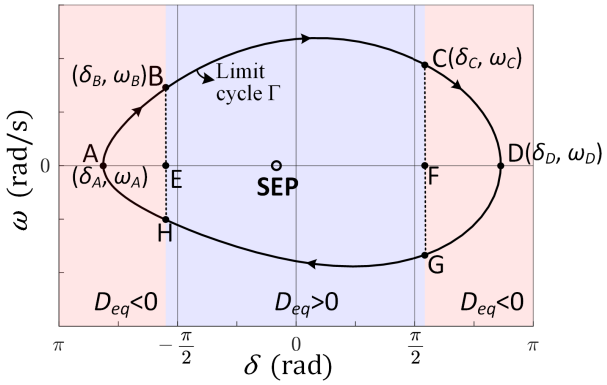


Figure 2.5: Limit cycle of the studied system.

2.3 Energy-Function-based Method for PLL

The energy-function-based method has long been recognized as a classical approach for analyzing transient stability in power systems, and numerous studies have attempted to extend this framework to the analysis of PLL [42, 48, 58, 57, 41, 59, 60, 61]. Although Chapter 4 has demonstrated that a global energy function does not exist for multi-machine systems containing GFL inverters, the energy-function-based approach remains applicable in single-machine systems, making it a valuable analytical tool and an active topic of current research.

In this section, we provide an overview of the Energy-Function-based method and compare the resulting ROA estimates derived from different Lyapunov functions. Furthermore, we abstract an energy function tailored for PI controllers. Unlike the traditional energy function, this formulation is more suitable for capturing the dynamics of PLLs. Importantly, the proposed energy function is not limited to PLLs but is also applicable to a broader class of nonlinear systems employing PI control. To illustrate its generality, we also present an application to a DC-voltage-controlled GFM inverter, which further demonstrates the effectiveness of the proposed energy-function construction.

2.3.1 Overview of the existing energy function for PLL

According to the "swing equation" of the PLL, given in (2.2), the traditional energy function [23] can be applied, as demonstrated in previous studies [58, 57, 60]. The energy function

can be expressed as

$$W(\delta,\omega) = \underbrace{\frac{1}{2}M_{\text{eq}}\omega^2}_{\text{kinetic energy}} + \underbrace{-X_g I_d\delta - U_g\cos\delta}_{\text{potential energy}}, \tag{2.16}$$

and its derivative is obtained as

$$\dot{W} = -D_{\text{eq}}\omega^2, \tag{2.17}$$

which represents the dissipative damping power.

However, unlike the situation in SGs or GFM inverters, the derivative of the energy function is not always non-positive. As a result, the level set used for estimating the ROA must be restricted to the region where D_{eq} remains positive, as illustrated by the red solid line in Figure 2.6. In Figure 2.6, the region where $D_{eq} > 0$ is indicated by the grey-shaded band (as annotated), while the remaining area corresponds to $D_{eq} < 0$. If the energy at the UEP, $W(\delta_{uep}, 0)$, is directly adopted as the critical energy (following the traditional approach in SGs), the resulting ROA estimation will be overly optimistic, as indicated by the red dotted line in Figure 2.6 (where part of the red dotted level set extends outside the real ROA). Consequently, the ROA estimated using the traditional energy/Lyapunov function is overly conservative. It is also worth noting that, in essence, EAC can be interpreted as an energy-based method in which the critical angle corresponds to zero kinetic energy and is associated with the UEP. As a result, EAC yields the same ROA estimate as the traditional energy-function-based approach and therefore inherits its limitations valid for ROA estimation in such systems.

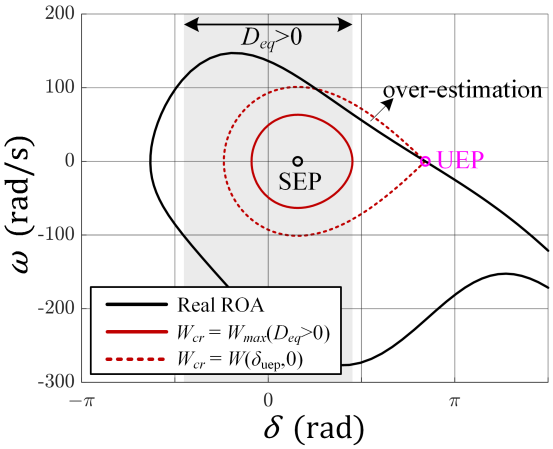


Figure 2.6: ROA estimation by traditional energy / Lyapunov function[2].

In order to enlarge the estimated ROA, [48] proposed a Lyapunov function, which we arrange under the (δ,ω) states as follows:

$$\begin{aligned} W(\delta,\omega) =& \frac{1}{2}\left[M_{eq}\omega - \frac{k_{\text{p,pll}}}{k_{\text{i,pll}}}\left(X_g I_d - U_g\sin\delta\right) - L_g I_d\left(\delta-\delta_{\text{sep}}\right)\right]^2 \\ &- M_{eq}\left(X_g I_d\delta + U_g\cos\delta\right) \end{aligned} \tag{2.18}$$

[2]Note that the phase space is 2π wrap-around and the phase angle δ is 2π-periodic. For clarity, all ROAs in this subsection are illustrated within a single 2π interval.

and the derivative is obtained as:

$$\dot{W} = -\frac{k_{\mathrm{p,pll}}}{k_{\mathrm{i,pll}}}\left(X_g I_d - U_g \sin\delta\right)\left[X_g I_d - U_g \sin\delta + \frac{k_{\mathrm{i,pll}}}{k_{\mathrm{p,pll}}} L_g I_d \left(\delta - \delta_{\mathrm{sep}}\right)\right] \tag{2.19}$$

To ensure that the derivative of the Lyapunov function is negative, both terms $(X_g I_d - U_g \sin\delta)$ and $\left[X_g I_d - U_g \sin\delta + \frac{k_{\mathrm{i,pll}}}{k_{\mathrm{p,pll}}} L_g I_d \left(\delta - \delta_{\mathrm{sep}}\right)\right]$ must be positive simultaneously. The first condition is satisfied when $\delta < \delta_{\mathrm{uep}}$, while the second condition is satisfied when $\delta < \delta^*$. δ^* is implicitly defined by $U_g \sin\delta^* - X_g I_d = \frac{k_{\mathrm{i,pll}}}{k_{\mathrm{p,pll}}} L_g I_d \left(\delta^* - \delta_{\mathrm{sep}}\right)$ and can be solved numerically, and the boundary δ^* is also illustrated in Figure 2.7. It can be observed that the estimated ROA is significantly enlarged compared with the result obtained from the traditional Lyapunov function.

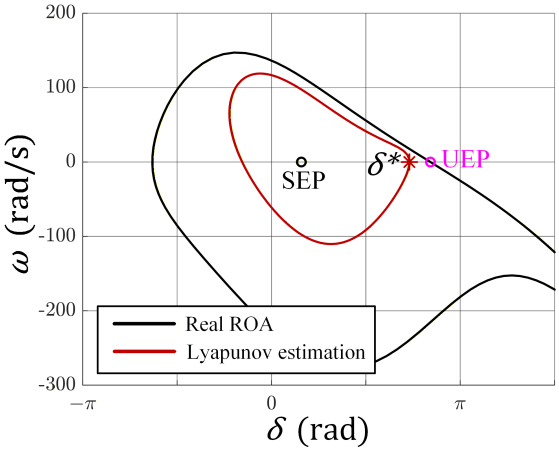


Figure 2.7: ROA estimation by Lyapunov function (2.18).

One type of energy function, termed the generalized energy function, was proposed in [62] and applied to a two–grid-following inverter scenario in [61]. In this work, the generalized energy function is applied to the PLL scenario. The energy function is

$$W(\delta,\omega) = \frac{1}{2} M_{eq}\omega^2 - X_g I_d \delta - U_g \cos\delta - \beta M_{eq}\omega\left(X_g I_d - U_g \sin\delta\right) \tag{2.20}$$

where β is a tunable parameter.

The derivative of this energy function is:

$$\dot{W} = -\begin{bmatrix} X_g I_d - U_g \sin\delta \\ \omega \end{bmatrix}^T \begin{bmatrix} \beta & -\frac{1}{2}\beta D_{eq} \\ -\frac{1}{2}\beta D_{eq} & D_{eq} - \beta M_{eq} U_g \cos\delta \end{bmatrix} \begin{bmatrix} X_g I_d - U_g \sin\delta \\ \omega \end{bmatrix} \tag{2.21}$$

To ensure that $\dot{W} \leqslant 0$, the parameter β must satisfy

$$0 < \beta < \frac{D_{eq}}{\frac{D_{eq}^2}{4} + M_{eq} U_g \cos\delta} = \beta_{\max}.$$

In Figure 2.8, the solid line represents the estimated ROA obtained from the Lyapunov/energy function (2.20), while the dotted lines correspond to $\dot{W} = 0$ from (2.21). Different shades

of red indicate different values of β. For each β, the largest level set for estimating the ROA is obtained when the solid line (level set) is tangent to the corresponding dotted line, which guarantees that the derivative of the energy function remains negative inside the level set. As shown in Figure 2.8, the estimated ROA is much less conservative compared with the traditional method. This also means that, unlike the traditional energy function approach where the critical energy is determined directly by the UEP, the critical energy in the generalized energy function is not easy to determine.

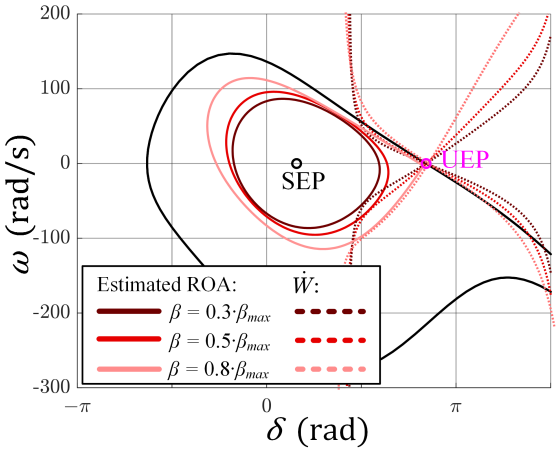


Figure 2.8: ROA estimation by Lyapunov function (2.20).

2.3.2 PI-controller energy function

The nonlinear system with controller can be abstracted to Figure 2.9. There are two mainstream controllers: one is the low-pass filter (LPF) controller and the other is the proportional–integral (PI) controller, as illustrated in Figure 2.9 (a) and (b). The nonlinear system is represented by $f(\delta)$.

For the LPF controller, it is straightforward to emulate the swing equation. The time constant and the gain of the LPF act as the equivalent inertia and damping. Specifically, the swing equation of the system in Figure 2.9 (a) can be written as

$$\begin{cases} \dot{\delta} = \omega \\ J\dot{\omega} = [y_{\text{ref}} - f(\delta)] - D\omega \end{cases} \tag{2.22}$$

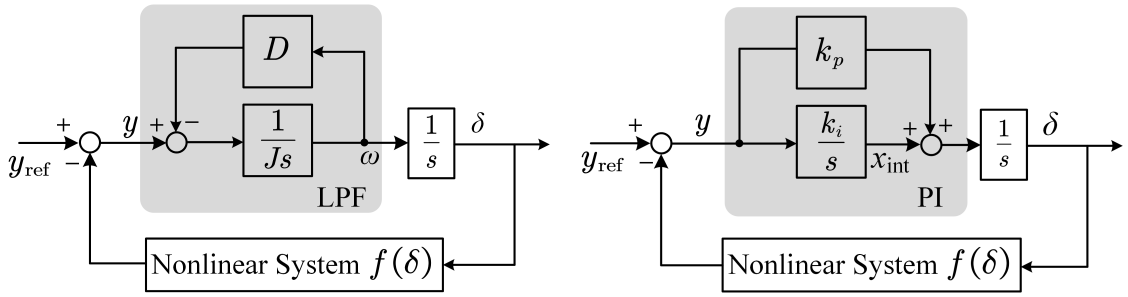
where $y_{\text{ref}} - f(\delta)$ serves as the synchronizing torque. The LPF therefore naturally realizes damping and inertia. The corresponding classical energy function is

$$W = \underbrace{\frac{1}{2}J\omega^2}_{\text{kineticenergy}} \underbrace{- \int [y_{\text{ref}} - f(\delta)]\, d\delta}_{\text{potentialenergy}} \tag{2.23}$$

with derivative

$$\dot{W} = -D\omega^2 \tag{2.24}$$

In the GFM inverter, $y_{\text{ref}} = P_{\text{ref}}$ represents the power reference, and the nonlinear system



(a) LPF controller. (b) PI controller.

Figure 2.9: Control block diagram of the nonlinear system.

corresponds to the active power $\frac{EU_g}{X_g}\sin\delta$. In this case, the energy function (2.23) reduces to the typical form

$$W = \tfrac{1}{2}J\omega^2 - P_{\text{ref}}\delta - \tfrac{EU_g}{X_g}\cos\delta.$$

The PI controller, shown in Figure 2.9 (b), is another widely used controller. The input $y = y_{\text{ref}} - f(\delta)$ is fed into the PI controller instead of the LPF. The integrator output is denoted as x_{int}, and the sum of the integrator and proportional parts is then passed to another integrator and then the nonlinear system $f(\delta)$. The corresponding swing equation is

$$\begin{cases} \dot{\delta} = \omega \\ \underbrace{\frac{1}{k_i}}_{J_{eq}}\dot{\omega} = f(\delta) - \underbrace{\frac{k_p}{k_i}\frac{\partial f(\delta)}{\partial \delta}}_{D_{eq}}\omega \end{cases} \tag{2.25}$$

Here, the equivalent damping D_{eq} is not constant but depends on $\frac{\partial f(\delta)}{\partial \delta}$. As a result, if the classical energy function is directly applied, the derivative of the energy function becomes indefinite and not necessarily non-positive, owing to the variation of D_{eq}.

To address this issue, we propose a dedicated energy function for the PI controller:

$$W = \frac{1}{2k_i}{x_{\text{int}}}^2 - \int \left[y_{\text{ref}} - f(\delta)\right] d\delta \tag{2.26}$$

Compared with (2.23), the kinetic energy is $\frac{1}{2k_i}{x_{\text{int}}}^2$. The derivative of the energy function (2.26) is

$$\dot{W} = -k_p\left[y_{\text{ref}} - f(\delta)\right]^2 \tag{2.27}$$

which is always non-positive.

It should be noted that the PI-controller energy function proposed in this thesis is general and is applicable to any nonlinear system equipped with a PI controller whose structure follows Figure 2.9 (b).

One typical example is the PLL. Since the PLL employs a PI controller instead of an LPF, the structure in Figure 2.9 is equivalent to the control structure of the PLL. In this case,

the input of the PI controller $y = y_{\text{ref}} - f(\delta)$ corresponds to the q-axis voltage v_q, where

$$v_q = X_g I_d + R_g I_q - U_g \sin\delta + \tfrac{\omega L_g I_d}{\omega_s},$$

which implies $y_{\text{ref}} = X_g I_d + R_g I_q$ and $f(\delta) = U_g \sin\delta - \frac{\omega L_g I_d}{\omega_s}$.

If the line dynamics are neglected, $f(\delta) = U_g \sin\delta$, and the energy function of the PLL derived from (2.26) is

$$W = \tfrac{1}{2k_i} {x_{\text{int}}}^2 - (X_g I_d + R_g I_q)\delta - U_g \cos\delta,$$

which is identical to (2.7). If the line dynamics are considered, $f(\delta) = U_g \sin\delta - \frac{\omega L_g I_d}{\omega_s}$, and the energy function (2.26) becomes

$$\begin{aligned} W =& \tfrac{1}{2k_i} {x_{\text{int}}}^2 - \int \left(X_g I_d + R_g I_q - U_g \sin\delta + \tfrac{\omega L_g I_d}{\omega_s} \right) d\delta \\ =& \tfrac{1}{2k_i} \left(\omega - k_{\text{p,pll}} v_q\right)^2 - \left(X_g I_d + R_g I_q\right)\delta - U_g \cos\delta - \int \tfrac{\omega L_g I_d}{\omega_s}\, d\delta, \end{aligned} \tag{2.28}$$

where $x_{\text{int}} = \omega - k_{\text{p,pll}} v_q$, and $v_q = X_g I_d + R_g I_q - U_g \sin\delta + \frac{\omega L_g I_d}{\omega_s}$ as defined above. In (2.28), the term $\int \frac{\omega L_g I_d}{\omega_s}\, d\delta$ is path-dependent, arising from line dynamics. One method to approximate this path-dependent term is the ray approximation [23, 59], where the integral is represented by a straight line (ray) passing through the SEP. Specifically, it is expressed as

$$\int \tfrac{\omega L_g I_d}{\omega_s}\, d\delta \approx \tfrac{1}{2} \left(\delta - \delta_{sep}\right) \tfrac{\omega L_g I_d}{\omega_s}. \tag{2.29}$$

While the ray approximation yields a reasonably large ROA estimate, it does not guarantee strict conservativeness. As shown by the blue curve in Figure 2.10, there is a slight overestimation along a certain direction, occurring in a small region of the phase plane near the UEP and visible as a minor 'leakage' beyond the real ROA. This leakage is confined to a small wedge near the UEP, whose projections are 0.116 rad on the δ-axis (about 6.67°) and about 9.09 rad/s on the ω-axis; and over-estimation can only occur when the fault-on trajectory passes through this wedge.

Herein, we adopt the critical trajectory approximation [125]. In this method, instead of using a ray through the SEP, the path-dependent term is represented by the critical trajectory passing through the UEP. Precisely, in the critically stable case, the post-fault trajectory approaches the UEP along the stability boundary $\mathcal{C}$ (i.e., the stable manifold of the UEP). This boundary segment from (δ, ω) to the UEP is approximated by the straight line $\mathcal{L}$ connecting (δ, ω) and $(\delta_{\text{uep}}, 0)$, such that the integral $\int \omega\, \mathrm{d}\delta$ reduces to the area of a triangle with base $(\delta_{\text{uep}} - \delta)$ and height ω in the (δ, ω) plane. Accordingly, this path-dependent term can be expressed as

$$\begin{aligned} \int_{\mathcal{C}:(\delta_{\text{uep}},0)\to(\delta,\omega)} \frac{L_g I_d}{\omega_s}\, \omega\, \mathrm{d}\delta &= -\int_{\mathcal{C}:(\delta,\omega)\to(\delta_{\text{uep}},0)} \frac{L_g I_d}{\omega_s}\, \omega\, \mathrm{d}\delta \\ &\geqslant -\int_{\mathcal{L}:(\delta,\omega)\to(\delta_{\text{uep}},0)} \frac{L_g I_d}{\omega_s}\, \omega\, \mathrm{d}\delta = -\frac{\omega\left(\delta_{\text{uep}} - \delta\right)}{2} \cdot \frac{L_g I_d}{\omega_s}. \end{aligned} \tag{2.30}$$

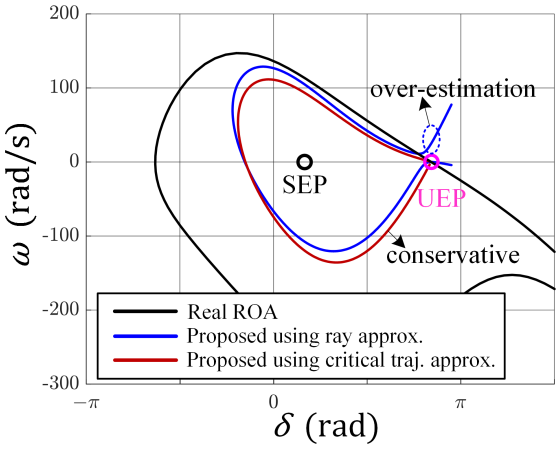


Figure 2.10: ROA of PLL estimated by proposed PI-controller Energy function.

As a result,

$$\text{Eq. (2.28)} \leqslant \tfrac{1}{2k_i}\left(\omega - k_{\text{p,pll}} v_q\right)^2 - \left(X_g I_d + R_g I_q\right)\delta - U_g \cos\delta + \omega \frac{\delta_{\text{uep}} - \delta}{2} \cdot \frac{L_g I_d}{\omega_s}. \quad (2.31)$$

Equation (2.31) ensures a conservative estimation of the ROA by using the level set crossing the energy at the UEP, as the red line plotted in Figure 2.10, since the estimated energy is always larger than the exact energy that contains the path-dependent term.

2.3.3 More applications of the PI-controller energy function

The DC-voltage-controlled GFM inverter—also referred to as the matching-control or voltage-forming (VFM) inverter—has become a recent research hotspot, as it enables both DC-voltage regulation and active-power tracking compared with the traditional GFM inverter [136, 55, 137]. The control structure of the VFM inverter is illustrated in Figure 2.11.

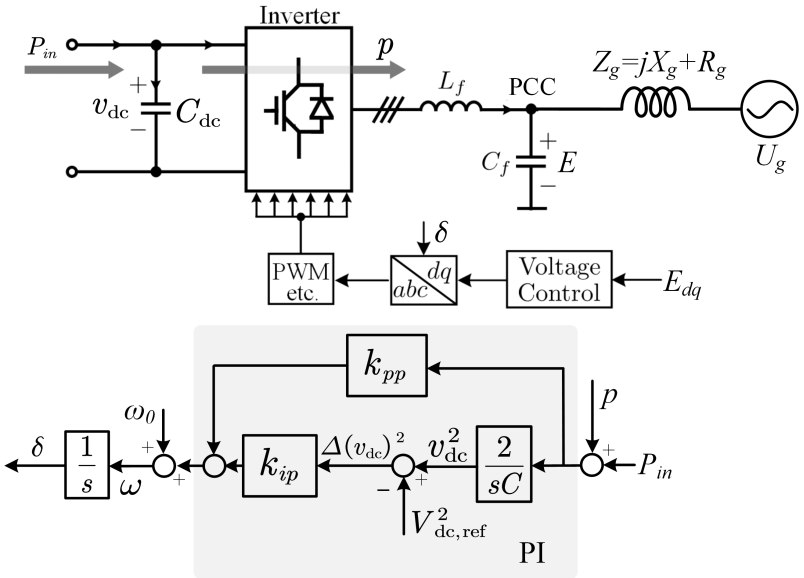


Figure 2.11: control structure of VFM inverter (DC-voltage-controlled GFM).

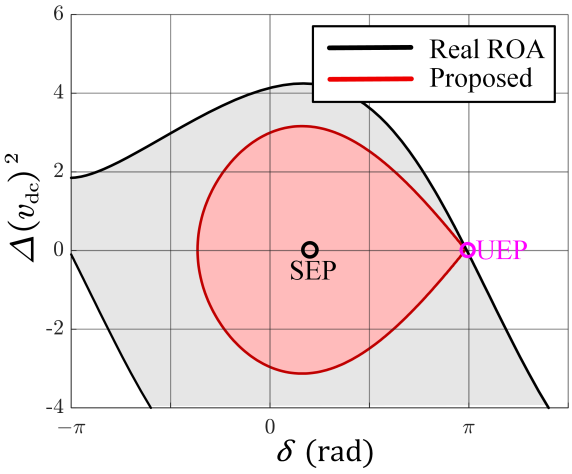


Figure 2.12: ROA of VFM inverter (DC-voltage-controlled GFM).

Unlike the traditional GFM inverter where the controller is implemented by a LPF, the VFM scheme can be realized by a PI controller, as shown in Figure 2.11. The voltage angle is driven by the PI output; the DC-link capacitor serves as the integrator, and the power feedforward acts as the proportional part. The feedforward with gain k_{pp} provides damping to the overall system, while the DC-voltage control gain k_{ip} achieves DC-voltage regulation [136, 55, 137].

For a single VFM–infinite-bus system as shown in Figure 2.11, the parameters are chosen as $k_{pp} = 2 \cdot 2\pi$ pu, $k_{ip} = 1 \cdot 2\pi$ pu, DC-link capacitor $C_{\mathrm{dc}} = 12.5$ pu, DC-voltage reference $V_{\mathrm{dc,ref}} = 2.5$ pu, and grid impedance $0.5j + 0.05$ pu. The real ROA is shown by the gray-shaded area in Figure 2.12. The vertical axis denotes the error of the squared DC voltage, i.e., $\Delta(v_{\mathrm{dc}})^2 = v_{\mathrm{dc}}^2 - V_{\mathrm{dc,ref}}^2$. According to the proposed energy function in (2.26), the energy function for the VFM inverter is

$$\begin{aligned} W &= \frac{C}{4} k_{ip} \big[\Delta(v_{\mathrm{dc}})\big]^2 - \int (P_{in} - p)\, \mathrm{d}\delta \\ &= \frac{C}{4} k_{ip} \big[\Delta(v_{\mathrm{dc}})\big]^2 - P_{in}\delta - \frac{X_g}{R_g^2 + X_g^2} E U_g \cos\delta + \frac{R_g U_g^2}{R_g^2 + X_g^2}\delta - \frac{R_g U_g E}{R_g^2 + X_g^2} \sin\delta, \end{aligned} \tag{2.32}$$

and its derivative is

$$\dot{W} = -k_{pp} (P_{in} - p)^2 , \tag{2.33}$$

which is non-positive.

The ROA estimated by the proposed energy function is shown by the red-shaded region in Figure 2.12. The estimation is reasonable and conservative, which is desirable for stability assessment.

2.4 Results of HIL Experiment and EMT Simulation

The EMT simulation is implemented in MATLAB/Simulink, where the EMT averaging model is employed to represent the converter by neglecting the detailed switching behaviors

Table 2.1: Simulation and HIL experiment parameters

Parameters	Simulation (pu)	HIL experiment	
		SI	pu
Grid impedance Z_l	$0.1j + 0.01$	$0.152\,\text{mH} + 4.8\,\text{m}\Omega$	$0.1j + 0.01$
Grid impedance Z_g	$0.4j + 0.044$	$0.606\,\text{mH} + 19.2\,\text{m}\Omega$	$0.4j + 0.04$
PLL parameter $k_{p,\text{pll}}$	$10 \cdot 2\pi$	$10 \cdot 2\pi$	–
PLL parameter $k_{i,\text{pll}}$	$100 \cdot k_{p,\text{pll}}$	$100 \cdot k_{p,\text{pll}}$	–
Current control bandwidth	600 Hz	600 Hz	–
Switching frequency	Averaging model	10 kHz	–
Control frequency	–	10 kHz	–
LC filter L_f	0.05	$75.7\,\mu\text{H}$	0.05
LC filter C_f	0.02	$133.7\,\mu\text{F}$	0.02
DC capacitor C_{dc}	12.5	83 mF	12.5
d-axis current reference I_d	1, −0.8	1449 A, −1159 A	1, −0.8
q-axis current reference I_q	0, ±0.6	0, ±870 A	0, ±0.6
Fault resistance	1e−3	$0.48\,\text{m}\Omega$	1e−3
DC voltage V_{dc}	2.5	1725 V	2.5
Grid voltage U_g	1	690 V	1
Base Capacity S_B	1	1 MW	1
Base voltage V_B	1	690 V	1
Base Frequency ω_s	50 Hz	50 Hz	–

of power electronic components such as IGBTs and SiC MOSFETs [130]. The hardware-in-the-loop (HIL) experiment is realized using an OPAL-RT real-time simulator (OPAL-5707), leveraging the embedded FPGA core within the eHS toolbox. This setup achieves a simulation timestep of up to 200 ns, enabling highly detailed real-time modeling of the converter. The overall configuration of the HIL system is illustrated in Figure 2.13, where a DSP controller generates PWM signals to control the converter. The relevant simulation and experimental parameters are listed in Table 2.1. Both the converter's switching frequency and DSP control frequency are set to 10 kHz. It should be noted that this thesis focuses on transient stability and large-signal control dynamics, rather than

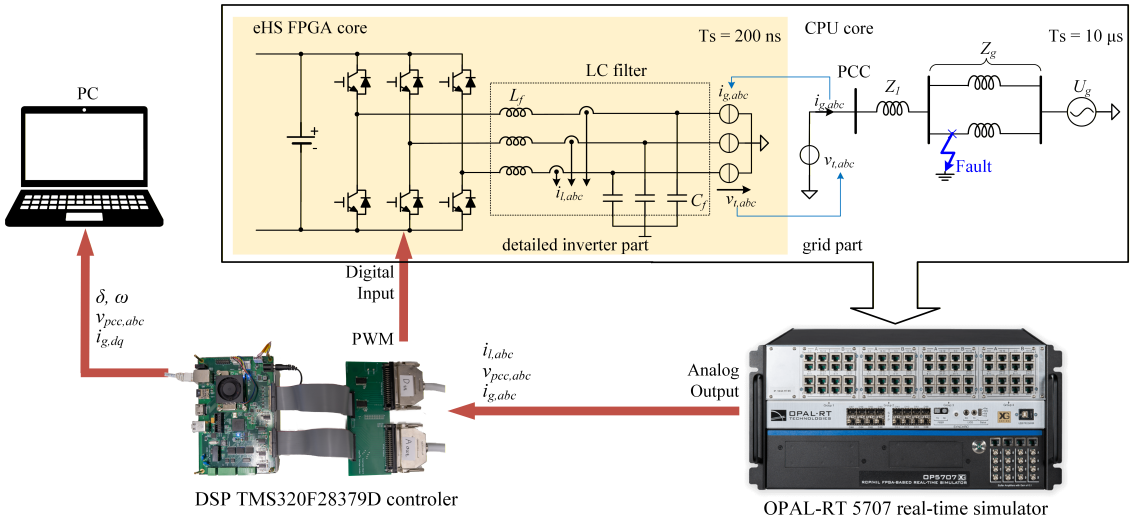
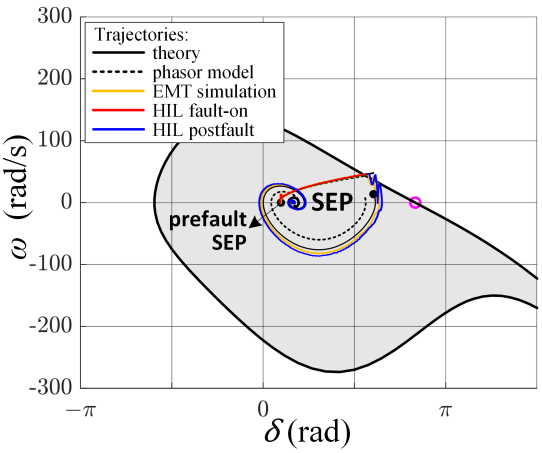
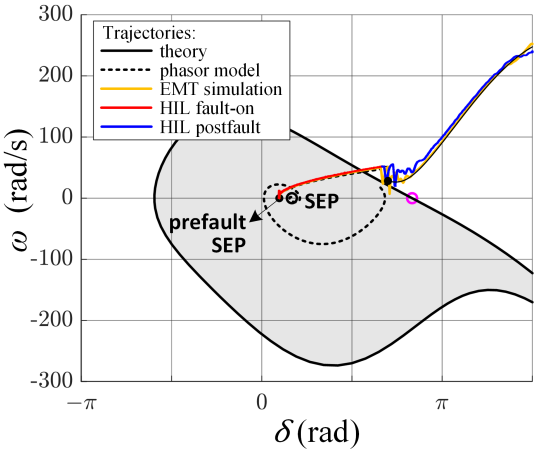


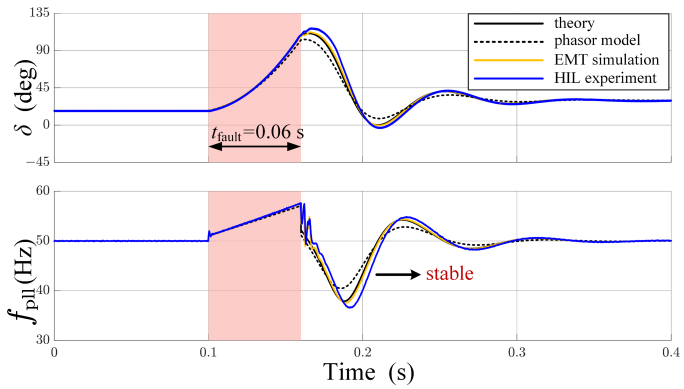
Figure 2.13: HIL Experiment Setup.



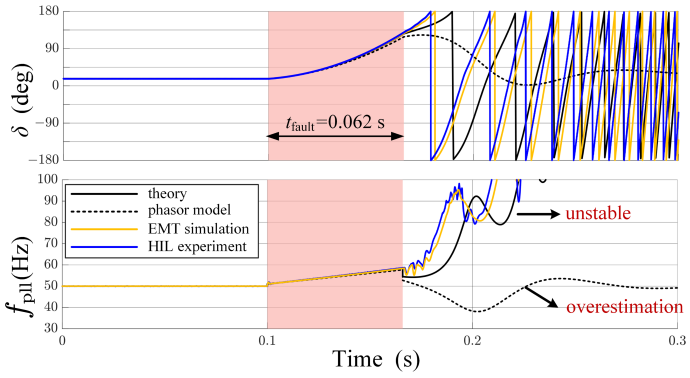
(a) phase portrait. $t_{\text{fault}} = 0.06$ s.



(b) phase portrait. $t_{\text{fault}} = 0.062$ s.



(c) time domain. $t_{\text{fault}} = 0.06$ s.

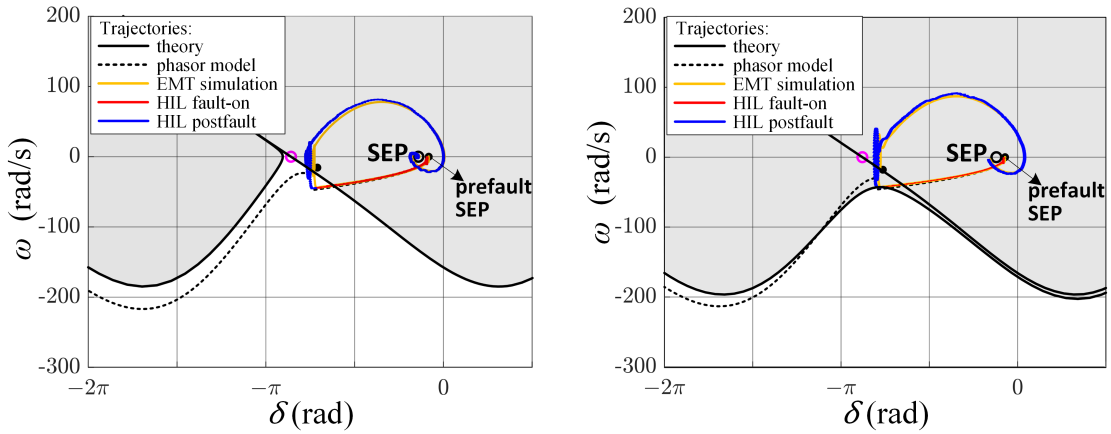


(d) time domain. $t_{\text{fault}} = 0.062$ s.

Figure 2.14: Results of Inverter Mode under critical fault clearing time, and comparison of different models.

on detailed converter hardware design and modulation. Accordingly, this representative and broadly adopted switching frequency is selected, which is applicable across different inverter types and power ratings, as commonly adopted in IBR transient stability studies (e.g., [50, 27, 43, 138, 139]). In this context, the switching frequency primarily affects control delay and the design of the inner current-loop bandwidth.

At t = 0.1 s, a three-phase-to-ground fault is simulated on one of the parallel transmission



(a) phase portrait. I_d = -0.8 pu, I_q = +0.6 pu, t_{fault} = 0.09 s.

(b) phase portrait. I_d = -0.8 pu, I_q = - 0.6 pu t_{fault} = 0.078 s

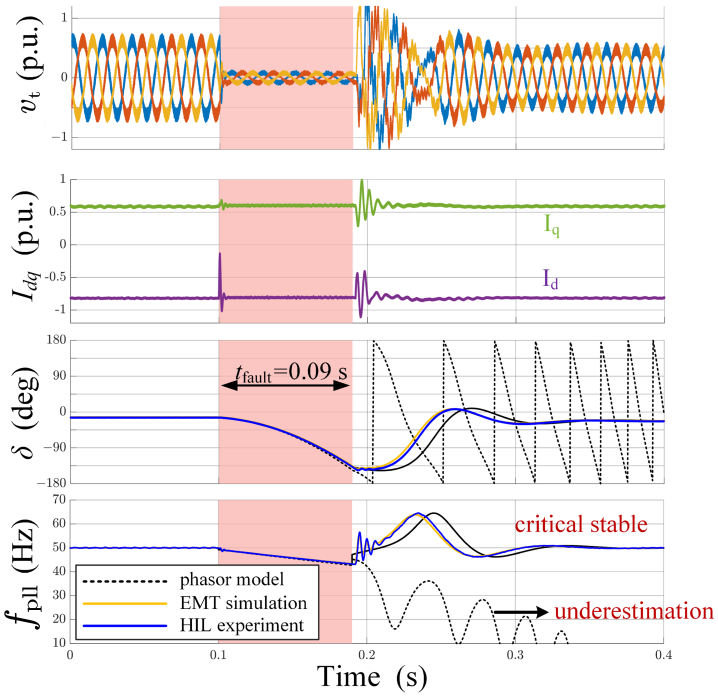
Figure 2.15: Results of rectifier Mode under critical fault clearing time, and comparison of different models (phase portrait).

lines, as indicated in Figure 2.13. After a specific fault-clearing time (t_{fault}), the affected transmission line is cut.

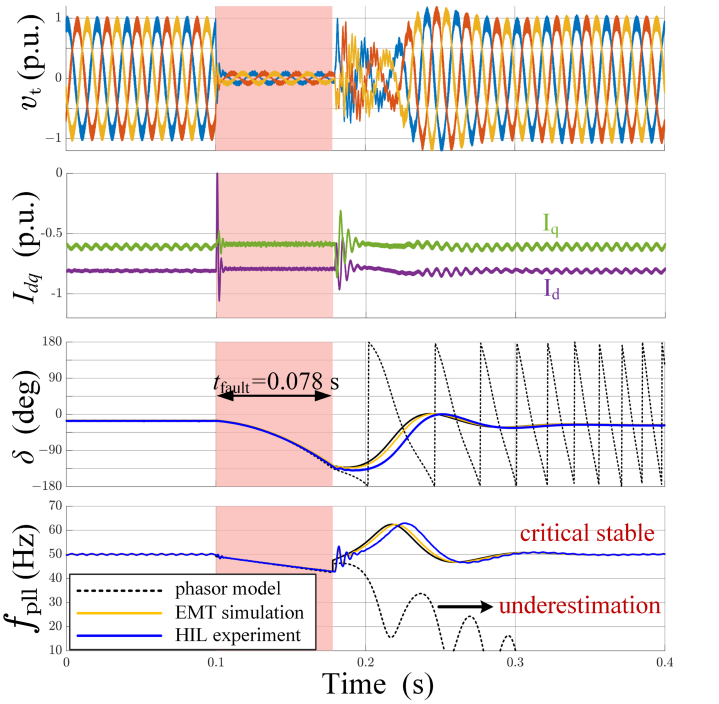
When the converter operates as an inverter (with $I_d > 0$, supplying active power to the grid), the CCT is approximately 0.061 s. Comparative results of different models for fault-clearing times of $t_{\text{fault}} = 0.06$ s and 0.062 s are presented in Figure 2.14. The PLL output frequency is denoted as $f_{\text{pll}} = (\omega + \omega_s)/2\pi$. When $t_{\text{fault}} = 0.06$ s, the real system remains stable, whereas it becomes unstable at $t_{\text{fault}} = 0.062$ s. The phasor model, which neglects line dynamics, overestimates the ROA, erroneously predicting stability even when the real system becomes unstable. As shown in Figure 2.14 (d), the real system becomes unstable, whereas the phasor model still predicts stability, indicating that the phasor model overestimates the ROA in inverter operation.

The bandwidth of the inner current control loop is set relatively low at 600 Hz. Compared to theoretical calculations, the EMT simulation includes the dynamics of the current control loop in Simulink. As noted in [84], the transfer function from δ to I_d acts similarly to a high-pass filter with positive gain, causing an increase in δ or ω to induce a small positive perturbation on I_d. This perturbation exacerbates acceleration, thus reducing the system's transient stability. The HIL experimental results closely reflect the actual inverter behavior—including factors such as switching losses, voltage limits, etc.—while, compared with the EMT trajectories, exhibiting slight delays and more pronounced harmonic distortions. These discrepancies are mainly attributed to controller delays and non-ideal PWM switching effects under large disturbances. Nevertheless, the difference in CCT between EMT simulation and HIL experiments is less than 0.001 s around the numerical CCT of 0.061 s, indicating that the overall transient stability behavior and conclusions remain consistent.

When configured as a rectifier ($I_d < 0$), absorbing active power from the grid), the converter is tested with a power factor set at 0.8 and a reactive current (I_q) of ± 0.6 pu, injecting



(a) I_d = -0.8 pu, I_q = +0.6 pu, t_{fault} = 0.09 s.



(b) I_d = -0.8 pu, I_q = -0.6 pu, t_{fault} = 0.078 s.

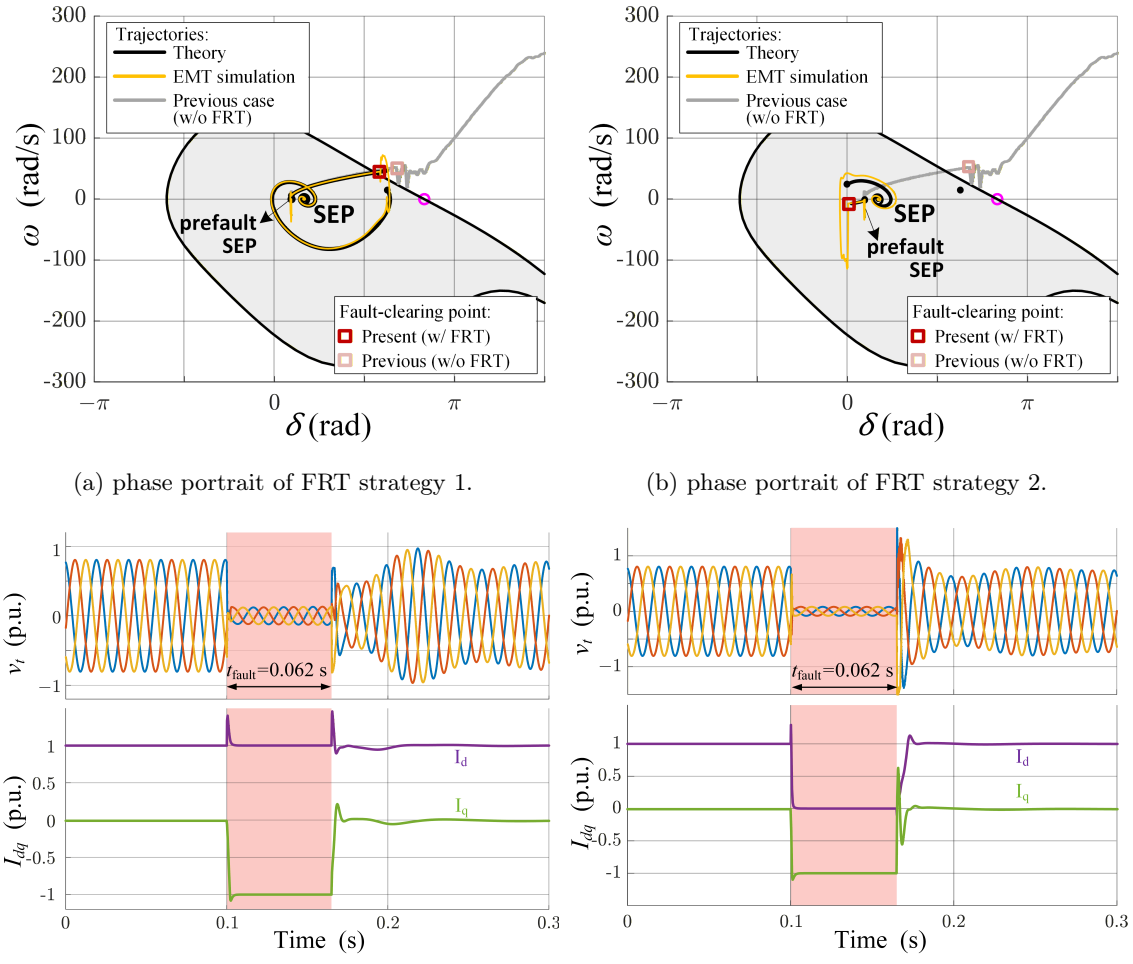
Figure 2.16: Time-domain HIL results of rectifier Mode under critical fault clearing time, and comparison of different models.

or absorbing reactive power, respectively. The results under these conditions are depicted in Figure 2.15 and Figure 2.16. Notably, with I_q = 0.6 pu (absorbing reactive power), the CCT significantly increases to around 0.09 s, whereas it decreases to approximately 0.078 s when I_q = -0.6 pu (injecting reactive power), along with a corresponding reduction

in the ROA. This behavior is primarily attributed to the resistance of the transmission lines; a positive I_q is advantageous for preventing the rectifier from decelerating, a scenario common in distribution networks with relatively high resistances.

Additionally, Figure 2.15 and Figure 2.16 reveals that the phasor model, neglecting line dynamics, exhibits less stability than the actual system, resulting in a reduced ROA and thus underestimating the transient stability of the GFL rectifier. As shown in Figure 2.16, the real system remains stable, whereas the phasor model predicts instability, indicating that the phasor model underestimates the ROA in rectifier operation.

Similar to the inverter scenario, inclusion of the current control loop in simulations shows that a slight decrease in δ introduces a negative perturbation on I_d, thereby improving stability. Consequently, simulation waveforms precede the theoretical waveforms. Finally, the HIL experimental results, accounting comprehensively for realistic operational factors,



(a) phase portrait of FRT strategy 1.

(b) phase portrait of FRT strategy 2.

(c) time domain of FRT strategy 1.

(d) time domain of FRT strategy 2.

Figure 2.17: EMT simulation results with FRT, compared with the corresponding non-FRT cases under identical system parameters and fault conditions. All cases are consistent with Figure 2.14 (b),(d), with the same fault-clearing time $t_{\text{fault}} = 0.062$ s. FRT strategy 1 maintains active power during the fault, whereas FRT strategy 2 enforces zero active power.

align closely with the EMT simulations.

Although fault-ride-through (FRT) strategies during grid faults are not the main focus of this thesis, their potential influence on transient stability is briefly examined to clarify the underlying stability mechanism.

The same system parameters and fault scenario as in Figure 2.14 (b),(d) are considered. In the baseline case without FRT, the system becomes unstable when the fault duration reaches 0.062 s. It is now assumed that the GFL inverter is able to detect the fault and apply a grid-code-compliant FRT strategy. According to the relevant grid code [140], no explicit requirement is imposed on active power during the fault, except that active power output must be restored immediately after fault clearance.

First, an FRT strategy that maintains active power while injecting rated reactive current during the fault is examined. The corresponding phase portrait and time-domain responses are shown in Figure 2.17 (a),(c). Compared with the non-FRT case, reactive current injection significantly slows down the fault-on trajectory, such that the fault-clearing state lies inside the ROA of the post-fault system. As a result, the system remains stable. The theoretical critical CCT increases from 0.062 s to approximately 0.068 s. This behavior can be explained by the PLL swing equation (2.2). In the presence of non-zero line resistance, I_q reduces the acceleration of the PLL state during the fault, thereby delaying its departure from the stability boundary. If the line resistance were negligible, the stabilizing effect of reactive current injection would theoretically diminish.

An additional FRT strategy is then considered, in which active power is reduced to zero during the fault. The corresponding results are shown in Figure 2.17 (b),(d). In this case, the fault-on trajectory evolves much more slowly, and the system state remains close to the pre-fault equilibrium at the same clearing time of 0.062 s. The theoretical critical CCT increases to 0.23 s. The trajectory is observed to move toward decreasing phase angle δ. Literature [141] also indicates that, with appropriate alignment of current components and grid impedance, the PLL state may theoretically remain stationary during the fault.

It is emphasized that the key principle underlying this thesis remains unchanged: transient stability assessment can be decomposed into (i) the ROA of the post-fault system and (ii) the system state at the fault-clearing instant. If the resulting clearing state inside the ROA, the system is transient stable.

Finally, although some FRT strategies such as PLL freezing may keep the system state close to equilibrium during the fault, small grid-frequency deviations can introduce phase mismatches at fault clearance [142]. If such deviations lie outside the ROA, instability may still occur, further highlighting the importance of an ROA-based interpretation of transient stability.

2.5 Summary

In this chapter, the manifold characteristics and ROA of PLL in GFL converter have been comprehensively investigated, with emphasis on the effects of operating mode (inverter or rectifier), modeling choices (with or without inductive line dynamics), and controller parameters. Specifically, line dynamics cause an overestimation of the ROA under inverter operation, while causing an underestimation of ROA under rectifier operation. A rigorous theoretical proof has also been provided to establish that limit cycles cannot occur in rectifier mode, in contrast to inverter mode where limit cycles may arise. It was found that increasing the integral gain of the PLL ($k_{\mathrm{i,pll}}$) consistently reduces the ROA in inverter mode, and the overdamped PLL design is a better choice for GFL inverters.

Furthermore, this chapter has revisited existing Lyapunov-function-based approaches for analyzing the PLL and then proposed a dedicated energy function tailored for PI controllers. This *PI-controller energy function* enables the estimation of ROA of a PLL in a single GFL inverter. Compared with the traditional energy function, it provides less conservative ROA estimates and allows the energy at the UEP to be conveniently used as the critical energy level. In addition, the proposed energy function is not limited to PLL-based GFL inverters but is generalizable to other nonlinear systems with PI control. As an example, its applicability is validated on a DC-voltage-controlled GFM inverter.

Finally, a HIL experimental platform was established to validate the theoretical analysis and simulation results. The comparative results clearly indicate the differences between the theoretical model, phasor model, EMT simulation, and actual HIL experimental outcomes. The EMT simulations closely match the theoretical predictions, with minor deviations attributed to the inner current control loop dynamics. The HIL experimental results, accounting comprehensively for practical considerations such as switching behavior, control delays, and hardware constraints, closely align with the EMT simulation results, thus confirming the effectiveness and accuracy of the presented analysis.

Chapter 3

Large-Signal Stability of Power Systems with Mixtures of GFL, GFM and GSP Inverters

This chapter elucidates the interaction mechanisms of inverters with heterogeneous control, covering GFL, GFM, and GSP inverters, to determine the stability boundaries of a system with mixtures of inverters. The generalized model for large-signal dynamics of two-inverter systems with various inverter combinations are derived. This establishes that no energy function exists for systems containing heterogeneous inverters, implying that traditional direct methods of stability assessment cannot be applied to such systems. To overcome this barrier, a manifold theory is employed to accurately determine the ROA of such systems. To address the computational complexity of the manifold theory, reduced-order models of inverter are used based on multiscale analysis. The large-signal stability margin is assessed by the shortest distance from a stable SEP to the boundary of the ROA, which is called the *stability radius (SR)*. Bifurcation phenomena are also observed in systems of GFL inverters and are studied, which shows that the limit cycle and periodical stable orbit emerge, introduced by GFL inverter. The manifold analysis, verified by EMT simulation, demonstrates that GFM and GSP inverters significantly enhance the large-signal stability of a two-inverter system where the other inverter is GFL, with GFM being slightly better than GSP. Such stability enhancement is attributed to the voltage support effects of GSP and GFM inverters. The improvement is maximized if the GFM or GSP inverter is placed at the mid-point of the transmission line, where the voltage is lowest. All findings in this chapter are validated through both EMT simulations and power hardware-in-the-loop (PHIL) experiments.

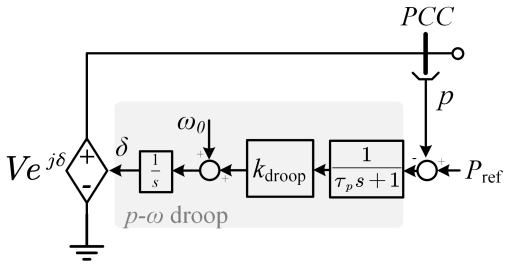
3.1 Modelling and Order-reduction of Two-Inverter Systems

The manifold theory has been applied to single-inverter systems in Chapter 2, but obstacles are encountered in multi-inverter systems, due to the difficulties in computing and

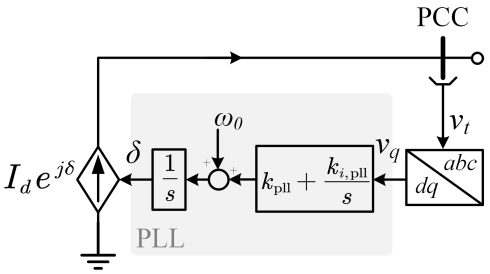
visualizing the stable manifolds of high-order systems. In this chapter, we first perform model order reduction on inverters based on multiscale analysis and thereby extend the manifold theory to two-inverter systems.

This section establishes a generic reduced-order model for two-inverter systems with different combinations, and then applies the manifold theory to identify the ROA of these systems to assess their large-signal stability.

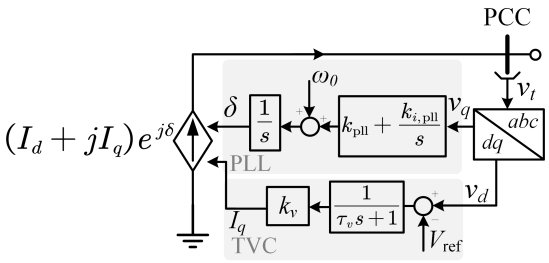
3.1.1 Large-signal modeling and order reduction of different inverter types



(a) modelling of GFM inverters.



(b) modelling of GFL inverters.



(c) modelling of GSP inverters.

Figure 3.1: Large-signal modeling of different types of inverters.

Building on the basic concepts introduced in Chapter 1, the control blocks and large-signal modeling of a GFM, GFL, and GSP inverter are depicted in Figure 3.1 (a), (b), and (c), respectively. The order reduction method we use is based on the multi-timescale characteristics of inverter control [143, 30]. The inner loops of inverters are usually very fast and therefore can be represented as controlled current or voltage sources. Furthermore, we assume that the PLL of the GFL inverters and the droop control of GFM inverters are overdamped. Specifically, in the GFM inverter, the time constant τ_p of the low-pass filter in the p-ω droop control (PSC) is set to be small to make the angle dynamics overdamped [6]. As such, the droop control is treated as an algebraic gain with no state, so the order of the model is reduced to a single state δ as below

$$\dot{\delta} = k_{\text{droop}}(P_{\text{ref}} - p) - \omega_0 \tag{3.1}$$

where δ is the internal voltage angle of the GFM inverter, and ω_0 is the nominal angular frequency of the grid. In the GFL inverter, the PLL is designed as proportion dominant, i.e. $k_{\text{i,pll}} \ll k_{\text{pll}}$, where $k_{\text{i,pll}}$ and k_{pll} are the integral and proportional gain of the PLL. This

makes PLL overdamped helpful for the angle stability of GFL inverters [53, 144]. Under this assumption, the output of the integral controller in the PLL, ω_i, can be assumed fixed to the prefault value during the transient, that is, $\omega_i \approx \omega_0$. As a result, the model of an GFL inverter is also reduced to a single state

$$\dot{\delta} = k_{\text{pll}} v_q + \omega_i - \omega_0 \approx k_{\text{pll}} v_q. \tag{3.2}$$

where δ is the internal PLL angle. On top of the GFL inverter, the GSP inverter incorporates TVC—i.e., a v_d-i_q voltage control with gain k_v to enhance voltage support through reactive current injection. This is an approximation of V-i_q droop as per grid codes [145, 140], provided that PLL angle is aligned with grid voltage implying $v_d \approx v_t$ where v_t is the magnitude of grid voltage measured at the inverter terminal. The time constant τ_v of the low-pass filter in the v_d-i_q voltage control is also assumed to be small [82], which means that the voltage control does not introduce extra states in the model.

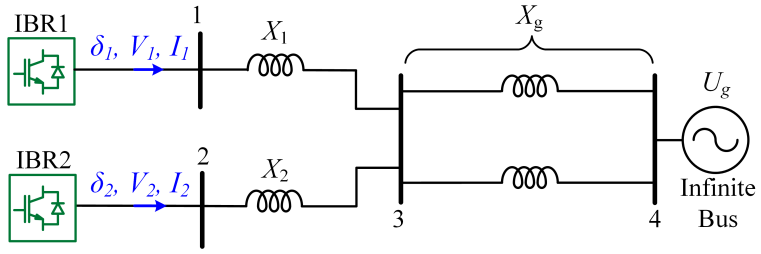


Figure 3.2: Two-inverter system.

3.1.2 Complete two-inverter system

In summary, the GFM, GFL, and GSP inverters in our large-signal analysis can all be reduced to first-order models with δ being the sole state. This leads to the reduced-order model for the two-inverter-infinite-bus system displayed in Figure 3.2:

$$\begin{cases} \dot{\delta}_1 = k_1 \left[C_1 - A_1 \sin(\delta_1 - \delta_2) - B_1 \sin \delta_1 + D_1 \cos(\delta_1 - \delta_2) + \varepsilon \right] \\ \dot{\delta}_2 = k_2 \left[C_2 - A_2 \sin(\delta_2 - \delta_1) - B_2 \sin \delta_2 + D_2 \cos(\delta_1 - \delta_2) \right] \end{cases} \tag{3.3}$$

This system contains two IBRs, i.e. IBR1 and IBR2, each configured to operate in either GFL, GFM, or GSP mode. For any combinations of GFL, GFM, and GSP, the model has the same format but the coefficients are different, which are summarized in Table 3.1. In the GFL inverter, I_d denotes the d-axis current reference. The terms V_1 or V_2 represent the terminal voltages of the GFM inverters, while V_{ref} denotes the voltage reference used in the voltage control of the GSP inverter. Some auxiliary symbols are used in (3.3) to simplify notation, as defined below

$$\begin{gathered} X_{\Delta 12} = \frac{X_1 X_2 + X_1 X_g + X_2 X_g}{X_g},\ X_{\Delta g1} = \frac{X_1 X_2 + X_1 X_g + X_2 X_g}{X_2},\ X_{\Delta g2} = \frac{X_1 X_2 + X_1 X_g + X_2 X_g}{X_1} \\ X_{\Sigma 1} = X_1 + X_g,\ X_{\Sigma 2} = X_2 + X_g \\ X_{1+2//g} = X_1 + \frac{X_g X_2}{X_{\Sigma 2}}, X_{2+1//g} = X_1 + \frac{X_g X_1}{X_{\Sigma 1}} \end{gathered} \tag{3.4}$$

If a GSP inverter is present in the system, a small residual term ε appears in Eq.

Table 3.1: Coefficients of the Expression of Two-Inverter System

IBR1	IBR2	k_1	A_1	B_1	C_1	D_1	ε	k_2	A_2	B_2	C_2	D_2
GFM	GFM	k_{droop1}	$\frac{V_1V_2}{X_{\Delta 12}}$	$\frac{V_1U_g}{X_{\Delta g1}}$	P_{ref1}	0	0	k_{droop2}	$\frac{V_1V_2}{X_{\Delta 12}}$	$\frac{V_2U_g}{X_{\Delta g2}}$	$P_{2\text{ref}}$	0
GFM	GFL	k_{droop}	0	$\frac{U_gV_1}{X_{\Sigma 1}}$	P_{ref}	$\frac{X_gI_{d2}}{X_{\Sigma 1}}V_1$	0	k_{pll}	$\frac{X_g}{X_{\Sigma 1}}V_1$	$\frac{X_1}{X_{\Sigma 1}}U_g$	$X_{2+1//g}I_{d2}$	0
GFM	GSP	k_{droop}	$\frac{V_{\text{ref}}V_1}{X_{\Delta 12}}$	$\frac{V_1U_g}{X_{\Delta g1}}$	P_{ref}	0	ε_{mp}	k_{pll}	$\frac{X_g}{X_{\Sigma 1}}V_1$	$\frac{X_2}{X_{\Sigma 2}}U_g$	$X_{2+1//g}I_{d2}$	0
GFL	GFL	k_{pll1}	0	U_g	$X_{\Sigma 1}I_{d1}$	X_gI_{d2}	0	k_{pll2}	0	U_g	$X_{\Sigma 1}I_{d1}$	X_gI_{d1}
GFL	GSP	k_{pll1}	$\frac{X_g}{X_{\Sigma 2}}V_{\text{ref}}$	$\frac{X_2}{X_{\Sigma 2}}U_g$	$X_{1+2//g}I_{d1}$	0	ε_{lp}	k_{pll2}	0	U_g	$X_{\Sigma 2}I_{d2}$	X_gI_{d1}

(3.3). These terms are typically small and are associated with the voltage control gain k_v. Specifically, they can be expressed as

$$\begin{aligned}\varepsilon_{lp} =&\epsilon_{v1}g_1\left(\delta_1-\delta_2\right)+\epsilon_{\text{pll}}h_1\left(\delta_1-\delta_2\right)\\ \varepsilon_{mp} =&\epsilon_{v2}g_2\left(\delta_1-\delta_2\right)+\epsilon_{\text{pll}}h_2\left(\delta_1-\delta_2\right)\end{aligned} \tag{3.5}$$

where ε_{lp} and ε_{mp} represent the residual term ε for GFL-GSP and GFM-GSP combinations respectively, ϵ_vs are voltage control errors defined as $\epsilon_{v1} \triangleq \frac{1}{k_vX_{\Sigma 2}+1}$ and $\epsilon_{v2} \triangleq \frac{1}{k_vX_{2+1//g}+1}$, ϵ_{pll} is PLL error $\epsilon_{\text{pll}} \triangleq v_{q2}$, and g and h are error functions whose detailed expressions are given in [146]. If k_{pll2} is sufficiently large, implying that the PLL dynamics of the GSP inverter are faster than those of IBR1, ϵ_{pll} can be considered negligible. Moreover, if k_v approaches infinity, ϵ_v approaches zero, indicating that the GSP inverter behaves equivalently to a GFM inverter under ideal voltage regulation. The detailed derivation of the two-inverter model presented in (3.3), (3.5) and Table 3.1 are illustrated in Appendix A.1.

The model order reduction approach used here seems radical, but it turns out to have good accuracy, as is to be validated later in Section 3.6.2. This is due to the fact that the angle dynamics of inverters (PLL of GFL and angle swing of GFM) can be designed overdamped thanks to the high controllability of inverters.

3.2 Non-existence of Energy Function in the System Containing GFL inverters

For simplicity, the effect of transfer conductance is first neglected and the network is assumed to be lossless. If the system comprises only GFM, the differential equations describing the system dynamics contain only sine terms, such as $A_i\sin(\delta_1-\delta_2)$. In two-inverter case, there is a global energy function in the form of

$$W\left(\delta_1,\delta_2\right)=-\frac{C_1}{A_1}\delta_1-\frac{C_2}{A_2}\delta_2-\cos\left(\delta_1-\delta_2\right)-\frac{B_1}{A_1}\cos\delta_1-\frac{B_2}{A_2}\cos\delta_2 \tag{3.6}$$

For power systems comprising both SGs and GFM inverters, assume there are m GFM inverters and n SGs, where $n\in\mathbb{N}$, $m\in\mathbb{N}$, and $m+n\in\mathbb{N}^+$. The model of each apparatus

is illustrated in (3.7a) and (3.7b), in which (3.7a) represents the dynamics of SG, while (3.7b) represents the dynamics of GFM inverters. The voltage of the k-th GFM inverter is denoted as V_k.

$$\begin{cases} \dot{\delta}_i = \omega_i - \omega_n \\ M_i\dot{\omega}_i = P_i - D_i\omega_i - \sum\limits_{j\neq i,j=1}^{n} E_iE_jB_{ij}\sin\left(\delta_i-\delta_j\right) - \sum\limits_{l\neq i,l=1}^{m} E_iV_lB_{il}\sin\left(\delta_i-\delta_l\right) \\ \qquad = -\dfrac{\partial W\left(\delta,\omega\right)}{\partial\delta_i} - D_i\omega_i \end{cases} \tag{3.7a}$$

$$\begin{cases} \dot{\delta}_k = k_{\text{droop,k}}\left[P_k - \sum\limits_{l\neq k,l=1}^{m} V_kV_lB_{kl}\sin\left(\delta_k-\delta_l\right) - \sum\limits_{j\neq k,j=1}^{n} V_kE_jB_{kj}\sin\left(\delta_k-\delta_j\right)\right] \\ \qquad = -k_{\text{droop,k}}\dfrac{\partial W\left(\delta,\omega\right)}{\partial\delta_k} \end{cases} \tag{3.7b}$$

Thus the energy function of mixed SG and GFM inverters system can be expressed as follows:

$$\begin{aligned} W\left(\delta,\omega\right) = &-\sum_{i=1}^{n} P_i\delta_i - \sum_{i=1}^{n}\sum_{j=i+1}^{n+1} E_iE_jB_{ij}\cos\left(\delta_i-\delta_j\right) \\ &-\sum_{k=1}^{m-1}\sum_{l=k+1}^{m} V_kV_lB_{ij}\cos\left(\delta_k-\delta_l\right) - \sum_{k=1}^{m}\sum_{i=1}^{n} V_kE_iB_{ki}\cos\left(\delta_k-\delta_i\right) \\ &+\frac{1}{2}\sum_{i=1}^{n}{\omega_i}^2M_i \end{aligned} \tag{3.8}$$

The derivative of this general function with respect to time is

$$\frac{d}{dt}W\left(\delta,\omega\right) = -\sum_{k=1}^{m}\frac{{\dot{\delta}_k}^2}{k_{gfmk}} - \sum_{i=1}^{n}{\omega_i}^2D_i \leqslant 0 \tag{3.9}$$

which is non-positive. To sum up, in mixed SG and GFM inverter systems, there exists an energy function, and thus the direct method developed for legacy SG-based power systems can be applied.

On the other hand, if the system includes at least one GFL inverter, a cosine term of the form $D_i\cos(\delta_1-\delta_2)$ appears in the nonlinear differential equations. Chiang [35] showed that if the system dynamics, as described by (3.3), involve cosine terms, then no energy function exists. Accordingly, the proposition for systems containing GFL inverters is re-stated as follows:

Proposition 3.1. *As for the nonlinear dynamic system represented by Eq. (3.3), if there exists a cosine term, the energy function does not exist.*

Proof. The general process to construct an energy function in the GFM and SG systems

is to find $W(\cdot)$ that satisfies

$$\begin{cases} \dot{\delta}_1 = -k_1 \frac{\partial W}{\partial \delta_1} \\ \dot{\delta}_2 = -k_2 \frac{\partial W}{\partial \delta_2} \end{cases} \tag{3.10}$$

However, when Eq.(3.3) contain cosine term $D_i \cos(\delta_1 - \delta_2)$, Eq.(3.10) cannot be satisfied. Because Eq.(3.10) and Eq.(3.3) violates Poincaré's Lemma [31, 147], that is

$$\begin{aligned} \frac{1}{A_1 k_1} \frac{\partial \dot{\delta}_1}{\partial \delta_2} &= \cos(\delta_1 - \delta_2) + \frac{D_1}{A_1} \sin(\delta_1 - \delta_2) \\ \neq \frac{1}{A_2 k_2} \frac{\partial \dot{\delta}_2}{\partial \delta_1} &= \cos(\delta_1 - \delta_2) - \frac{D_2}{A_2} \sin(\delta_1 - \delta_2) \end{aligned} \tag{3.11}$$

As a result, the energy function construction procedure cannot be applied to a nonlinear dynamic system represented by Eq. (3.3). Moreover, Figure 3.7 (d) and Figure 3.8 (d) in Section 3.4 demonstrate that a closed orbit (limit cycle) emerges in certain cases for systems containing GFL inverters. This contradicts the fundamental property that systems admitting an energy function cannot exhibit closed orbits. Consequently, even in the absence of transfer conductance, no energy function exists for systems that include GFL inverters. □

All of these necessitated the development of a new approach for assessing large-signal stability with a high penetration of GFL inverters.

3.3 Stability Radius (SR) based on Manifold Theory

For the two-dimensional system analyzed in this chapter, the UEPs on the stability boundary are either type-I or type-II. Following the manifold theory (introduced in Chapter 2 Section 2.1.1), the real ROA is obtained by backward-time integration along the stable eigenvector(s) of each type-I UEP in the phase plane; it is shown as the black curve in Figure 3.3. The stability radius (SR) is then used to measure the large-signal stability margin, defined as the shortest distance from the SEP to the ROA boundary, highlighted by the red circle in Figure 3.3.

Figure 3.3 contrasts the SR with other stability assessment methods for the two-inverter system. Notably, the critical clearing angle (CCA) is indicated by the projection of the real ROA onto the δ_1, δ_2 coordinates, depicted as $\delta_{\text{CCA1,2}}$ and can also by the intersection between the sine function $U_g \sin\delta$ and the blue solid curve. Due to the existence of interaction terms [e.g. $\cos(\delta_2 - \delta_1)$ in (3.3)], there is the difference between the blue solid curve and the ideal dotted lines [e.g. constant value $C_{1,2}$ in (3.3)], highlighted by the blue shaded area. Previous methods, cited in [148, 113], use the CCA of one critical GFL as a large-signal stability index, but this often overestimates the ROA and overlooks the other inverter, as shown in the grey rectangle area in Figure 3.3[1]. In particular, if two inverters are connected to an infinite bus individually, then the ROA is square, decoupling δ_1 and

[1]The angle variables δ_1 and δ_2 are 2π-periodic; for clarity, only one fundamental period is shown in the figure.

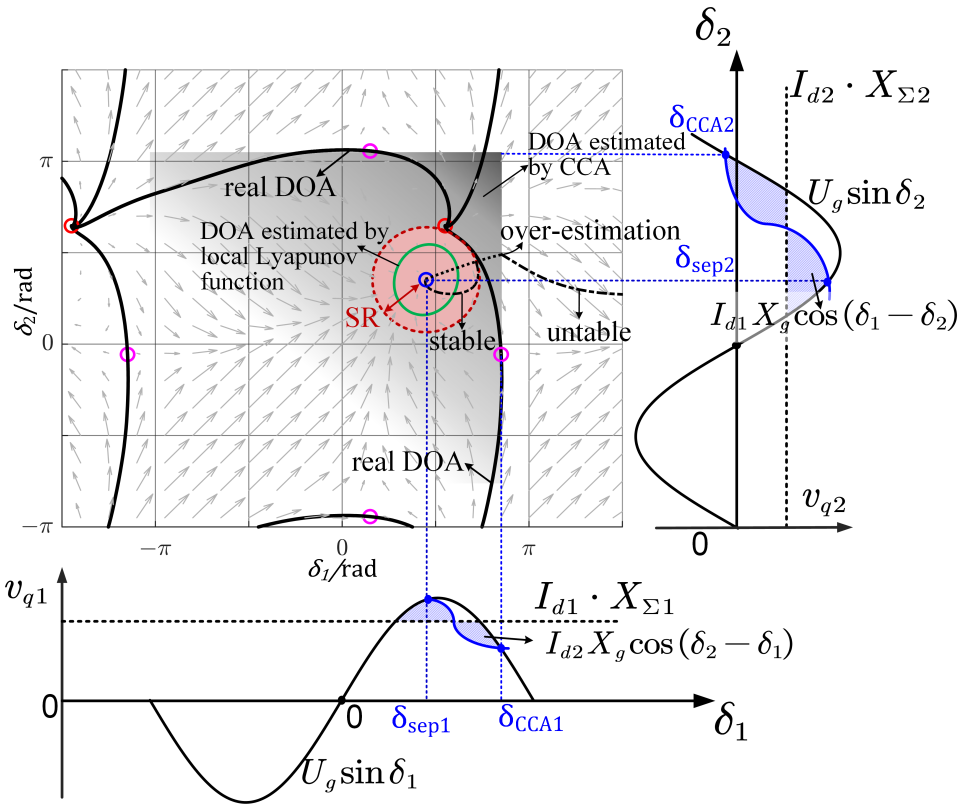


Figure 3.3: Comparison between SR and other large-signal stability assessment methods. On the phase-plane plot, the ROA is shown with a solid black line (manifold theory), gray rectangular shading (CCA method), and green line (local Lyapunov method). The SR is a red dashed line. The SEP is an open blue circle.

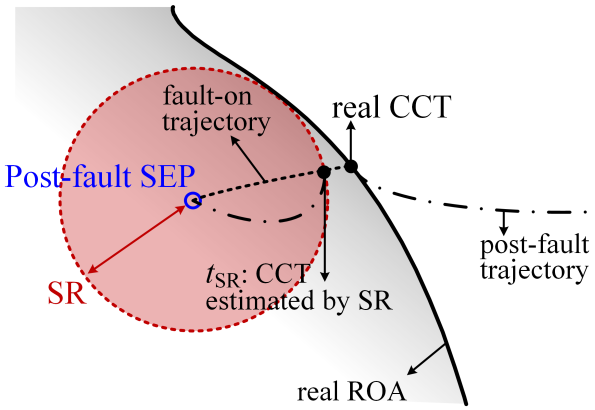


Figure 3.4: Relationships among proposed metrics.

δ_2, and the SR being the minimum of δ_{CCA1} and δ_{CCA2}. The local Lyapunov function to estimate the ROA is also plotted as the green curve in Figure 3.3, which is an approach to address the situation where the global energy function does not exist. It can be seen that the local Lyapunov method usually produces an under-estimate of the ROA, and is more conservative than the real ROA and SR.

The calculation of SR is straightforward: it requires recording the shortest distance to the post-fault SEP during the process of reverse integration, and no need for storing shape

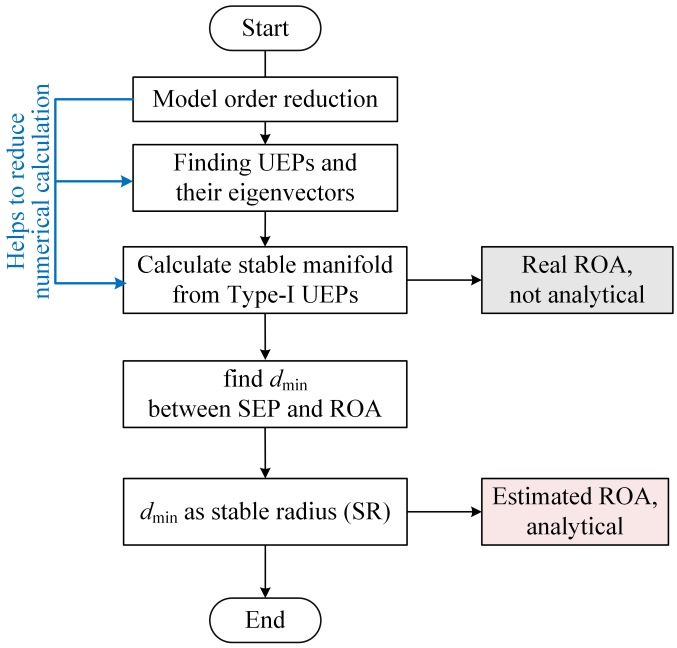


Figure 3.5: Procedure for ROA and SR computation in multi-inverter systems.

information of stable boundaries which is convenient to implement. More specifically, as shown in Algorithm 2.1, only the minimum distance between the manifold and the SEP needs to be recorded, which directly yields the SR. Furthermore, critical clearing time (CCT) can be estimated based on SR. The specific steps to estimate CCT are: 1) Integrate the fault-on trajectory $\phi_f(x,t)$; 2) At the time t_{SR}, $\phi_f(x,t_{\mathrm{SR}})$ is outside of the circle of SR, but $\phi_f(x,t_{\mathrm{SR}}-\Delta t)$ of the previous time step is inside of the circle of SR; 3) The t_{SR} is the CCT estimated by SR. Figure 3.4 illustrates the relationships between SR, t_{SR}, real ROA, and the estimated and real CCT. Since the SR is entirely inside the real ROA, the CCT estimated by SR, t_{SR}, is conservative and guaranteed.

The complete procedure for this analysis framework is illustrated in Figure 3.5. SR provides a conservative but generic estimation of the stability margin, as it is independent of the location and type of faults. It is also less conservative than local Lyapunov-function bounds since it can capture the true stability boundary. Moreover, SR directly evaluates the stability margin as a single geometric scalar, which is easier to compare than the full ROA shape. Using SR, we quantify the contributions of different inverters in improving the large-signal stability amid inverter interactions in the subsequent analysis.

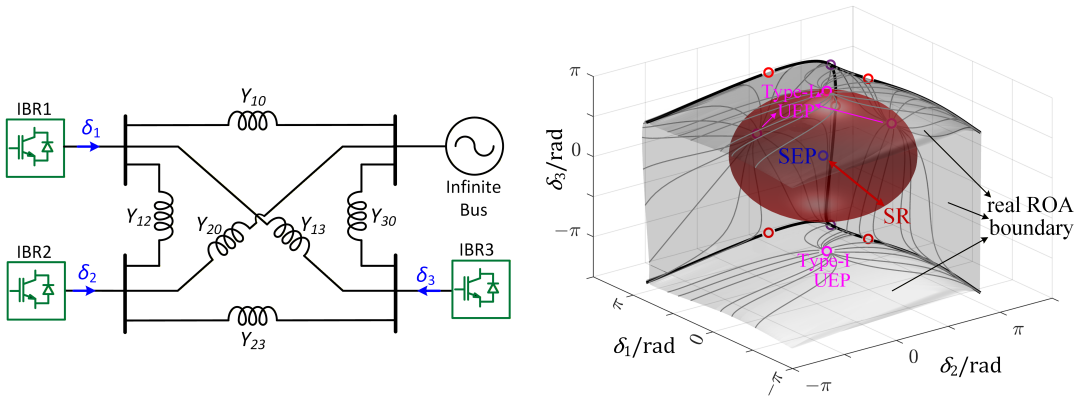
If fault clearing occurs at a time that gives a position outside the ROA of the SEP, the trajectory will not converge to this SEP. It should be noted that, even though sometimes the trajectory may converge to a different SEP that is one period away from the original SEP, this is considered unstable in engineering terms [149, 127]. This case is analogous to the pole slipping of a synchronous generator and can compromise distance protection[150, 151], cause reverse power flow [144], over-voltage, and voltage oscillations [82] in inverters. This pole slipping phenomenon of inverters will be explained in detail in the following large-signal interaction between different types of inverters.

In summary, the manifold theory completely describes the dynamic behavior in the phase plane, and the SR is utilized on the basis of the manifold theory, which can access the large-signal stability, as an extension of CCA in a high-dimensional space.

Generalize the concept of SR

Although not a central focus of this Chapter, the concept of SR can be extended, from a theoretical perspective, to general high-dimensional nonlinear systems. Since direct visualization of high-dimensional ROA is inherently nontrivial, a three-dimensional system is used here solely as an illustrative example to demonstrate the general applicability of the SR concept. The test system is the three-IBR infinite-bus network shown in Figure 3.6 (a), where IBR1 operates as a GFL inverter and IBR2–IBR3 are configured as GFM inverters. The system parameters are $k_{\text{pll}} = k_{\text{droop1}} = k_{\text{droop2}} = 10 \cdot 2\pi$, $Y_{10} = Y_{20} = Y_{30} = j\,2$ pu, and $Y_{12} = Y_{23} = Y_{13} = j\,0.5$ pu. Under this configuration, the calculated SR is 2.26 rad.

The numerical results are plotted in Figure 3.6 (b)[2]. The grey shaded surfaces represent the real ROA boundary, which is formed by the stable manifolds of type-I UEPs, while the grey trajectories lying on these illustrate representative stable-manifold flows. The ROA is obtained following the same procedure as in Algorithm 2.1. The computation of the SR follows the same procedure described earlier in this Section. The resulting SR is illustrated as a red sphere centered at the SEP, which is fully contained within the ROA and tangential to the stability boundary. In practice, the SR is obtained by recording only the minimum distance from the stable manifold to the SEP, without reconstructing the high-dimensional stability boundary, making it potential applicability for characterizing stability margins in large-scale systems.



(a) (b)

Figure 3.6: Illustration of the SR concept for a three-dimensional system: (a) three-IBR infinite-bus network; (b) visualization of the ROA and SR, where the grey surfaces represent the real stability boundary (boundary of the ROA), and the red sphere denotes the SR centered at the SEP.

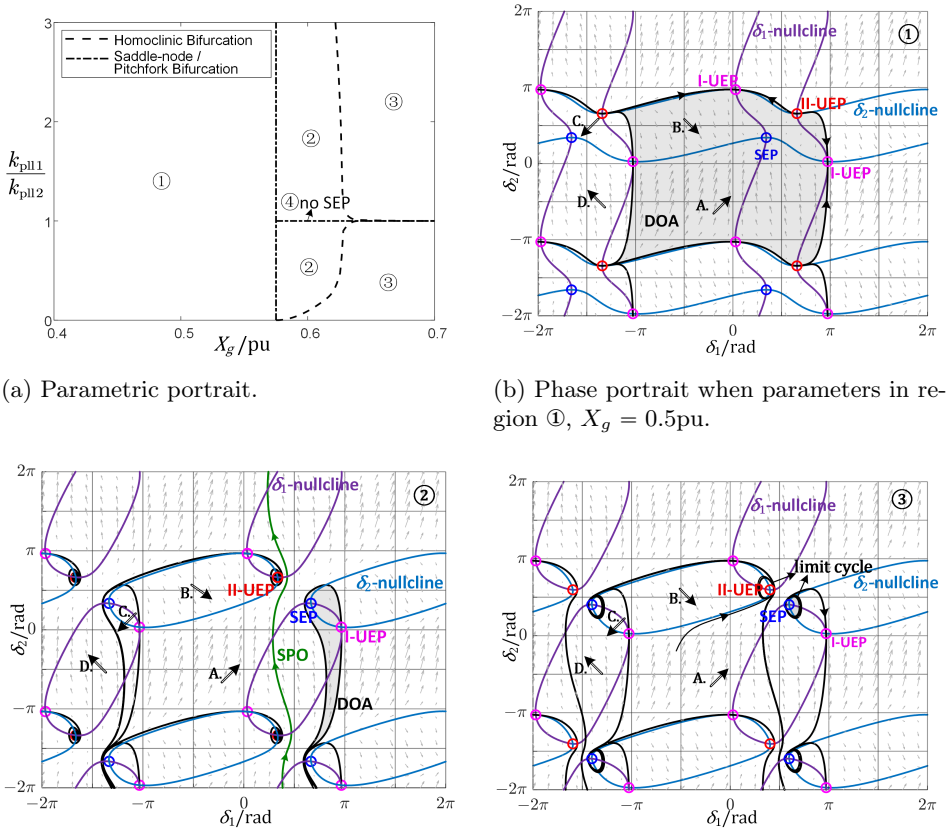
[2]Similar to the two-dimensional case, the three angle variables $(\delta_1, \delta_2, \delta_3)$ are also 2π-periodic. For clarity of visualization, only one period is displayed in the figure.

3.4 Manifold Property and Bifurcation Phenomenon in Two-Inverter System

Bifurcation refers to changes in equilibrium points (EPs), periodic orbits, or their stability as a parameter is varied [152, 153]. This section investigates bifurcation phenomena in two-inverter systems containing GFL inverters.

3.4.1 Bifurcation in two GFL inveter system [$D_1 \neq 0, D_2 \neq 0$ in (3.3)]

Figure 3.7 illustrates the bifurcation in a system with two parallel GFL inverters. The impact of parameters such as grid impedance X_g and the ratio of PLL gains in two IBRs, $k_{\text{pll1}}/k_{\text{pll2}}$, on bifurcation is depicted in Figure 3.7 (a). The system parameters are as follows (as an example): $I_{1d} = I_{2d} = 0.8$, $X_1 = X_2 = 0.1$. The manifolds corresponding to different parameter regions, divided by Figure 3.7 (a), are shown in Figure 3.7 (b), (c), and (d). Here, SEP, Type-I UEP, and Type-II UEP are indicated by blue, magenta, and red hollow points, respectively. The stable manifolds of UEPs, represented by black solid lines, outline the stability region of SEP. Grey arrows represent the vector field. Herein, the nullcline concept [31] is introduced. The δ_1-nullcline is defined as $\{\delta_1, \delta_2 : f_1(\delta_1, \delta_2) = \dot{\delta}_1 = 0\}$



(a) Parametric portrait.

(b) Phase portrait when parameters in region ①, $X_g = 0.5$pu.

(c) Phase portrait when parameters in region ②, $X_g = 0.6$pu.

(d) Phase portrait when parameters in region ③, $X_g = 0.7$pu.

Figure 3.7: Bifurcation diagram for two GFL inverter systems. [$k_{\text{pll1}} = 2.5 \times 2\pi$, $k_{\text{pll2}} = 10 \times 2\pi$, that is, $k_{\text{pll1}}/k_{\text{pll2}} = 0.25$ in (b), (c), (d)]

plotted as purple lines, while the δ_2-nullcline is defined as $\{\delta_1, \delta_2 : f_2(\delta_1, \delta_2) = \dot{\delta}_2 = 0\}$ plotted as blue lines in Figure 3.7 (b), (c), and (d). These two types of nullclines divide the phase plane into four regions (A, B, C, D), each representing different directions of the vector field. The basic direction of the vector field in region A is upper left, region B is lower right, region C is lower left, and region D is upper left.

For small X_g, neither limit cycles nor periodic orbits exist. When $k_{\text{pll1}} = k_{\text{pll2}}$, increasing X_g causes the SEP and a type-II UEP to approach and eventually annihilate, consistent with region ④ in Fig. 3.7 (a). When the two GFL inverters have unequal control gains or unequal line impedances ($X_1 \neq X_2$), a stable periodic orbit (SPO) emerges (green trajectory in Fig. 3.7 (c)); trajectories starting outside the ROA are attracted to this SPO. As X_g increases further, a pair of limit cycles appears: the SEP becomes enclosed by an unstable limit cycle, while the type-II UEPs are enclosed by a stable one (Fig. 3.7 (d)). A still larger X_g eliminates the SEP.

3.4.2 Bifurcation in the GFL and GFM inverter system [$D_1 = 0, D_2 \neq 0$ in (3.3)]

Figure 3.8 shows the bifurcation for a system with GFL (IBR1) and GFM (IBR2) inverters, with the effects of X_g and the ratio $k_{\text{pll}}/k_{\text{droop}}$ on bifurcation depicted in Figure 3.8 (a). The other parameters are $X_1 = 0.66$, $X_2 = 0.2$, $I_{1d} = 1$, $P_{ref} = 0.6$ (as an example). The phase plane manifolds for different parameter regions, divided by Figure 3.8 (a), are shown in Figure 3.8 (b), (c), and (d). SEP, Type-I UEP, and Type-II UEP are indicated by blue, magenta, and red hollow points, respectively, while the δ_1-nullcline and δ_2-nullcline are represented by purple and blue lines, respectively.

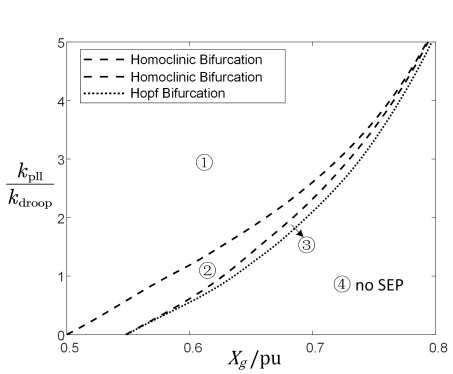
Similarly, for small X_g, no limit cycle or periodical orbit exists. As X_g increases, the δ_2-nullcline fails to stretch across the phase plane, and the SPO appears (green trajectory in Figure 3.8 (c)). Further increases in X_g lead to the emergence of an unstable limit cycle (Figure 3.8 (d)). Beyond this point, no SEP remains.

3.4.3 Existence of SPO

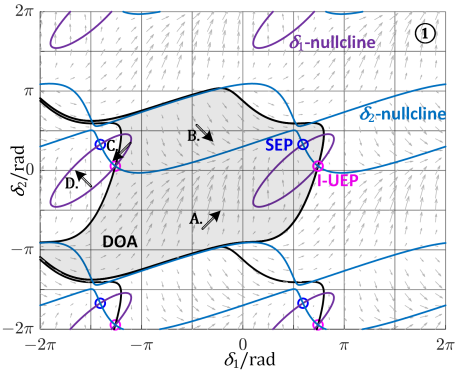
The foregoing analysis shows that the SPO attracts trajectories in the phase plane and drives the state unbounded, thereby jeopardizing stability. Based on the vector-field directions defined by the nullclines, we state:

Statement. A trajectory cannot cross the δ_1 – nullcline from right to left, nor the δ_2 – nullcline from bottom to top.

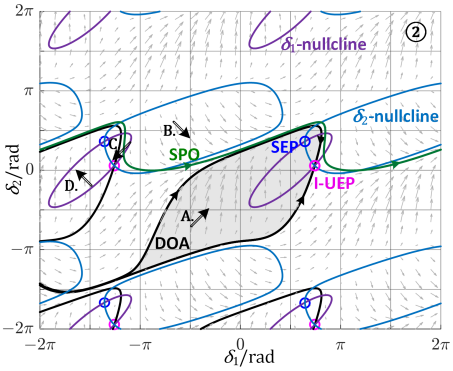
When the δ_2-nullcline can stretch from $\delta_1 = -\infty$ to $\delta_1 = +\infty$ in the phase plane, there is no SPO, as shown in Figure 3.7 (b) compared to Figure 3.7 (c). In this scenario, regions B and C, where $\dot{\delta}_2 < 0$, stretch across the entire plane, preventing any potential SPO from spanning from $\delta_2 = -\infty$ to $\delta_2 = +\infty$. Consequently, the absence of SPO is guaranteed if the δ_1-nullcline and the δ_2-nullcline extend across the phase plane.



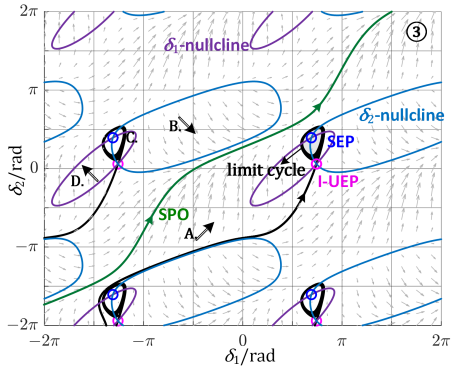
(a) Parametric portrait.



(b) Phase portrait when parameters in region ①, $X_g = 0.5$pu.



(c) Phase portrait when parameters in region ②, $X_g = 0.55$pu.



(d) Phase portrait when parameters in region ③, $X_g = 0.6$pu.

Figure 3.8: Bifurcation diagram for paralleled GFM and GFL inverter systems. [$k_{\text{pll}} = 1.5 \times 2\pi$, $k_{\text{droop}} = 2.5 \times 2\pi$, that is,$k_{\text{pll}}/k_{\text{droop}} = 0.6 \times 2\pi$ in (b), (c), (d)]

In the two-GFL inverter system, the sign of $\dot{\delta}_1$ corresponds to the q-axis voltage of IBR1 v_{1q}, and the sign of $\dot{\delta}_2$ corresponds to the q-axis voltage of IBR2 v_{2q}. According to the statement above, sufficient condition for the non-existence of SPO can be expressed as follows:

$$\forall\, \delta_2\, \exists\, \delta_1 \text{ s.t. } v_{1q} < 0 \quad \text{and} \quad \forall\, \delta_1\, \exists\, \delta_2 \text{ s.t. } v_{2q} < 0, \tag{3.12}$$

This condition is equivalent to:

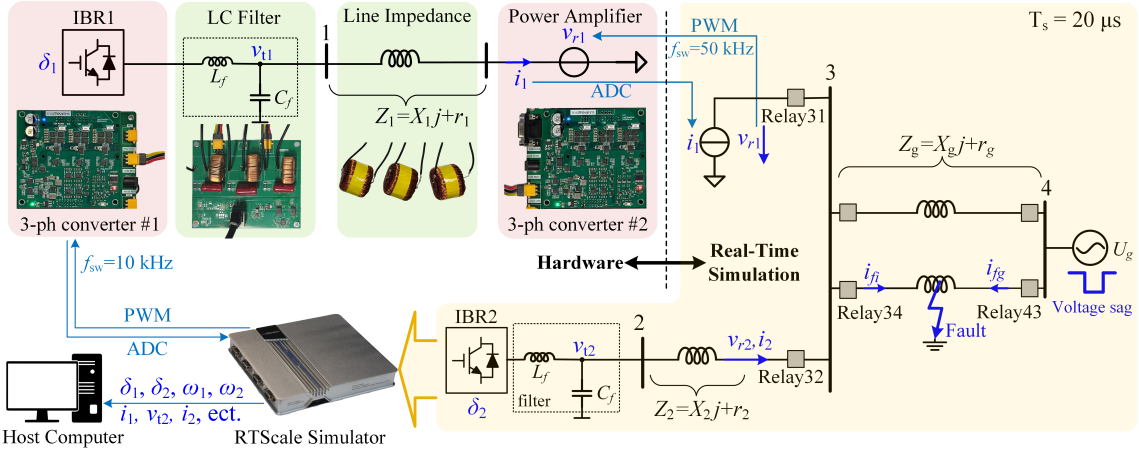
$$X_g < \min\left(\frac{U_g - X_1 I_{1d}}{I_{1d} + I_{2d}}\right) \tag{3.13}$$

Under the parameters in this section, $\min\left(\frac{U_g - X_1 I_{1d}}{I_{1d} + I_{2d}}\right) = 0.575$, corresponding to the dash point line in Figure 3.7 (a).

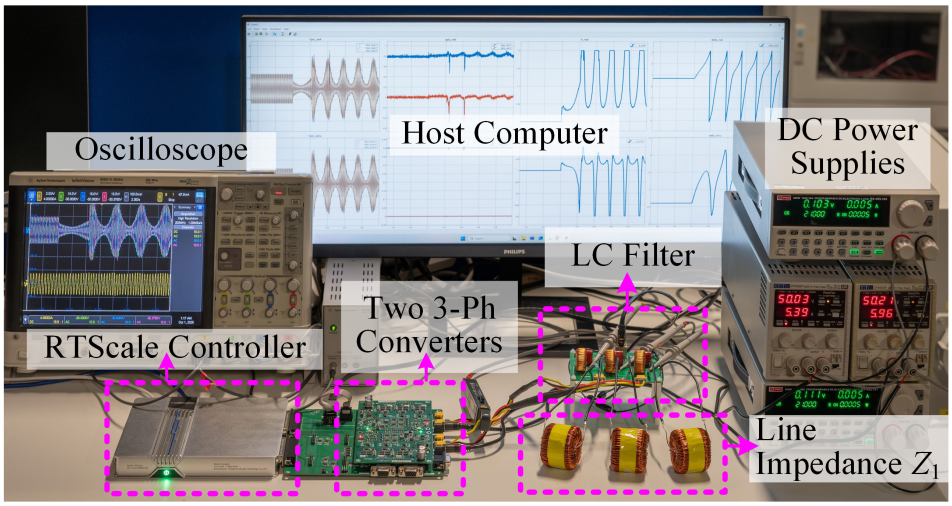
3.5 PHIL Platform and EMT Simulation Setup

To validate the findings in the following sections, a power-hardware-in-the-loop (PHIL) platform was built, as shown in Figure 3.9. The two-inverter configuration in Figure 3.2 is realized in Figure 3.9 (a). In the PHIL setup, the system is partitioned into two parts:

the portion to the left of Bus 3 in Figure 3.2—namely IBR1 and its line impedance X_1 (i.e., Z_1)—is implemented as physical hardware, while the remaining network is executed on a real-time simulator. The platform employs three-phase power converters built with BSC052N08NS5 MOSFETs. One converter serves as the physical IBR1, followed by an LC filter (parameters in Table 3.2) and the line impedance Z_1. The second converter operates as a power amplifier, interfacing the physical plant with the real-time simulation. Both the power amplifier and the real-time simulator run at 50 kHz, which is also the current and voltage sampling rate, allowing high-fidelity emulation. The time axis in the following sections is referenced to the fault event, with $t = 0$ denoting the fault inception. The experiments use the RTScale real-time simulator [154], which also executes the IBR1 controller. IBR1 is a physical inverter with a switching frequency of 10 kHz. The system bases and ratings are listed in Table 3.2. The RTScale simulator communicates with a host computer for controller programming and system monitoring. All experimental data are logged on the host computer, and electrical quantities in the physical plant are measured with an oscilloscope.



(a) Tested two-inverter system and configuration.



(b) Platform setup.

Figure 3.9: PHIL experimental platform.

Table 3.2: System Parameters in PHIL Platform

Parameters	Value
Base capacity S_b	60 V·A
Base voltage V_b	22.8 V
Base current I_b	2.6 A
Base impedance Z_b	8.64 Ω
Base frequency $\omega_s/2\pi$	50 Hz
LC filter of IBR1 L_f	1.7 mH (0.0618 pu)
LC filter of IBR1 C_f	10 μF (0.027 pu)
Line impedance Z_1	5.5 mH + 55 mΩ ($0.2j + 0.006$ pu) or 13.8 mH + 100 mΩ ($0.5j + 0.01$ pu)
DC-link voltage of two 3-ph converters U_{dc}	54 V (2.4 pu)
Switching frequency of IBR1 (converter #1)	10 kHz
Switching frequency of power amplifier (converter #2)	50 kHz
Timestep of real-time simulation	20 μs
IBR1 control frequency	10 kHz

In this chapter, we also construct an EMT simulation platform that uses exactly the same per-unit (pu) values as the PHIL experiment. The EMT model is implemented in MATLAB/Simulink, and simulations are performed to complement the experiments, to facilitate comparison with the experimental results and mutual validation, and to benchmark the outcomes against the theoretical calculation. Both the EMT and experimental detailed models follow the configuration shown in Figure 3.9 (a). For later reference, Figure 3.9 (a) also annotates relevant electrical quantities, including relay indices and the symbols used for voltages and currents.

3.6 GFL-GFL Interaction

In the study of this Section, both IBR1 and IBR2 of Figure 3.2 [or Figure 3.9 (a)] are initially configured as GFL inverters.

The PLLs of two inverters are designed to be over-damped, with the integral gain $k_{\text{i,pll}}$ set to one-tenth of the proportional gain k_{pll}. Under this configuration, the contribution of the integral term is negligible, and the proportional term primarily governs the dynamic behavior. The line impedance X_g is set to either 0.35 pu or 0.4 pu and is composed of two parallel lines of $2X_g$. A short-circuit fault is applied in the middle of one of the two lines and that line is removed at fault clearance, giving a doubling of the effective impedance between busses 3 and 4 and a new operating point for the system. The fault initiates at time 0 s and is of variable duration. Detailed system parameters for the PHIL experiment and the EMT simulation are given in Table 3.2 (mentioned before and applicable to all subsequent PHIL cases) and Table 3.3, respectively. Both the EMT simulation and the PHIL experiment are conducted to validate the manifold theory for finding SR, and the

Table 3.3: Detailed System Parameters in GFL-GFL Inverters System

Parameters	**Value (pu)**
Grid voltage U_g	1
LC Filter of IBR2 $L_f j + r_f$	$0.05j + 0.001$
LC Filter of IBR2 C_f	0.02
Inner current control loop bandwidth	1.2 kHz
PLL controller of IBR1 k_{pll1}	$10 \times 2\pi$
PLL controller of IBR1 $k_{\text{i,pll1}}$	2π
PLL controller of IBR2 k_{pll2}	$10 \times 2\pi$
PLL controller of IBR2 $k_{\text{i,pll2}}$	2π
Frequency limit of PLL ω_{limit}	± 0.2
Current reference of IBR1 I_{d1}	0.8
Current reference of IBR2 I_{d2}	0.4
Line impedance Z_1	$0.2j + 0.006$
Line impedance Z_2	$0.2j + 0.002$
Line impedance Z_g	$0.35j$ or $0.4j$
Fault resistance R_f	0.02

The EMT simulation and PHIL experiment share the same per-unit parameters.

Table 3.4: Comparison between SR-based CCT estimation and the theoretical CCT obtained from the real ROA

Grid impedance	SR	SR-based CCT t_{SR}	theoretical CCT
$X_g = 0.4$ pu	0.53 rad	0.131 s	0.137 s
$X_g = 0.35$ pu	0.90 rad	0.212 s	0.240 s

estimate of CCT from SR (t_{SR}).

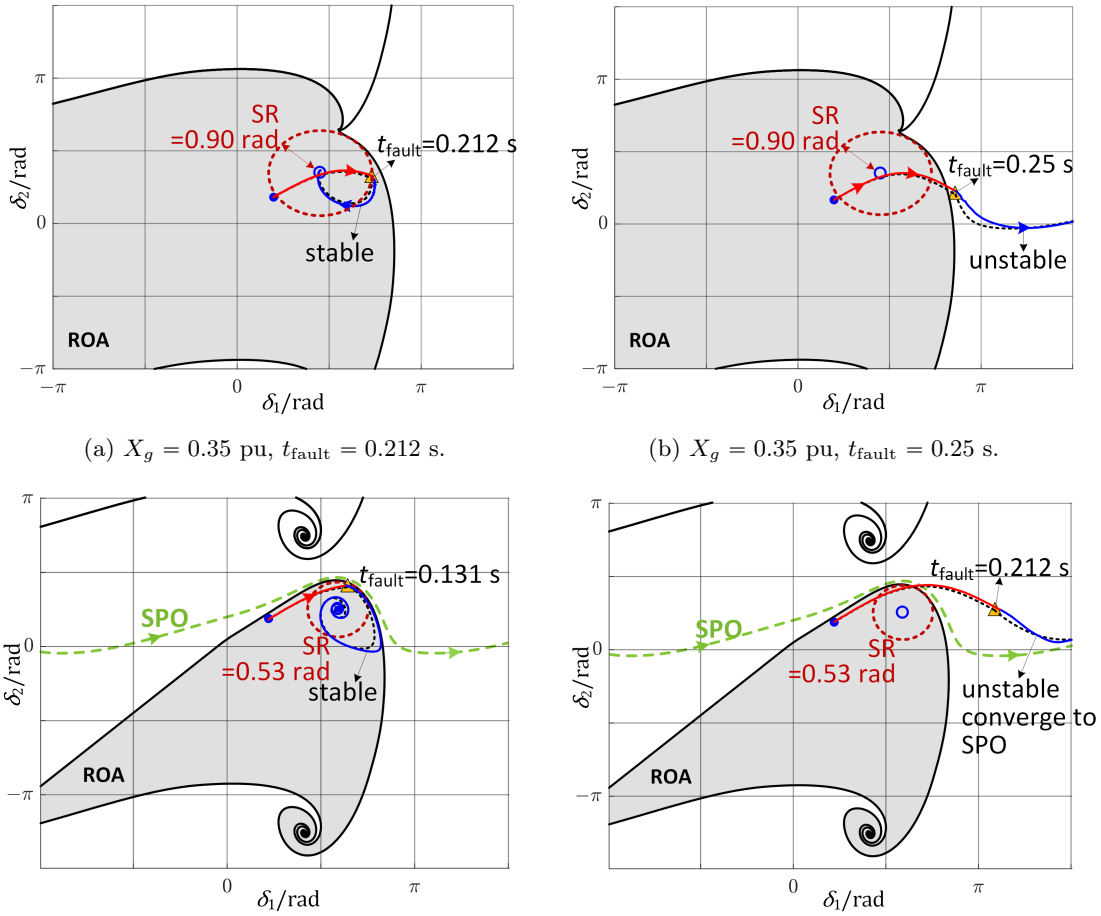
3.6.1 Large-Signal Instability Mode versus Grid Inductance

The SR-based CCT estimation results are summarized in Table 3.4, which provide a conservative estimate of the CCT. In the case of $X_g = 0.35$ pu, the calculated metrics are: SR of radius 0.90 rad and a CCT estimated via the SR of $t_{\text{SR}} = 0.212$ s. The fault clearing time is set at two values: 0.212 s to match the estimated CCT and 0.25 s to exceed it.

In the case of $X_g = 0.4$ pu, the SR is decreased to a radius of 0.53 rad and CCT reduced to $t_{\text{SR}} = 0.131$ s. The fault clearing times are set to 0.131 s to match and 0.212 s to exceed.

Using the manifold theory, the ROA can be drawn in terms of δ_1 and δ_2 phase-plane as shown by the gray shading in Figure 3.10. The ROA is shown for the two choices of X_g and two choices of fault-clearing time. The pre-fault stable equilibrium is marked with a solid blue dot. During the fault, as the two PLLs are perturbed, the system follows the phase-plane trajectory of the red line according to the δ_1 and δ_2 found in the EMT simulation. Under this is a black dashed line, and closely resembling it, which is the trajectory found by numerical integration of the simplified (theoretical) model.

The SR is indicated by the red dashed circle and it can be seen that the location at fault clearance (yellow triangle) is on the SR circle if the fault clearing time is set to $t_{\text{fault}} = t_{\text{SR}}$, c.f., sub-figures (a) and (c). When $t_{\text{fault}} > t_{\text{SR}}$, the yellow triangle is outside the SR circle,



(a) $X_g = 0.35$ pu, $t_{\text{fault}} = 0.212$ s.

(b) $X_g = 0.35$ pu, $t_{\text{fault}} = 0.25$ s.

(c) $X_g = 0.4$ pu, $t_{\text{fault}} = 0.131$ s.

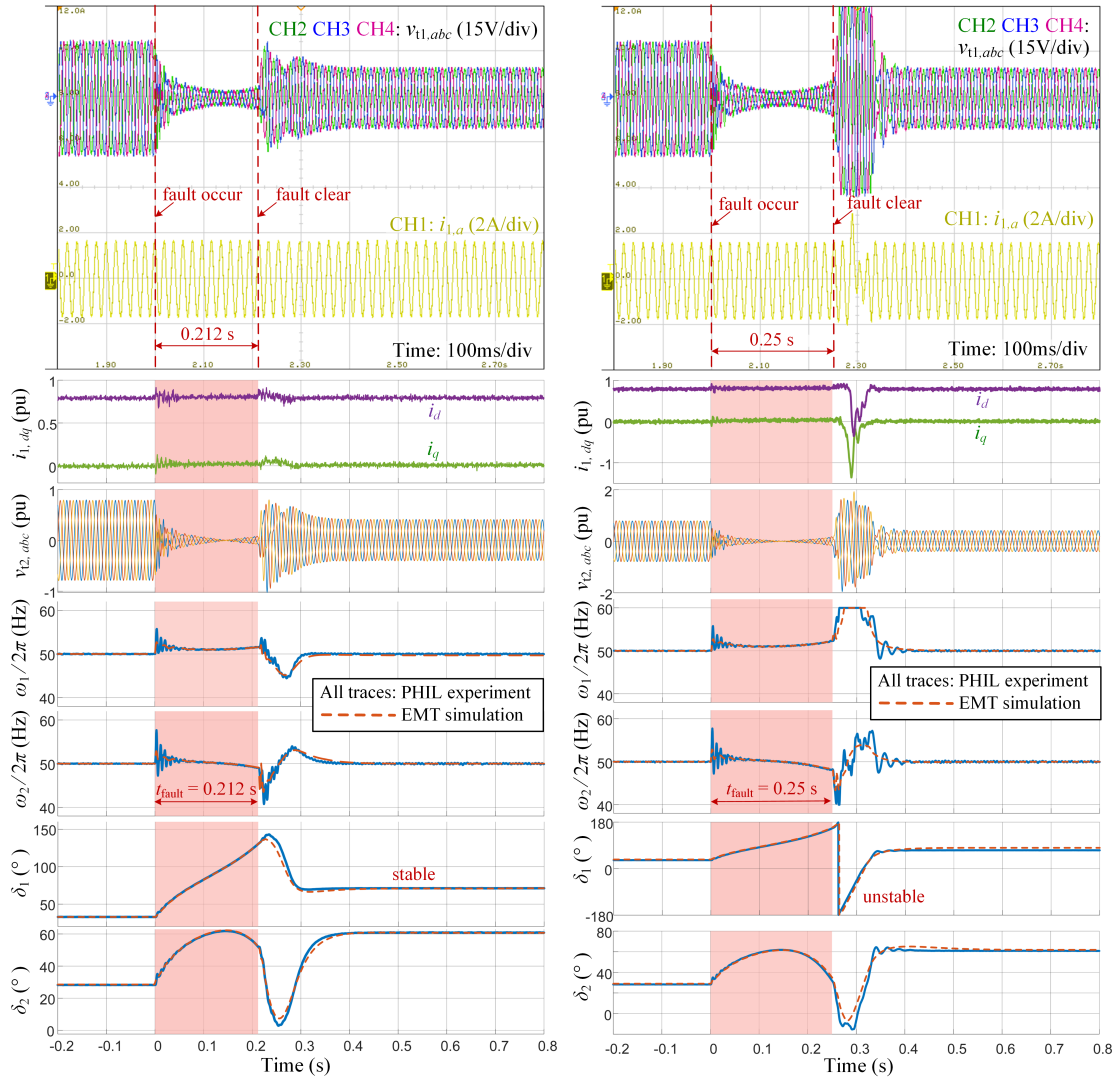
(d) $X_g = 0.4$ pu, $t_{\text{fault}} = 0.212$ s.

Figure 3.10: Phase portraits of two GFL inverters for four test conditions as assessed by the manifold theory. Pre-fault SEP is marked with a solid blue dot, the post-fault SEP with a hollow blue dot, and the fault clearing point with a yellow triangle. The dashed black line represents the analytical trajectories. Trajectories generated by EMT simulations are represented as red lines during the fault and blue lines post-fault. The green dashed line, where it exits, is a stable periodic orbit. This color convention is applied in subsequent similar figures.

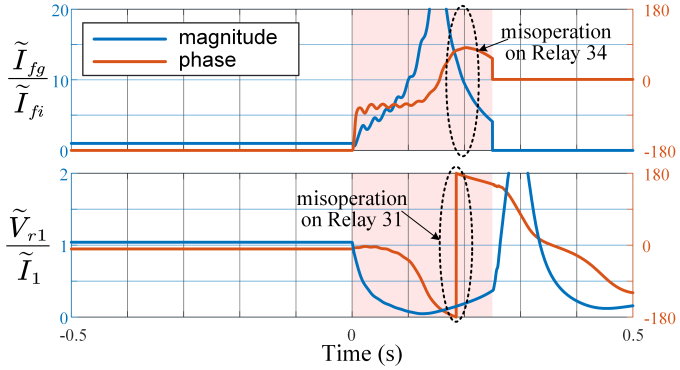
c.f., sub-figures (b) and (d).

Post-fault, the system trajectory (blue solid line) moves to a new[3] SEP marked by an hollow blue dot for $t_{\text{fault}} = t_{\text{SR}}$, and diverges for $t_{\text{fault}} > t_{\text{SR}}$. The effectiveness of the SR in predicting behavior is confirmed. The divergent trajectories may converge to a different SEP elsewhere on the phase plane, but this is considered unstable in practical terms in the same way as pole-slipping of a synchronous machine. PHIL experiment results for the $X_g = 0.35$ pu case and two clearing times are shown in Figure 3.11 (a) and (b). In Figure 3.11 (a)–(b), the angle (δ_1, δ_2) and angular speed (ω_1, ω_2) traces by EMT simulation are overlaid as orange dashed lines for comparison with experimental measurements. The PHIL results closely match the EMT simulations, thereby validating both the experimental platform and the simulation model.

[3]New because the line impedance is doubled.



(a) $t_{\text{fault}} = 0.212$ s. (b) $t_{\text{fault}} = 0.25$ s.



(c) Measurements of relays under $t_{\text{fault}} = 0.25$ s.

Figure 3.11: PHIL experiment results of two paralleled GFL inverters under $X_g = 0.35$ pu.

The theoretical model on which SR is based ignored the dynamics of the inner current loop and the integral terms in the PLL, so it is approximate. However, the comparison of EMT results (in red and blue lines) with the reduced-order model (in the dashed black line) shows that there is little impact on the results.

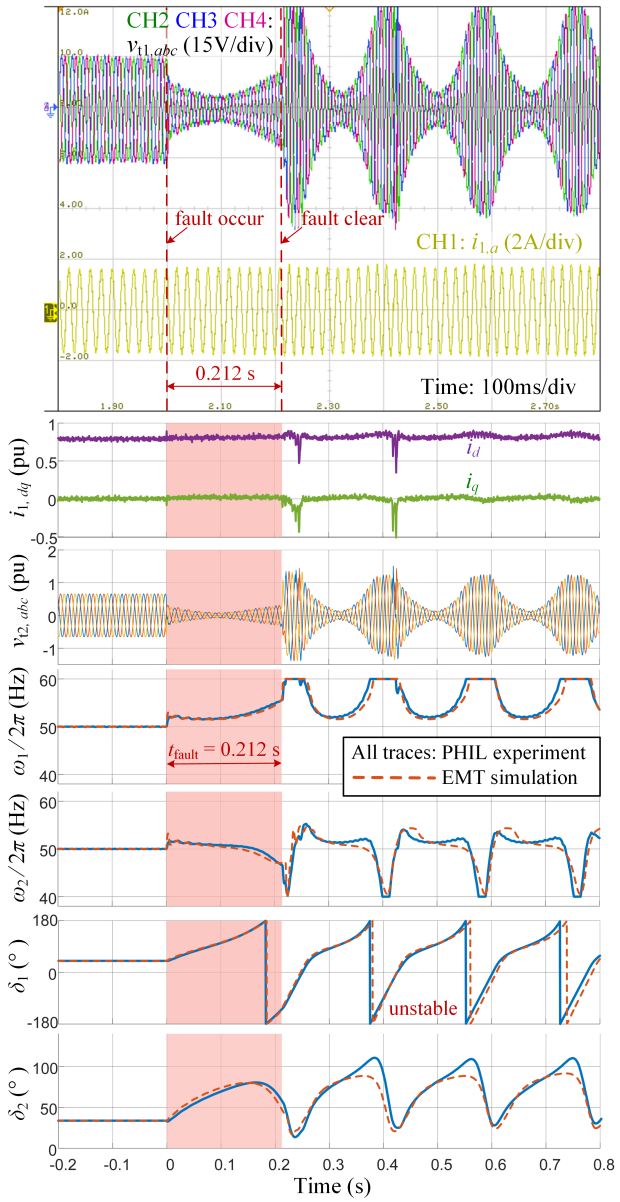


Figure 3.12: PHIL experimental results of two paralleled GFL inverters under $X_g = 0.4$ pu, $t_{\text{fault}} = 0.212$ s.

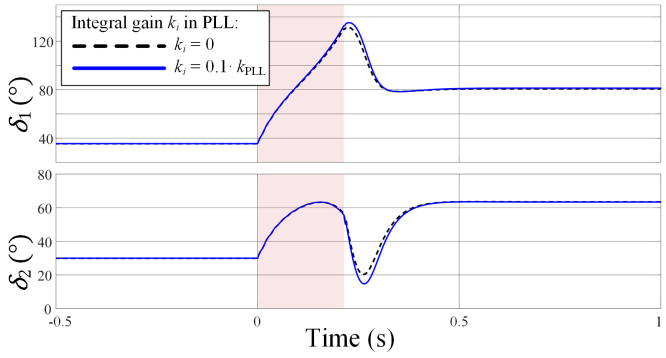
In the case of $X_g = 0.4$ pu, Fig. 3.10 (c) and (d), a stable periodical orbit (SPO) is present in the post-fault system and has been shown by a green dashed curve in the phase plane. The SPO is an additional instability mode in this case, and if the fault trajectory leaves the ROA, as it does for $t_{\text{fault}} > t_{\text{SR}}$ in Fig. 3.10 (d), the trajectory converges to this SPO, leading to continuous divergence of δ_1 and sustained oscillations in δ_2. The results of the PHIL experiment are recorded in Figure 3.12, which aligns closely with the EMT simulation. This instability mode is different from the instability mode under $X_g = 0.35$ pu.

Although not the primary focus of this chapter, a brief analysis is provided to explain the implications of inverter pole-slipping. The ratio of the fault current from the grid side ($\tilde{I}_{fg}$) and the inverter side ($\tilde{I}_{fi}$) for $t_{\text{fault}} = 0.25$ is shown in Figure 3.11 (c) in terms of phasor. At time 0.7s, the angle of $\tilde{I}_{fg}$ leads $\tilde{I}_{fi}$ by approximately 90 degrees, which can result in the misoperation of Relay 34 [the location of which is illustrated in Figure 3.9 (a)], as noted

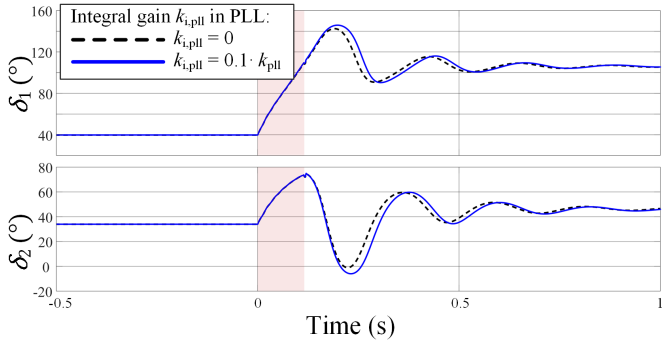
in [150]. Additionally, the impedance measurement by Relay 1 is shown in Figure 3.11 (c), with the measured impedance becoming capacitance, signaling a fault in the transmission line between bus 1 and bus 3 in Figure 3.9 (a) (or Figure 3.2). During this pole-slipping process, the IBR will suffer from reverse power injection, which is not permissible. In addition, in the experiment, a slight increase in the DC-link voltage is observed during pole slipping; this rise is limited because the DC side is supplied by a regulated constant-voltage source in the PHIL setup. Moreover, as seen in Figure 3.11 (b), the GFL inverter output current becomes briefly uncontrolled around $t \approx 0.3$ s due to over-modulation at the instant of slip. In power systems, the pole-slipping also normally triggers out-of-step tripping (OST), leading to the disconnection of the GFL inverter from the grid [155, 156]. Consequently, pole slipping is inadmissible in practical applications, both for power systems and for the safe operation of the inverter.

3.6.2 Validation of the Order Reduction Approach

Now we validate the accuracy of the order reduction approach introduced in Section II-A. The PLL is configured with different integral gains $k_{\mathrm{i,pll}}$ and the EMT simulation results are presented in Figure 3.13. The duration of the faults is shown by the pink shading. For both cases in (a) and (b) with different X_g and t_{fault}, the EMT simulation shows a good match between the results with and without integral gains ($k_{\mathrm{i,pll}} = 0$ and $k_{\mathrm{i,pll}} = 0.1 \cdot k_{\mathrm{pll}}$). Moreover, quantitative comparison shows that the difference in the real CCT with and without the integral gain is less than 2% in both cases. Specifically, the analytically



(a) $X_g = 0.35$ pu, $t_{\mathrm{fault}} = 0.212$ s.



(b) $X_g = 0.4$ pu, $t_{\mathrm{fault}} = 0.131$ s.

Figure 3.13: Comparison of EMT simulation results with different $k_{\mathrm{i,pll}}$ in PLL for different X_g and t_{fault}.

computed real CCTs are 0.137 s for $X_g = 4$ pu and 0.240 s for $X_g = 3.5$ pu, while the corresponding EMT simulations, in which $k_i = k_{\text{pll}}$ is added, can maintain stable when t_{fault} is 0.135 s and 0.235 s, respectively. This indicates that the reduced-order model neglecting the integral control in PLL presents a good approximation, provided that the PLL is designed to be overdamped. Additionally, since the SR-based CCT estimation is inherently conservative, the theoretically computed CCT based on SR guarantees stability in EMT simulations, as consistently verified across all the case studies throughout this chapter.

3.7 GFL-GFM(GSP) Interaction

The effect of voltage support on the large-signal stability of a system that includes a GFL inverter was investigated in this section. Referring to Figure 3.9 (a), IBR1 is configured as a GFL inverter, and IBR2 is set as either a GFM or a GSP inverter. The transmission line parameters are set as follows: $X_1 = 0.5$ pu, $X_2 = 0.15$ pu, and the grid impedance X_g is 0.3 pu under pre-fault conditions, increasing to 0.6 pu after the fault is cleared. Detailed system parameters are provided in Table 3.5 and Table 3.2.

3.7.1 Comparison of GFM and GSP inverters

The results of the CCT estimation based on SR are summarized in Table 3.6, providing conservative CCT estimates.

Equations (A.4) and (A.7) in A.1 reveal that when the voltage control gain k_v in the GSP inverter is large, both the GFM inverter and the GSP inverter exhibit similar dynamics so similar transient stability of a neighboring GFL inverter might be expected. For a fair comparison, when IBR2 is configured as a GSP inverter, its PLL gain is set to $k_{\text{pll2}} = k_{\text{droop}}/X_{\Sigma 2}$, so that the equivalent gain of IBR2 [k_2 in general expression (3.3)] remains consistent whether it operates as a GFM or a GSP inverter. A three-phase-to-ground fault is initiated at 0 s, with the fault located 80 % of the distance along X_g from the infinite bus.

The phase portraits of the system before, during, and after the fault, with IBR2 configured as either a GFM inverter or a GSP inverter, are shown in Figure 3.14. Again, the ROA is shown as a gray-shaded area, the trajectories of the IBRs obtained from numerical calculations on the simplified analytical model are shown as black dashed lines, and the fault-clearing points are marked with yellow triangles. The trajectories obtained from EMT simulations are shown as red lines during the fault and blue lines post-fault. The EMT simulation results closely match their corresponding numerical calculations.

Figure 3.14 (a) shows phase-plane results for IBR2 configured as a GFM inverter. The SR has a radius of 0.65 rad, and the CCT estimated by the SR is $t_{\text{SR}} = 0.28$ s. When t_{fault} is set to this value, the post-fault trajectory of the EMT simulation converges to the post-fault SEP, confirming that t_{SR} is a good and slightly conservative estimate of the

Table 3.5: Detailed System Parameters in GFL - GFM(GSP) Inverters System

Parameters	Value (pu)
Grid voltage U_g	1
Impedance Z_1	0.5j+0.025
Impedance (include virtual one) Z_2	0.1j+0.002
Impedance $2Z_g$	0.6j+0.03
Fault resistance R_f	0.001
Fault position (from the infinite bus)	0.8
IBR1 - GFL	
Inner current control loop bandwidth	1.2 kHz
PLL controller k_{pll1}	$2.5 \times 2\pi$
PLL controller $k_{\text{i,pll}}$	$0.2 \times 2\pi$
Frequency limit of PLL ω_{limit}	± 0.2
Current reference I_{d1}	1
IBR2 - GFM	
$p-\omega$ droop gain k_{droop}	$2.5 \times 2\pi$
Power reference P_{ref}	0.6 in Section 3.7.1, 0 in Section 3.7.2
AC Voltage V_2	1
Inner voltage control loop bandwidth	200 Hz
Inner current control loop bandwidth	1 kHz
LC filter of IBR2 $L_f j + r_f$	0.2j+0.02
LC filter of IBR2 C_f	0.1
Current limit I_{limit}	5
$p-\omega$ droop time constant τ_p	$1/(25 \times 2\pi)$
IBR2 - GSP	
Voltage droop k_v	1 or 4 in Section 3.7.1,2 in Section 3.7.2
Voltage reference V_{ref}	1
Current reference I_{d2}	0.6 in Section 3.7.1, 0 in Section 3.7.2
Voltage droop filter time scale τ_v	$1/(50 \times 2\pi)$
PLL controller k_{pll2}	$k_{\text{droop}} \cdot \frac{1}{X_{\Sigma 2}}$

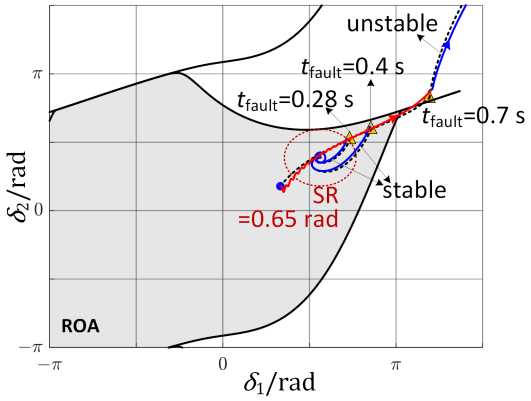
The EMT simulation and PHIL experiment share the same per-unit parameters.

critical clearing time. The conservativeness is seen from $t_{\text{fault}} = 0.4$ s also being stable. The system is unstable at $t_{\text{fault}} = 0.7$ s.

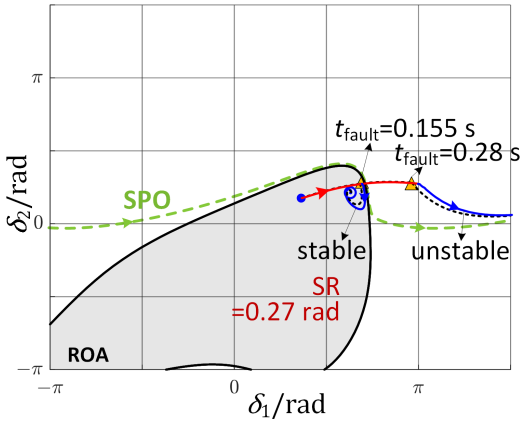
The corresponding PHIL experimental results are shown in Figure 3.15 with $t_{\text{fault}} = 0.28$ s seen to be stable in Figure 3.15. (a) and $t_{\text{fault}} = 0.7$ s unstable in Figure 3.15. (b). The EMT simulation traces are overlaid for comparison with the experimental measurements, and the discrepancies are small. Furthermore, Figure 3.15 (c) shows the phase difference between the currents through Relay 34 (I_{fi}) and Relay 43 (I_{fg}) exceeds -90° and approaches -180°, which would lead to mal-operation of distance protection relay[150] and is why this

Table 3.6: Comparison between SR-based CCT estimation and the theoretical CCT for different IBR2 configurations

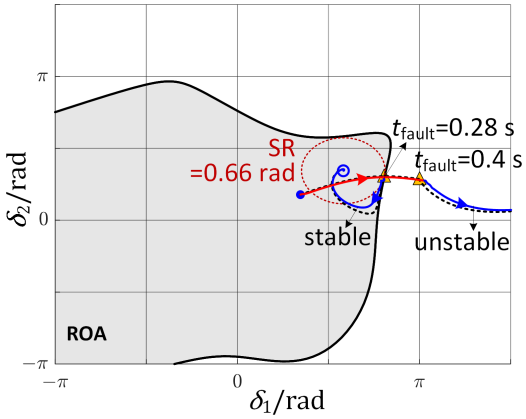
IBR2 configuration	SR	SR-based CCT t_{SR}	theoretical CCT
GSP $k_v = 1$	0.27 rad	0.155 s	0.156 s
GSP $k_v = 4$	0.66 rad	0.28 s	0.283 s
GFM (best)	0.65 rad	0.28 s	0.56 s



(a) IBR2 is realized by GFM.



(b) IBR2 is realized by GSP inverter under $k_v = 1$.



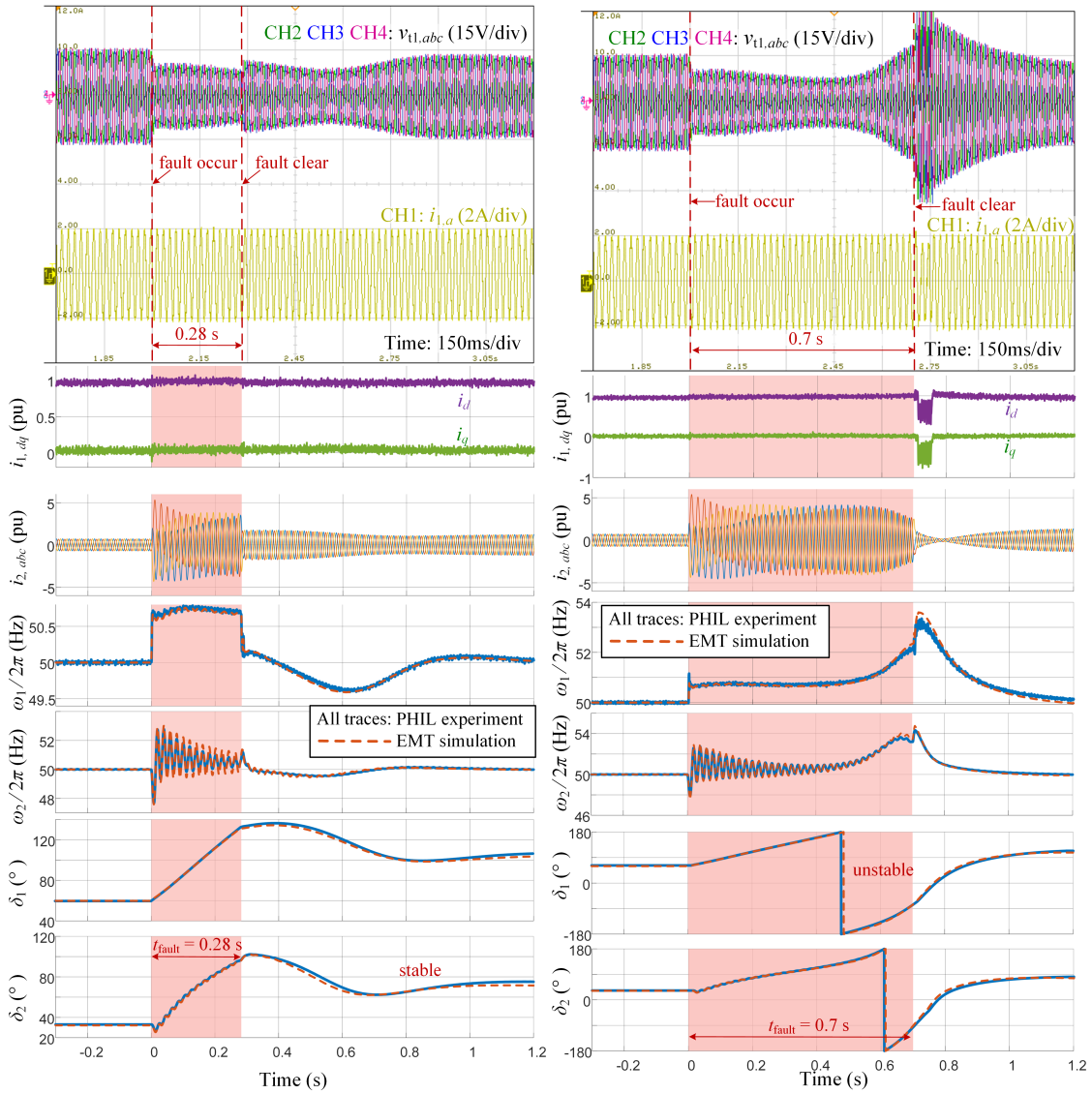
(c) IBR2 is realized by GSP inverter under $k_v = 4$.

Figure 3.14: The phase portrait of the system before, during and after the fault for various t_{fault} as marked on the figures. Color scheme for lines and markers follows that of Figure 3.10.

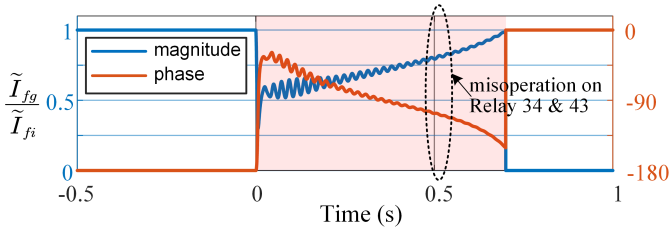
condition is dangerous.

Turning now to IBR2 configured as a GSP inverter. Figure 3.14 (b) shows results for when the voltage control gain is small, $k_v = 1$. Compared to Figure 3.14 (a), the SR is much smaller which is 0.27 rad, and t_{SR} is 0.155 s. An SPO outside the ROA is plotted in green dashed curves. If $t_{\text{fault}} = 0.28$ s, the trajectory converges to this SPO, rendering the system unstable. The corresponding time domain results, shown in Figure 3.16 (a) demonstrate the divergence of δ_1 to positive infinity and oscillation of δ_2.

If the voltage control gain is increased to $k_v = 4$, the ROA is expanded as shown in Figure 3.14 (c). The SR at 0.66 rad becomes comparable to that of the system in which IBR2 operates as a GFM inverter and t_{SR} becomes 0.28 s. A difference is that with the GFM inverter, the ROA is larger along the δ_1-axis. For instance, when $t_{\text{fault}} = 0.4$ s the system loses stability with the GSP inverter but remains stable when using the GFM inverter despite the near identical SR and t_{SR}. The PHIL experimental results for $t_{\text{fault}} = 0.28$ s are presented in Figure 3.16 (b), showing that a higher k_v provides enhanced voltage support, maintaining the terminal voltage of IBR2 even under severe fault conditions. Again, the experiment results align with the EMT simulation.



(a) $t_{\text{fault}} = 0.28$ s. (b) $t_{\text{fault}} = 0.7$ s.



(c) Measurements of Relay 34 & 43 under $t_{\text{fault}} = 0.7$ s.

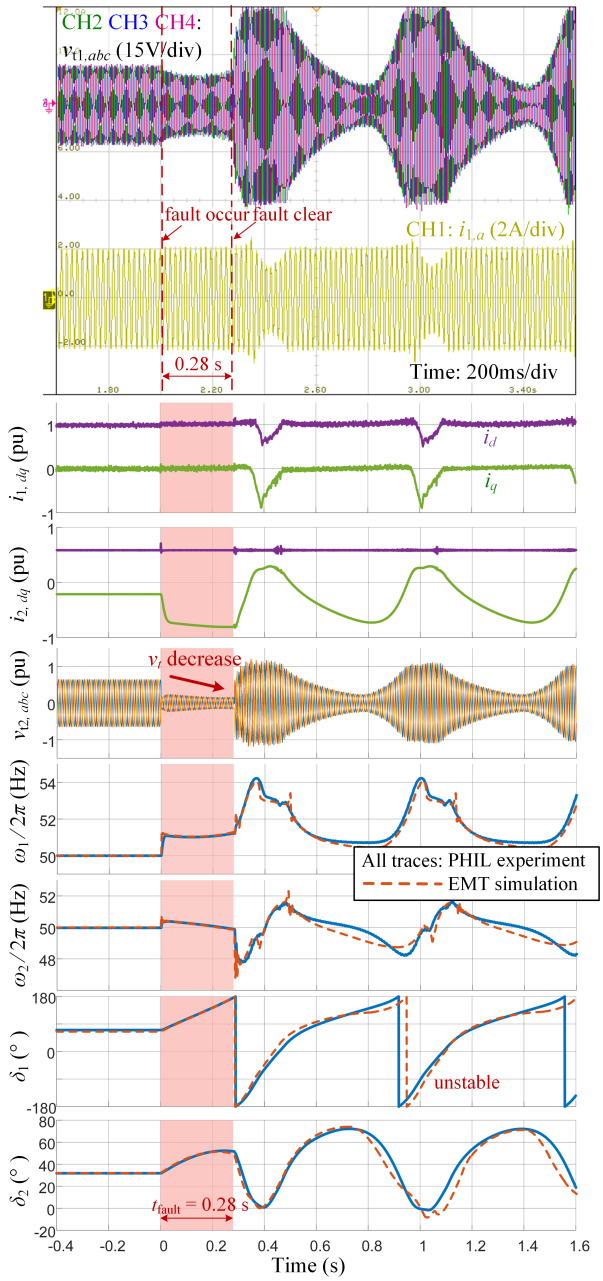
Figure 3.15: PHIL experimental results for the case where IBR2 is realized by GFM inverter.

Figure 3.17 illustrates the ROA of the GSP inverters under different voltage control gain k_v and PLL gain k_{pll2}. As k_v increases, the ROA expands, improving the system's large-signal stability. Under large k_v, the ROA is very near the ROA of the system where IBR2 is a GFM inverter depicted by the black line. The ROA is even closer to that of the GFM case if bandwidth of the PLL2 k_{pll2} is high, as seen in Figure 3.17 (b). This indicates that a

GFL inverter with voltage control can provide very similar transient stability enhancement to a GFM inverter when the PLL dynamics are fast and the voltage control gain k_v is large.

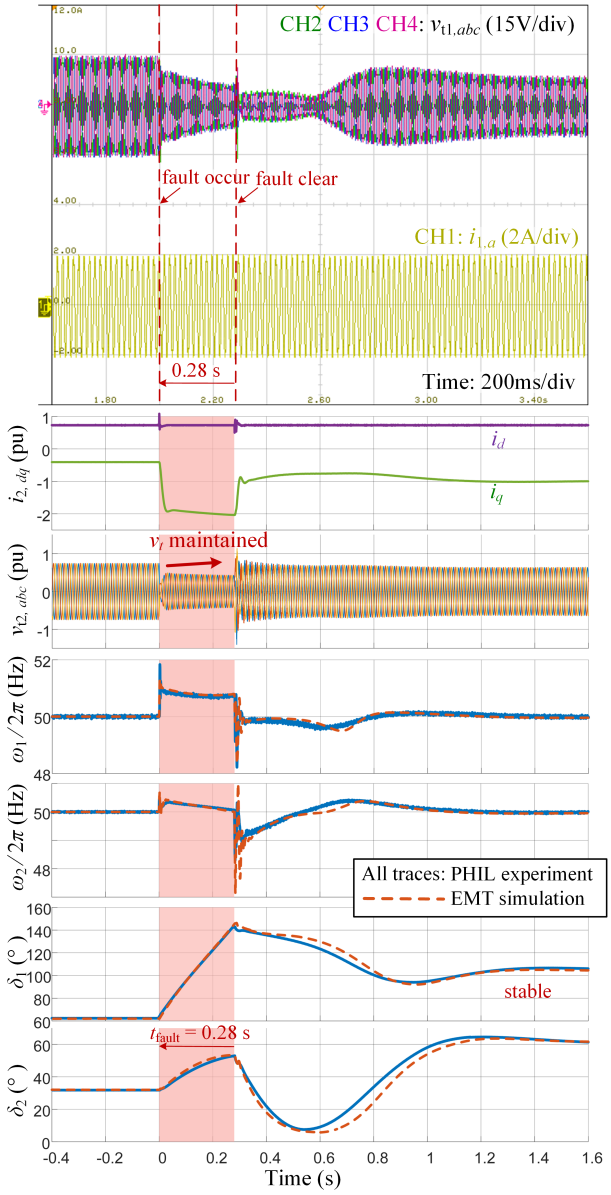
3.7.2 Impact of the location of GFM and GSP inverter on transient stability enhancement

The impact on ROA and SR of varying the connection point of the IBR2 acting as a GSP inverter was investigated by testing variations of grid impedance X_g and X_1 but with the total transmission line impedance ($X_{\Sigma 1} = X_1 + X_g = 1.1$ pu) kept constant. The fault type is changed to a remote fault simulated as a voltage sag of 0.1 pu at the infinite bus



(a) Voltage control gain $k_v = 1$.

Figure 3.16: PHIL experimental results under $t_{\text{fault}} = 0.28$ s for the case where IBR2 is configured as a GSP with two different values of k_v.

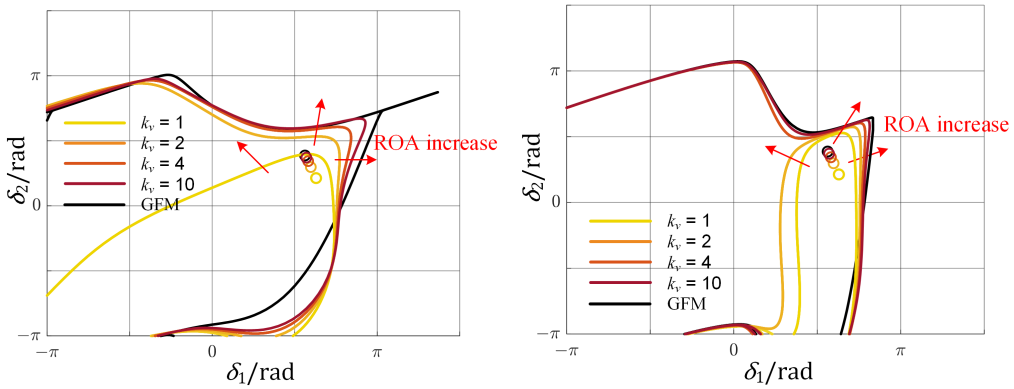


(b) Voltage control gain $k_v = 4$.

Figure 3.16: PHIL experimental results under $t_{\text{fault}} = 0.28$ s for the case where IBR2 is configured as a GSP with two different values of k_v. (continued)

and the fault duration is set to 0.1 s and 0.25 s.

The resulting ROA for six cases are illustrated in Figure 3.18. The left column has results for a GFM inverter and the right column for a GSP inverter. The top row is for the IBR2 (GFM or GSP inverter) near the IBR1 (GFL inverter) and is further away in the middle and bottom rows. Examining Figure 3.18 shows that, regardless of whether the IBR2 is a GFM or GSP inverter, when it is placed in the middle of the transmission line, it is most beneficial to the large-signal stability of the system. When the IBR2 is too near to the grid, its ability to improve voltage regulation is diminished because of proximity to an infinite bus. In the extreme case, when it is connected to the grid directly, there would be no interaction between the IBR2 and IBR1. Conversely, if the IBR2 is positioned too close to



(a) $k_{\text{pll2}} = k_{\text{droop}} = 2.5 \times 2\pi$.

(b) $k_{\text{pll2}} = k_{\text{droop}} = 10 \times 2\pi$.

Figure 3.17: The change of ROA with respect to voltage control gain k_v and PLL bandwidth of GSP inverter.

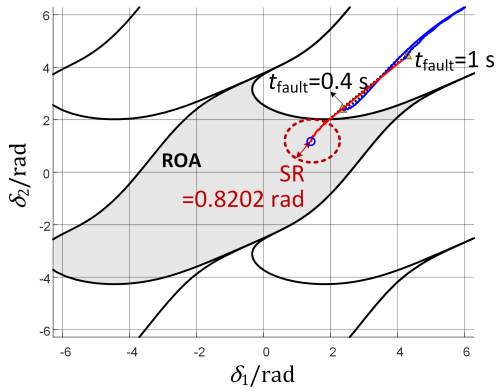
IBR1, the impedance between the IBR2 and the grid denoted as X_g, becomes large. Since the IBR2 must absorb active power from IBR1 and transfer it to the grid, this large X_g reduces the transmission capacity from IBR2 to the grid and can lead to instability in the IBR2 itself. As illustrated in Figure 3.18 (a) and (b), the SEP is very close to the upper boundary of ROA, which results in small SR and t_{SR}. In particular, when IBR2 is placed at the same location as IBR1, the system even lacks an equilibrium point. Additionally, it is important to note that if there is no IBR2, the system becomes unstable even though the IBR1 is configured as a GSP inverter. This indicates that voltage control in the GSP inverter, while ineffective for improving the stability of the GSP inverter itself, can enhance the stability of other IBRs. The enhancement is maximized if it is placed at the midpoint of the transmission line.

3.8 GFM-GSP Interaction

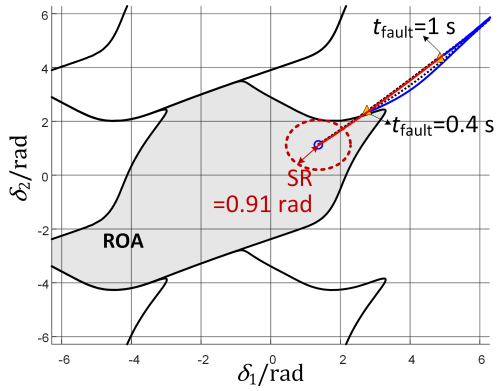
This section investigates the impact of voltage support provided by a GSP inverter on the large-signal stability of a GFM inverter.

Referring to the arrangement in Figure 3.9 (a), IBR1 is configured as a GFM inverter, feeding power to the grid via the transmission line $X_1 + X_g = 1.1$ pu. The output power of IBR1 is set to $P_{\text{ref}} = 0.8$ pu IBR2 is configured as a GSP inverter and is connected to the transmission line through quite a small impedance $X_2 = 0.1$ pu. Detailed system parameters are provided in Table 3.7 and Table 3.2. A three-phase-to-ground short-circuit fault is applied 80% of the distance along the transmission line X_g from the infinite bus.

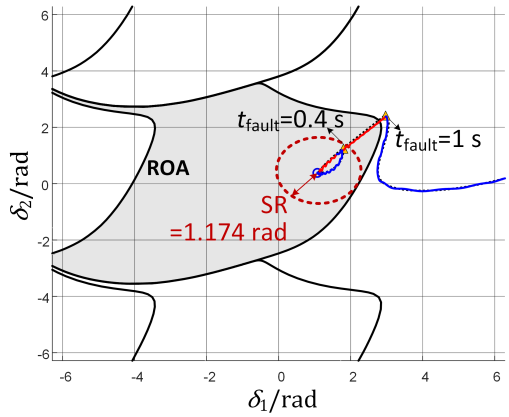
The effect of voltage control of GSP inverter was tested by comparing performance with three choices of voltage control gains k_v of 0, 2 and 4 and the resulting phase portraits are shown in Figure 3.19 (a), (b) and (c). The results about CCT estimation by SR under different voltage control gains are summarized in Table 3.8. The CCTs estimated by SR of the reduced-order model for the three cases are $t_{\text{SR}} = 0.15$ s, 0.31 s, and 0.45 s, and the fault clearing time is set to these values, that is, $t_{\text{fault}} = t_{\text{SR}}$. The red solid lines are



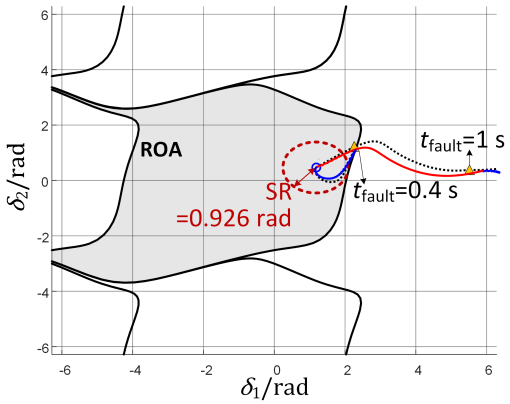
(a) GFM near the IBR1, $X_1 = 0.2$ pu, $X_g = 0.9$ pu



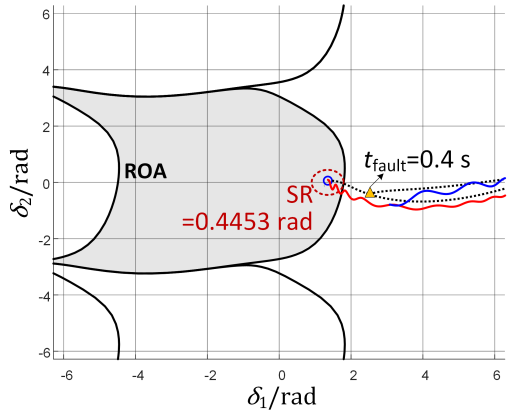
(b) GSP near the IBR1, $X_1 = 0.2$ pu, $X_g = 0.9$ pu



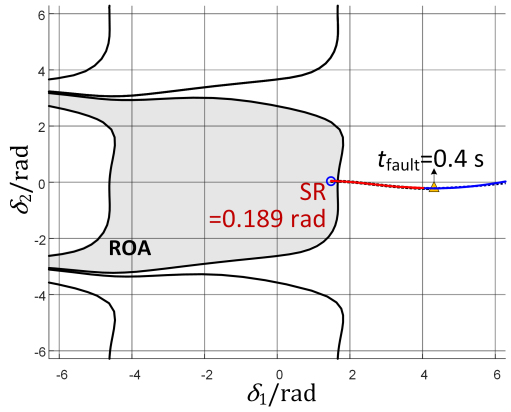
(c) GFM placed intermediately, $X_1 = 0.5$ pu, $X_g = 0.6$ pu



(d) GSP placed intermediately, $X_1 = 0.5$ pu, $X_g = 0.6$ pu



(e) GFM near the grid, $X_1 = 0.9$ pu, $X_g = 0.2$ pu



(f) GSP near the grid, $X_1 = 0.9$ pu, $X_g = 0.2$ pu

Figure 3.18: The EMT simulation results, ROA and SR under various locations of IBR2 (t_{fault}=0.4 s, 1 s). Color scheme for lines and markers follows that of Figure 3.10.

trajectories while the fault is applied and the blue solid lines are the post-fault trajectories, both from EMT simulation. The trajectories are also found from the integration of the reduced-order model and are shown as black dashed lines. It is seen that increasing k_v leads

Table 3.7: Detailed System Parameters in GFM - GSP Inverters System

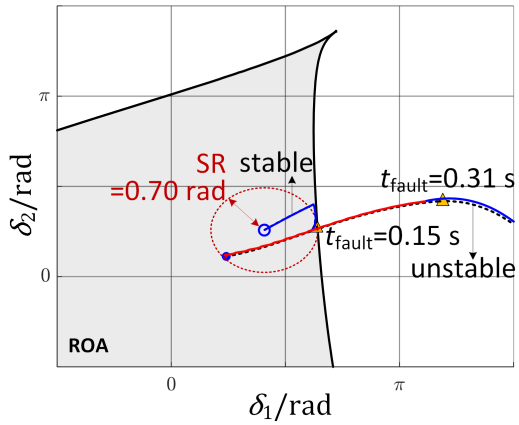
Impedance Z_1	0.5j+0.025
Impedance Z_2	0.1j+0.002
Impedance $2Z_g$	0.6j+0.03
Fault resistance R_f	0.001
Fault position (from the infinite bus)	0.8
IBR1 - GFM	
$p-\omega$ droop gain k_{droop}	$2.5 \times 2\pi$
Power reference P_{ref}	0.8
AC Voltage V_1	1
Inner voltage control loop bandwidth	200 Hz
Inner current control loop bandwidth	1 kHz
Current limit I_{limit}	5
$p-\omega$ droop time constant τ_p	$1/(25 \times 2\pi)$
IBR2 - GSP	
voltage control gain k_v	0, 2, or 4
Voltage reference V_{ref}	1
Current reference I_{d2}	0.2
Voltage control filter time scale τ_v	$1/(50 \times 2\pi)$
PLL controller k_{pll2}	$6 \times 2\pi$

to a corresponding increase in SR, thereby enhancing the system's large-signal stability. Without voltage control (pure GFL inverter), Figure 3.19 (a), the SR and t_{SR} is much smaller and making the system prone to instability, and adding voltage support in the transmission line of GFM inverters lessens the risk of large-signal instability. The results also further confirm SR can provide conservative and accurate estimations of large-signal stability.

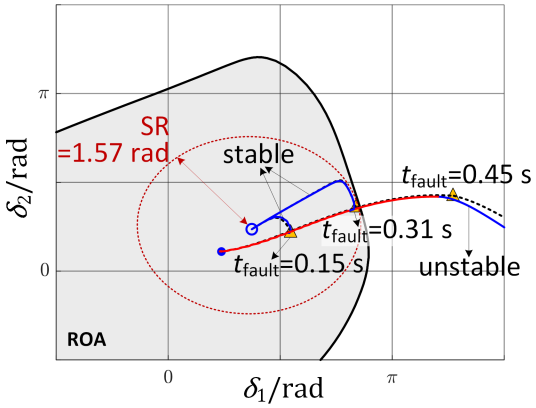
Figure 3.20 shows how the ROA and SR change with system parameters. The change of ROA with increasing k_v is shown in subplot (a) (other system parameters remain constant) and subplot (b) is the corresponding change in SR with the system becoming more stable for large k_v and approaching the situation where IBR2 was a GFM inverter. Although the large k_v in the GSP inverter enhances large-signal stability, it introduces a trade-off with small-signal stability. In particular, excessively high voltage-control bandwidth may destabilize the system due to interactions with the inner current control loop [157], which makes high k_v impractical and thus, GFM inverters remain superior to GSP inverters in this context. All parameters chosen in this thesis are verified through small-signal stability analysis first. Subplots (c) and (d) show the effect of the location of the GSP inverter on the ROA and SR. The value of X_g is varied while keeping the total impedance for IBR1,

Table 3.8: Comparison between SR-based CCT estimation and the theoretical CCT obtained from the real DOA under different GSP voltage gains

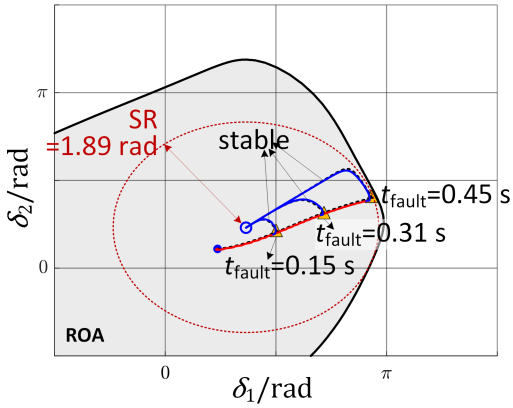
IBR2 configuration	SR	SR-based CCT t_{SR}	theoretical CCT
GSP $k_v = 0$	0.70 rad	0.15 s	0.155 s
GSP $k_v = 2$	1.57 rad	0.31 s	0.32 s
GSP $k_v = 4$ (Best)	1.89 rad	0.45 s	0.46 s



(a) $k_v = 0$ (GFL inverter) .



(b) $k_v = 2$ in GSP inverter.



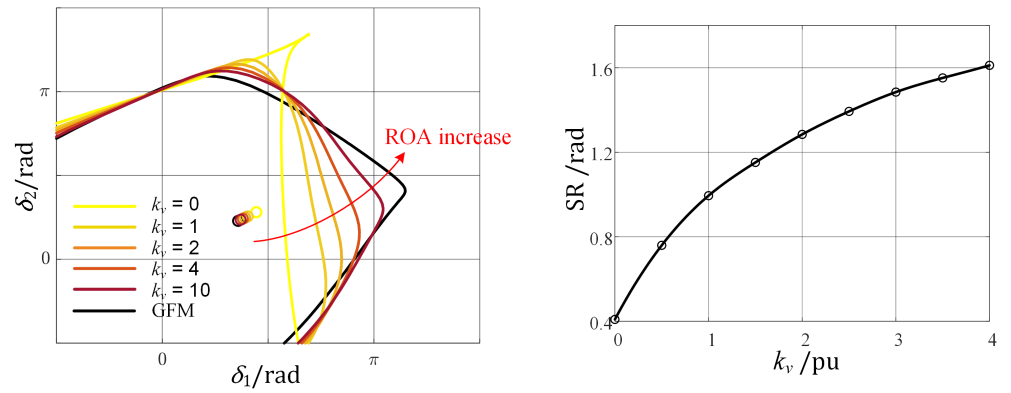
(c) $k_v = 4$ in GSP inverter.

Figure 3.19: The phase portraits of GFM inverter and GSP inverter with three choices of voltage control gains. Fault duration set to estimated critical clearing time for each case ($t_{\text{fault}} = 0.15$ s, 0.31 s, and 0.45 s respectively). Color scheme for lines and markers follows that of Figure 3.10.

$X_1 + X_g$, constant at 1.1 pu. The results show that when IBR2 is placed too close to either IBR1 or the infinite bus, the ROA decreases. The ROA and SR are maximized when $X_1 \approx X_g$, consistent with the conclusions drawn in Section 3.7.2.

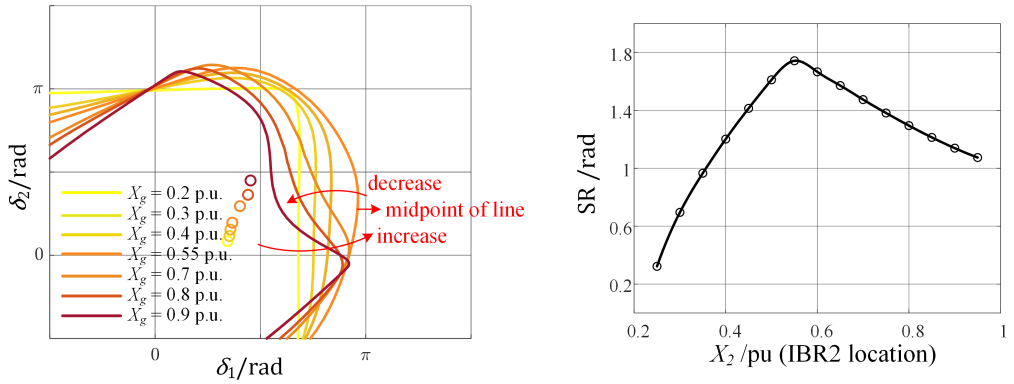
3.9 Summary

This chapter recognizes the non-existence of a global energy function for systems containing GFL inverters and discusses the difficulties in large-signal stability analysis that follow from that non-existence. A manifold theory was applied to reduced-order models of IBR to give an accurate estimation of the ROA which defines the limit of large-signal stable operation. The method is computationally efficient compared to EMT simulation and the accuracy of the method has been established in comparison to simulation. To evaluate the large-signal stability of multiple inverter systems, an assessment metric termed the *stability radius (SR)* has been proposed which is a circle centered at a SEP that exactly touches the ROA. The effectiveness of SR in giving a conservative estimate of the critical clearing time of faults for various combinations of GFL, GFM, and GSP inverters and variations of connection points



(a) change of ROA

(b) change of SR



(c) change of ROA

(d) change of SR

Figure 3.20: The change of ROA and SR with respect to (a)(b) voltage control gain k_v, and (c)(d) location of GSP inverter in the transmission line (The total impedance of transmission line $X_g + X_1 = 1.1$ pu is kept constant).

has been confirmed by comparison with both PHIL experiment and EMT simulations.

The large-signal stability of pairs of inverters, GFL-GFL, GFL-GFM, and GFL-GSP was assessed with the manifold theory and confirmed by both PHIL experiment and EMT simulation. By accurately depicting the manifold between these inverters, a new large-signal instability mode was identified when the trajectories converged to a stable periodic orbit (SPO). Compared to a GFL inverter, a GSP inverter can provide voltage support, which improves the large-signal stability of the other IBR, whether GFM or GFL, particularly when that inverter is connected to the grid via weak transmission lines. The improvement is maximized if the GSP inverter is placed at the mid-point of the transmission line. When one of the two IBRs is configured as a GFM inverter, compared to a GSP inverter, improved voltage control is observed. Although with high voltage control gain k_v, the GSP case can approach the GFM case, but high droop gain is known to degrade the small-signal stability.

Chapter 4

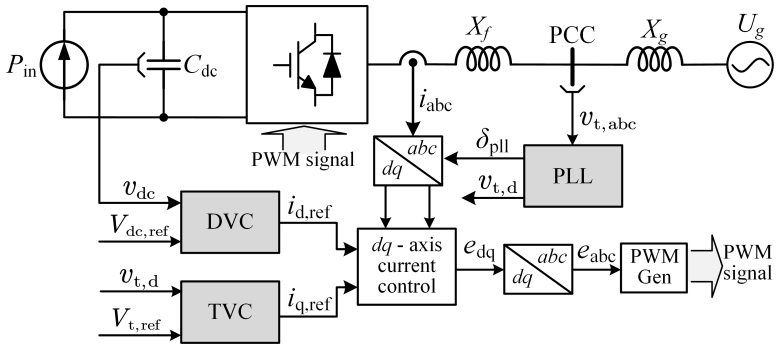
Consideration of Control-Loop Interaction in Transient Stability of Grid-Following Inverters using Bandwidth Separation Method

Simple analysis in which outer loop controllers are idealized is not sufficient, and interactions of the non-linear dynamics of PLL with the dynamics of the DVC and, where present, the TVC. An asymptotic analysis approach, termed *bandwidth separation method*, is proposed in this Chapter. This method enables simplification and order reduction of the original differential equations when sufficient bandwidth separation exists. Through this method, the interaction between the DVC and PLL is explicitly characterized, revealing that such adverse interaction degrades system stability and shrinks the stability region. The analysis also indicates that voltage collapse, rather than PLL loss of synchronization alone, is often the root cause of transient instability. Optimal bandwidth configurations for PLL and DVC are identified under various grid fault conditions: a larger PLL bandwidth improves resilience to phase jump faults, while a larger DVC bandwidth enhances tolerance to power fluctuations. In addition, the influence of the TVC loop is analyzed, showing that a high TVC bandwidth can mitigate the destabilizing effects of PLL–DVC interaction and further improve transient stability. All analytical findings are validated through HIL experiments.

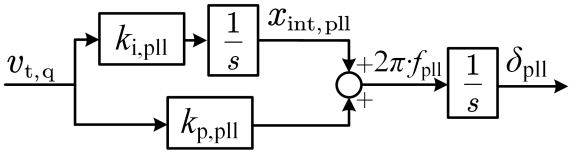
4.1 Proposed Bandwidth Separation Method

4.1.1 Modelling of Multiple Control Loops in GFL Inverter

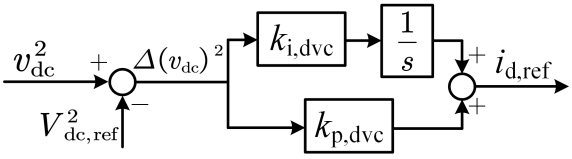
The diagram of a single-machine infinite-bus system and control loops in the GFL inverter, including PLL, DVC, and TVC, is shown in Figure 4.1. The grid is represented by U_g with fundamental frequency ω_s. In general, the control bandwidth of the outer loop is much



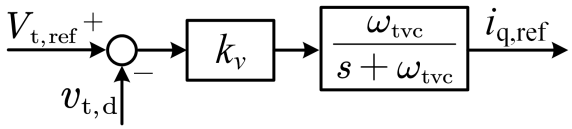
(a) Overall control system structure.



(b) Phase-locked loop (PLL).



(c) DC-link voltage control (DVC).



(d) Terminal voltage control (TVC).

Figure 4.1: System diagram of grid-following inverter.

less than that of the inner current loop, and thus a grid-following inverter can be modeled as a controlled current source (that is, $i_d = i_{\mathrm{d,ref}}$, $i_q = i_{\mathrm{q,ref}}$) when analyzing its transient dynamics [50, 6]. Typical formats of outer loop control will now be discussed. As for PLL, a PI controller is used to drive the observed q-axis voltage $v_{\mathrm{t,q}}$ to zero, as shown in Figure 4.1 (b). The nonlinear dynamics can be expressed as follows:

$$\begin{cases} \frac{d}{dt}\delta = k_{\mathrm{p,pll}} v_{\mathrm{t,q}} + x_{\mathrm{int,pll}} \\ \frac{d}{dt} x_{\mathrm{int,pll}} = k_{\mathrm{i,pll}} v_{\mathrm{t,q}} \\ v_{\mathrm{t,q}} = X_g i_d + i_q R_g - U_g \sin\delta + i_d \dot{\delta} L_g/\omega_s \end{cases} \tag{4.1}$$

where $x_{\mathrm{int,pll}}$ is the output of the integrator inside the PI controller and δ represents the angle difference between the PLL and the grid.

The DVC is illustrated in Figure 4.1 (c). The variable $\Delta\,(v_{dc})^2$ is defined as the deviation between the square of the actual DC-link voltage and its reference, given by $v_{\mathrm{dc}}^2 - V_{\mathrm{dc,ref}}^2$, and PI controller is then employed to regulate the voltage by adjusting the d-axis current

reference [92, 6]. The nonlinear dynamics can be expressed as follows:

$$\begin{cases} \frac{d}{dt} i_d = k_{\mathrm{i,dvc}} \Delta \left(v_{\mathrm{dc}}\right)^2 + k_{\mathrm{p,dvc}} \frac{2}{C_{dc}/\omega_s} \left(P_{in} - p\right) \\ \frac{d}{dt} \Delta \left(v_{\mathrm{dc}}\right)^2 = \frac{2}{C_{\mathrm{dc}}/\omega_s} \left(P_{in} - p\right) \\ p = v_{\mathrm{t,dq}}{}^{\intercal} \cdot i_{\mathrm{dq}} = i_d U_g \cos\delta - i_q U_g \sin\delta + i_{dq}^2 R_g \end{cases} \tag{4.2}$$

In terms of TVC, droop control with a low-pass filter is typically employed to regulate the injection of reactive current according to grid codes [145, 140, 158], as shown in Figure 4.1 (d). This control approximates the standard v_t-i_q droop characteristic, assuming the PLL angle is aligned with the grid voltage such that $v_{\mathrm{t,d}} \approx v_t$, where v_t is the terminal voltage measured at the PCC in Figure 4.1 (d). In this figure, ω_{tvc} denotes the cut-off frequency of the low-pass filter, and k_v is the voltage control (droop) gain in TVC. The nonlinear dynamics can be expressed as follows:

$$\begin{cases} \frac{1}{\omega_{\mathrm{tvc}}} \cdot \frac{d}{dt} i_q = -i_q + \left(v_{\mathrm{t,d}} - V_{\mathrm{t,ref}}\right) \cdot k_v \\ v_{\mathrm{t,d}} = U_g \cos\delta + i_d R_g - i_q X_g + i_q \dot{\delta} L_g / \omega_s \end{cases} \tag{4.3}$$

Equations (4.1), (4.2), and (4.3) can be re-written in ordinary differential equation (ODE) format as:

$$\frac{1}{\omega_{\mathrm{pll}}} \cdot \frac{d}{dt} \begin{bmatrix} \delta \\ x_{\mathrm{int,pll}} \end{bmatrix} = \begin{bmatrix} f_{\mathrm{pll},1}\left(\delta, i_d, \frac{x_{\mathrm{int,pll}}}{\omega_{\mathrm{pll}}}\right) \\ f_{\mathrm{pll},2}\left(\delta, i_d, x_{\mathrm{int,pll}}\right) \end{bmatrix} \tag{4.4a}$$

$$\frac{1}{\omega_{\mathrm{dvc}}} \cdot \frac{d}{dt} \begin{bmatrix} i_d \\ \omega_{\mathrm{dvc}} \Delta \left(v_{\mathrm{dc}}\right)^2 \end{bmatrix} = \begin{bmatrix} f_{\mathrm{dvc},1}\left(\delta, i_{\mathrm{dq}}, \omega_{\mathrm{dvc}} \Delta \left(v_{dc}\right)^2\right) \\ f_{\mathrm{dvc},2}\left(\delta, i_{\mathrm{dq}}\right) \end{bmatrix} \tag{4.4b}$$

$$\frac{1}{\omega_{\mathrm{tvc}}} \cdot \frac{d}{dt} i_q = f_{\mathrm{tvc}}\left(\delta, i_q\right) \tag{4.4c}$$

in which the resistance of the grid impedance has been treated as negligible.

In the system defined by (4.4), the control bandwidths of the PLL, DVC, and TVC loops are denoted by ω_{pll}, ω_{dvc}, and ω_{tvc}, respectively. Their values are given by $\omega_{\mathrm{pll}} = k_{\mathrm{p,pll}}$, $\omega_{\mathrm{dvc}} = \frac{2}{C_{\mathrm{dc}}/\omega_s} \cdot k_{\mathrm{p,dvc}}$. The derivation of the bandwidth expressions, the controller designs and the detailed mathematical expressions for all functions appearing in (4.4) are provided in Appendix B.1.

Eq. (4.4) constitutes the full-order model of the outer loop control system and it can be seen that it is 5^{th} order, which is relatively high, and includes several nonlinear terms introduced by the PLL, the power calculation, and the dq transform. Thus, it is not straightforward to analyze the transient stability of the full system model and an appropriate approach is required to simplify and reduce the order of the ODE model.

4.1.2 Bandwidth Separation Method and Analysis Steps

The proposed method is underpinned by singular perturbation theory [132, 31, 133], which enables the decomposition of a dynamical system into slow and fast subsystems under

sufficient time-scale separation. A standard singularly perturbed system takes the form:

$$\begin{aligned} \dot{\mathbf{X}} &= f(\mathbf{X}, \mathbf{Y}, \varepsilon) \\ \varepsilon \dot{\mathbf{Y}} &= g(\mathbf{X}, \mathbf{Y}, \varepsilon) \end{aligned} \tag{4.5}$$

where ε is a small positive parameter, and $\mathbf{X}$ and $\mathbf{Y}$ denote slow and fast variables, respectively. As $\varepsilon \to 0$, the system reduces to a differential-algebraic form:

$$\begin{aligned} \dot{\mathbf{X}} &= f(\mathbf{X}, \mathbf{Y}, 0) \\ \mathbf{0} &= g(\mathbf{X}, \mathbf{Y}, 0) \end{aligned} \tag{4.6}$$

According to Tikhonov's theorem (Theorem 11.2 in [31]), if the fast subsystem is exponentially stable for fixed $\mathbf{X}$, the solution $\mathbf{Y}$ quickly converges to the algebraic constraint $g(\mathbf{X}, \mathbf{Y}, 0) = \mathbf{0}$, and the reduced-order differential-algebraic equation (DAE) approximates the full system with an $O(\varepsilon)$ error. In addition, Theorem 16-8 in [32] shows that the stability boundary of the full system can be approximated by combining the stability region of the slow subsystem with the union of stable manifolds of the fast subsystem. This implies that if both subsystems are individually stable, the full system is also stable [159].

It can be seen that the ODE model represented by (4.4) has the explicit singular perturbation structure of (4.5). When the bandwidths of the three outer loops of a GFL inverter are very different, the singular perturbation theory can be applied to can be applied to separate the system into fast and slow subsystems, enabling the derivation of a reduced-order DAE model to capture the system dynamics. In this framework, the control loops with the larger bandwidths can be regarded as the fast subsystem, and the reciprocal of this bandwidth serves as the time-scale parameter ε in (4.5) of the fast subsystem. Loops whose reciprocal bandwidths are $O(\varepsilon)$ or smaller are included in the fast subsystem, while the remaining loops constitute the slow subsystem.

A time-domain simulation comparison is carried out in Section 4.2, which demonstrates that if the bandwidths of outer control loops in GFL inverters differ by a factor of 7-8, then a good approximation of the DAE model can be obtained. Such bandwidth separation may be prevalent in the industry so that the loops can be tuned independently of each other.

The analysis steps in next Section are as follows:

1. Determine the stability region Ω_f of the fastest control loop. At this stage, the variables in the other two loops are treated as slow variables and approximated as constants.

2. Determine the stability region Ω_m of the intermediate-speed control loop. At this stage, the fastest loop is reduced to an algebraic equation, while the slowest loop variables remain constant.

3. Determine the stability region Ω_s of the slowest control loop. At this stage, the other two control loops are considered fast and reduced to algebraic equations.

4. The overall stability region of the full-order ODE system is the intersection of the three individual stability regions, i.e.,

$$\Omega_{\text{overall}} = \Omega_f \cap \Omega_m \cap \Omega_s.$$

5. Repeat the above steps for all possible bandwidth separation choices.

For each loop's analysis, the reduced-order DAE is of order no more than two, which simplifies the derivation of stability regions and provides physical insight.

4.2 Control Loops Analysis based on Proposed Method

In subsection 4.2.1 and subsection 4.2.2, only PLL and DVC control loops are first considered regardless of the dynamics of TVC, where i_q is treated as a constant (typically $i_q = 0$). The effect of TVC is discussed in subsection 4.2.3.

4.2.1 Bandwidth sequence: ω_{pll} sufficiently larger than ω_{dvc}

With ω_{pll} sufficiently larger than ω_{dvc}, the PLL subsystem (4.1) is considered as a fast subsystem, and rapidly converges to the algebraic equation (4.7a). The DVC subsystem (4.2) is treated as the slow subsystem. Substituting (4.7a) into (4.2) yields a reduced-order model for the DVC dynamics, expressed in (B.8) and rearranged as (4.7b). This reduced model accurately captures the system behavior, and approximates the original full-order system with an error of order $O(\varepsilon)$. The full derivation is given in Appendix B.2.1.

$$\delta = \text{asin}(\frac{X_g i_d}{U_g}) \tag{4.7a}$$

$$\begin{cases} \frac{d}{dt} i_d = k_{\text{p,dvc}} \frac{2}{C_{\text{dc}}/\omega_s} \left[P_{in} - p\left(i_d\right)\right] + k_{\text{i,dvc}} \Delta\left(v_{\text{dc}}\right)^2 \\ \frac{d}{dt} \Delta\left(v_{\text{dc}}\right)^2 = \frac{2}{C_{\text{dc}}/\omega_s} \left[P_{in} - p\left(i_d\right)\right] \end{cases} \tag{4.7b}$$

where,

$$p\left(i_d\right) = i_d \sqrt{{U_g}^2 - \left(i_d X_g\right)^2} - i_d i_q X_g$$

Stability analysis

It can be shown that $p\left(i_d\right)$ is a convex function, which typically intersects the input power P_{in} at two points: one is a SEP, denoted $i_{\text{d,sep}}$, and the other is an UEP, denoted $i_{\text{d,uep}}$. An example characteristic curve of $p\left(i_d\right)$ is illustrated with the solid line on upper axes of Figure 4.2. The corresponding ROA, is shown as the shaded area on the lower axes in Figure 4.2. The ROA is bounded by the stable manifold of the UEP according to the stability region theory in [32].

To ensure that the PLL subsystem remains stable while acting as a fast loop, the current

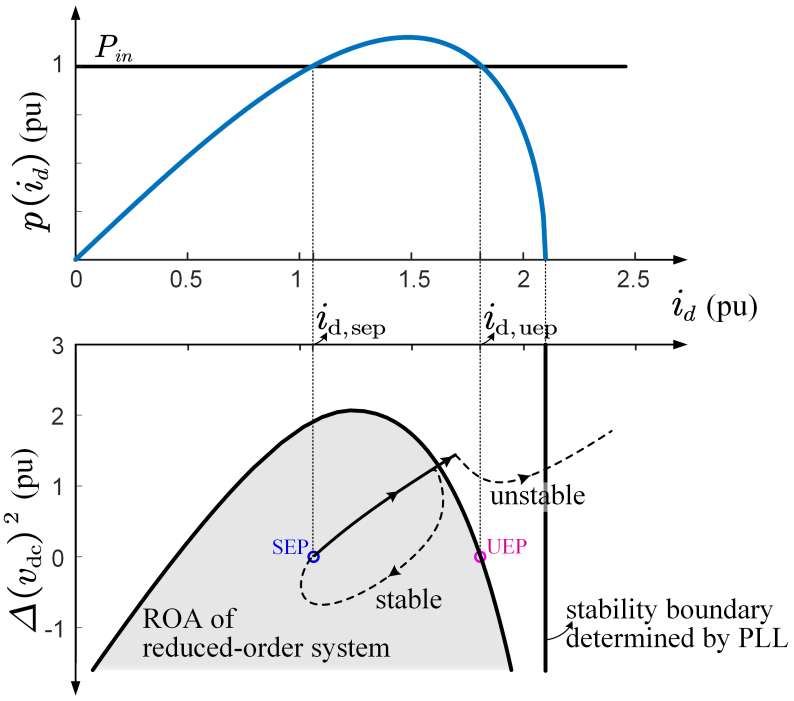


Figure 4.2: Example curve of $p(i_d)$ (blue line on upper axes) and stability region (ROA) of DVC (lower axes) when $\omega_{\mathrm{pll}} \gg \omega_{\mathrm{dvc}}$.

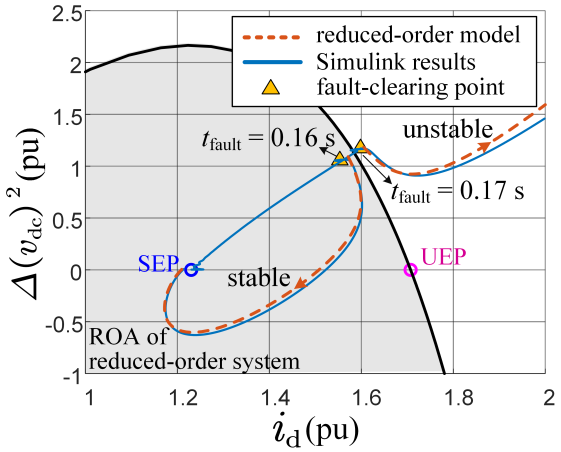
i_d must satisfy:

$$i_d < i_{\mathrm{d,max}} = \min \left\{ \frac{U_g}{X_g}, \frac{\sqrt{{U_g}^2 - (X_g i_d)^2}}{\zeta_{\mathrm{pll}} L_g/\omega_s}, \frac{1}{\omega_{\mathrm{pll}} L_g} \right\}$$

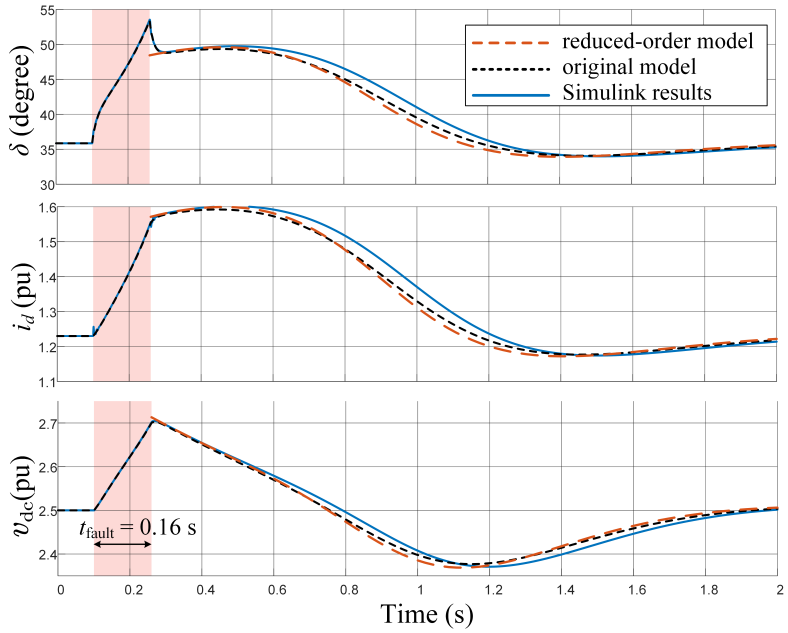
as derived in (B.4). This constraint, which ensures convergence of PLL dynamics, is also plotted as a vertical black line in Figure 4.2, which usually lies outside the DVC's stability region. This means that the stability of the PLL does not guarantee overall system stability if the DVC dynamics lie outside their stability region. This highlights that the slow loop can dominate the full-system behavior even when the fast loop is well-behaved. Furthermore, configuring $k_{\mathrm{i,pll}} = \zeta_{\mathrm{pll}} \cdot k_{\mathrm{p,pll}}$ results in an overdamped PLL, which expands the allowable range of δ from $(-2\pi+\delta_{\mathrm{uep,pll}}, \delta_{\mathrm{uep,pll}})$ (where $\delta_{\mathrm{uep,pll}}$ represents the UEP in PLL subsystem, see Figure B.1 in Appendix B.2.1 or analysis in Section 2.2.1 Chapter 2). In summary, all these mean that the stability region for i_d is shrunk compared to the standalone PLL.

Herein, the maximum output power of grid-following inverters is also discussed. The maximum value of output power is $p(i_d)_{\max} = U_g^2/2X_g$ at $i_d = U_g/(\sqrt{2}X_g)$ when there is no q-axis current injection, $i_q = 0$. If $P_{\mathrm{in}} < p(i_d)_{\max}$, namely $U_g < \sqrt{2P_{\mathrm{in}}X_g}$, does not satisfy, there is no equilibrium point, and the DVC will be unstable first before PLL. This observation aligns with the small-signal constraints on X_g and P_{in} discussed in [90]. In addition, a negative i_q can lift the curve of $p(i_d)$, thereby expanding the stability region.

Herein, the maximum output power of grid-following inverters is also discussed. The maximum value of output power is $p(i_d)_{\max} = U_g^2/2X_g$ at $i_d = U_g/(\sqrt{2}X_g)$ when there is



(a) phase portrait.



(b) Time domain comparison.

Figure 4.3: Theoretical and simulation results under $\omega_{\text{pll}} = 15$ Hz $\times 2\pi$, $\omega_{\text{dvc}} = 2$ Hz $\times 2\pi$, with a 0.9 pu voltage sag fault. The corresponding CCT is approximately 0.16 s.

no q-axis current injection, $i_q = 0$. If $P_{\text{in}} < p(i_d)_{\max}$, namely $U_g < \sqrt{2P_{\text{in}}X_g}$, does not satisfy, there is no equilibrium point, and the DVC will be unstable first before PLL. This observation aligns with the small-signal constraints on X_g and P_{in} discussed in [90]. In addition, a negative i_q can lift the curve of $p(i_d)$, thereby expanding the stability region.

Model validation

To verify the accuracy of the model reduction, numerical results from the original ODE model (4.4), the reduced DAE model (4.7), and EMT simulations implemented in MATLAB /Simulink are compared, which are shown in Figure 4.3. Detailed simulation parameters are listed in Table B.1 in Appendix B.3. The PLL bandwidth is configured as 15 Hz, while the DVC bandwidth is 2 Hz. The critical clearing time (CCT) is found to be $t_{\text{fault}} = 0.16$ s; when the clearing time increases to 0.17 s, the system becomes unstable, as illustrated in

Figure 4.3 (a).

From the time-domain comparison in Figure 4.3 (b), the reduced-order model (orange dotted line) closely matches the full-order ODE model (black dotted line) and the EMT simulation (blue solid line). Specifically, for the i_d time-domain trajectory in Figure 4.3 (b), the maximum deviation between the reduced-order model and the original ODE model is 0.0194 pu, corresponding to 1.44%, while the maximum deviation between the EMT simulation and the original ODE model is 0.041 pu (3.03%). By performing a more refined time-domain scan of the fault clearing time, the theoretical CCT of the original ODE model is 0.163 s, the CCT predicted by the reduced-order model is 0.164 s, and the EMT simulation yields a CCT of 0.163 s. The discrepancy among these results is within 1 ms, indicating excellent agreement in both trajectory prediction and stability margin estimation. For the variable δ, the full-order model (black dotted line) rapidly converges to the algebraic approximation (4.7a) (orange dashed line), confirming the fast dynamics' behavior. For i_d and $\Delta\left(v_{\mathrm{dc}}\right)^2 = v_{\mathrm{dc}}^2 - V_{\mathrm{dc,ref}}^2$, the reduced model (4.7b) achieves an $O(\varepsilon)$ approximation of the full-order model. To improve accuracy at the initial instant, an initial value correction is applied. The rapid decay of the fast dynamics can be regarded as a small initial-value perturbation acting on the slow subsystem, yielding $O(\varepsilon^2)$ accuracy. Specifically, the initial values for i_d and $\Delta\left(v_{\mathrm{dc}}\right)^2$ are corrected as $i_d(0) - i_d^*(0)$ and $\Delta\left(v_{\mathrm{dc}}\right)^2(0) - i_d^*(0)$ and $[\Delta\left(v_{\mathrm{dc}}\right)^2]^*(0)$, respectively. The expressions for $i_d^*(0)$ and $[\Delta\left(v_{\mathrm{dc}}\right)^2]^*(0)$ are provided by (B.9) in Appendix B.2.1, accounting for the boundary-layer dynamics induced by the fast convergence of δ. It should also be noted that as the PLL bandwidth is further reduced, the approximation accuracy of the reduced-order model gradually deteriorates. When the PLL bandwidth decreases to 10 Hz (corresponding to approximately five times the DVC bandwidth), the maximum time-domain i_d trajectory error increases to 0.22 pu (14.38%), and the CCT deviation grows to about 8 ms (exceeding 5%). A further reduction of the PLL bandwidth ultimately leads to the breakdown of the reduced-order approximation.

The minor discrepancies between the original model and the Simulink simulation are primarily attributed to unmodeled dynamics such as the inner current control loop and the LC filter, which are not captured in the reduced-order formulation.

4.2.2 Bandwidth sequence: ω_{dvc} sufficiently larger than ω_{pll}

Stability analysis

With ω_{dvc} sufficiently larger than ω_{pll}, the DVC subsystem (4.2) is considered as a fast subsystem, and rapidly converges to the algebraic equation (4.8a). The PLL subsystem (4.1) is treated as the slow subsystem. It can be shown (see Appendix B.2.2) that when $-\pi/2 > \delta > \pi/2$, the DVC subsystem is globally asymptotically stable, since DVC is linear with respect to its state variables, i_d and $\Delta\left(v_{\mathrm{dc}}\right)^2$. Substituting (4.8a) into the PLL dynamics (4.1) yields a reduced-order model for the slow PLL subsystem, described in (4.8b). This reduced model provides an accurate approximation of the full-order system,

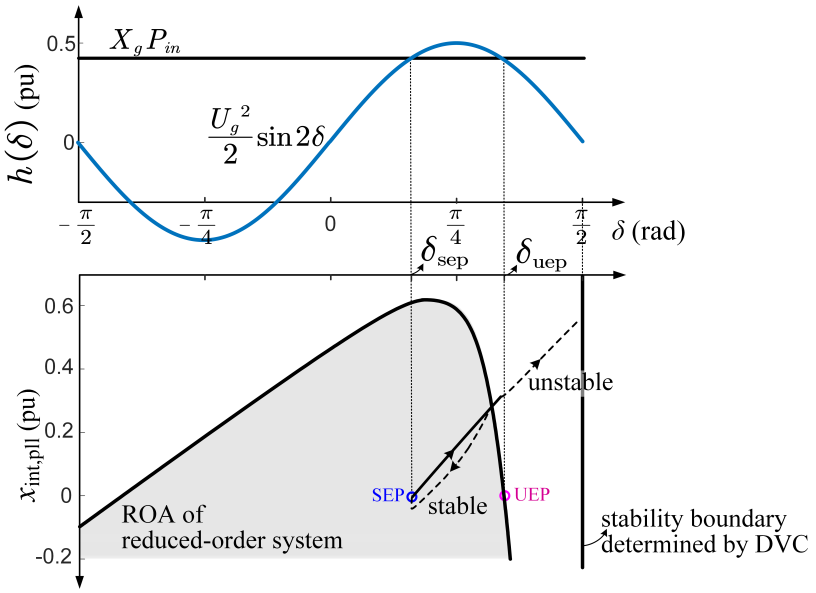


Figure 4.4: Example curve of $h(\delta)$ (blue line on upper axes) and stability region (ROA) of PLL (lower axes) when $\omega_{\text{dvc}} \gg \omega_{\text{pll}}$.

with an error of order $O(\varepsilon)$.

$$i_d = \frac{P_{in} + i_q U_g \sin\delta}{U_g \cos\delta} \tag{4.8a}$$

$$\begin{cases} \dot{\delta} = \frac{k_{\text{p,pll}}}{\lambda(\delta)} \cdot [X_g P_{in} - h(\delta)] + \frac{P_{in}}{\lambda(\delta)} \cdot x_{\text{int,pll}} \\ \dot{x}_{\text{int_}pll} = \frac{k_{\text{i,pll}}}{\lambda(\delta)} \cdot [X_g P_{in} - h(\delta) + P_{in} L_g \cdot x_{\text{int,pll}}] \end{cases} \tag{4.8b}$$

where,

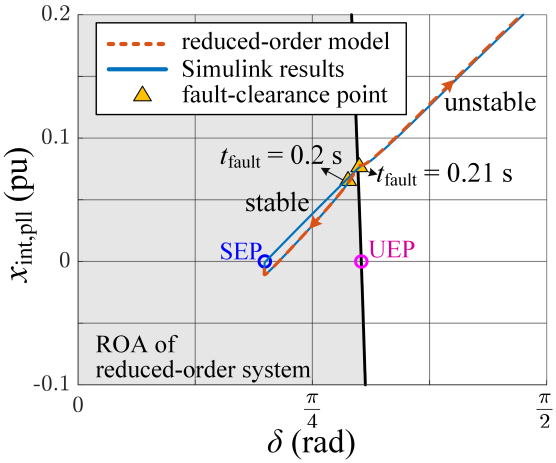
$$h(\delta) = \frac{U_g^2}{2}\sin 2\delta - i_q X_g U_g \sin\delta = \frac{U_g^2}{2}\sin 2\delta \ (\text{if } i_q = 0)$$

$$\lambda(\delta) = U_g \cos\delta - k_{\text{p,pll}} L_g/\omega_s \cdot (P_{in} + i_q U_g \sin\delta)$$

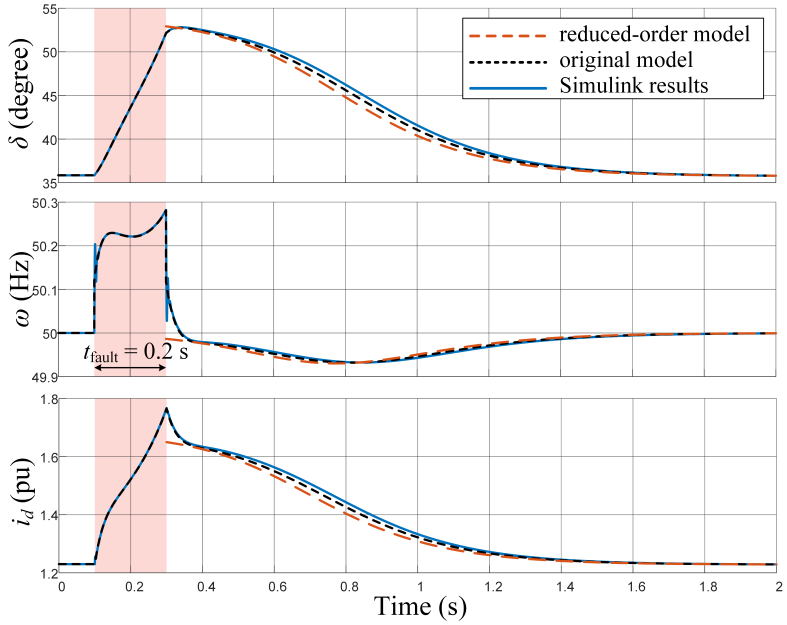
The function $X_g P_{\text{in}}$ and the curve $h(\delta)$ are plotted in Figure 4.4. The two intersection points, δ_{sep} and δ_{uep}, correspond to the SEP and UEP, respectively. It can be shown that $\lambda(\delta)$ remains positive due to the limitation for current and PLL bandwidth. Compared to the standalone PLL system, the sinusoidal function is reduced to a period of π instead of 2π, resulting in $\delta_{\text{sep}} \in (0, \pi/4)$ and $\delta_{\text{uep}} \in (\pi/4, \pi/2)$. The corresponding stability region of the reduced-order system, bounded by the stable manifold of the UEP [32], is shown as the gray shaded area in Figure 4.4. Relative to the standalone PLL case, this stability region is visibly reduced. Additionally, the feasible region of δ defined by the stability condition of DVC subsystem, $-\pi/2 > \delta > \pi/2$, is indicated by the vertical black line. Typically, this constraint lies outside the reduced-order system's stability region.

Model validation

Similarly, to verify the accuracy of the model reduction, numerical results from the original ODE model (4.4), the reduced DAE model (4.8), and Simulink-based simulations



(a) Phase portrait.



(b) Time domain comparison.

Figure 4.5: Theoretical and simulation results under $\omega_{\text{pll}} = 2$ Hz $\times 2\pi$, $\omega_{\text{dvc}} = 15$ Hz $\times 2\pi$, with a 0.9 pu voltage sag fault. The corresponding CCT is approximately 0.2 s.

are compared, which are shown in Figure 4.3. Detailed simulation parameters are listed in Table B.1 in Appendix B.3. From the time-domain comparison in Figure 4.5 (b), the reduced-order model (orange dotted lines) closely matches the full-order ODE model (black dotted line) and EMT simulation (blue solid line). Specifically, for the δ time-domain trajectory in Figure 4.5 (b), the maximum deviation between the reduced-order model and the original ODE model is 0.89 degrees, corresponding to 2.1%, while the maximum deviation between the EMT simulation and the original ODE model is 0.52 degree (1.2%). Moreover, under a more refined time-domain scan, CCTs identified from these three models also differ by less than 1 ms, indicating a high level of consistency in transient stability assessment. For the variable i_d, the full-order model (black dotted line) rapidly converges to the algebraic approximation (4.8a) (orange dashed line), confirming the fast dynamics behavior of the DVC loop. To improve accuracy at the initial instant, an initial value correction is applied. The rapid decay of the fast dynamics can be regarded as a $O(\varepsilon)$ small initial-value

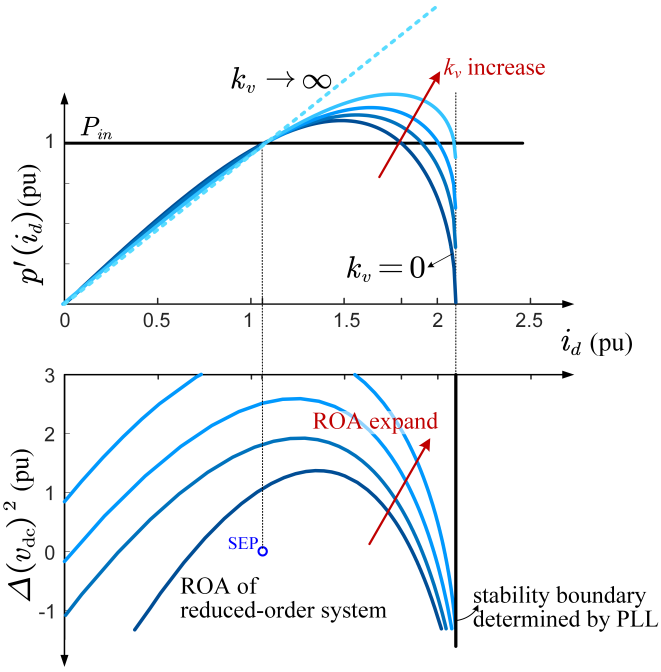


Figure 4.6: Example curve of $p'(i_d)$ (upper axes) and stability region (ROA) of DVC (lower axes) when ω_{tvc} and $\omega_{\text{pll}} \gg \omega_{\text{dvc}}$.

perturbation acting on the slow subsystem, yielding $O(\varepsilon^2)$ accuracy. Specifically, the initial values for δ and $x_{\text{int,pll}}$ are corrected as $\delta(0) - \delta^*(0)$ and $x_{\text{int,pll}}(0) - x^*_{\text{int,pll}}(0)$, respectively. The expressions for δ^* and $x^*_{\text{int,pll}}$ are provided by (B.9) in Appendix B.2.2, accounting for the boundary-layer dynamics induced by the fast convergence of i_d.

4.2.3 Impact of TVC control loop

According to (4.4), the TVC loop has no direct influence on the PLL, as the PLL dynamics are independent of i_q. Therefore, the TVC primarily affects the DVC subsystem. Consequently, the bandwidth relationship between the DVC and TVC loops becomes critical. If the TVC bandwidth is lower than that of the DVC, i_q can be regarded as quasi-static from the perspective of the DVC dynamics and thus has negligible impact on the analysis presented in the previous two sections. However, when the TVC bandwidth exceeds that of the DVC, there are two possible scenarios:

Bandwidth sequence: ω_{tvc} and $\omega_{\text{pll}} \gg \omega_{\text{dvc}}$

As shown in Appendix B.2.2, regardless of whether the PLL bandwidth is higher or lower than that of the TVC, the TVC subsystem always remains stable. As a result, the PLL and TVC loops can be jointly treated as a fast subsystem and represented by a set of algebraic equations (4.9a) and (4.9b). By substituting these algebraic expressions into the original DVC model (4.2), a new reduced-order differential equation for the DVC dynamics is obtained, as expressed in (4.9c).

$$\delta = \operatorname{asin}\left(\frac{X_g i_d}{U_g}\right) \tag{4.9a}$$

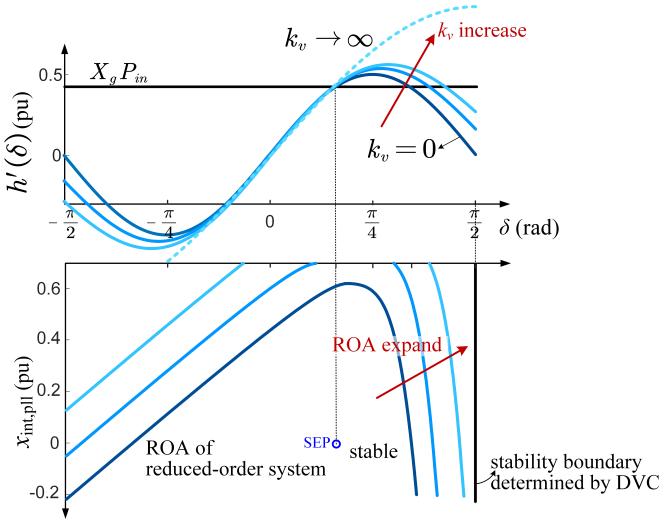


Figure 4.7: Example curve of $h'(\delta)$ (upper axes) and stability region (ROA) of PLL (lower axes) when $\omega_{\text{tvc}} \gg \omega_{\text{dvc}} \gg \omega_{\text{pll}}$.

$$-i_q = \frac{k_v}{k_v X_g + 1} \cdot (V_{ref} - U_g \cos\delta) \tag{4.9b}$$

$$\begin{cases} \frac{d}{dt} i_d = k_{\text{p,dvc}} \frac{2}{C_{\text{dc}}/\omega_s} \left[P_{in} - p'(i_d)\right] + k_{\text{i,dvc}} \Delta (v_{\text{dc}})^2 \\ \frac{d}{dt} \Delta (v_{\text{dc}})^2 = \frac{2}{C_{\text{dc}}/\omega_s} \left[P_{in} - p'(i_d)\right] \end{cases} \tag{4.9c}$$

where,

$$\begin{aligned} p' &= \underbrace{\frac{U_g V_{ref}}{X_g + 1/k_v} \sin\delta}_{\text{synchronous power}} + \underbrace{\left(\frac{1}{X_g} - \frac{1}{X_g + 1/k_v}\right) \frac{{U_g}^2}{2} \sin 2\delta}_{\text{saliency power}} \\ &= \frac{1}{k_v X_g + 1} \cdot \underbrace{i_d \sqrt{U_g - (i_d X_g)^2}}_{p(i_d)} + \frac{k_v X_g}{k_v X_g + 1} \cdot V_{ref} i_d \end{aligned}$$

Compared to (4.7), the power function $p(i_d)$ in (4.9) is modified to $p'(i_d)$, as shown in Figure 4.6. The curve of $p'(i_d)$ is elevated relative to $p(i_d)$, without altering the steady-state operating point of the system. As a result, the stability region of the reduced-order system is expanded, as illustrated in Figure 4.6. The expression of $p'(i_d)$ structurally resembles the power expression of a salient-pole synchronous generator [20]. In this analogy, $1/k_v$ can be interpreted as an additional impedance on the d-axis, and V_{ref} acts as the internal voltage reference. The deeper blue curve represents the ROA with a larger voltage control gain k_v. As $k_v \to \infty$, the terminal voltage is well regulated to V_{ref}, and the output power p' approaches a straight line through the SEP: $i_d \cdot V_{\text{ref}}$. In this sense, the DVC subsystem becomes decoupled from the PLL and remains always stable.

Bandwidth sequence: $\omega_{\text{tvc}} \gg \omega_{\text{dvc}} \gg \omega_{\text{pll}}$

Under this bandwidth configuration, both the DVC and TVC loops can be approximated by algebraic equations, as given in (4.10a) and (4.10b). Substituting these expressions into

the original PLL dynamics yields the reduced-order differential equation in (4.10c).

$$i_d = \frac{P_{in} + i_q U_g \sin\delta}{U_g \cos\delta} \tag{4.10a}$$

$$-i_q = \frac{k_v}{k_v X_g + 1} \cdot (V_{ref} - U_g \cos\delta) \tag{4.10b}$$

$$\begin{cases} \dot{\delta} = \frac{k_{\mathrm{p,pll}}}{\lambda(\delta)} \cdot [X_g P_{in} - h'(\delta)] + \frac{P_{in}}{\lambda(\delta)} \cdot x_{\mathrm{int,pll}} \\ \dot{x}_{\mathrm{int_}pll} = \frac{k_{\mathrm{i,pll}}}{\lambda(\delta)} \cdot [X_g P_{in} - h'(\delta) + P_{in} L_g \cdot x_{\mathrm{int,pll}}] \end{cases} \tag{4.10c}$$

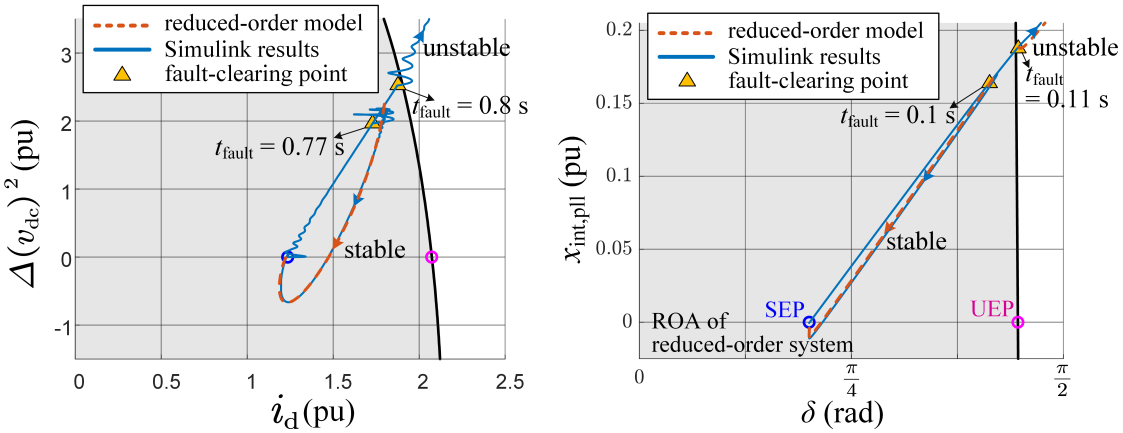
where,

$$h'(\delta) = \frac{k_v X_g}{1 + k_v X_g} \cdot V_{ref} U_g \sin\delta + \frac{1}{1 + k_v X_g} \cdot h(\delta)$$

Compared to the expression in (4.8b), the nonlinear term $h(\delta)$ is replaced by $h'(\delta)$, as shown in Figure 4.7. The curve of $h'(\delta)$ is elevated relative to $h(\delta)$, an expanded stability region for the PLL. The deeper blue curve represents the ROA with a larger voltage control gain k_v. As $k_v \to \infty$, $h'(\delta)$ is the sinusoidal function with a period of 2π resembling the conventional PLL model, which contrasts with the original $h(\delta)$, which is a $\pi-$periodic sinusoidal function.

Model validation

To further validate the accuracy of the model reduction with TVC included, comparisons are made between the reduced-order models (4.9), (4.10), and EMT simulations in MATLAB/Simulink. The resulting trajectories are shown in Figure 4.8. It is evident that the inclusion of the TVC loop enlarges the stability region compared to the cases without TVC. In both Figure 4.8 (a) and (b), the trajectories of the reduced-order models (orange dotted lines) closely match the simulations (blue solid lines). Specifically, under critical stability conditions, the maximum deviation between the reduced-order model and the original ODE model is limited to 0.078 pu (5.3%) for the i_d trajectory and 1.3 degrees (2.6%) for



(a) $\omega_{\mathrm{dvc}} = 2$ Hz $\times 2\pi$, $\omega_{\mathrm{pll}} = 15$ Hz $\times 2\pi$.

(b) $\omega_{\mathrm{pll}} = 2$ Hz $\times 2\pi$, $\omega_{\mathrm{dvc}} = 15$ Hz $\times 2\pi$.

Figure 4.8: The phase portrait comparison between simulation and reduced-order model, with a 0.6 pu voltage sag fault, $\omega_{\mathrm{tvc}} = 20$ Hz $\times 2\pi$, $k_v = 2$.

the δ trajectory. The EMT simulations exhibit minor oscillations, while showing consistent transient stability behavior. Moreover, the CCT identified from the reduced-order models and EMT simulations agree well, at approximately $t_{\text{fault}} = 0.77$ s and 0.1 s for the two scenarios.

4.2.4 Stability region (ROA) versus bandwidth configuration

According to the results of the analysis, the stability regions are summarized in Table 4.1. The overall stability region is shrunk compared with the PLL-alone system. In summary, a higher bandwidth DVC enlarges the region mainly along the DVC-state subspace [states i_d and $\Delta\left(v_{\text{dc}}\right)^2$], whereas a higher bandwidth PLL enlarges it along the PLL-state subspace [states angle difference δ and $x_{\text{int,pll}}$]. Including a fast TVC mitigates the adverse effects of PLL–DVC coupling on transient stability.

Table 4.1: ROA Comparison and Parameters Feasible Region under Different Control Loop Configurations

Parameter	PLL-alone (i_d is fixed)	Bandwidth sequence $\omega_{\text{pll}} \gg \omega_{\text{dvc}}$		Bandwidth sequence $\omega_{\text{dvc}} \gg \omega_{\text{pll}}$	
		No / slow TVC	Fast TVC	No / slow TVC	Fast TVC
Grid voltage U_g	$U_g > i_d X_g$	$U_g > \sqrt{2P_{\text{in}}X_g}$ [worse]	mitigated[1]	$U_g > \sqrt{2P_{\text{in}}X_g}$ [worse]	mitigated
ROA of DVC state	$i_d < i_{\text{d,max}}$	reduced	mitigated	whole DVC phase plane	whole DVC phase plane
ROA of PLL state	$\delta < \delta_{\text{uep,pll}}$	same as PLL-alone	same as PLL-alone	reduced	mitigated

[1] "mitigated" indicates that the inclusion of the TVC enlarges the ROA in some extent, while adverse effects associated with fast PLL (reduced DVC stability) or fast DVC (reduced PLL stability) may still persist.

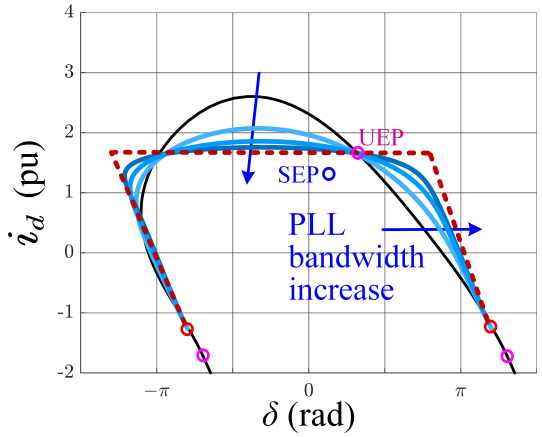
4.3 ROA Trends with Changes in Control-Loop Bandwidth

Even though, in practice, the bandwidths of different control loops may not always be ideally separated, the proposed analysis method can still indicate trends in characteristics and guide the design choices of control loop bandwidths. In this subsection, we examine how the ROA varies with changes in control loop bandwidths, thereby offering further qualitative insights into their relationship.

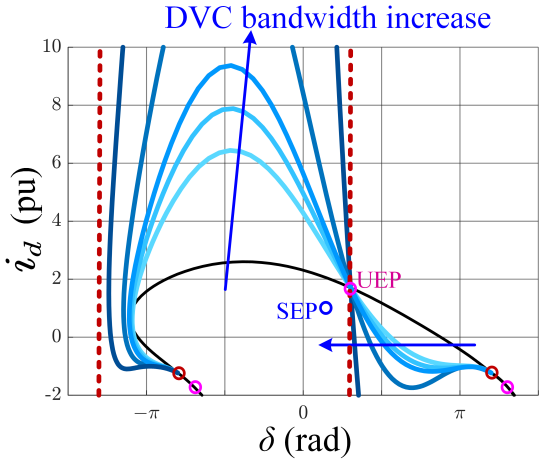
For simplicity of analysis, we assume that both PLL and DVC are implemented as overdamped first-order controllers (i.e., proportional control only), rather than PI controllers. Specifically, the damping factors are set to $\zeta_{\text{pll}} = 0$ and $\zeta_{\text{dvc}} = 0$ (definitions given in Appendix B.1). Under this assumption, the system dynamics (4.4) reduce to:

$$\frac{1}{\omega_{\text{pll}}} \cdot \frac{d}{dt}\delta = f_{\text{pll},1}\left(\delta, i_d, 0\right) \tag{4.11a}$$

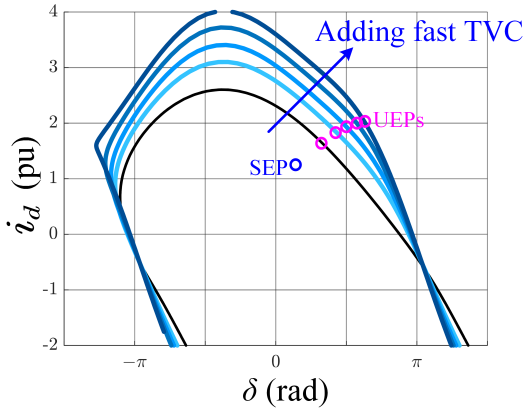
$$\frac{1}{\omega_{\text{dvc}}} \cdot \frac{d}{dt} i_d = f_{\text{dvc},1}\left(\delta, i_{\text{dq}}, 0\right) \tag{4.11b}$$



(a) Change of the ROA with increasing of PLL bandwidth ω_{pll}.



(b) Change of the ROA with increasing of DVC bandwidth ω_{dvc}.



(c) Change of the ROA with increasing of TVC droop gain k_v.

Figure 4.9: Examples of how the ROA varies with control parameters in the δ–i_d phase plane.

$$\frac{1}{\omega_{\text{tvc}}} \cdot \frac{d}{dt} i_q = f_{\text{tvc}}(\delta, i_q) \tag{4.11c}$$

The bandwidth separation method is applied, and the effect of TVC is neglected first. In this case, the PLL dynamics in (4.11a) and the DVC dynamics in (4.11b) are analyzed jointly, and their ROAs are projected onto the δ–i_d phase plane by using the manifold theory, as shown in Figure 4.9 (a) and (b).

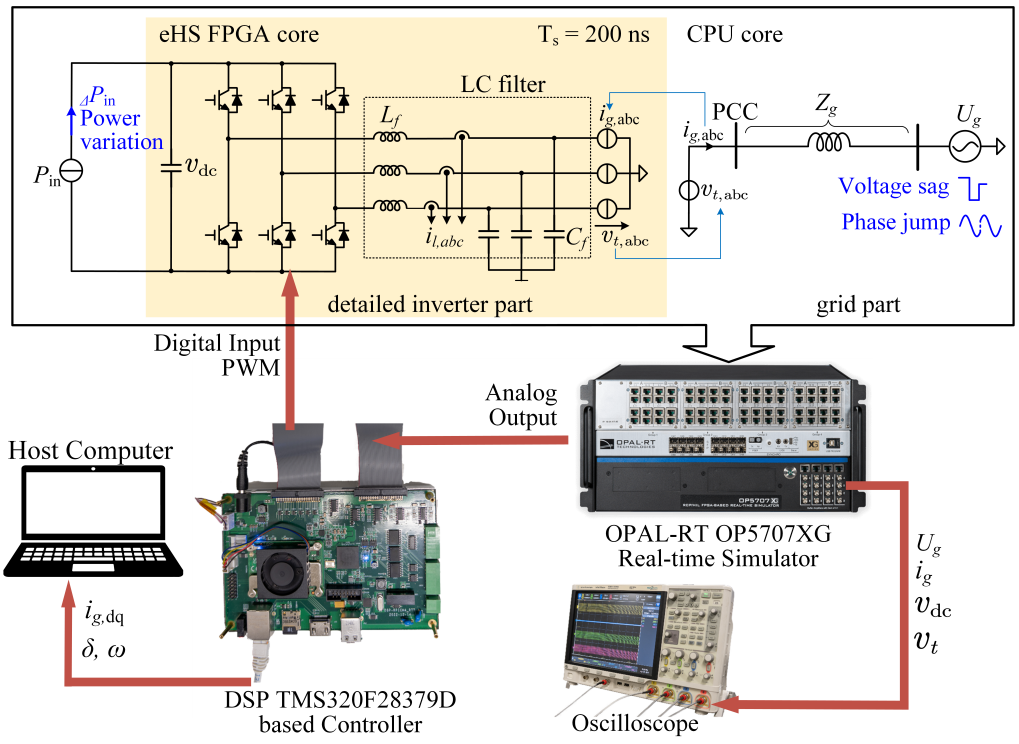
In Figure 4.9 (a), the black curve is the stability boundary (ROA) when the PLL and DVC have identical bandwidths. Deeper blue indicates a larger PLL bandwidth. The locations of the SEP and UEP are unchanged by the PLL bandwidth. As the PLL bandwidth increases, the ROA contracts along the i_d direction but expands along the δ direction, approaching the red dashed limit. The red dashed segments correspond to the proportional–control limit discussed for Figure 4.2: the segment parallel to the δ axis enforces the DVC constraint $i_d < i_{d,\text{uep}}$, while the slanted segment is the PLL constraint that a SEP must exist for the

given i_d. In Figure 4.9 (b), the black curve again denotes the equal-bandwidth baseline, and deeper blue indicates a larger DVC bandwidth. Increasing the DVC bandwidth causes the ROA to extend essentially without bound in the i_d direction, while compressing in the δ direction, until the red dashed boundary is reached. This limit coincides with the first-order (proportional PLL) case in Figure 4.4: δ must remain below its UEP, whereas i_d can, in principle, span the whole plane. In Figure 4.9 (c), a fast TVC is included. As the voltage control gain k_v increases (deeper blue), the overall ROA enlarges and the UEP moves outward.

These trends, once again, are consistent with the preceding analysis and Table 4.1: increasing DVC bandwidth enlarges the stability region along the DVC-state subspace, whereas increasing PLL bandwidth enlarges it along the PLL-state subspace. Taking this further, the key insight is that there is a trade-off between phase-angle stability and dc-link stability in large-signal stability; a sufficiently fast TVC relaxes this trade-off by expanding the ROA of both.

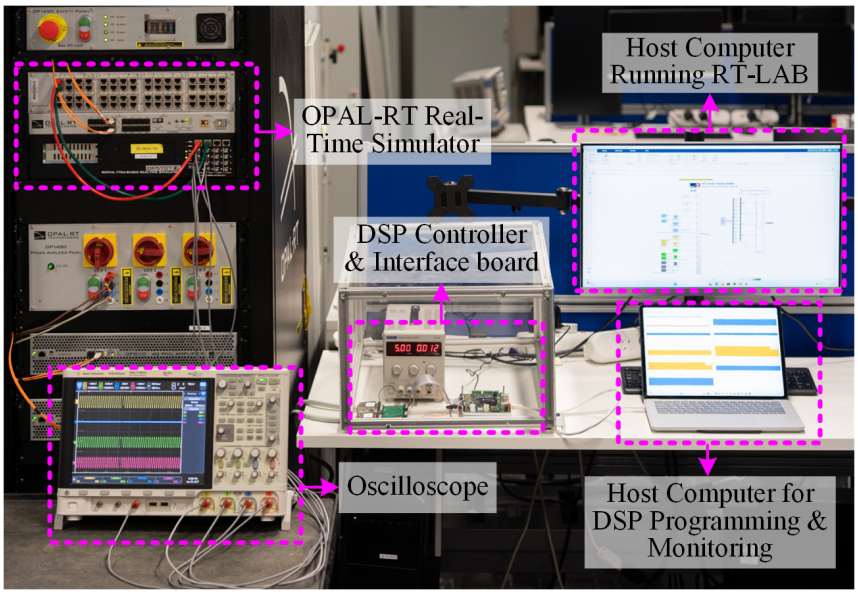
4.4 Analysis under Various Faults and HIL Experiment Results

In order to verify the above theoretical analysis and investigate the interaction among control loops, hardware-in-the-loop (HIL) experimental results are discussed in this section. The experimental platform is shown in Figure 4.10. The setup employs the OPAL-RT real-time simulator OP5707XG equipped with the eHS FPGA-based toolbox, which can reach



(a) Tested system and configuration.

Figure 4.10: HIL experimental platform.



(b) Platform setup.

Figure 4.10: HIL experimental platform. (continued)

200 ns real-time step, enabling highly detailed real-time modeling of the inverter. The 1 MVA GFL inverter system is built inside the OPAL-RT real-time simulator, as depicted in Figure 4.10 (a). The studied GFL inverter is representative of the grid-side inverter in Type-IV wind turbines. The detailed system parameters are listed in Table B.1 in Appendix B.2.3. Three typical faults, including voltage sag fault, phase jump, and input power variation are emulated inside the OPAL-RT real-time simulator. The controller is implemented by the DSP TMS320F28379. The controller acquires analog signals from the OP5707XG and generates PWM signals to drive the power electronics devices of the GFL inverter. Both the switching frequency and the DSP control frequency are set to 10 kHz. Key signals, including grid voltage $U_{g,a}$, output current $i_{g,a}$, terminal voltage at PCC $v_{\mathrm{t,a}}$ (all phase A), and the deviation of the DC-link voltage $v_{\mathrm{dc}} - V_{\mathrm{dc,ref}}$ are measured by the oscilloscope. Other control variables, such as angle difference between the PLL and the grid δ, frequency of PLL f_{pll}, and i_d, i_q are monitored via the host computer through DSP data upload. All results presented in this section are obtained from HIL experiments.

4.4.1 Voltage sag fault

In Figure 4.11, the system is PLL standalone, that is, there are no DVC or TVC control loops. Under this configuration, the system remains stable even when the grid voltage drops to 0.6 pu without fault clearance. However, when both PLL and DVC loops are included, a 0.9 pu voltage sag under a weak grid [short circuit ratio (SCR) of 2.1 herein] results in the absence of an equilibrium point (EP), and the system diverges during the fault. This is because the existence condition for an EP becomes $U_g > \sqrt{2P_{\mathrm{in}}X_g} = 0.97$ pu when both DVC and PLL exist, which is more restrictive than the standalone PLL case where $U_g > i_d X_g = 0.47$. For instance, in Figure 4.12 (b), if the DVC loop is considered and the fault clearing time exceeds $t_{\mathrm{fault}} = 0.24$ s, the system will lose stability. This indicates that it is usually not easy for the PLL alone to cause system instability, but the

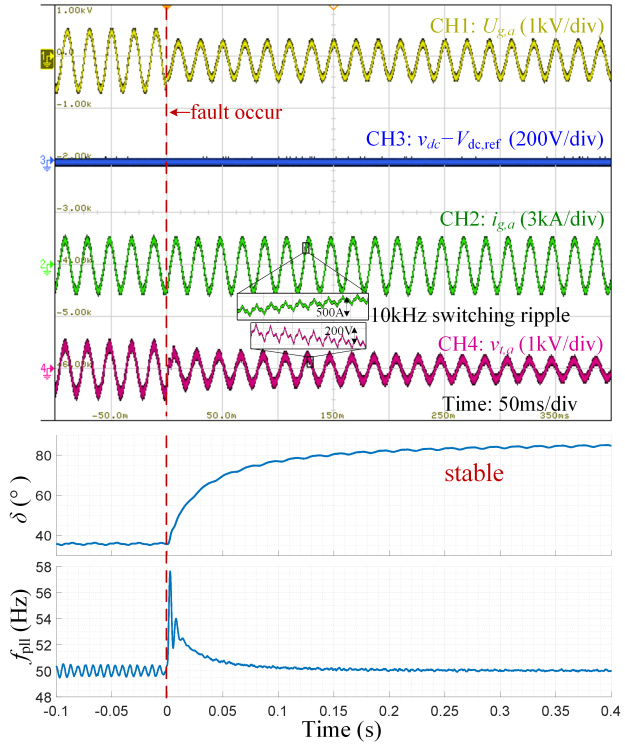


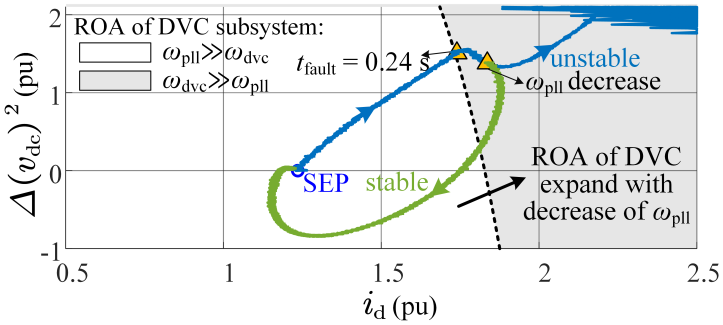
Figure 4.11: PLL standalone system under 0.6 pu voltage sag fault with $\omega_{\text{pll}} = 16$ Hz $\times 2\pi$, $i_d = i_{\text{d,sep}}$ to achieve $P_{\text{in}} = 1$ pu active power output.

interaction between DVC and PLL is the main factor for the instability. The previous works [27, 58, 42, 39, 53, 47, 160] do not take this situation into account.

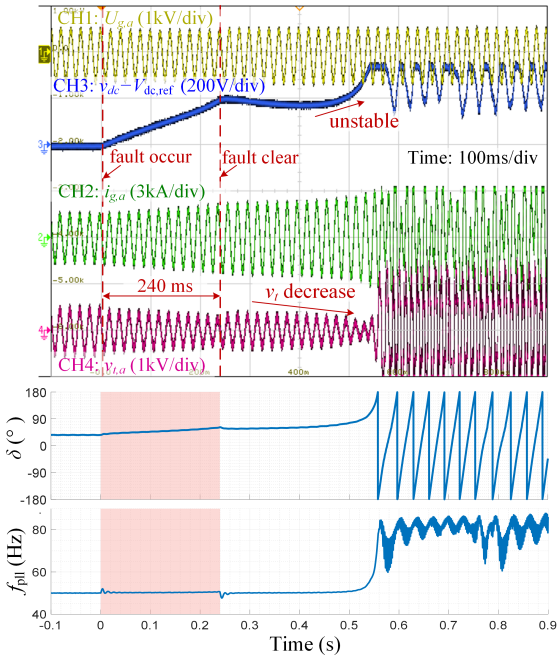
In Figure 4.12 (b), the DVC is added, and the 0.9 pu voltage sag fault occurs at 0 s and is cleared at 0.24 s. Even though TVC is added, guaranteeing the existence of SEP during fault, the system may finally destabilize. This is because the bandwidth of TVC is too low for i_q to be adjusted effectively before the system becomes unstable. Precisely, in Figure 4.12 (b) configuration, the bandwidth of DVC is 2 Hz much smaller than that of PLL, and the CCT is nearly 0.24 s. After the fault is cleared, the DVC loop becomes unstable first, eventually causing the PLL and the whole system to lose stability.

The key mechanism of this large-signal instability is the adverse interaction loop between i_d and δ and the consequent voltage collapse. Even when the fault is cleared, the DVC controller tends to inject more i_d in an attempt to regulate the DC voltage. The increase of i_d will cause δ increase, which will, however, decrease the terminal voltage v_t, even after the fault is cleared. The reduction of v_t leads to a decrease in output power and a further attempt to increase in i_d. This instability mechanism is illustrated in Figure 4.13 (b). As seen in Figure 4.12 (b), v_t continues to decline and i_d increasing finally to its limit 3.1 kA. Once $i_d > U_g/X_g$, the PLL subsystem then also becomes unstable. The DC-link voltage finally oscillates around 2 kV due to the DC chopper circuit, and cannot be restored.

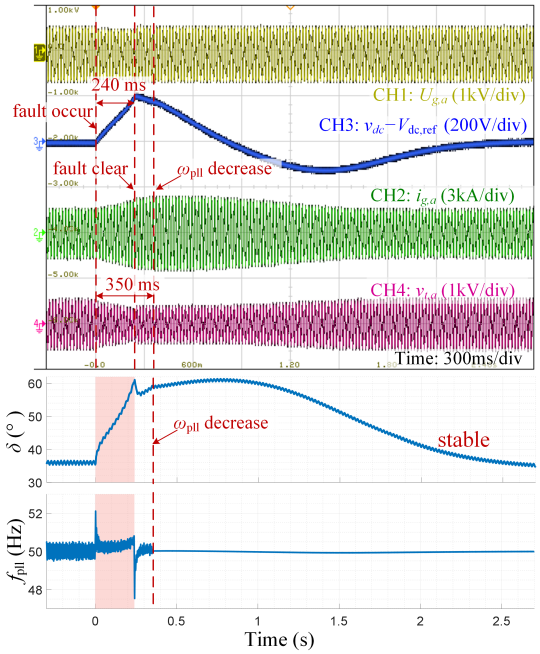
In Figure 4.12 (c), ω_{pll} is reduced to 0.4 Hz at 0.35 s after the fault is cleared. This renders DVC the fast subsystem and extends its stability region across the whole phase plane, as seen in Figure 4.12 (a). Since δ remains within the ROA of the PLL subsystem at 0.35 s,



(a) Phase portraits in DVC state phase plane under ω_{dvc} maintained at 16 Hz × 2π (blue line) and ω_{pll} decreased to 0.4 Hz × 2π at 0.35 s (green line). The yellow triangle represents the fault clearing point and the point when PLL parameters change.



(b) Time-domain results when ω_{pll} maintained at 16 Hz × 2π.

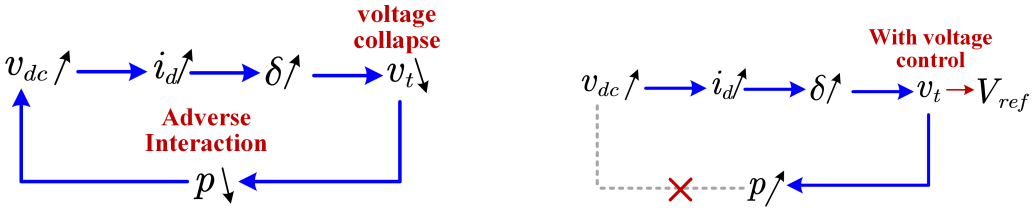


(c) Time-domain results when ω_{pll} decreased to 0.4 Hz × 2π at 0.35 s.

Figure 4.12: GFL inverter under 0.9 pu voltage sag fault with slow TVC. ω_{tvc} = 0.3 Hz×2π, ω_{pll} = 16 Hz × 2π, ω_{dvc} = 2 Hz × 2π, and fault clearing time t_{fault}=0.24 s.

and the DVC states are also within their new ROA, the system converges to its SEP. The reduction in ω_{pll} limits the rapid growth of δ, thereby interrupting the adverse interaction that would otherwise reduce v_t.

Compared to Figure 4.12 (b), the change in Figure 4.14 is the increase of TVC bandwidth to 20 Hz, which is significantly higher than DVC. This allows i_q to respond rapidly before the system becomes unstable, maintaining overall stability even without fault clearance. The injected i_q helps sustain the terminal voltage v_t. As discussed in Section III, when $k_v \to \infty$, v_t becomes tightly regulated to V_{ref}, and the increase of δ due to i_d no longer reduces power output. This breaks the adverse interaction loop as illustrated in Figure 4.13. Therefore, voltage instability is the fundamental cause of instability in GFL inverters with DVC. A



(a) Mechanism of voltage collapse.

(b) TVC stabilization mechanism.

Figure 4.13: Adverse interaction between PLL and DVC and the resulting voltage-collapse mechanism.

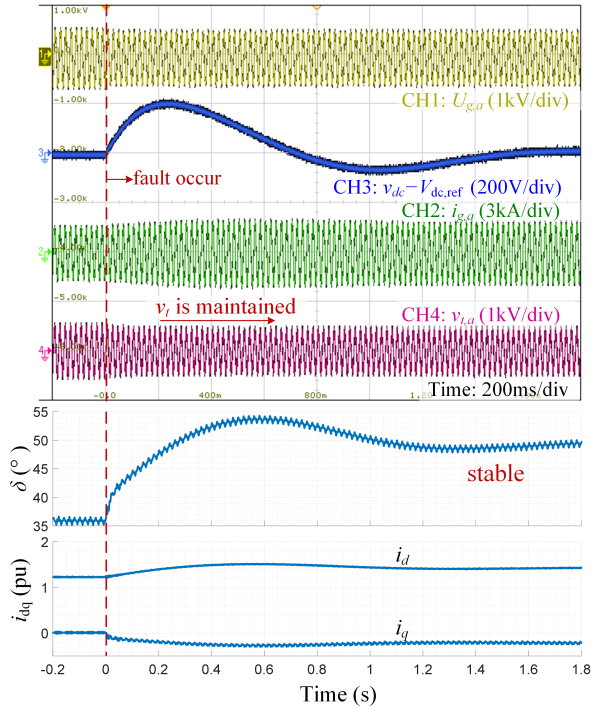
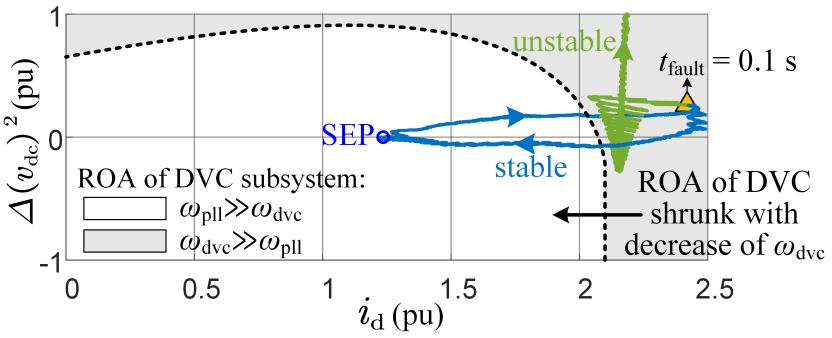


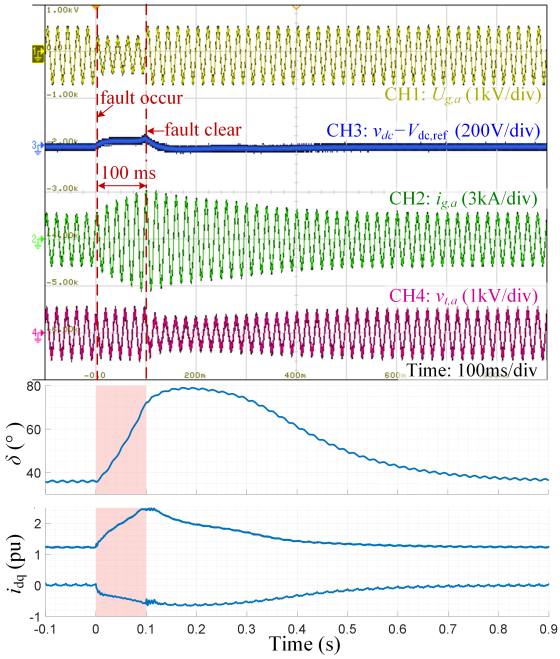
Figure 4.14: GFL inverter under 0.9 pu voltage sag fault without fault clearance, with fast TVC $\omega_{\text{tvc}} = 20$ Hz $\times 2\pi$,$\omega_{\text{pll}} = 16$ Hz $\times 2\pi$,$\omega_{\text{dvc}} = 2$ Hz $\times 2\pi$, and without fault clearance.

higher TVC bandwidth improves v_t regulation and contributes to transient stability. This benefit is also consistent with the small-signal analysis in [90].

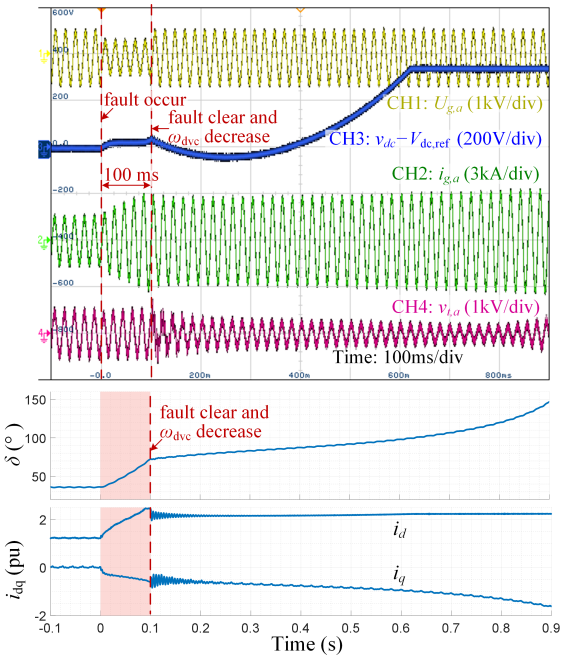
In Figure 4.15, the bandwidths of PLL, DVC, and TVC are set to 2 Hz, 15 Hz, and 20 Hz respectively, which is the same as the configuration in Figure 4.8 (b). The UEP is located at $\delta_{\text{uep}} = 80.3°$ and the CCT under 0.6 pu voltage sag fault is 0.1 s. In Figure 4.15 (b), the DVC loop is significantly faster than the PLL. When the fault is cleared at $t_{\text{fault}} = 0.1$ s, the system remain critically stable with δ staying below δ_{uep}. The trajectory projected onto the DVC state phase plane is plotted in Figure 4.15 (a). Since the DVC acts as the fast subsystem, its states can stabilize over the entire phase plane as long as the slow PLL remains stable. By contrast, in Figure 4.15 (c), the DVC bandwidth is reduced to 0.4 Hz, making it the slowest control loop. At the fault clearing point, the projected trajectory in Figure 4.15 (a) shows i_d exceeding 2 pu, which lies outside the ROA of the DVC subsystem in its slow configuration. Consequently, the system under a slow DVC configuration loses stability. The underlying mechanism is as follows: when ω_{dvc} is high, i_d can respond rapidly



(a) Phase portraits in DVC state phase plane under ω_{dvc} maintained at 15 Hz × 2π (blue line) and ω_{dvc} decreased to 0.4 Hz × 2π at 0.1 s when fault is cleared (green line). The yellow triangle represents the fault clearing point.



(b) Time-domain results when ω_{dvc} maintained at 15 Hz × 2π.



(c) Time-domain results when ω_{dvc} decreased to 0.4 Hz × 2π at 0.1 s when fault is cleared.

Figure 4.15: GFL inverter under 0.6 pu voltage sag fault with fast TVC. ω_{tvc} = 20 Hz × 2π, ω_{pll} = 2 Hz × 2π, ω_{dvc} = 15 Hz × 2π, and fault clearing time t_{fault}=0.1 s.

to regulate the DC voltage, with δ remaining relatively constant. However, when ω_{dvc} is low, the PLL becomes comparatively faster. In this case, the increase in i_d leads to a rapid rise in δ, which in turn reduces v_t and the output power. As illustrated in Figure 4.15 (c), this destabilizes the DVC control loop, resulting in a DC voltage rise toward its upper limit and eventual system instability.

4.4.2 Phase jump

This section investigates the system response under phase jump disturbances. The bandwidths of the PLL and DVC are initially set to 1Hz and 8Hz, respectively, placing the PLL as the slowest control loop. According to the previous analysis, this configuration yields a UEP at $\delta_{\text{uep}} = 54°$, corresponding to the smallest stability region in Figure 4.16. When the phase jump value $_{\Delta}\varphi$ is 15°, 19°, 21°, 25°, and 48°, the system trajectories are plotted

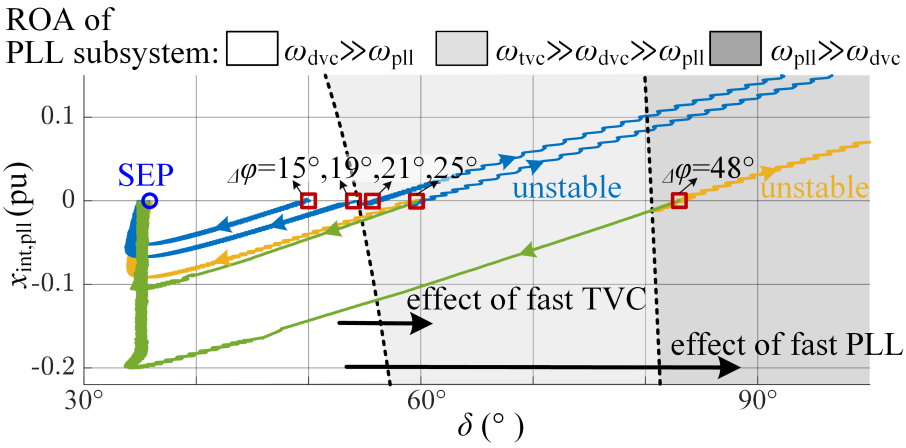
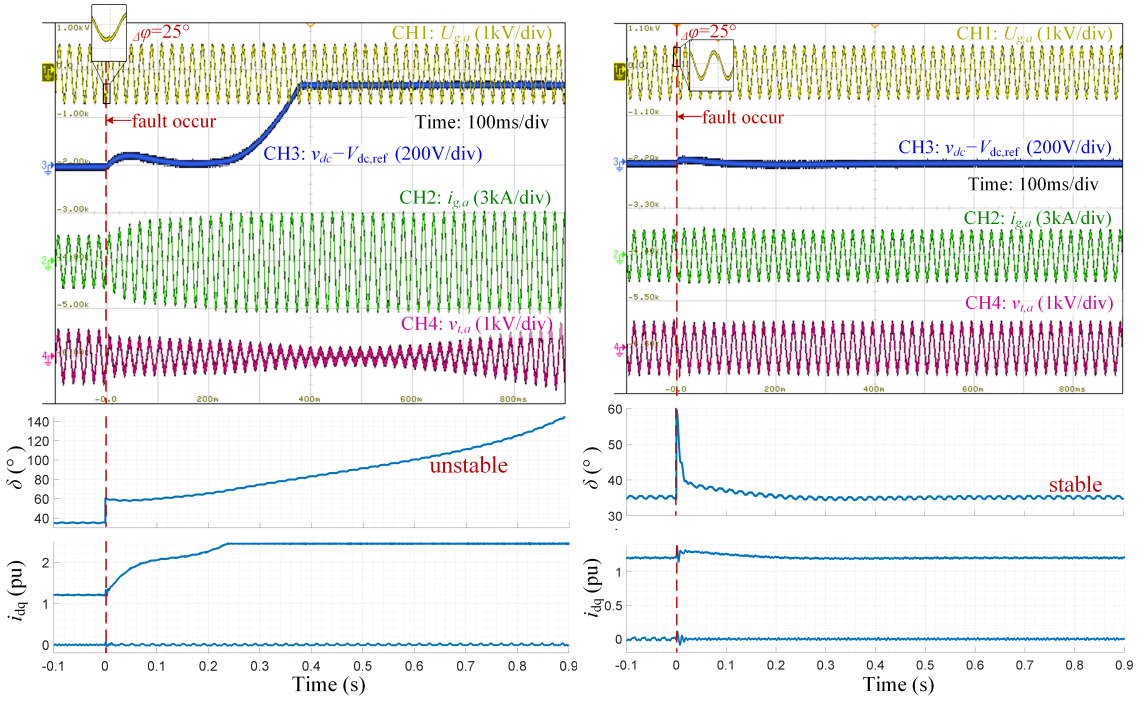


Figure 4.16: Phase portraits of phase jump fault under $\Delta\varphi$ =15, 19, 21, 25, 48 degrees. Blue trajectories: ω_{pll} = 1 Hz × 2π, ω_{dvc} = 8 Hz × 2π, no TVC; green trajectories: ω_{pll} increased to 20 Hz × 2π; orange trajectories: fast TVC is added with ω_{tvc} = 20 Hz × 2π, ω_{pll} remained at 1 Hz × 2π. The red rectangles represent the fault-occurring point.



(a) Bandwith of PLL is maintained at 1 Hz.

(b) Bandwith of PLL is increased to 20 Hz.

Figure 4.17: Time-domain results for GFL inverter under 25 degree phase jump fault with ω_{dvc} = 8 × 2π.

in Figure 4.16 as blue lines. These results align with the theoretically derived ROA of the reduced-order system under the $\omega_{dvc} \gg \omega_{pll}$ configuration.

By increasing the PLL bandwidth to 20Hz, the system can remain stable even under a 48° phase jump as shown by green trajectories in Figure 4.16. Figure 4.17 compares time-domain simulations under a 25° phase jump with ω_{pll} at 1Hz and 20Hz, respectively. In Figure 4.17 (a), due to the relatively high bandwidth of DVC, i_d rises rapidly following the phase jump in an attempt to regulate output power and DC voltage, which leads to a

subsequent increase in δ. This, in turn, further boosts i_d, eventually pushing it to its limit of 2.5 pu, thereby causing the system to destabilize. In contrast, when the PLL is faster, as shown in Figure 4.17 (b), δ is quickly adjusted by the PLL first, allowing the DVC then to follow the correct regulation. As a result, the system remains stable. Alternatively, even without modifying the PLL bandwidth, adding a fast TVC loop can expand the ROA of the DVC subsystem. However, this improvement is limited, with the UEP boundary extended only to $\delta_{\text{uep}} = 80^\circ$. In Figure 4.16, the system becomes marginally unstable for a 48° phase jump as evidenced by the orange trajectory. In comparison, simply increasing the PLL bandwidth, without TVC, significantly enlarges the stability region, theoretically extending beyond $\delta_{\text{uep}} > 90^\circ$ and approaching that of a standalone PLL system.

It is also important to note that the ability to suppress phase jump disturbances depends primarily on the relative speeds of the PLL and DVC loops. Similar stabilizing effects can be achieved by reducing the DVC bandwidth either. Overall, a relatively fast PLL loop is more effective in enhancing transient stability under phase jump conditions.

4.4.3 Input power variation

This section analyzes synchronization loss caused by large power steps. Initially, the PLL and DVC bandwidths are set to 18 Hz and 3 Hz, respectively, i.e., $\omega_{\text{pll}} \gg \omega_{\text{dvc}}$. According to the previous analysis, this configuration corresponds to the smallest ROA for the reduced-order system in the DVC state phase plane in Figure 4.18. When input power steps from 0.45 pu to 1 pu, the original SEP lies outside the new SEP's ROA, leading to transient instability illustrated by the blue trajectory in Figure 4.18. This behavior is further illustrated in the time-domain response in Figure 4.19 (a), where the GFL inverter attempts to increase i_d to maintain DC voltage. However, due to the fast PLL, the increase in δ leads to power delivery failure. Around 0.7 s, the inverter can no longer sustain 1 pu power output, resulting in rapid terminal voltage saturation and subsequent system instability. This phenomenon reflects large-signal instability, differing from small-signal cases reported in [91]. From the voltage response, the volatege is "first swing" stable but eventually unstable, and this instability mode is not captured in [94, 96].

When the PLL bandwidth is reduced to 0.4 Hz while keeping the bandwidth of DVC unchanged, the system achieves the largest ROA in the DVC state phase plane. In this configuration, the system can remain stable when the input power steps from 0.2 pu to 1 pu, as illustrated by green trajectories in Figure 4.18 and the corresponding time-domain results in Figure 4.19 (b). The relatively slower PLL alows the DVC to regulate i_d before δ significantly increases, and then the PLL slowly tracks the new SEP. Additionally, fast TVC can also increase ROA in the DVC phase plane, as seen in Figure 4.18, but the improvement is limited compared to directly reducing PLL bandwidth or increasing DVC bandwidth. Even with TVC, stability cannot be guaranteed for more severe disturbances such as inverter restarts.

After major grid faults, the grid-side inverter may shut down and later restart. During restart, the DC voltage is initially near its upper limit (e.g., 3 pu) due to the chopper

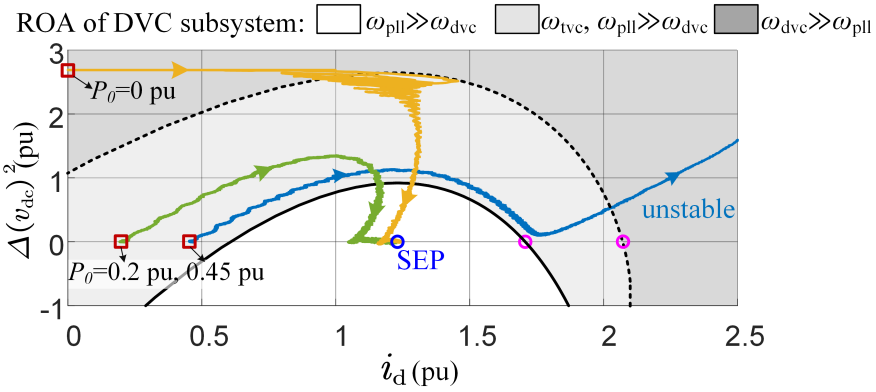
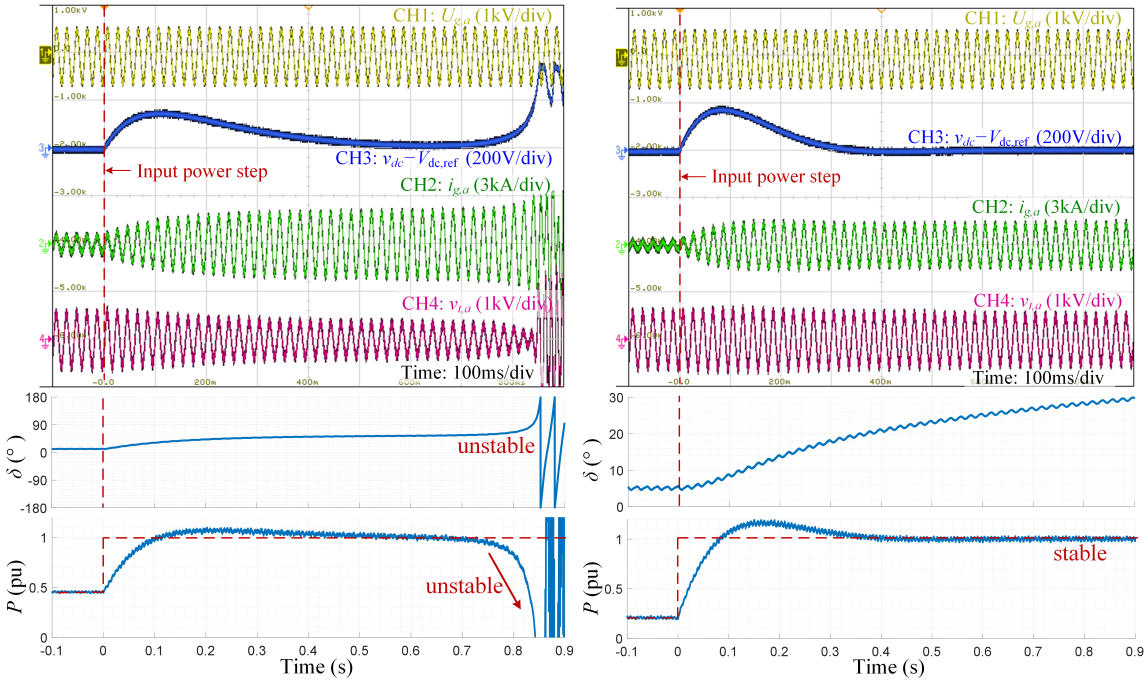


Figure 4.18: Phase portrait under input power step changes from 0, 0.2 pu, and 0.45 pu to 1 pu. Blue trajectories: $\omega_{\text{pll}} = 18$ Hz $\times 2\pi$, $\omega_{\text{dvc}} = 3$ Hz $\times 2\pi$, no TVC. Green trajectories: ω_{pll} decreased to 0.5 Hz $\times 2\pi$, ω_{dvc} unchanged, no TVC. Orange trajectories: ω_{pll} decreased to 0.5 Hz $\times$ 2π, ω_{dvc} unchanged, with fast TVC added at $\omega_{\text{tvc}} = 20$ Hz $\times 2\pi$. The red rectangles represent the initial operating point.



(a) Input power step from $P_{\text{in}} = 0.45$ pu to 1 pu with $\omega_{\text{pll}} = 18$ Hz $\times 2\pi$, $\omega_{\text{dvc}} = 3$ Hz $\times 2\pi$.

(b) Input power step from $P_{\text{in}} = 0.2$ pu to 1 pu with ω_{pll} reduced to 0.4 Hz $\times 2\pi$, while ω_{dvc} remains at 3 Hz $\times 2\pi$.

Figure 4.19: Time-domain results of the GFL inverter under input power step changes.

circuit, and the output power jumps from 0 to 1 pu. If the PLL bandwidth remains high, instability occurs even with fast TVC during restart, because the initial point lies outside the ROA of SEP. In Figure 4.18, with ω_{pll} reduced to 0.4 Hz and TVC added, the inverter trajectory (orange line) starts from $i_d = 0$, $\Delta(v_{dc})^2 = v_{\text{dc}}^2 - V_{\text{dc,ref}}^2 = 2.75$ pu and converges to SEP. The time-domain results are shown in Figure 4.20. The overall control sequence is that the PLL converges first, and then its speed slows down, after which the DVC is added to let the DC voltage move to the SEP.

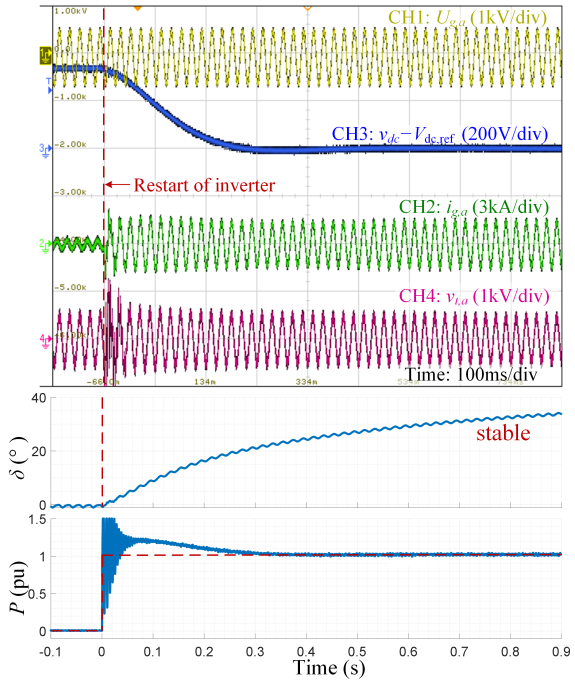


Figure 4.20: Time-domain response of the GFL inverter during restart. The output power steps from 0 to 1 pu. Control parameters: $\omega_{\text{pll}} = 0.5$ Hz $\times 2\pi$, ω_{dvc} unchanged, and fast TVC added with $\omega_{\text{tvc}} = 20$ Hz $\times 2\pi$.

4.5 Summary

This Chapter proposes a *bandwidth separation method* to analyze the transient stability of the GFL inverter, considering the interaction among three outer control loops: PLL, DVC, and TVC. By using this asymptotic analysis approach, the model order can be reduced, which provides physical insight into the nonlinear dynamics under large disturbances. The ROA for each subsystem can also be derived systematically under sufficient bandwidth separation. The analysis reveals that the interaction between PLL and DVC loops significantly degrades system stability and reduces the overall stability region. A relatively large PLL bandwidth enlarges the ROA along the PLL-state subspace but narrows the ROA in the DVC state subspace, and can induce voltage collapse through adverse interaction with i_d. Conversely, a relatively large DVC bandwidth enlarges ROA along the DVC-state subspace but narrows the ROA in the PLL state subspace. That is, there is a trade-off between phase-angle stability and dc-link stability in large-signal stability. A fast TVC loop, when configured with a higher bandwidth than the DVC, can effectively mitigate this adverse interaction between PLL and DVC, and expand the stability region in both PLL and DVC subspace.

Under voltage sag conditions, the root cause of instability is identified as voltage collapse, arising from the aforementioned adverse interaction between PLL and DVC. This mechanism highlights that GFL inverters are more vulnerable to losing stability than what conventional PLL-only analyses suggest, a factor often overlooked in prior studies. Incorporating a fast TVC loop is shown to weaken this adverse interaction and enhance the

inverter's output power capability under transient stability. Moreover, the study identifies optimal bandwidth configurations under different disturbance types. A fast PLL improves resilience to phase jumps, while a slower PLL or a faster DVC is more effective in handling power variations, restart scenarios, and voltage-sag ride-through. An adaptive PLL, which is slow in general but accelerates during a phase jump, is suggested as the best way. The addition of a fast TVC loop further improves stability by reinforcing terminal voltage regulation and alleviating the PLL–DVC adverse interaction effects.

All theoretical results are validated through HIL experiments and simulations, confirming the accuracy of the reduced models and the findings of the proposed analysis method. Even though sometimes the control loop bandwidths may not be ideally separated in all inverters, the proposed analysis method can still indicate trends in characteristics and guide the design choices of inverter control loop bandwidths.

Chapter 5

Conclusions and Future Work

5.1 Contributions and Conclusions

In terms of methodological advances, this thesis has set out the following:

1. An analysis framework combining manifold theory and model-order reduction was created to analyze multi-inverter systems containing GFL inverters. A measure named stability radius (SR), derived from this framework, is proposed for assessing the extent of the transient stability region.

2. A bandwidth separation method was proposed for GFL inverters with multiple outer control loops (PLL, DVC, TVC). By exploiting time-scale separation, reduced-order models were obtained, which provide physical insight into nonlinear dynamics under large disturbances. The ROA of each subsystem can be derived providing that sufficient bandwidth separation exists.

3. A new energy function tailored for PI controllers was designed and it enables accurate estimation of the stability region of a single GFL inverter. The energy function was generalizable to other nonlinear PI-controlled systems and was demonstrated on a DC-voltage-controlled GFM inverter.

Using the analysis tools described above approaches, the following findings have been obtained:

1. The manifold characteristics of GFL inverters strongly depends on their operating mode (that is, inverter vs. rectifier), on the line dynamics, and on individual control parameters. Inductive line dynamics introduce negative damping for inverters (leading to over-estimation of the ROA if ignored) but positive damping for rectifiers (leading to under-estimation of the ROA). Further, a rigorous proof was found that GFL rectifiers are not susceptible to limit cycles under any conditions, which stands in contrast to GFL inverters, where unstable limit cycles may occur.

2. Increasing the integral gain $k_{i,\mathrm{pll}}$ of the PLL in a GFL inverter reduces the ROA in

inverter mode; hence, an overdamped PLL design for GFL inverter is recommended.

3. In multi-inverter systems containing GFL units, global energy functions do not exist, ruling out classical direct methods of stability analysis. Manifold-based reduced-order analysis provides accurate ROA estimation with significantly lower computational cost.

4. Manifold analysis reveals new instability modes such as convergence to stable periodic orbits. GSP inverters enhance large-signal stability of companion inverters, with maximum benefit when placed at line mid-points. GFM inverters provide stronger support, though high droop gains may harm small-signal stability.

5. Bandwidth separation analysis identifies adverse PLL–DVC interaction as the main cause of voltage collapse after fault. Fast PLL bandwidth narrows the DVC-plane ROA, while fast DVC bandwidth narrows the PLL-plane ROA. That is, there is a trade-off between phase angle stability and DC-link stability.

6. A sufficiently fast TVC loop mitigates the PLL–DVC negative interaction, enlarges the ROA of both subsystems, and enhances overall transient stability.

7. Disturbance-specific bandwidth guidelines were identified: a fast PLL improves resilience to phase jumps, a slower PLL or faster DVC helps with power variations and restarts, and a fast TVC consistently reinforces voltage regulation.

All theoretical findings were validated through EMT simulations, CHIL experiments, and PHIL experiments.

5.2 Future Work

The following items of work have been identified to deepen or extend the outcomes presented in the thesis.

1. Extend the proposed analysis framework by combining manifold theory with model-order reduction in order to tackle further examples of IBR grids, including different inverter types (e.g., GFM variants and hybrid synchronization controls) and further examples of topologies (e.g., grids with SG dynamics or islanded power systems).

2. Apply the proposed PI-based energy function to multi-inverter systems composed of DC-voltage-controlled GFMs (i.e., without GFL units), finding controlling UEP or critical energy, and evaluating the accuracy of the energy function results against manifold-based ROA boundaries.

3. Apply the bandwidth separation analysis framework and reduced-order model of a GFL inverter with multi-control loops to multi-inverter systems.

4. Develop higher-order (that is, beyond first-order) singular-perturbation models to improve quantitative fidelity; this can be applied to GFM systems with line dynamics

and to GFM architectures with an outer voltage loop, so that high-bandwidth inner-loop effects are captured via the slow-state derivatives while keeping the reduced order equal to that of slow states.

5. For large-scale power systems, the proposed analysis framework can be combined with power system grouping (e.g., following practices commonly adopted in EEAC) and aggregation techniques at the system level, such that the stability analysis is performed on a reduced system representation. At the numerical level, efficient nonlinear algebraic solvers can be employed to accelerate UEP identification as the system dimension increases.

Bibliography

[1] Wolfgang Obergassel, Christof Arens, Lukas Hermwille, Nicolas Kreibich, Florian Mersmann, Hermann E. Ott, and Hanna Wang-Helmreich. *Phoenix from the Ashes — An Analysis of the Paris Agreement to the United Nations Framework Convention on Climate Change*. Tech. rep. Part I. Wuppertal Institute for Climate, Environment and Energy, 2015. URL: https://epub.wupperinst.org/frontdoor/index/index/year/2016/docId/6373.

[2] International Renewable Energy Agency (IRENA). *IRENA Data and Statistics: Renewable Capacity*. Accessed: 2025-09-03. 2024. URL: https://www.irena.org/Statistics.

[3] General Electric. *DolWin3 HVDC Voltage Source Converters for Efficient Connection of Renewable Energy*. https://www.gegridsolutions.com/products/applications/hvdc/hvdc-vsc-dolwin3-casestudy-en-2018-11-grid-pea-0578.pdf. Accessed: 2025-09-04. 2019.

[4] Siemens Energy. *We Connect Europe: Nemo Link Supplies Electricity across Borders*. https://www.siemens-energy.com/global/en/news/magazine/2020/intereuropean-hvdc-linknemolink.html. Accessed: 2025-09-04. 2020.

[5] F. Blaabjerg, R. Teodorescu, M. Liserre, and A.V. Timbus. "Overview of Control and Grid Synchronization for Distributed Power Generation Systems". In: *IEEE Transactions on Industrial Electronics* 53.5 (2006), pp. 1398–1409.

[6] Xiongfei Wang, Mads Graungaard Taul, Heng Wu, Yicheng Liao, Frede Blaabjerg, and Lennart Harnefors. "Grid-Synchronization Stability of Converter-Based Resources—An Overview". In: *IEEE Open Journal of Industry Applications* 1 (2020), pp. 115–134.

[7] Yunjie Gu, Yitong Li, Yue Zhu, and Timothy C Green. "Impedance-based whole-system modeling for a composite grid via embedding of frame dynamics". In: *IEEE Transactions on Power Systems* 36.1 (2020), pp. 336–345.

[8] Yunjie Gu and Timothy C. Green. "Power System Stability With a High Penetration of Inverter-Based Resources". In: *Proceedings of the IEEE* 111.7 (2023), pp. 832–853.

[9] Yitong Li, Yunjie Gu, and Timothy C Green. "Revisiting grid-forming and grid-following inverters: A duality theory". In: *IEEE Transactions on Power Systems* 37.6 (2022), pp. 4541–4554.

[10] Pedro Rodríguez, Josep Pou, Joan Bergas, J Ignacio Candela, Rolando P Burgos, and Dushan Boroyevich. "Decoupled double synchronous reference frame PLL for power converters control". In: *IEEE Transactions on Power Electronics* 22.2 (2007), pp. 584–592.

[11] P. Rodriguez, A. Lunar, R. Teodorescu, F. Iov, and F. Blaabjerg. "Fault ride-through capability implementation in wind turbine converters using a decoupled double synchronous reference frame PLL". In: *2007 European Conference on Power Electronics and Applications*. 2007, pp. 1–10.

[12] Sai Sowmya Nagam, Bikash C. Pal, Heng Wu, and Frede Blaabjerg. "Synchronization Stability Analysis of SRF-PLL and DSOGI-PLL Using Port-Hamiltonian Framework". In: *IEEE Transactions on Control Systems Technology* 33.3 (2025), pp. 952–962.

[13] Xiuqiang He, Changjun He, Sisi Pan, Hua Geng, and Feng Liu. "Synchronization Instability of Inverter-Based Generation During Asymmetrical Grid Faults". In: *IEEE Transactions on Power Systems* 37.2 (2022), pp. 1018–1031.

[14] Remus Teodorescu, Marco Liserre, and Pedro Rodriguez. *Grid converters for photovoltaic and wind power systems*. John Wiley & Sons, 2011.

[15] Dong Dong, Bo Wen, Dushan Boroyevich, Paolo Mattavelli, and Yaosuo Xue. "Analysis of phase-locked loop low-frequency stability in three-phase grid-connected power converters considering impedance interactions". In: *IEEE transactions on industrial electronics* 62.1 (2014), pp. 310–321.

[16] Guoxuan Cui, Zhongda Chu, and Fei Teng. "Control-mode as a grid service in software-defined power grids: Gfl vs gfm". In: *IEEE Transactions on Power Systems* 40.1 (2024), pp. 314–326.

[17] Guoxuan Cui, Hongyang Jia, Ning Zhang, and Fei Teng. "How many grid-forming converters are needed?—A techno-economic perspective". In: *iEnergy* 4.2 (2025), pp. 79–85.

[18] Sayed Ali Khajehoddin, Masoud Karimi-Ghartemani, and Mohammad Ebrahimi. "Grid-Supporting Inverters With Improved Dynamics". In: *IEEE Transactions on Industrial Electronics* 66.5 (2019), pp. 3655–3667.

[19] Yifan Zhang, Yunjie Gu, Yue Zhu, Timothy C. Green, and Hsiao-Dong Chiang. "On the Interaction in Transient Stability of Two-Inverter Power Systems containing GFL inverter Using Manifold Method". In: *arXiv* (Jan. 2025). arXiv: 2501.05994 [eess.SY]. URL: https://arxiv.org/abs/2501.05994.

[20] Prabha Kundur. "Power system stability and control". In: *New York: McGraw* (1994).

[21] Nikos Hatziargyriou, Jovica Milanovic, Claudia Rahmann, Venkataramana Ajjarapu, Claudio Canizares, Istvan Erlich, David Hill, Ian Hiskens, Innocent Kamwa, Bikash Pal, et al. "Definition and classification of power system stability–revisited & extended". In: *IEEE Transactions on Power Systems* 36.4 (2020), pp. 3271–3281.

[22] Zhenping Guo, Xiaowen Su, Kaiyang Huang, Kai Sun, Srdjan Simunovic, and Hsiao-Dong Chiang. "Efficient Simulation of Cascading Outages Using an Energy Function-Embedded Quasi-Steady-State Model". In: *IEEE Transactions on Power Systems* 40.4 (2025), pp. 2983–2993.

[23] Hisao-Dong Chiang. *Direct Methods for Stability Analysis of Electric Power Systems: Theoretical Foundation, BCU Methodologies, and Applications*. John Wiley & Sons, 2011.

[24] Australian Energy Market Commission (AEMC). *Black System South Australia: Final Report*. Tech. rep. Accessed: 2025-09-05. AEMC, 2017.

[25] North American Electric Reliability Corporation (NERC). *April and May 2018 Solar Photovoltaic Disturbance Reports*. Tech. rep. Accessed: 2025-09-05. NERC, 2018.

[26] ENTSO-E. *28 April 2025 Iberian Blackout*. https://www.entsoe.eu/publications/blackout/28-april-2025-iberian-blackout/. Accessed: 2025-09-05. 2025.

[27] Mads Graungaard Taul, Xiongfei Wang, Pooya Davari, and Frede Blaabjerg. "An Overview of Assessment Methods for Synchronization Stability of Grid-Connected Converters Under Severe Symmetrical Grid Faults". In: *IEEE Transactions on Power Electronics* 34.10 (2019), pp. 9655–9670.

[28] Xiuqiang He and Hua Geng. "PLL Synchronization Stability of Grid-Connected Multiconverter Systems". In: *IEEE Transactions on Industry Applications* 58.1 (2022), pp. 830–842.

[29] Xiuqiang He and Hua Geng. "Transient stability of power systems integrated with inverter-based generation". In: *IEEE Transactions on power systems* 36.1 (2020), pp. 553–556.

[30] Yifan Zhang, Yitong Li, Yunjie Gu, and Timothy C Green. "Consideration of Control-Loop Interaction in Transient Stability of Grid-Following Inverters using Bandwidth Separation Method". In: *2023 11th International Conference on Power Electronics and ECCE Asia (ICPE 2023-ECCE Asia)*. IEEE. 2023, pp. 1294–1301.

[31] Hassan K Khalil. *Nonlinear Systems*. USA: Prentice-Hall, 1996.

[32] Hsiao-Dong Chiang and Luís FC Alberto. *Stability Regions of Nonlinear Dynamical Systems: Theory, Estimation, and Applications*. Cambridge University Press, 2015.

[33] M. Pai and P. Murthy. "On Lyapunov functions for power systems with transfer conductances". In: *IEEE Transactions on Automatic Control* 18.2 (1973), pp. 181–183.

[34] J. Willems. "Direct method for transient stability studies in power system analysis". In: *IEEE Transactions on Automatic Control* 16.4 (1971), pp. 332–341.

[35] H.-D. Chiang. "Study of the Existence of Energy Functions for Power Systems with Losses". In: *IEEE Transactions on Circuits and Systems* 36.11 (1989), pp. 1423–1429.

[36] H.R. Pota and P.J. Moylan. "A New Lyapunov Function for Interconnected Power Systems". In: *Proceedings of the 28th IEEE Conference on Decision and Control,* 1989, 2181–2185 vol.3.

[37] Newton G Bretas and Luis FC Alberto. "Lyapunov Function for Power Systems with Transfer Conductances: Extension of the Invariance Principle". In: *IEEE Transactions on Power Systems* 18.2 (2003), pp. 769–777.

[38] H-D Chiang, Morris W Hirsch, and Felix Fulih Wu. "Stability regions of nonlinear autonomous dynamical systems". In: *IEEE Transactions on Automatic Control* 33.1 (2002), pp. 16–27.

[39] Xiuqiang He, Hua Geng, and Shaokang Ma. "Transient stability analysis of grid-tied converters considering PLL's nonlinearity". In: *CPSS Transactions on Power Electronics and Applications* 4.1 (2019), pp. 40–49.

[40] Mads Graungaard Taul, Xiongfei Wang, Pooya Davari, and Frede Blaabjerg. "An efficient reduced-order model for studying synchronization stability of grid-following converters during grid faults". In: *2019 20th Workshop on Control and Modeling for Power Electronics (COMPEL)*. IEEE. 2019, pp. 1–7.

[41] Diptak Pal and Bijaya Ketan Panigrahi. "Reduced-Order Modeling and Transient Synchronization Stability Analysis of Multiple Heterogeneous Grid-Tied Inverters". In: *IEEE Transactions on Power Delivery* 38.2 (2023), pp. 1074–1085.

[42] Qi Hu, Lijun Fu, Fan Ma, and Feng Ji. "Large Signal Synchronizing Instability of PLL-Based VSC Connected to Weak AC Grid". In: *IEEE Transactions on Power Systems* 34.4 (2019), pp. 3220–3229.

[43] Qi Zhang, Yunjie Gu, Dong Liu, Chenxu Wang, Kehu Yang, and Zhe Chen. "Transient stability of grid following inverters: The impacts of damping and fault ride-through". In: *Energy Internet* 1.2 (2024), pp. 150–165.

[44] Yujun Li, Yiyuan Lu, Yingyi Tang, and Zhengchun Du. "Conditions of existence and uniqueness of limit cycle for grid-connected VSC with PLL". In: *IEEE Transactions on Power Systems* 39.1 (2023), pp. 706–719.

[45] Yiyuan Lu, Zhengchun Du, Yujun Li, and Yumeng Zhang. "Nonlinear damping property and limit cycle of VSC". In: *IEEE Transactions on Power Delivery* 37.5 (2022), pp. 4485–4488.

[46] Jingxi Yang, K Tse Chi, Meng Huang, Dong Liu, Chao Charles Liu, and Xikun Fu. "Comparison of homoclinic bifurcations between grid-following and grid-forming converters". In: *IEEE Transactions on Industrial Electronics* 71.5 (2023), pp. 4731–4741.

[47] Rui Ma, Jinxin Li, Jürgen Kurths, Shijie Cheng, and Meng Zhan. "Generalized swing equation and transient synchronous stability with PLL-based VSC". In: *IEEE Transactions on Energy Conversion* 37.2 (2021), pp. 1428–1441.

[48] Yu Zhang, Chen Zhang, and Xu Cai. "Large-Signal Grid-Synchronization Stability Analysis of PLL-Based VSCs Using Lyapunov's Direct Method". In: *IEEE Transactions on Power Systems* 37.1 (2022), pp. 788–791.

[49] Jingxi Yang, K Tse Chi, Meng Huang, and Xikun Fu. "Homoclinic bifurcation of a grid-forming voltage source converter". In: *IEEE Transactions on Power Electronics* 36.11 (2021), pp. 13176–13187.

[50] Mads Graungaard Taul, Chao Wu, Shih-Feng Chou, and Frede Blaabjerg. "Optimal Controller Design for Transient Stability Enhancement of Grid-Following Converters Under Weak-Grid Conditions". In: *IEEE Transactions on Power Electronics* 36.9 (2021), pp. 10251–10264. ISSN: 0885-8993 1941-0107.

[51] Ziqian Yang, Rui Ma, Shijie Cheng, and Meng Zhan. "Nonlinear Modeling and Analysis of Grid-Connected Voltage-Source Converters under Voltage Dips". In: *IEEE Journal of Emerging and Selected Topics in Power Electronics* 8.4 (2020), pp. 3281–3292.

[52] Michael Dellnitz and Andreas Hohmann. "A Subdivision Algorithm for the Computation of Unstable Manifolds and Global Attractors". In: *Numerische Mathematik* 75 (1997), pp. 293–317.

[53] Heng Wu and Xiongfei Wang. "Design-Oriented Transient Stability Analysis of PLL-Synchronized Voltage-Source Converters". In: *IEEE Transactions on Power Electronics* 35.4 (2019), pp. 3573–3589.

[54] Donghua Pan, Xiongfei Wang, Fangcheng Liu, and Rongliang Shi. "Transient Stability of Voltage-Source Converters With Grid-Forming Control: A Design-Oriented Study". In: *IEEE Journal of Emerging and Selected Topics in Power Electronics* 8.2 (2020), pp. 1019–1033.

[55] Liang Zhao, Zheming Jin, and Xiongfei Wang. "Transient Stability of Grid-Forming Converters with Flexible DC-Link Voltage Control". In: *2022 International Power Electronics Conference (IPEC-Himeji 2022- ECCE Asia)*. 2022, pp. 1648–1653.

[56] Teng Liu, Xiongfei Wang, and Fangcheng Liu. "Impact of DC-link voltage control on transient stability of PLL-synchronized voltage-source converters". In: *2022 International Power Electronics Conference (IPEC-Himeji 2022-ECCE Asia)*. IEEE. 2022, pp. 435–439.

[57] Zhen Tian, Yingjie Tang, Xiaoming Zha, Jianjun Sun, Meng Huang, Xikun Fu, and Fei Liu. "Hamilton-Based Stability Criterion and Attraction Region Estimation for Grid-Tied Inverters Under Large-Signal Disturbances". In: *IEEE Journal of Emerging and Selected Topics in Power Electronics* 10.1 (2022), pp. 413–423.

[58] Xikun Fu, Jianjun Sun, Meng Huang, Zhen Tian, Han Yan, Herbert Ho-Ching Iu, Pan Hu, and Xiaoming Zha. "Large-signal stability of grid-forming and grid-following controls in voltage source converter: A comparative study". In: *IEEE Transactions on Power Electronics* 36.7 (2020), pp. 7832–7840.

[59] Diptak Pal, Bijaya Ketan Panigrahi, Brian Johnson, D. Venkatramanan, and Sairaj Dhople. "Large-signal Stability Analysis of Three-phase Grid-following Inverters". In: *IEEE Transactions on Energy Conversion* (2023), pp. 1–15.

[60] Milad Zarif Mansour, Si Phu Me, Sajjad Hadavi, Babak Badrzadeh, Alireza Karimi, and Behrooz Bahrani. "Nonlinear Transient Stability Analysis of Phased-Locked Loop-Based

Grid-Following Voltage-Source Converters Using Lyapunov's Direct Method". In: *IEEE Journal of Emerging and Selected Topics in Power Electronics* 10.3 (2022), pp. 2699–2709.

[61] Xikun Fu, Meng Huang, Chi K. Tse, Jingxi Yang, Yangjian Ling, and Xiaoming Zha. "Synchronization Stability of Grid-Following VSC Considering Interactions of Inner Current Loop and Parallel-Connected Converters". In: *IEEE Transactions on Smart Grid* 14.6 (2023), pp. 4230–4241.

[62] Luís Fernando Costa Alberto, Daniel S. Siqueira, Newton Geraldo Bretas, and Hsiao-Dong Chiang. "Generalized Energy Functions for a Class of Third-Order Nonlinear Dynamical Systems". In: *IEEE Transactions on Automatic Control* 66.7 (2021), pp. 3111–3122.

[63] Nathan Baeckeland, Diptak Pal, Gab-Su Seo, Brian Johnson, and Sairaj Dhople. "Large-Signal Stability Analysis of Grid-Forming Inverters With Equivalent-Circuit Models". In: *IEEE Transactions on Energy Conversion* 40.3 (2025), pp. 2453–2465.

[64] P. Magne, D. Marx, B. Nahid-Mobarakeh, and S. Pierfederici. "Large-Signal Stabilization of a DC-Link Supplying a Constant Power Load Using a Virtual Capacitor: Impact on the Domain of Attraction". In: *IEEE Transactions on Industry Applications* 48.3 (2012), pp. 878–887.

[65] X. Li et al. "The Largest Estimated Domain of Attraction and its Applications for Transient Stability Analysis of PLL Synchronization in Weak-Grid-Connected VSCs". In: *IEEE Transactions on Power Systems* (2022), pp. 1–14.

[66] Yawen Ding, Fei Gao, and Muhammad Mansoor Khan. "Transient Stability Analysis of Microgrid Considering Impact of Grid-Following Converter's Current Controller". In: *IEEE Transactions on Power Electronics* 39.8 (2024), pp. 9100–9106.

[67] Zachary William Jarvis-Wloszek. *Lyapunov based analysis and controller synthesis for polynomial systems using sum-of-squares optimization.* University of California, Berkeley, 2003.

[68] Chen Zhang, Marta Molinas, Zheng Li, and Xu Cai. "Synchronizing Stability Analysis and Region of Attraction Estimation of Grid-Feeding VSCs Using Sum-of-Squares Programming". In: *Frontiers in Energy Research* 8 (2020), p. 56.

[69] M. Anghel, F. Milano, and A. Papachristodoulou. "Algorithmic Construction of Lyapunov Functions for Power System Stability Analysis". In: *IEEE Transactions on Circuits and Systems I: Regular Papers* 60.9 (2013), pp. 2533–2546.

[70] Ziqian Zhang, Robert Schuerhuber, Lothar Fickert, Katrin Friedl, Guochu Chen, and Yongming Zhang. "Domain of Attraction's Estimation for Grid Connected Converters With Phase-Locked Loop". In: *IEEE Transactions on Power Systems* 37.2 (2022), pp. 1351–1362.

[71] Jintao Lei, Xin Xiang, Boxin Liu, Wuhua Li, and Xiangning He. "Transient Stability Analysis of Grid Forming Converters Based on Damping Energy Visualization and Geometry Approximation". In: *IEEE Transactions on Industrial Electronics* 71.3 (2024), pp. 2510–2521.

[72] Qiannan Qu, Xin Xiang, Kai Xin, Yunfeng Liu, Wuhua Li, and Xiangning He. "Transient Stability Analysis of Hybrid GFL-GFM System Considering Various Damping Effects". In: *IEEE Transactions on Industrial Electronics* (2025).

[73] Jintao Lei, Xin Xiang, Qiannan Qu, Wuhua Li, and Xiangning He. "The Analysis and Calculation of Power Angle Transient Characteristics in VSG Control using Parameter-perturbation-based Averaging Method". In: *IEEE Transactions on Industrial Electronics* (2022). Early Access, pp. 1–13.

[74] Jiantao Zhao, Meng Huang, Han Yan, Chi K. Tse, and Xiaoming Zha. "Nonlinear and Transient Stability Analysis of Phase-Locked Loops in Grid-Connected Converters". In: *IEEE Transactions on Power Electronics* 36.1 (2021), pp. 1018–1029.

[75] Rui Ma, Meng Zhan, Kezheng Jiang, Dan Liu, Pan Hu, and Shijie Cheng. "Transient Stability Assessment of Renewable Dominated Power Systems by the Method of Hyperplanes". In: *IEEE Transactions on Power Delivery* 38.5 (2023), pp. 3455–3468.

[76] Rui Ma and Meng Zhan. "Transient Stability Assessment and Dynamic Security Region in Power Electronics Dominated Power Systems". In: *2022 IEEE International Conference on Power Systems Technology (POWERCON)*. IEEE. 2022, pp. 1–6.

[77] Yusheng Xue, Thierry Van Custem, and Mania Ribbens-Pavella. "Extended Equal Area Criterion Justifications, Generalizations, Applications". In: *IEEE Transactions on Power Systems* 4.1 (1989), pp. 44–52.

[78] Mania Pavella, Damien Ernst, and Daniel Ruiz-Vega. *Transient stability of power systems: a unified approach to assessment and control*. Springer Science & Business Media, 2012.

[79] Minghui Yin, CY Chung, KP Wong, Yusheng Xue, and Yun Zou. "An improved iterative method for assessment of multi-swing transient stability limit". In: *IEEE Transactions on Power Systems* 26.4 (2011), pp. 2023–2030.

[80] Junru Chen, Muyang Liu, Hua Geng, Terence O'Donnell, and Federico Milano. "Impact of PLL frequency limiter on synchronization stability of grid feeding converter". In: *IEEE Transactions on Power Systems* 37.3 (2022), pp. 2487–2490.

[81] Tianhao Wu, Qirong Jiang, Meng Huang, and Xiaorong Xie. "Synchronization Stability of Grid-Following Converters Governed by Saturation Nonlinearities". In: *IEEE Transactions on Power Systems* 37.5 (2022), pp. 4102–4106.

[82] Xinshuo Wang, Heng Wu, and Xiongfei Wang. "Transient Overvoltage Analysis of Grid-Following VSCs during Fault Recovery". In: *2023 11th International Conference on Power Electronics and ECCE Asia (ICPE 2023-ECCE Asia)*. IEEE. 2023, pp. 2404–2409.

[83] Xilin Li, Pan Feng, Ruiqi Zhang, Zhen Tian, Meng Huang, Xiaoming Zha, Xiaoling Xiong, and Pan Hu. "Transient Stability Evaluation and Decoupled Control for Grid-Following Converters Considering Nonideal Alternating Current Control". In: *IEEE Transactions on Power Electronics* 40.7 (2025), pp. 8990–9005.

[84] Qi Hu, Lijun Fu, Fan Ma, Feng Ji, and Yan Zhang. "Analogized Synchronous-Generator Model of PLL-Based VSC and Transient Synchronizing Stability of Converter Dominated Power System". In: *IEEE Transactions on Sustainable Energy* 12.2 (2021), pp. 1174–1185.

[85] Yumei Ma, Donghai Zhu, Ziqin Zhang, Xudong Zou, Jiabing Hu, and Yong Kang. "Modeling and Transient Stability Analysis for Type-3 Wind Turbines Using Singular Perturbation and Lyapunov Methods". In: *IEEE Transactions on Industrial Electronics* 70.8 (2023), pp. 8075–8086.

[86] Junru Chen, Muyang Liu, Terence O'Donnell, and Federico Milano. "Impact of Current Transients on the Synchronization Stability Assessment of Grid-Feeding Converters". In: *IEEE Transactions on Power Systems* 35.5 (2020), pp. 4131–4134.

[87] Liang Zhao and Xiongfei Wang. "Transient Performance of Grid-Forming VSCs with High-Switching-Frequency Power Devices". In: *2024 IEEE Energy Conversion Congress and Exposition (ECCE)*. IEEE. 2024, pp. 1491–1497.

[88] Yifan Zhang, Chushan Li, Chengmin Li, Zhen Xin, Runtian Chen, Wuhua Li, Xiangning He, and Hao Ma. "A SiC and Si Hybrid Five-Level Unidirectional Rectifier for Medium Voltage Applications". In: *IEEE Transactions on Industrial Electronics* 69.8 (2022), pp. 7537–7548.

[89] Pian Zhou, Xiaoming Yuan, Jiabing Hu, and Yunhui Huang. "Stability of DC-link voltage as affected by phase locked loop in VSC when attached to weak grid". In: *2014 IEEE PES General Meeting| Conference & Exposition*. IEEE. 2014, pp. 1–5.

[90] Yunhui Huang and Dong Wang. "Effect of control-loops interactions on power stability limits of VSC integrated to AC system". In: *IEEE Transactions on Power Delivery* 33.1 (2017), pp. 301–310.

[91] Guanglu Wu, Bing Zhao, Xi Zhang, Shanshan Wang, Agusti Egea-Alvarez, Yuanyuan Sun, Yingbiao Li, Deyang Guo, and Xiaoxin Zhou. "Impact of non-minimum-phase zeros on the weak-grid-tied VSC". In: *IEEE Transactions on Sustainable Energy* 12.2 (2020), pp. 1115–1126.

[92] Diptak Pal and Bijaya Ketan Panigrahi. "Impact of DC-Bus Voltage Control on Synchronization Stability of Grid-Tied Inverters". In: *IEEE Transactions on Circuits and Systems II: Express Briefs* 69.6 (2022), pp. 2782–2786. ISSN: 1549-7747 1558-3791.

[93] Yangjian Ling, Meng Huang, Xiaoming Zha, Weibing Li, Dingguo Jiang, and Junxian Li. "Transient Stability Analysis of Grid-Connected Converter with Considering DC-Link Dynamics". In: *2024 CPSS & IEEE International Symposium on Energy Storage and Conversion (ISESC)*. 2024, pp. 786–792.

[94] Indla Rajitha Sai Priyamvada and Sarasij Das. "Online assessment of transient stability of grid connected PV generator with DC link voltage and reactive power control". In: *IEEE Access* 8 (2020), pp. 220606–220619.

[95] Yumei Ma, Donghai Zhu, Jiabing Hu, Dan Liu, Xiaotong Ji, Xudong Zou, and Yong Kang. "Reduced-order modeling and transient stability analysis of grid-connected VSC in DC-link voltage control timescale". In: *IEEE Journal of Emerging and Selected Topics in Power Electronics* 12.3 (2024), pp. 2981–2993.

[96] Zhanqi Huang, Chao Wu, Yong Wang, and Shiyang Li. "Transient Stability Analysis and Enhancement of Grid-Following Converters Considering DC Voltage Dynamics Under Power Step". In: *2024 IEEE 10th International Power Electronics and Motion Control Conference (IPEMC2024-ECCE Asia)*. 2024, pp. 2401–2405.

[97] Bo Wen, Dushan Boroyevich, Rolando Burgos, Paolo Mattavelli, and Zhiyu Shen. "Analysis of DQ small-signal impedance of grid-tied inverters". In: *IEEE Transactions on Power Electronics* 31.1 (2015), pp. 675–687.

[98] Ömer Göksu, Remus Teodorescu, Claus Leth Bak, Florin Iov, and Philip Carne Kjær. "Instability of wind turbine converters during current injection to low voltage grid faults and PLL frequency based stability solution". In: *IEEE Transactions on Power Systems* 29.4 (2014), pp. 1683–1691.

[99] Hua Geng, Lu Liu, and Ruiqi Li. "Synchronization and reactive current support of PMSG-based wind farm during severe grid fault". In: *IEEE Transactions on Sustainable Energy* 9.4 (2018), pp. 1596–1604.

[100] Istvan Erlich, Fekadu Shewarega, Stephan Engelhardt, Jorg Kretschmann, Jens Fortmann, and Friedrich Koch. "Effect of wind turbine output current during faults on grid voltage and the transient stability of wind parks". In: *2009 IEEE Power & Energy Society General Meeting*. IEEE. 2009, pp. 1–8.

[101] Bernd Weise. "Impact of K-factor and active current reduction during fault-ride-through of generating units connected via voltage-sourced converters on power system stability". In: *IET Renewable Power Generation* 9.1 (2015), pp. 25–36.

[102] Mads Graungaard Taul, Xiongfei Wang, Pooya Davari, and Frede Blaabjerg. "Robust fault ride through of converter-based generation during severe faults with phase jumps". In: *IEEE Transactions on Industry Applications* 56.1 (2019), pp. 570–583.

[103] Junru Chen, Wenjia Si, Muyang Liu, and Federico Milano. "On the Impact of the Grid on the Synchronization Stability of Grid-Following Converters". In: *IEEE Transactions on Power Systems* 38.5 (2023), pp. 4970–4973.

[104] M. G. Taul, X. Wang, P. Davari, and F. Blaabjerg. "Systematic Approach for Transient Stability Evaluation of Grid-Tied Converters During Power System Faults". In: *Proc. IEEE Energy Conversion Congress and Exposition (ECCE)*. 2019, pp. 5191–5198.

[105] H. Wu and X. Wang. "Transient Stability Impact of the Phase-Locked Loop on Grid-Connected Voltage Source Converters". In: *Proc. International Power Electronics Conference (IPEC)*. 2018, pp. 2673–2680.

[106] H. Wu and X. Wang. "An Adaptive Phase-Locked Loop for the Transient Stability Enhancement of Grid-Connected Voltage Source Converters". In: *Proc. IEEE Energy Conversion Congress and Exposition (ECCE)*. 2018, pp. 5892–5898.

[107] H. Wu and X. Wang. "Transient Angle Stability Analysis of Grid-Connected Converters with the First-Order Active Power Loop". In: *Proc. IEEE Applied Power Electronics Conference and Exposition (APEC)*. 2018, pp. 3011–3016.

[108] Xiuqiang He, Hua Geng, Jiangbei Xi, and Josep M. Guerrero. "Resynchronization Analysis and Improvement of Grid-Connected VSCs During Grid Faults". In: *IEEE Journal of Emerging and Selected Topics in Power Electronics* 9.1 (2021), pp. 438–450.

[109] Yushuang Liu, Hua Geng, Changjun He, Wenze Ding, Chen Shen, and Geng Yang. "Equivalent Aggregated Modeling of Multi-VSC System for Transient Synchronization Stability Analysis". In: *IEEE Transactions on Power Systems* 39.2 (2024), pp. 4296–4310.

[110] Chenhang Xu, Zhixiang Zou, Jiajun Yang, Zheng Wang, Wu Chen, and Giampaolo Buticchi. "Transient Stability Analysis and Enhancement of Grid-Forming and Grid-Following Converters". In: *IEEE Journal of Emerging and Selected Topics in Industrial Electronics* 5.4 (Oct. 2024), pp. 1396–1407.

[111] Mads Graungaard Taul, Xiongfei Wang, Pooya Davari, and Frede Blaabjerg. "Reduced-Order and Aggregated Modeling of Large-Signal Synchronization Stability for Multiconverter Systems". In: *IEEE Journal of Emerging and Selected Topics in Power Electronics* 9.3 (2021), pp. 3150–3165.

[112] Xikun Fu, Meng Huang, Shangzhi Pan, and Xiaoming Zha. "Cascading Synchronization Instability in Multi-VSC Grid-Connected System". In: *IEEE Transactions on Power Electronics* 37.7 (2022), pp. 7572–7576.

[113] Xiangtong Yi, Yelun Peng, Quan Zhou, Wen Huang, Lijia Xu, Z John Shen, and Zhikang Shuai. "Transient Synchronization Stability Analysis and Enhancement of Paralleled Converters Considering Different Current Injection Strategies". In: *IEEE Transactions on Sustainable Energy* 13.4 (2022), pp. 1957–1968.

[114] Yukun Wang, Donghai Zhu, Yihang Yang, Xudong Zou, Jiabing Hu, and Yong Kang. "Fixed Angle Difference Control for Multi-Converter Grid-Connected System to Improve Transient Stability During Grid Faults". In: *2023 IEEE 6th International Electrical and Energy Conference (CIEEC)*. IEEE. 2023, pp. 4351–4356.

[115] K. Jia, Z. Li, X. Zhang, Y. Xu, J. Fang, and Z. Xu. "Synchronization stability analysis of multi-VSG systems: A perturbation perspective". In: *CSEE Journal of Power and Energy Systems* 9.5 (2023), pp. 1479–1490.

[116] Y. Wang, C. Li, L. Huang, and X. Wang. "Nonlinear Modeling and Stability Analysis of Grid-Forming Inverters Considering Coupling Dynamics". In: *IEEE Transactions on Power Electronics* 38.7 (2023), pp. 8193–8207.

[117] Jiantao Zhao, Meng Huang, and Xiaoming Zha. "Transient Stability Analysis of Grid-Connected VSIs via PLL Interaction". In: *2018 IEEE International Power Electronics and Application Conference and Exposition (PEAC)*. IEEE. 2018, pp. 1–6.

[118] Yicheng Xue, Zheren Zhang, Nan Zhang, Wen Hua, Guoteng Wang, and Zheng Xu. "Transient Stability Analysis and Enhancement Control Strategies for Interconnected AC Sys-

tems with VSC-Based Generations". In: *International Journal of Electrical Power & Energy Systems* 149 (2023), p. 109017.

[119] Huijie Cheng, Wen Huang, Chao Shen, Yelun Peng, Zhikang Shuai, and Z. John Shen. "Transient Voltage Stability of Paralleled Synchronous and Virtual Synchronous Generators With Induction Motor Loads". In: *IEEE Transactions on Smart Grid* 12.6 (2021), pp. 4983–4999.

[120] Zhen Tian, Xilin Li, Xiaoming Zha, Yingjie Tang, Pengfei Sun, Meng Huang, and Pan Yu. "Transient synchronization stability of an islanded AC microgrid considering interactions between grid-forming and grid-following converters". In: *IEEE Journal of Emerging and Selected Topics in Power Electronics* 11.4 (2023), pp. 4463–4476.

[121] Yingjie Tang, Zhen Tian, Xiaoming Zha, Xilin Li, Meng Huang, and Jianjun Sun. "An Improved Equal Area Criterion for Transient Stability Analysis of Converter-Based Microgrid Considering Nonlinear Damping Effect". In: *IEEE Transactions on Power Electronics* 37.9 (Sept. 2022), pp. 11272–11284.

[122] Changjun He, Xiuqiang He, Hua Geng, Huadong Sun, and Shiyun Xu. "Transient Stability of Low-Inertia Power Systems With Inverter-Based Generation". In: *IEEE Transactions on Energy Conversion* 37.4 (Dec. 2022), pp. 2903–2912.

[123] Cong Luo, Yandong Chen, Mingkun Gao, Yingying Zhang, and Shuhan Liao. "Transient Stability Analysis of Parallel Grid-Tied Grid-Forming Inverters". In: *International Conference of Electrical, Electronic and Networked Energy Systems*. Springer. 2024, pp. 434–442.

[124] Young-Hyun Moon, Byoung-Kon Choi, and Tae-Hoon Roh. "Estimating the domain of attraction for power systems via a group of damping-reflected energy functions". In: *Automatica* 36.3 (2000), pp. 419–425.

[125] Qiannan Qu, Xin Xiang, Jintao Lei, Wuhua Li, and Xiangning He. "Transient Stability Analysis for Paralleled System of Virtual Synchronous Generators Based on Damping Energy Visualization and Approximation". In: *IEEE Transactions on Power Electronics* 39.12 (2024), pp. 15785–15799.

[126] Cong Luo, Shuhan Liao, Yandong Chen, and Meng Huang. "Quantitative Transient Stability Analysis for Parallel Grid-Tied Grid-Forming Inverters Considering Reactive Power Control". In: *IEEE Transactions on Power Electronics* 40.4 (2025), pp. 4780–4786.

[127] Xiuqiang He, Sisi Pan, and Hua Geng. "Transient Stability of Hybrid Power Systems Dominated by Different Types of Grid-Forming Devices". In: *IEEE Transactions on Energy Conversion* 37.2 (2022), pp. 868–879.

[128] Debjyoti Chatterjee, Bowen Yang, Brian Johnson, and Gab-Su Seo. "Interaction Energy-Based Transient Stability Framework for Multi-Grid-Forming Inverter Systems". In: *2025 IEEE Energy Conversion Conference Congress and Exposition (ECCE)*. 2025, pp. 1–8.

[129] Hang Zhang, Yan Xu, and Zhaoyang Dong. "Impact Study of Virtual Synchronous Generators on Power System Transient Stability". In: *2024 IEEE Power & Energy Society General Meeting (PESGM)*. IEEE. 2024, pp. 1–5.

[130] Jose Daniel Lara, Rodrigo Henriquez-Auba, Deepak Ramasubramanian, Sairaj Dhople, Duncan S Callaway, and Seth Sanders. "Revisiting power systems time-domain simulation methods and models". In: *IEEE Transactions on Power systems* 39.2 (2023), pp. 2421–2437.

[131] D Venkatramanan and Vinod John. "Dynamic phasor modeling of SRF-PLL based grid-tie inverter under islanded conditions". In: *2018 IEEE Energy Conversion Congress and Exposition (ECCE)*. IEEE. 2018, pp. 5670–5676.

[132] Donald R Smith. *Singular-perturbation theory: an introduction with applications*. Cambridge University Press, 1985.

[133] RE O'Malley Jr. "On nonlinear singularly perturbed initial value problems". In: *SIAM review* 30.2 (1988), pp. 193–212.

[134] Yifan Zhang, Y. Li, Yunjie Gu, A. Cheng, and Timothy C. Green. "Manifold Property of GFL Converter: Impact of Modelling and Operating Condition". In: *Smart Power & Energy Security* (2025). Accepted for publication; in press.

[135] Yiyuan Lu, Zhengchun Du, Yujun Li, and Yumeng Zhang. "Nonlinear Damping Property and Limit Cycle of VSC". In: *IEEE Transactions on Power Delivery* 37.5 (2022), pp. 4485–4488.

[136] Cheng Ai, Yitong Li, Ziwen Zhao, Yunjie Gu, and Jinjun Liu. "An Extension of Grid-Forming: A Frequency-Following Voltage-Forming Inverter". In: *IEEE Transactions on Power Electronics* 39.10 (2024), pp. 12118–12123.

[137] Liang Zhao, Zheming Jin, and Xiongfei Wang. "Small-Signal Synchronization Stability of Grid-Forming Converters With Regulated DC-Link Dynamics". In: *IEEE Transactions on Industrial Electronics* 70.12 (2023), pp. 12399–12409.

[138] Jinming Xu, Zihan Ling, Hanxu Diao, and Shaojun Xie. "Transient Stability Analysis and Damping Control of Grid-Following Inverters Considering DC-Link Voltage Control and Its Output Limit". In: *IEEE Transactions on Industrial Electronics* (2025).

[139] Teng Liu and Xiongfei Wang. "Physical insight into hybrid-synchronization-controlled grid-forming inverters under large disturbances". In: *IEEE Transactions on Power Electronics* 37.10 (2022), pp. 11475–11480.

[140] EON Netz. "Grid Code—High and Extra High Voltage. E. ON Netz GmbH". In: *Tech. Rep* (2006).

[141] ShaoKang Ma, Hua Geng, Lu Liu, Geng Yang, and Bikash C Pal. "Grid-synchronization stability improvement of large scale wind farm during severe grid fault". In: *IEEE Transactions on Power Systems* 33.1 (2017), pp. 216–226.

[142] UK NationalGrid. *Performance of phase-locked loop based converters*. Tech. rep. tech. rep, 2017. URL: https://www.neso.energy/document/102876/download.

[143] Yunjie Gu, Nathaniel Bottrell, and Timothy C. Green. "Reduced-Order Models for Representing Converters in Power System Studies". In: *IEEE Transactions on Power Electronics* 33.4 (2018), pp. 3644–3654.

[144] Yitong Li and Yunjie Gu. "Whole-System First-Swing Stability of Inverter-Based Inertia-Free Power Systems". In: *arXiv preprint arXiv:2207.03292* (2022).

[145] Chen Zhao, Dan Sun, Heng Nian, and Yue Fan. "Reactive Power Compensation Control of PV Systems for Improved Power Transfer Capability in Weak Grid". In: *2020 12th IEEE PES Asia-Pacific Power and Energy Engineering Conference (APPEEC)*. IEEE. 2020, pp. 1–5.

[146] [Online]. Available: https://github.com/Future-Power-Networks/Publications/tree/v1.0-paper-snapshot/LargeSignal. Version v1.0-paper-snapshot.

[147] Romeo Ortega, Martha Galaz, Alessandro Astolfi, Yuanzhang Sun, and Tielong Shen. "Transient stabilization of multimachine power systems with nontrivial transfer conductances". In: *IEEE Transactions on Automatic Control* 50.1 (2005), pp. 60–75.

[148] Chao Shen, Zhikang Shuai, Yang Shen, Yelun Peng, Xuan Liu, Zuyi Li, and Z John Shen. "Transient Stability and Current Injection Design of Paralleled Current-Controlled VSCs and Virtual Synchronous Generators". In: *IEEE Transactions on Smart Grid* 12.2 (2020), pp. 1118–1134.

[149] J. Zaborszky, G. Huang, B. Zheng, and T.-C. Leung. "On the Phase Portrait of a Class of Large Nonlinear Dynamic Systems Such as the Power System". In: *IEEE Transactions on Automatic Control* 33.1 (1988), pp. 4–15.

[150] Yu Fang, Ke Jia, Zhe Yang, Yanbin Li, and Tianshu Bi. "Impact of Inverter-Interfaced Renewable Energy Generators on Distance Protection and an Improved Scheme". In: *IEEE Transactions on Industrial Electronics* 66.9 (2019), pp. 7078–7088. ISSN: 0278-0046 1557-9948.

[151] Juan Carlos Quispe H, Héctor Villarroel-Gutiérrez, and Eduardo Orduña. "Analyzing Short-Circuit Current Behavior Caused by Inverter-Interfaced Renewable Energy Sources. Effects on Distance Protection". In: *2020 IEEE PES Transmission & Distribution Conference and Exhibition - Latin America (T & D LA)*. 2020, pp. 1–6.

[152] John Michael Tutill Thompson, H Bruce Stewart, and Rick Turner. "Nonlinear Dynamics and Chaos". In: *Computers in Physics* 4.5 (1990), pp. 562–563.

[153] Yuri A Kuznetsov, Iu A Kuznetsov, and Y Kuznetsov. *Elements of Applied Bifurcation Theory*. Vol. 112. Springer, 1998.

[154] InsRealm Technology Co., Ltd. *Official website*. Accessed: Sep. 17, 2025. 2025. URL: https://www.insrealm.co.uk/.

[155] Guoqing Gao, Frede Blaabjerg, and Yanbo Wang. "Multi-time Scale Fault Characteristics of HVDC-Connected Offshore Wind Farm and the Coordination with Different Protection Schemes: A Review". In: *2023 25th European Conference on Power Electronics and Applications (EPE'23 ECCE Europe)*. IEEE. 2023, pp. 1–11.

[156] Siemens AG. *Energy Sector: User Manual Distance Protection 7SA522 V4.61*. C53000-G1176-C155-5. Online. Siemens AG. 2019. URL: http://www.siprotec.com.

[157] Linbin Huang, Huanhai Xin, Zhiyi Li, Ping Ju, Hui Yuan, Zhou Lan, and Zhen Wang. "Grid-Synchronization Stability Analysis and Loop Shaping for PLL-Based Power Converters With Different Reactive Power Control". In: *IEEE Transactions on Smart Grid* 11.1 (2020), pp. 501–516.

[158] T Tenne. "Requirements for offshore grid connections in the grid of TenneT TSO GmbH". In: *Arnhem, Netherlands* (2012).

[159] Christian Kuehn and Christian Kuehn. "Chaos in Fast-Slow Systems". In: *Multiple Time Scale Dynamics* (2015), pp. 431–475.

[160] Jiantao Zhao, Meng Huang, Han Yan, Chi K Tse, and Xiaoming Zha. "Nonlinear and transient stability analysis of phase-locked loops in grid-connected converters". In: *IEEE Transactions on Power Electronics* 36.1 (2020), pp. 1018–1029.

[161] [Online]. Available: https://github.com/Future-Power-Networks/Publications/tree/v1.0-paper-snapshot/BandwidthSeperation. Version v1.0-paper-snapshot.

Appendix A

Appendix for Chapter 3

A.1 Derivation for Two-Inverter Systems

A.1.1 Both IBRs are GFM inverters

When both the two IBRs in Figure 3.2 are GFM inverters, the nonlinear differential equations describing the system are as follows:

$$\begin{cases} \dot{\delta}_1 = k_{gfm1}[P_{1ref} - \frac{V_1 V_2 \sin(\delta_1 - \delta_2)}{X_{\Delta 12}} - \frac{V_1 U_g}{X_{\Delta g1}} \sin \delta_1] \\ \dot{\delta}_2 = k_{gfm1}[P_{2ref} - \frac{V_1 V_2 \sin(\delta_2 - \delta_1)}{X_{\Delta 12}} - \frac{V_2 U_g}{X_{\Delta g2}} \sin \delta_2] \end{cases} \tag{A.1}$$

The expression of $X_{\Delta 12}$, $X_{\Delta g1}$, $X_{\Delta g2}$ is as follows:

$$\begin{aligned} X_{\Delta 12} &= \frac{X_1 X_2 + X_1 X_g + X_2 X_g}{X_g}, \\ X_{\Delta g1} &= \frac{X_1 X_2 + X_1 X_g + X_2 X_g}{X_2}, \\ X_{\Delta g2} &= \frac{X_1 X_2 + X_1 X_g + X_2 X_g}{X_1}. \end{aligned} \tag{A.2}$$

In (A.1), δ_1, δ_2, and P_{1ref}, P_{2ref} represent the power angles, and the power references of the two GFM inverters respectively. V_1 and V_2 are the voltages of two GFM inverters.

A.1.2 Both IBRs are GFL inverters

When both the two IBRs in Figure 3.2 are GFL inverters, the nonlinear differential equations describing the system are as follows:

$$\begin{cases} \dot{\delta}_1 = k_{\text{pll1}} \left[X_{1sum} I_{1d} + X_g I_{2d} \cos(\delta_2 - \delta_1) - U_g \sin \delta_1 \right] \\ \dot{\delta}_2 = k_{\text{pll2}} \left[X_{2sum} I_{2d} + X_g I_{1d} \cos(\delta_1 - \delta_2) - U_g \sin \delta_2 \right] \end{cases} \tag{A.3}$$

The expression of X_{1sum}, X_{2sum} are

$$X_{\Sigma 1} = X_1 + X_g,\ X_{\Sigma 2} = X_2 + X_g$$

In (A.3), δ_1, δ_2, and I_{1d}, I_{2d} represent the angles of PLL, and the current references on d-axis of the two GFL inverters respectively.

A.1.3 Combination of a GFL and GFM inverter

When IBR1 is the GFL inverter and IBR2 is the GFM inverter in Figure 3.2, the nonlinear differential equations describing the system can be expressed in (A.4)

$$\begin{cases} \dot{\delta}_1 = k_{\text{pll}} \left[X_{1+2//g} I_{1d} - \dfrac{X_g}{X_{2sum}} V_2 \sin(\delta_1 - \delta_2) - \dfrac{X_2}{X_{2sum}} U_g \sin \delta_1 \right] \\ \dot{\delta}_2 = k_{\text{droop}} \left[P_{ref} + \dfrac{X_g I_{1d}}{X_{2sum}} V_2 \cos(\delta_1 - \delta_2) - \dfrac{U_g V_2}{X_{2sum}} \sin \delta_2 \right] \end{cases} \tag{A.4}$$

where $X_{1+2//g}$ and $X_{2+1//g}$ are defined as

$$X_{1+2//g} = X_1 + \frac{X_g X_2}{X_{\Sigma 2}}, \; X_{2+1//g} = X_1 + \frac{X_g X_1}{X_{\Sigma 1}}$$

A.1.4 Combination of a GFL and GSP inverter

When IBR1 is the GFL inverter and IBR2 is the GSP inverter in Figure 3.2, the nonlinear differential equations describing the system can be expressed jointly by (A.5) and (A.6).

$$\begin{cases} \dot{\delta}_1 = k_{\text{pll1}} \left[X_{\Sigma 1} I_{1d} - U_g \sin \delta_1 + X_g I_{2d} \cos(\delta_2 - \delta_1) - X_g I_{2q} \sin(\delta_2 - \delta_1) \right] \\ \dot{\delta}_2 = k_{\text{pll2}} \left[X_{\Sigma 2} I_{2d} - U_g \sin \delta_2 + X_g I_{1d} \cos(\delta_1 - \delta_2) \right] \end{cases} \tag{A.5}$$

$$\begin{cases} V_{2d} = U_g \cos \delta_2 - X_g I_{1q} \cos(\delta_1 - \delta_2) - X_g I_{1d} \sin(\delta_1 - \delta_2) - X_{sum2} I_{2q} \\ I_{2q} = k_q (V_{2d} - V_{ref}) \end{cases} \tag{A.6}$$

where k_q is the droop coefficient in TVC, and the d-axis voltage and its voltage reference of the GSP inverter (IBR2) are denoted as V_{2d} and V_{ref} respectively. Combining $\epsilon_v \triangleq 1/(k_v X_{\Sigma 2} + 1)$, (A.5) and (A.6), the equations can be rearranged as

$$\begin{cases} \dot{\delta}_1 = k_{\text{pll1}} \left[X_{1+2//g} I_{d1} - \dfrac{X_g V_{ref}}{X_{\Sigma 2}} \sin(\delta_1 - \delta_2) - \dfrac{X_2 U_g}{X_{\Sigma 2}} \sin \delta_1 + \varepsilon_{lp}(k_v, k_{\text{pll2}}, (\delta_1 - \delta_2)) \right] \\ \dot{\delta}_2 = k_{\text{pll2}} \left[X_{\Sigma 2} I_{d2} + X_g I_{d1} \cos(\delta_1 - \delta_2) - U_g \sin \delta_2 \right] \end{cases} \tag{A.7}$$

where

$$\begin{aligned} \varepsilon_{lp} &= \epsilon_v g_1(\delta_1 - \delta_2) + \epsilon_{\text{PLL}} h_1(\delta_1 - \delta_2) \\ g_1(\delta_1 - \delta_2) &= \frac{X_g}{X_{\Sigma 2}} V_{ref} \sin(\delta_1 - \delta_2) + \frac{X_g}{X_{\Sigma 2}} U_g \cos \delta_2 \sin(\delta_2 - \delta_1) \\ &\quad + \frac{X_g^2}{X_{\Sigma 2}} I_{d1} \sin(\delta_2 - \delta_1)^2 \\ h_1(\delta_1 - \delta_2) &= \frac{X_g}{X_{\Sigma 2}} \cos(\delta_1 - \delta_2) \end{aligned} \tag{A.8}$$

In (A.8), the definition of $\epsilon_v \triangleq 1/(k_v X_{\Sigma 2} + 1)$ represents the voltage control error. The $\epsilon_{\text{PLL}} \triangleq \dot{\delta}_2 / k_{\text{pll2}} = v_{q2}$ represents dynamics of the difference between the angle of PLL in

IBR2 and its steady state. When k_{pll2} is large enough, which means that the dynamic of PLL in IBR2 is much faster than PLL1 in IBR1, the perturbed term ϵ_{PLL} can be regarded as zero. Also, when the voltage control gain k_v is large enough, indicating more effective voltage control with smaller error, the term ϵ_v is approximately 0. Under this case ($\epsilon_v \approx 0$, $\epsilon_{\text{PLL}} \approx 0$), the sets of Equations (A.4) and (A.7) are identical, and they share the same form as shown in Eq. 3.3 in Chapter 4, which is:

$$\begin{cases} \dot{\delta}_1 = k_{\text{pll1}} \left[X_{1+2//g} I_{1d} - \dfrac{X_g}{X_{\Sigma 2}} V_{ref} \sin(\delta_1 - \delta_2) - \dfrac{X_2}{X_{\Sigma 2}} U_g \sin \delta_1 \right] \\ \dot{\delta}_2 = k_2 \left[C_2 - U_g \sin \delta_2 + I_{1d} X_g \cos(\delta_1 - \delta_2) \right] \end{cases} \tag{A.9}$$

where C_2 represents a constant.

A.1.5 Combination of GFM and GSP inverter

When IBR1 is the GFM inverter and IBR2 is the GSP inverter in Figure 3.2, the nonlinear differential equations describing the system can be expressed jointly by (A.10) and (A.11)

$$\begin{cases} \dot{\delta}_1 = k_{\text{droop}} \left[P_{ref} + \dfrac{X_g I_{2d}}{X_{\Sigma 1}} V_1 \cos(\delta_2 - \delta_1) - \dfrac{X_g I_{2q}}{X_{\Sigma 1}} V_1 \sin(\delta_2 - \delta_1) \right. \\ \qquad \left. - \dfrac{U_g V_1}{X_{\Sigma 1}} \sin \delta_1 \right] \\ \dot{\delta}_1 = k_{\text{pll}} \left[X_{2+1//g} I_{2d} - \dfrac{X_g}{X_{\Sigma 1}} V_1 \sin(\delta_2 - \delta_1) - \dfrac{X_1}{X_{\Sigma 1}} U_g \sin \delta_2 \right] \end{cases} \tag{A.10}$$

$$\begin{cases} v_{2d} = \dfrac{X_g}{X_{\Sigma 1}} V_1 \cos(\delta_2 - \delta_1) + \dfrac{X_1}{X_{\Sigma 1}} U_g \cos \delta_2 - X_{2+1//g} I_{2q} \\ I_{2q} = k_q (v_{2d} - v_{ref}) \end{cases} \tag{A.11}$$

which can be simplified to

$$\begin{cases} \dot{\delta}_1 = k_{\text{droop}} \left[P_{ref} - \dfrac{V_{ref} V_1 \sin(\delta_1 - \delta_2)}{X_{\Delta 12}} - \dfrac{V_1 U_g \sin \delta_1}{X_{\Delta g1}} + \varepsilon_{mp}(k_v, k_{\text{pll}}, (\delta_1 - \delta_2)) \right] \\ \dot{\delta}_2 = k_{\text{pll}} \left[X_{2+1//g} I_{d2} - \dfrac{X_g V_1}{X_{\Sigma 1}} \sin(\delta_2 - \delta_1) - \dfrac{X_2 U_g}{X_{\Sigma 1}} \sin \delta_2 \right] \end{cases} \tag{A.12}$$

where

$$\begin{aligned} \varepsilon_{mp} &= \epsilon_v g_2(\delta_1 - \delta_2) + \epsilon_{\text{PLL}} h_2(\delta_1 - \delta_2) \\ g_2(\delta_1 - \delta_2) &= -\frac{X_g}{X_{\Delta 12} X_{\Sigma 1}} {V_1}^2 \cos(\delta_1 - \delta_2) \sin(\delta_1 - \delta_2) \\ &\quad - \frac{X_1}{X_{\Delta 12} X_{\Sigma 1}} V_g V_1 \cos \delta_2 \sin(\delta_1 - \delta_2) \\ &\quad + \frac{V_1 V_{ref}}{X_{\Delta 12}} \sin(\delta_1 - \delta_2) \\ h_2(\delta_1 - \delta_2) &= \frac{V_1 \cos(\delta_1 - \delta_2)}{X_{\Delta 12}} \end{aligned} \tag{A.13}$$

In (A.13), the definition of $\epsilon_v \triangleq 1/\left(k_v X_{2+1//g} + 1\right)$ represents the voltage control error. The $\epsilon_{\text{PLL}} \triangleq \dot{\delta}_2 / k_{\text{pll}} = v_{q2}$ represents dynamics of the difference between the angle of PLL in IBR1 and its steady state. When k_{pll} is large enough, which means that the dynamic

of PLL is much faster than GFM, the perturbed term ϵ_{PLL} can be regarded as zero. Also, when the voltage control gain k_v is large enough, indicating more effective voltage control with smaller error, the term ϵ_v is approximately 0. Under this case ($\epsilon_v \approx 0$, $\epsilon_{\text{PLL}} \approx 0$), the sets of Equations (A.12) and (A.1) are identical, and they share the same form as shown in Eq. 3.3 in Chapter 4, which is:

$$\begin{cases} \dot{\delta}_1 = k_1 \left[C_1 - A_1 \sin\left(\delta_1 - \delta_2\right) - B_1 \sin \delta_1 \right] \\ \dot{\delta}_2 = k_2 \left[C_2 - A_2 \sin\left(\delta_2 - \delta_1\right) - B_2 \sin \delta_2 \right] \end{cases} \tag{A.14}$$

where C_1, C_2, A_1, A_2, B_1, B_2 represent constants.

A.2 Source Code and Simulations

All EMT simulations and code for the calculation of ROA in this Chapter can be found in [146].

Appendix B

Appendix for Chapter 4

B.1 Full-Order ODE Model of GFL Inverter

In this chapter, the PLL is designed to be over-damped, while the DVC and the inner current loop are implemented as typical second-order systems. The PI controllers are designed in the small-signal domain. The closed-loop transfer function of the PLL is given by

$$G_{\text{pll}}(s) = \frac{\Delta\delta}{\Delta V_q} = \frac{k_{\text{p,pll}} + k_{\text{i,pll}}/s}{s + V_d(k_{\text{p,pll}} + k_{\text{i,pll}}/s)}$$

according to [97]. Assuming $V_d \approx 1$ at steady state and neglecting the integral term, which corresponds to an overdamped PLL design, we have $G_{\text{pll}}(j\omega_{\text{pll}})|_{\omega_{\text{pll}}=k_{\text{p,pll}}} = -3$ dB. This overdamped setting is commonly adopted since the small integral term and large proportional term are beneficial to transient stability (see Chapter 2). Such an overdamped design has also been adopted in [144, 53, 107, 108]. In this Chapter, we define $\zeta_{\text{pll}} = k_{\text{i,pll}}/k_{\text{p,pll}}$.

The closed-loop transfer function of the DVC is:

$$G_{\text{dvc}}(s) = \frac{k_{\text{p,dvc}} + k_{\text{i,dvc}}/s}{sC_{\text{dc}}/\omega_s + k_{\text{p,dvc}} + k_{\text{i,dvc}}/s}$$

and the gains are selected as $k_{\text{p,dvc}} = \frac{C_{\text{dc}}/\omega_s}{2} \cdot \omega_{\text{dvc}}$ and $k_{i,\text{dvc}} = \zeta_{\text{dvc}}\frac{C_{\text{dc}}/\omega_s}{2} \cdot {\omega_{\text{dvc}}}^2$. When $\zeta_{\text{dvc}} = 1/4$, the DVC becomes a critically damped second-order system [9], with $G_{\text{dvc}}(j\omega_{\text{dvc}}) \approx -3$ dB. The same PI design approach is also applied to the inner current loop.

By substituting the above expressions for loop bandwidths, the nonlinear differential equations in (4.1),(4.2), and (4.3) can be reformulated as (4.4), and the detailed expressions in (4.4) are as follows:

$$\begin{aligned} f_{\text{pll},1}\left(\delta, i_d, \frac{x_{\text{int,pll}}}{\omega_{\text{pll}}}\right) =& \frac{X_g i_d - U_g \sin\delta + x_{\text{int,pll}}/\omega_{\text{pll}}}{1 - k_{\text{p,pll}} L_g/\omega_{\text{s}} \cdot i_d} \\ f_{\text{pll},2}\left(\delta, i_d, x_{\text{int,pll}}\right) =& \zeta_{\text{pll}} \frac{X_g i_d - U_g \sin\delta + x_{\text{int,pll}} i_d L_g/\omega_{\text{s}}}{1 - k_{\text{p,pll}} L_g/\omega_{\text{s}} \cdot i_d} \end{aligned} \tag{B.1a}$$

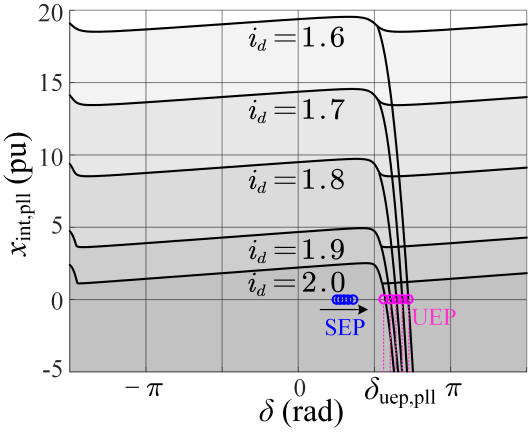


Figure B.1: Stability region of PLL subsystem under different i_d ($\omega_{\text{pll}} = 15$ Hz $\times 2\pi$).

$$\begin{aligned} f_{\text{dvc},1}\left(\delta, i_{\text{dq}}, \omega_{\text{vdc}}\Delta\left(v_{\text{dc}}\right)^2\right) =& P_{in} - i_d U_g \cos\delta + i_q U_g \sin\delta \\ &+ \frac{C_{\text{dc}}/\omega_s}{2}\zeta_{\text{dvc}}\omega_{\text{dvc}}\Delta\left(v_{\text{dc}}\right)^2 \end{aligned} \tag{B.1b}$$

$$f_{\text{dvc},2}\left(\delta, i_{\text{dq}}\right) = \frac{2}{C_{\text{dc}}/\omega_s}\left(P_{in} - i_d U_g \cos\delta + i_q U_g \sin\delta\right)$$

$$f_{\text{tvc}}\left(\delta, i_q\right) = -i_q + k_v U_g \cos\delta - k_v i_q X_g - k_v V_{ref} \tag{B.1c}$$

B.2 Reduced-Order Model Derivation

B.2.1 Bandwidth sequence: ω_{pll} larger than ω_{dvc}

The PLL (4.1) is considered as fast subsystem, and defining $\varepsilon = \frac{1}{\omega_{\text{pll}}} \cdot (1 - k_{\text{p,pll}} L_g/\omega_{\text{s}} \cdot i_d)$, It clear that as $\omega_{\text{pll}} \to \infty$, $\varepsilon \to 0$. Introducing the fast time-scale $\tau = t/\varepsilon$, the fast subsystem equations become:

$$\begin{cases} \frac{d}{d\tau}\delta = (X_g i_d - U_g \sin\delta) + \frac{x_{\text{int_pll}}}{\omega_{pll}} \\ \frac{d}{d\tau}x_{\text{int,pll}} = \zeta_{\text{pll}}(X_g i_d - U_g \sin\delta + x_{\text{int,pll}} L_g/\omega_s \cdot i_d) \end{cases} \tag{B.2}$$

Since ω_{pll} is large, $x_{\text{int,pll}}/\omega_{\text{pll}} \approx 0$. Under a fixed i_d, this subsystem rapidly converges to a SEP defined by:

$$\bar{\delta} = \text{asin}\left(\frac{X_g i_d}{U_g}\right), \bar{x}_{\text{int,pll}} = 0 \tag{B.3}$$

The SEP is uniformly exponentially stable if the following conditions hold:

$$i_d < \frac{\sqrt{{U_g}^2 - \left(X_g i_d\right)^2}}{\zeta_{\text{pll}} L_g/\omega_s}, i_d < U_g/X_g, i_d < 1/\omega_{\text{pll}} L_g \tag{B.4}$$

And the stability region for different i_d is illustrated in Figure B.1. Following singular perturbation theory, we represent the fast dynamics as:

$$\delta\left(t\right) = \bar{\delta}\left(t\right) + \delta^*\left(\tau\right) + O\left(\varepsilon\right) \tag{B.5}$$

where the boundary-layer dynamics satisfy:

$$\frac{d}{d\tau}\delta^*(\tau) = X_g i_d - U_g \sin\left(\operatorname{asin}\left(\frac{X_g i_d}{U_g}\right) + \delta^*(\tau)\right) \tag{B.6}$$

The DVC loop is the slow subsystem. Following the asymptotic expansion methodology of O'Malley and Smith [132, 133], the slow variables are expanded as:

$$i_d = \bar{i}_d + \varepsilon i_d^*(\tau) + O(\varepsilon) \tag{B.7}$$

where $\bar{i}_d$ and $\overline{\Delta(v_{\mathrm{dc}})^2}$ satisfy the reduced-order slow subsystem equations:

$$\frac{d}{dt}\begin{bmatrix} \bar{i}_d \\ \overline{\Delta(v_{\mathrm{dc}})^2} \end{bmatrix} = \begin{bmatrix} \omega_{\mathrm{dvc}} f_{\mathrm{dvc},1}\left(\bar{\delta}, i_{\mathrm{dq}}, \omega_{\mathrm{dvc}}\overline{\Delta(v_{\mathrm{dc}})^2}\right) \\ f_{\mathrm{dvc},2}\left(\bar{\delta}, i_{\mathrm{dq}}\right) \end{bmatrix} \tag{B.8}$$

with $\bar{\delta} = \operatorname{asin}\left(\frac{X_g i_d}{U_g}\right)$ substituted from the equilibrium of the fast subsystem.

The boundary-layer correction terms–$\varepsilon i_d^*(\tau)$ and $\varepsilon\left[\Delta(v_{\mathrm{dc}})^2\right]^*$–describe the rapid decay of the fast dynamics. They are $O(\varepsilon)$ in magnitude and vanish on the fast time scale τ; hence, they do not modify the reduced-order differential equations. They act only as initial-value corrections to the slow subsystem immediately at fault clearance. These corrections are approximated as:

$$\begin{aligned} {i_d}^*(\tau) &= -\omega_{\mathrm{dvc}} \int_\tau^\infty f_{\mathrm{dvc},1}\left(\bar{\delta}(0) + \delta^*(\tau), i_{\mathrm{dq}}(0), \omega_{\mathrm{dvc}}\Delta(v_{\mathrm{dc}})^2(0)\right) \\ &\quad - f_{\mathrm{dvc},1}\left(\bar{\delta}(0), i_{\mathrm{dq}}(0), \omega_{\mathrm{dvc}}\Delta(v_{\mathrm{dc}})^2(0)\right) d\tau \\ &\approx k_{\mathrm{p,dvc}} \frac{2}{C_{\mathrm{dc}}} U_g i_d(0) \sin\bar{\delta}(0) \cdot \frac{\delta(0) - \bar{\delta}(0)}{U_g \cos\bar{\delta}(0)} e^{-U_g \cos\bar{\delta}(0)\tau} \end{aligned} \tag{B.9a}$$

$$\begin{aligned} \left[\Delta(v_{\mathrm{dc}})^2\right]^*(\tau) &= -\int_\tau^\infty f_{\mathrm{DVC},2}\left(\bar{\delta}(0) + \delta^*(\tau), i_{\mathrm{dq}}(0), \omega_{\mathrm{dvc}}\Delta(v_{\mathrm{dc}})^2(0)\right) \\ &\quad - f_{\mathrm{DVC},2}\left(\bar{\delta}(0), i_{\mathrm{dq}}(0), \omega_{\mathrm{dvc}}\Delta(v_{\mathrm{dc}})^2(0)\right) d\tau \\ &\approx \frac{2}{C_{\mathrm{dc}}} U_g i_d(0) \sin\bar{\delta}(0) \cdot \frac{\delta(0) - \bar{\delta}(0)}{U_g \cos\bar{\delta}(0)} e^{-U_g \cos\bar{\delta}(0)\cdot\tau} \end{aligned} \tag{B.9b}$$

where $\delta(0)$ denotes the initial post-fault value, differing from $\bar{\delta}(0)$ which determined by the initial value of slow variables.

B.2.2 Bandwidth sequence: ω_{dvc} larger than ω_{pll}

The DVC (4.2) is considered as fast subsystem, and defining $\varepsilon = 1/\omega_{\mathrm{dvc}}$, It clear that as $\omega_{\mathrm{dvc}} \to \infty$, $\varepsilon \to 0$. Introducing the fast time-scale $\tau = t/\varepsilon$, and do variable substitution $\sigma = \omega_{\mathrm{dvc}} \cdot \Delta(v_{\mathrm{dc}})^2$, the fast subsystem equations become:

$$\begin{cases} \frac{d}{d\tau} i_d = (P_{in} - i_d U_g \cos\delta + i_q U_g \sin\delta) + \frac{C_{\mathrm{dc}}/\omega_s}{2}\zeta_{\mathrm{dvc}}\sigma \\ \frac{d}{d\tau}\sigma = \frac{2}{C_{\mathrm{dc}}}(P_{in} - i_d U_g \cos\delta + i_q U_g \sin\delta) \end{cases} \tag{B.10}$$

It is a linear differential equation for fixed δ, and it is easy to prove that if $\cos\delta > 0$, the Jacobian is negative, which means that the fast subsystem is globally asymptotically stable. They rapidly converges to $\bar{i}_d$ and $\bar{\sigma}$:

$$P_{in} - \bar{i}_d U_g \cos\delta + i_q U_g \sin\delta = 0, \bar{\sigma} = 0 \tag{B.11}$$

Similarly, following singular perturbation theory, the fast-subsystem dynamics can be expressed as:

$$\begin{cases} i_d(t) = \bar{i}_d(t) + i_d(\tau) + O(\varepsilon) \\ \sigma(t) = \bar{\sigma}(t) + \sigma(\tau) + O(\varepsilon) \end{cases} \tag{B.12}$$

where the boundary-layer dynamics satisfy:

$$\begin{cases} \frac{d}{d\tau} i_d^*(\tau) = -i_d^*(\tau) U_g \cos\delta(0) + \frac{C_{\mathrm{dc}}/\omega_s}{2} \zeta_{\mathrm{dvc}} \sigma^*(\tau) \\ \frac{d}{d\tau} \sigma^*(\tau) = -\frac{2}{C_{\mathrm{dc}}} i_d^*(\tau) U_g \cos\delta(0) \end{cases} \tag{B.13}$$

The PLL loop is the slow subsystem. Following the asymptotic expansion methodology [133, 132] the slow variables are expanded as:

$$\begin{cases} \delta(t) = \bar{\delta}(t) + \varepsilon\delta^*(\tau) + O(\varepsilon) \\ x_{\mathrm{int,pll}}(t) = \bar{x}_{\mathrm{int,pll}}(t) + \varepsilon x^*_{\mathrm{int,pll}}(\tau) + O(\varepsilon) \end{cases} \tag{B.14}$$

where $\bar{\delta}(t)$ and $\bar{x}_{\mathrm{int,pll}}$ satisfy the reduced-order slow subsystem equations:

$$\begin{bmatrix} \dot{\delta} \\ \dot{x}_{\mathrm{int,pll}} \end{bmatrix} = \begin{bmatrix} \omega_{\mathrm{pll}} f_{\mathrm{pll},1}\left(\delta, \bar{i}_d, \frac{x_{\mathrm{int,pll}}}{\omega_{\mathrm{pll}}}\right) \\ \omega_{\mathrm{pll}} f_{\mathrm{pll},2}(\delta, \bar{i}_d, x_{\mathrm{int,pll}}) \end{bmatrix} \tag{B.15}$$

with $\bar{i}_d$ substituted from the equilibrium of the fast subsystem.

The boundary layer correction terms $\varepsilon\delta^*(\tau)$ and $\varepsilon x^*_{\mathrm{int,pll}}(\tau)$ are $O(\varepsilon)$ in magnitude and decay rapidly on the fast time scale τ; thus do not affect the reduced-order slow-subsystem differential equations. They serve only as initial value corrections, representing the transient effect of boundary-layer dynamics on the slow subsystem immediately at the fault clearance. These corrections are approximated as:

$$\begin{aligned} \delta^*(\tau) &= -\omega_{\mathrm{pll}} \int_\tau^\infty f_{\mathrm{pll},1}\left(\delta(0), i_{\mathrm{d}}^*, \frac{x_{\mathrm{int,pll}}(0)}{\omega_{\mathrm{pll}}}\right) d\tau \\ x^*_{\mathrm{int,pll}}(\tau) &= -\omega_{\mathrm{pll}} \int_\tau^\infty f_{\mathrm{pll},2}(\delta(0), i_{\mathrm{d}}^*, x_{\mathrm{int,pll}}(0)) d\tau \end{aligned} \tag{B.16}$$

B.2.3 Stability analysis of TVC subsystem

Since the DVC loop does not affect the TVC loop, only the influence of the PLL is considered. The differential equation (4.3), which governs i_q, is a linear system with δ serving as the input. It is globally exponentially stable uniformly in δ, and therefore input-to-state stable (ISS) according to Lemma 4.6 in [31]. In particular, if $\delta(t)$ converges to a constant,

then $i_q(t)$ asymptotically converges to the corresponding steady-state value. In summary, if δ can be stable, then (4.3) is stable.

B.3 System Parameters

If not specified, the system parameters used in Chapter 4 are listed in Table B.1.

Table B.1: Parameters in Simulation and HIL Experiment

Parameters	Value[1]	
	Simulation	HIL Experiment
Base capacity S_b	1	1 MVA
Base voltage V_b	1	690 V
Base current I_b	1	1.45 kA
Base frequency $\omega_s/2\pi$	50 Hz	50 Hz
Grid voltage U_g	1 pu	690 V
Input power P_{in}	1 pu	1 MW
Short circuit ratio (SCR)	2.1	2.1
Grid impedance Z_g	$0.47j + 0.002$ pu	0.72mH + 0.95mΩ
DC voltage reference $V_{\text{dc,ref}}$	2.5 pu	1725 V
DC capacitor[2] C_{dc}	12.5 pu	83 mF
DC voltage limiter $V_{\text{dc,limit}}$	2-3 pu (±20%)	1380 - 2070 V
PLL PI controller	$k_{\text{p,pll}} = \omega_{\text{pll}}$ $k_{\text{i,pll}} = \zeta_{\text{pll}} \cdot k_{\text{p,pll}}$, $\zeta_{\text{pll}} = 1/4$	same
DVC PI controller	$k_{\text{p,dvc}} = \omega_{\text{dvc}} \cdot C_{\text{dc}}/2\omega_s$ $k_{\text{i,dvc}} = k_{\text{p,dvc}} \cdot \omega_{\text{dvc}}/4$	same
Droop gain in TVC k_v	2 pu	same
TVC voltage reference V_{ref}	0.81 pu	560 V
Inner current control loop bandwidth	1 kHz	same
Current limit[3] I_{limit}	2.5 pu	3.1 kA
LC filter L_f	0.05 pu	75.7 μH
LC filter C_f	0.01 pu	66.8 μF
Equivalent switching frequency[2]	averaging model	10 kHz
DSP control frequency	–	10 kHz

[1] The pu values in simulation and experiment are exactly the same.
[2] In practice, electrolytic and film capacitors are paralleled in the DC-link, resulting in negligible ESL and very small ESR; thus, ESL is neglected, and ESR is set to 0.001 pu.
[3] Rectangular current limiter.
[4] For MW-scale SiC converters, switching frequencies on the order of 10 kHz are generally achievable. Alternatively, by adopting multilevel topologies (e.g., five-level converters), 750 V 1.9 kA Si-IGBT power modules (such as the Infineon FS950R08A6P2B) can be operated at a switching frequency of 5 kHz, while achieving an equivalent switching frequency that is effectively doubled [88].

B.4 Source Code and Simulations

The EMT simulations and all numerical calculations in this Chapter are also available online at [161].